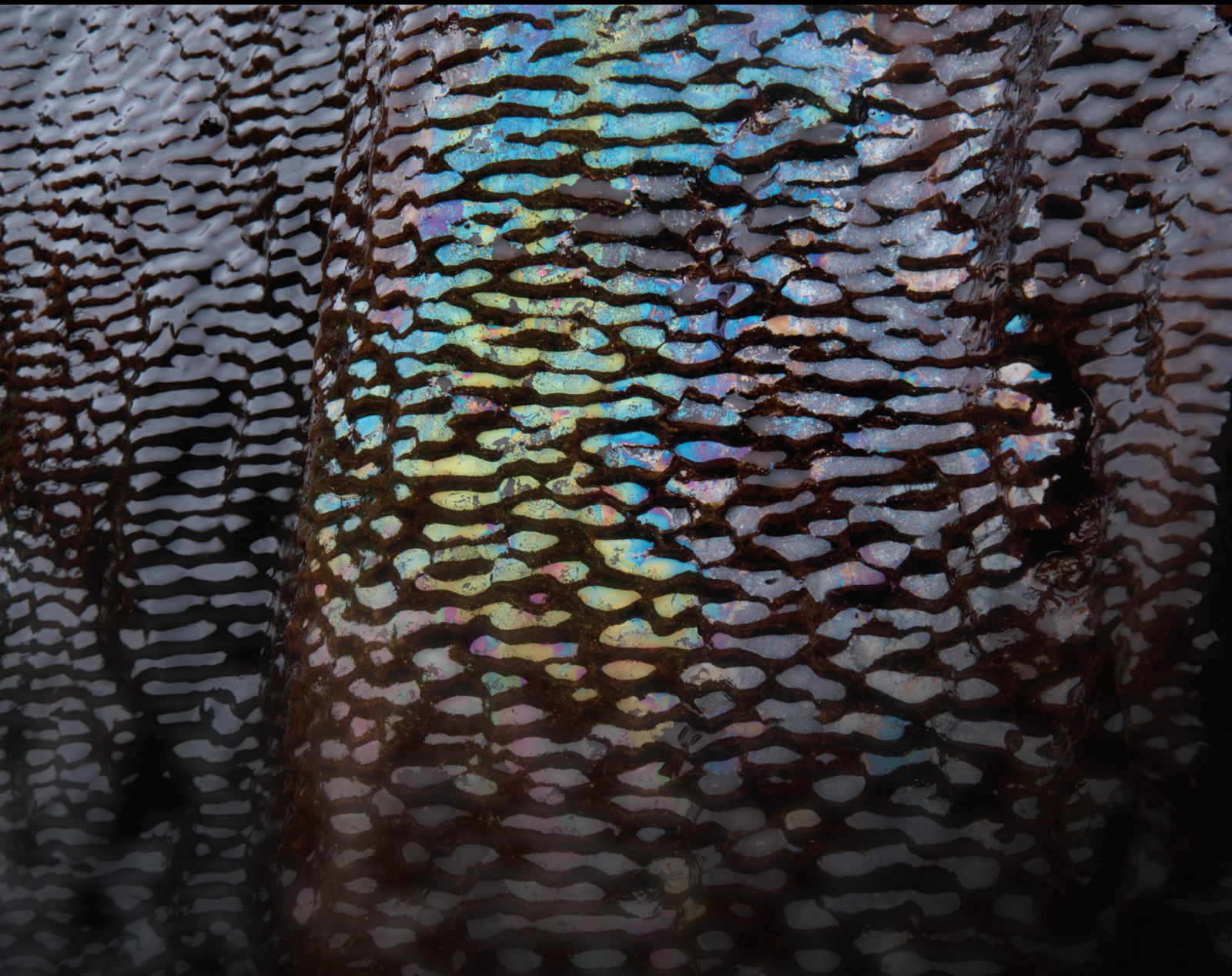


Recent Advances in Geological Hazards of Tunnel and Underground Engineering

Lead Guest Editor: Ying-chao Wang

Guest Editors: Yang Yu, Lei Wang, and Fan Geng





Recent Advances in Geological Hazards of Tunnel and Underground Engineering

Geofluids

Recent Advances in Geological Hazards of Tunnel and Underground Engineering

Lead Guest Editor: Ying-chao Wang

Guest Editors: Yang Yu, Lei Wang, and Fan Geng







Copyright © 2022 Hindawi Limited. All rights reserved.

This is a special issue published in "Geofluids." All articles are open access articles distributed under the Creative Commons Attribution License, which permits unrestricted use, distribution, and reproduction in any medium, provided the original work is properly cited.



























Chief Editor

































Umberta Tinivella, Italy

Associate Editors

Paolo Fulignati , Italy
Huazhou Li , Canada
Stefano Lo Russo , Italy
Julie K. Pearce , Australia

Academic Editors

Basim Abu-Jdayil , United Arab Emirates
Hasan Alsaedi , USA
Carmine Apollaro , Italy
Baojun Bai, USA
Marino Domenico Barberio , Italy
Andrea Brogi , Italy
Shengnan Nancy Chen , Canada
Tao Chen , Germany
Jianwei Cheng , China
Paola Cianfarra , Italy
Daniele Cinti , Italy
Timothy S. Collett , USA
Nicoló Colombani , Italy
Mercè Corbella , Spain
David Cruset, Spain
Jun Dong , China
Henrik Drake , Sweden
Farhad Ehya , Iran
Lionel Esteban , Australia
Zhiqiang Fan , China
Francesco Frondini, Italy
Ilaria Fuoco, Italy
Paola Gattinoni , Italy
Amin Gholami , Iran
Michela Giustiniani, Italy
Naser Golsanami, China
Fausto Grassa , Italy
Jianyong Han , China
Chris Harris , South Africa
Liang He , China
Sampath Hewage , Sri Lanka
Jian Hou, China
Guozhong Hu , China
Lanxiao Hu , China
Francesco Italiano , Italy
Azizollah Khormali , Iran
Hailing Kong, China

Karsten Kroeger, New Zealand
Cornelius Langenbruch, USA
Peter Leary , USA
Guangquan Li , China
Qingchao Li , China
Qibin Lin , China
Marcello Liotta , Italy
Shuyang Liu , China
Yong Liu, China
Yueliang Liu , China
Constantinos Loupasakis , Greece
Shouqing Lu, China
Tian-Shou Ma, China
Judit Mádl-Szonyi, Hungary
Paolo Madonia , Italy
Fabien Magri , Germany
Micòl Mastroicco , Italy
Agnes Mazot , New Zealand
Yuan Mei , Australia
Evgeniy M. Myshakin , USA
Muhammad Tayyab Naseer, Pakistan
Michele Paternoster , Italy
Mandadige S. A. Perera, Australia
Marco Petitta , Italy
Chao-Zhong Qin, China
Qingdong Qu, Australia
Reza Rezaee , Australia
Eliahu Rosenthal , Israel
Gernot Rother, USA
Edgar Santoyo , Mexico
Mohammad Sarmadivaleh, Australia
Venkatramanan Senapathi , India
Amin Shokrollahi, Australia
Rosa Sinisi , Italy
Zhao-Jie Song , China
Ondra Sracek , Czech Republic
Andri Stefansson , Iceland
Bailu Teng , China
Tivadar M. Tóth , Hungary
Orlando Vaselli , Italy
Benfeng Wang , China
Hetang Wang , China
Wensong Wang , China
Zhiyuan Wang , China
Ruud Weijermars , Saudi Arabia

Bisheng Wu , China
Da-yang Xuan , China
Yi Xue , China
HE YONGLIANG, China
Fan Yang , China
Zhenyuan Yin , China
Sohrab Zendehboudi, Canada
Zhixiong Zeng , Hong Kong
Yuanyuan Zha , China
Keni Zhang, China
Mingjie Zhang , China
Rongqing Zhang, China
Xianwei Zhang , China
Ye Zhang , USA
Zetian Zhang , China
Ling-Li Zhou , Ireland
Yingfang Zhou , United Kingdom
Daoyi Zhu , China
Quanle Zou, China
Martina Zucchi, Italy

Contents

The Progressive Failure Mechanism of the Tunnel-Slope System under Rainfall: An Experimental Investigation

Qinglei Jiao , Yingchao Wang , and Wen Jiang 



Research Article (16 pages), Article ID 1775049, Volume 2022 (2022)

Superimposed Stress Calculation of Soil Underlying Anchor Beam considering Anisotropy and Strength Nonhomogeneity

Fei Xu , Zhongshun Wang, Liming Zhou , Hemin Zheng, Bo Liu, Yuqiu Jiang, and Daili Wang

Research Article (12 pages), Article ID 5686814, Volume 2022 (2022)

Head-On Dynamic Manifestations in the Roadway Driving with Small Coal Pillar under the Influence of Roof Drainage: A Case Study from Uxin Banner

Yunhai Cheng , Fenghui Li , Xiufeng Zhang, Chao Wang, and Gangwei Li

Research Article (11 pages), Article ID 7447423, Volume 2022 (2022)

Impact of Depressurizing Boreholes on Energy Dissipation in Deep Roadway

Meng Wang, Zhixue Li, Yalong Xu , Zhenhua Li , Ruifu Yuan, Hongchao Zhao, and Guodong Li



Research Article (13 pages), Article ID 6821810, Volume 2022 (2022)

A New Bayesian Network Model for the Risk Assessment of Water Inrush in Karst Tunnels

Yingchao Wang , Yang Liu , Zhaoyang Li, and Wen Jiang



Research Article (12 pages), Article ID 5697710, Volume 2022 (2022)

A New Method of Seismic Source Parameter Estimation of a Locked-Segment Cracking Event

Bai-Cun Yang , Jian-Xin Bai, Yong-Ting Duan , and Cheng Cheng




Research Article (9 pages), Article ID 4224176, Volume 2022 (2022)

Analysis of Settlement Induced by Shield Construction of the Metro Passing under Existing Buildings Based on the Finite Difference Method

Rui Wang , Bin Zhang, and You Wang 

Research Article (15 pages), Article ID 1206867, Volume 2022 (2022)

Identification of Mine Water Source Based on AHP-Entropy and Set Pair Analysis

Xianming Zhao , Zhimin Xu , and Yajun Sun 




Research Article (10 pages), Article ID 3862746, Volume 2022 (2022)

Roadway Deformation and Control under Multidisturbed Secondary High Stress

Xiaoguang Sun, Haibin Wang, Xiaofang Wo , Zhimeng Sun, Wenliang Sun, and Chungue Li

Research Article (12 pages), Article ID 3166065, Volume 2022 (2022)


Numerical and Experimental Study on End Effect of Waste-Soil Samples under Uniaxial Compression

Yukai Wang , Xiaoli Liu , and Bo Pang 

Research Article (11 pages), Article ID 3014164, Volume 2022 (2022)



Influence of Arch Foot Defect of Primary Support on Mechanical Behaviors of an Arch Frame in Underground Tunnels

Yakun Wang, Junwei Guo , Jizeng Zhao, Xuxu Yang, Weiteng Li, and Junfeng Liu
Research Article (18 pages), Article ID 9593566, Volume 2022 (2022)

Research Article

The Progressive Failure Mechanism of the Tunnel-Slope System under Rainfall: An Experimental Investigation

Qinglei Jiao ^{1,2}, Yingchao Wang ^{1,3} and Wen Jiang ³

¹State Key Laboratory for Geomechanics and Deep Underground Engineering, China University of Mining and Technology, Xuzhou, Jiangsu 221116, China

²T. Y. Lin International Engineering Consulting (China) Co. Ltd. Xuzhou Branch, Xuzhou, Jiangsu 221116, China

³School of Mechanics and Civil Engineering, China University of Mining and Technology, Xuzhou, Jiangsu 221116, China

Correspondence should be addressed to Yingchao Wang; wangyingchao@cumt.edu.cn

Received 8 April 2022; Accepted 11 August 2022; Published 22 September 2022

Academic Editor: Mohammed Fattah

Copyright © 2022 Qinglei Jiao et al. This is an open access article distributed under the Creative Commons Attribution License, which permits unrestricted use, distribution, and reproduction in any medium, provided the original work is properly cited.

Tunnel excavation has always been an important reason for the stability failure of the tunnel-slope system at the portal section. In case of rainfall, it is likely to cause serious disasters such as tunnel vault collapse, water inrush from the tunnel face, and slope slip. In this study, the Sunjiaya tunnel of the Daping slope group was taken as the engineering background, and the tunnel model experiment system under the condition of rainfall and groundwater seepage was designed independently to explore the failure laws of slope instability induced by tunnel excavation under the condition of rainfall. Meanwhile, a fiber grating monitoring system was also used to measure the displacement, water content, earth pressure, and seepage pressure at different positions of the tunnel-slope system in the process of tunnel excavation under the condition of rainfall. The results show that the slope instability caused by rainfall infiltration is gradual. At the beginning of rainfall, the rainfall infiltration has little effect on the stability of the tunnel-slope system and then gradually increases with the continuous rainfall. Finally, the slope surface is uneven, and the phenomenon of gully and surface flow is serious. The foot of slope moves back continuously, resulting in overall collapse. Moreover, during the process of tunnel excavation, the cracks on the tunnel vault of the unburied tunnel lining develop in quadratic along the tunnel excavation direction, and the closer to the excavation section, the larger the collapse range. Finally, there is an integral collapse of the vault of tunnel excavation section. In addition, variation laws of parameters in the tunnel-slope system also provide an important explanation for the hysteresis of the stability failure of the tunnel-slope system. The results have important guiding significance for the stability of the tunnel-slope system during construction.

1. Introduction

When constructing tunnels in the central and western regions in China, it is inevitable to build tunnels in the slope because of various reasons such as the particularity of engineering, route planning, and incomplete survey quality, etc. There is often a “tunnel-slope” interaction at the entrance and exit of the tunnel when the tunnel is under construction [1]. Tunnel excavation destroys the stress balance and reduces the stability greatly [2]; in case of rainfall, it is easy to induce the creep deformation of the slope and even the overall slide [3–5]. Moreover, after the slope instability, the tunnel will have cracks, deformation, and even vault collapses [6, 7], which will seri-

ously affect the construction safety and the progress of engineering. Therefore, it is of great significance to study the influence of tunnel excavation on slope stability under the condition of rainfall to ensure the engineering safety and construction quality.

In recent years, the theoretical analysis of the interaction between the tunnel and slope has developed rapidly [8], which is the important means to evaluate the stability of the tunnel-slope system. Many useful theories, such as the transmitting coefficient method [9] and the limit analysis method [10], have been applied to reveal the formation mechanism and the failure mode of tunnel structure in slope areas. Moreover, in the analysis of the tunnel-slope interaction, the theory of the

beam on elastic foundation is also often widely used [11]. At present, the finite element method is generally used to solve the problem of elastic foundation beam. However, the finite element method has a large amount of calculation and requires many parameters, which often results in a large difference between the simulation results and the actual values [12, 13]. Therefore, the slip line theory provides a new idea to evaluate the stability of the tunnel-slope system. It plays an important role in the derivation of the disturbance range caused by the tunnel excavation and the minimum safe distance between the tunnel vault and slip zone [14]. Although these theories for evaluating the stability of the tunnel-slope system are mature and perfect, they still have many disadvantages. For example, the calculation process is complex and difficult to solve, the actual engineering parameters are imperfect, and the failure process of the slope instability cannot be observed.

The geomechanical model is also one of the important measures to predict the instability of the tunnel-slope system. Relevant experts and scholars in Japan first summed up the geological model of the tunnel deformation in the slope areas. After that, Ma [15] put forward five kinds of geological structure models of the slope disease and the tunnel deformation by investigating the deformation of the main railway tunnels in the mountain areas of China. On this basis, Tao [16] theoretically analyzed the stress mode and the deformation mechanism of tunnel under the combined action of slope thrust and ground pressure. Wu [17] further enriched the geomechanical model of the tunnel-slope system and finally obtained the interaction law of the tunnel-slope system. According to the above, when dividing the geological structure model of slope diseases and tunnel deformation, most experts mainly consider the rock structure characteristics, the spatial position relationship between the tunnel and the slope, and the time effect of surrounding rock deformation [18–20]; the combined influence of engineering disturbances and hydrogeological conditions are rarely considered.

Because the large-scale model experiment can be closely combined with the actual engineering background, many experts and scholars often use this method to study the stability of tunnels in landslide areas and have made a series of results. S. Ganger [21] first discussed the slope sliding problems caused by tunnel excavation construction through model experiments and summarized the causes of diseases. Then, Tao [22] and Wu et al. [23–25] studied the interaction mechanism between slope deformation and tunnel stress in a landslide section, the variation laws of tunnel lining pressure, and the deformation characteristics of the tunnel and slope through different model experiments. On the basis of previous studies, Zhang et al. [26], Yin et al. [27], and Chen [28] obtained the stress characteristics and disaster prevention measures of tunnel damage caused by landslide instability during the operation period by studying the reinforcement effect of anchor cable of different numbers of tunnels, the stress and deformation characteristics of self-anchored reinforcement structure, and the arrangement of rear embedded antislides piles at different spacing, which provided a reference for the tunnel design in the landslide areas. At present, more and more scholars have added more field conditions to the model experiment. By studying the landslide instability induced by rainfall infiltration, Ai et al. [29] and Gao et al.

[30] have obtained the catastrophic evolution processes of the tunnel-slope system and the stress characteristics of the tunnel. Through the shaking table model experiment of the tunnel structure, Li et al. [31] obtained the acceleration characteristics, formation deformation laws, and internal force distribution of the shallow buried bias and non-bias tunnel.

Other methods, such as the numerical simulation analysis and the engineering monitoring, are often used to analyze this problem [32, 33]. Xing et al. [34] investigated the influence of the tunnel excavation on the stability of the surrounding rock mass through a three-dimensional (3D) numerical analysis under the combined action of complex geologies and engineering disturbances. The displacement and strength degradation areas around the excavation areas were discussed in detail. This study provides effective suggestions for the stability evaluation and reasonable support after the tunnel excavation in complex geology. Through numerical simulation and model experiment, Zhang et al. [35] found that the influence range of the slope deformation caused by tunnel excavation is 1.5 times that of the tunnel span. Gattinoni et al. [36] reconstructed the conceptual model of both the slope dynamics and the tunnel construction at first. Then, based on numerical simulation, it is concluded that long and heavy rainfall can contribute to slope instability much more than tunnel excavation itself. Qin [37] studied the stability of slope before and after the tunnel excavation through the actual tunnel engineering monitoring, analyzed the failure mechanism of the side slope during tunnel construction, and finally concluded that the excavation of the portal section had the greatest impact on the stability of the slope.

To sum up, previous studies on this problem mainly use theoretical analysis and numerical simulation [38] and rarely consider the impact of rainfall during the tunnel excavation. Moreover, because the model experiment often requires specific instruments and equipment, the model experiment has certain difficulty, and it is difficult to obtain the experimental law, the results of the model experiment are relatively backward compared with those of other research methods. Therefore, this study intends to use the independently designed multifunctional platform for tunnel model experiment under the action of rainfall and groundwater seepage to carry out the model experiment research. Moreover, the fiber Bragg grating (FBG) monitoring system is used to measure the water content in different positions and depths of the tunnel-slope system, as well as the change laws of displacement, soil pressure, and seepage pressure in the upper part of the tunnel vault during the whole rainfall process. This study could provide an important basis for tunnel safety in construction in the slope area.

2. The Designment of the Model Experiment

2.1. Determine Similar Parameters. In this model experiment, the Sunjiaya tunnel of the Daping slope group was taken as the engineering background. Typical slope sections were selected for the model experiment [39, 40]. According to the actual engineering size and the model experiment box specifications, the geometric similarity ratio and the bulk similarity constant were selected in this experiment.

TABLE 1: The proportion of similar soil materials.

Name	Material	Ratio
Bedrock	Clay, lime	7:3
Slope	Medium sand, clay, talcum powder, water	11:3:4:2
Sliding zone	Laying talcum powder and water with double-layer plastic film	2:1
Tunnel lining	PVC pipe	With a diameter of 15 cm

$$S_L = 80, \quad S_Y = 1. \quad (1)$$

Based on the analysis of the seepage theory and the runoff theory, the Weber criterion can be used as the rainfall similarity criterion for the rainfall infiltration experiment. The relationship between the rain intensity scale and the geometric scale can be deduced as follows [41].

$$S_u = S_l^{-1/2}. \quad (2)$$

In the model experiment, the S_l is 80, and the similar scale of rain intensity S_u is 0.11. The rain type used in this model experiment is moderate rain (30 mm/d).

2.2. Choose Similar Materials. Based on mechanical parameters of prototype soil of the Sunjiaya tunnel of the Daping slope group and previous experiments [28, 29], the similar soil materials are proportioned in Table 1.

2.3. The Model Experiment Device. The independently designed tunnel model experiment system under the action of rainfall and groundwater seepage is composed of a model experiment box, artificial rainfall simulation system, groundwater seepage simulation system, tunnel excavation simulation system, ground stress loading system, and intelligent data collection system. It belongs to a multifunctional experiment platform.

The model box [42] is shown in Figure 1; the internal net size of the model experiment box is 2.5 m × 1.0 m × 1.4 m (length × width × height). There are two tunnel openings of different sizes on the front and side of the model box. The diameter of the front tunnel excavation hole is 30 cm, and the diameter of the side tunnel excavation hole is 20 cm. In the model experiment, the box can be adjusted using the lifting angle reasonably within the range of 0~30° according to the experiment requirements (the angle control accuracy is ± 1°, and the maximum lifting mass is 20 t). In addition, visual glasses are installed on the side of the model box, which is convenient to observe the phenomenon changes in the model experiment in real time. Four pieces of visualization glasses are installed on the side of each model box, and the size of each piece of visualization glass is 80 cm × 40 cm (length × width).

The artificial rainfall simulation system [42] is mainly composed of the rainfall device and the rainfall control system, as shown in Figures 2 and 3. In the rainfall control system, the appropriate rainfall intensity can be selected in the rain intensity selection areas according to the experiment requirements. There are four rainfall modes set in this system: light rain (5~10 mm/d), moderate rain (10~25 mm/d), heavy rain (25~50 mm/d), and torrential rain (50~70 mm/d). The rainfall

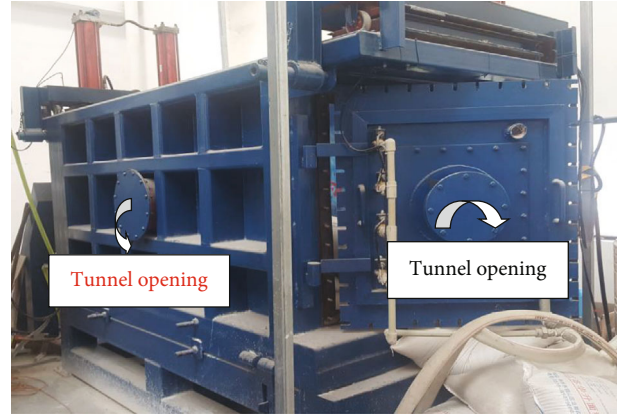


FIGURE 1: The model box [42].

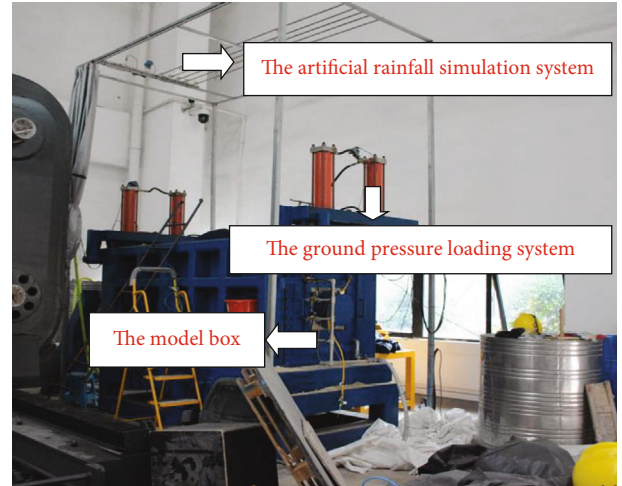


FIGURE 2: Three-dimensional tunnel model experiment system under rainfall and groundwater seepage [42].

and the dynamic rainfall curve can be viewed in the statistical rainfall curve column and the report viewing column in real time.

The rainfall device mainly adopts nozzle type sprayers, with a total of 15 sprayers, which are arranged in three columns with a spacing of 15 cm. Under the regulation of the rainfall control system, the rainfall sprinkler can automatically adjust the effective rainfall height within the range of 0~2 m and the spraying range (0~3 m²).

The groundwater seepage simulation system [42] is mainly composed of the intelligent pressurized water supply and the drainage system, as shown in Figure 4. In the intelligent



FIGURE 3: The rainfall control system.

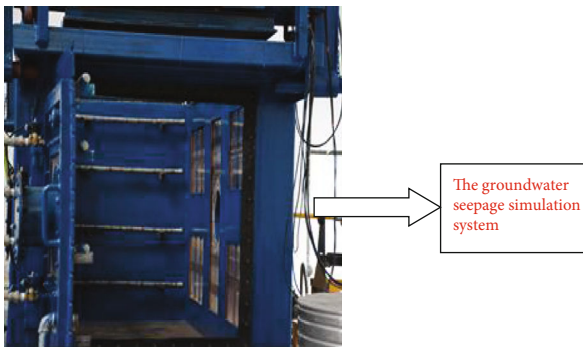


FIGURE 4: The groundwater seepage simulation system [42].



FIGURE 5: The tunnel excavation simulation system [42].



FIGURE 6: The ground stress loading system [42].

pressurized water supply system, the water supply conditions required by different experiments are mainly simulated by the layered water supply device. Among them, the layered water supply device is mainly arranged in four layers inside the model box. The total length of each layer of the water supply pipe is 80 cm, the diameter is 20 mm, and 2 mm small holes are distributed every 5 cm on the water pipe, which can meet the experiment water level requirements of 0.2 m minimum water level and 1.3 m maximum water level.

Through the combination of the intelligent data collection system and the groundwater seepage simulation system, parameters such as the pressure value of water supply pipeline of 0~0.6 MPa, the water supply flow of 0~08 m³/h, and the soil water content from 0 to 100% can be automatically collected. After the experiment is ended, the drain solenoid valve and multiple drain valves or the total drain port are opened according to the water level, and the water will be automatically discharged into the waste water collection box. The drainage system can stop working automatically when the drainage pipe does not emit water.

The tunnel excavation simulation system [42] is shown in Figure 5. The tunnel excavation device has four specifications of the excavation radius, including 15 cm, 20 cm, 25 cm, and 30 cm. The height of the support can be adjusted upward and downward, and the adjustment range is 0~130 cm. The excavation method adopts automatic drilling with an electric drilling rig, which can ensure the characteristics of the stability and the accuracy of excavation footage in the process of tunnel excavation.

The ground stress loading system [42] is mainly composed of two compression plates, each of which has an area of 0.3 m², as shown in Figure 6. The maximum pressure control range is 50 mm, and the maximum simulated ground stress is 1 MPa. It can remain stable for 7 days after the end of the pressurization.

The intelligent data collection system is mainly composed of the intelligent data collection system and the intelligent data analysis system, as shown in Figure 7. In the intelligent data collection system, the data collection is mainly carried out by the FBG demodulator and FBG monitoring elements, as shown in Figure 8. Among them, the FBG demodulator is a



FIGURE 7: The intelligent data collection system [43].

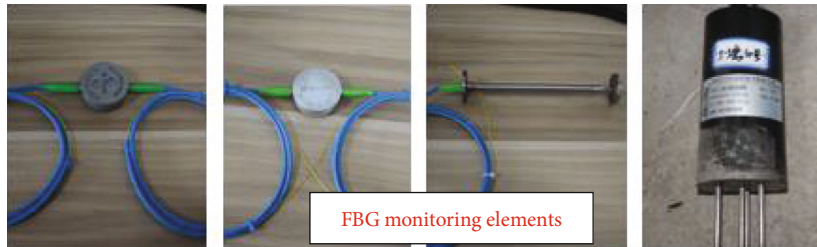


FIGURE 8: FBG monitoring elements [43].

universal 16-channel wavelength demodulator, which has the functions of 1525~1565 nm wavelength measurement range, 100 Hz wavelength demodulation rate, and the maximum capacity of 80 FBG sensors in a single channel. The main monitoring elements are fiber grating displacement gauge (accuracy: ± 0.05 mm, range: 0~40 mm), fiber grating earth pressure gauge (range: 0~1.6 MPa), and fiber grating seepage pressure gauge (range: 0~1.2 MPa). The water monitoring adopts a TDR III-type soil moisture sensor (accuracy (0~50%RH): $\pm 2\%$, range: 0~100%) in the slope. Through the intelligent data collection system and the intelligent data analysis system, the real-time monitoring and the dynamic analysis of monitoring data can be realized.

2.4. Experiment Steps

2.4.1. *Making Bedrock.* The bedrock is simulated with the mixture of clay and lime, and the bottom surface is made into a plane. Moreover, the model box is paved in layers every 10 cm and compacted layer by layer.

2.4.2. *Paving Strip.* As shown in Figure 9, the sliding material is simulated by the mixture of talcum powder and water in the middle of the double-layer plastic film. The composition ratio is 2:1, and the thickness of the strip is 5 cm.

2.4.3. *Burying Lining.* As shown in Figure 10, the supporting structure of the tunnel portal section is simulated by a PVC pipe. According to the geometric similarity ratio, the PVC pipe with a diameter of 20 cm, a length of 20 cm, and a thickness of 0.3 cm is selected for simulation.

2.4.4. *Making Slope.* The slope is simulated by the mixture of medium sand, clay, talc powder, and water. After mixing the



FIGURE 9: The paving of sliding belt materials.



FIGURE 10: The embedment of the PVC pipe.

simulated materials evenly, each 10 cm layer was paved into the model box and compacted layer by layer.

2.5. *The Embedding of Sensors.* Fiber grating sensors are mainly arranged in the model box in two layers, in which

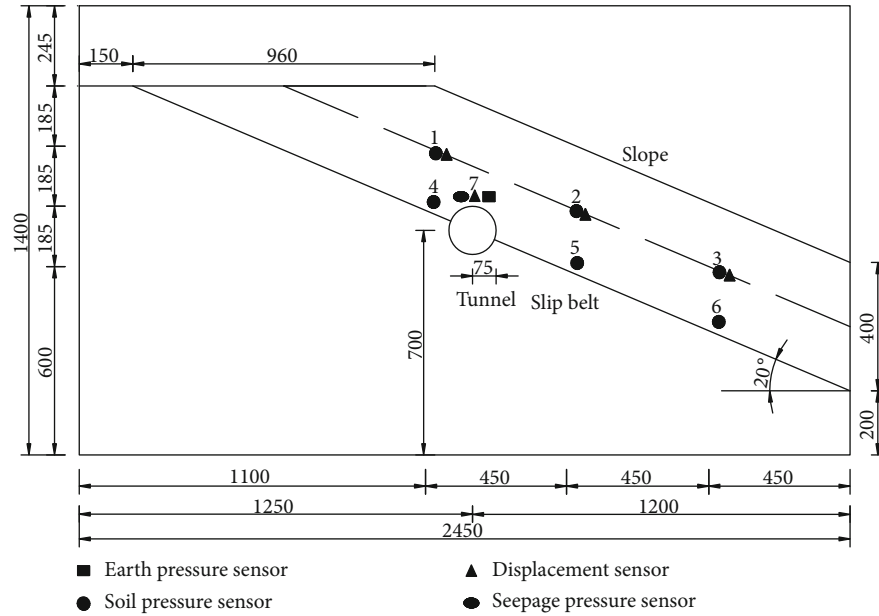


FIGURE 11: The section view of the tunnel-slope system model experiment (unit: mm).

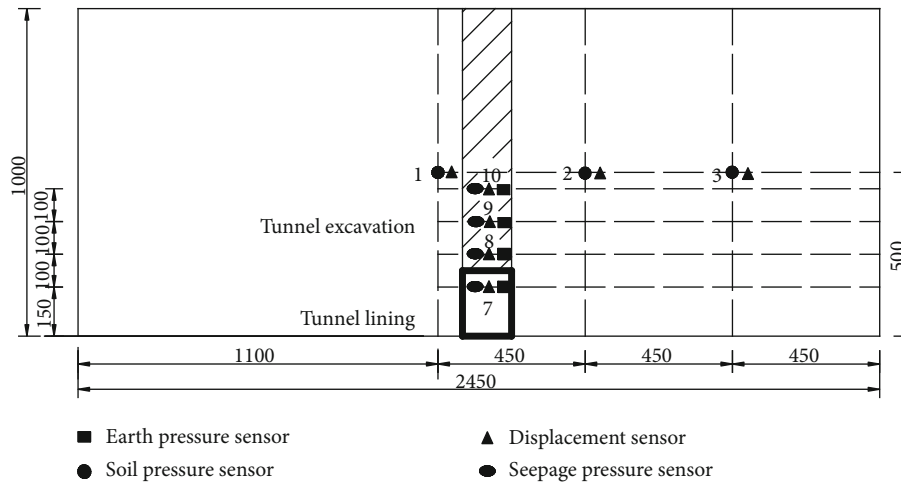


FIGURE 12: The top view of the tunnel-slope system model experiment (unit: mm).

those sensors are arranged parallel to the slide and 5 cm above the slide in the first layer. They are mainly arranged at the front, middle, and back edges of the slope. The second layer is arranged in the middle of the slope and is parallel to the first layer.

In the direction of the tunnel excavation, three sensors (displacement sensor, seepage pressure sensor, and soil pressure sensor) are arranged at 1R on the top of the tunnel vault along the direction of the tunnel axis. Specific arrangement can be seen in Figures 11 and 12.

3. The Analysis of Stability Changes of the Tunnel-Slope System during Rainfall

3.1. *The Analysis of Stability Changes during Tunnel Excavation.* Under rainfall conditions, tunnel excavation is mainly divided into the following three stages: (1) the development stage of

rainfall infiltration, (2) the development stage of the seepage channels inside the tunnel, and (3) the development stage of the tunnel arch collapse. To facilitate the control of excavation footage, the current footage of each excavation is 3 cm, which is equivalent to 3 m of the blasting excavation in actual construction. In this experiment, the electric drill is used to excavate in the form of full section for 9 times in total. When the tunnel is excavated to the ninth time, the whole tunnel vault collapses suddenly and the experiment ends.

3.1.1. *The First Stage: The Development Stage of Rainfall Infiltration.* During the first and second tunnel excavation (as shown in Figures 13(a) and 13(b)), due to the short rainfall time, the rainwater only infiltrates to the shallower position of the slope. At this time, the tunnel wall and the tunnel face are dry and smooth without falling blocks and sand. The overall self-stability of the tunnel is good.



(a) First excavation



(b) Second excavation



(c) Third excavation



(d) Fourth excavation

FIGURE 13: Continued.



(e) Fifth excavation



(f) Sixth excavation



(g) Seventh excavation



(h) Eighth excavation

FIGURE 13: Continued.



(i) Ninth excavation

(j) Water inrush from tunnel

(k) Tunnel excavation footage

FIGURE 13: The analysis of stability of the tunnel during excavation.

3.1.2. *The Second Stage: The Development Stage of the Seepage Channel inside the Tunnel.* The tunnel face after the third excavation is shown in Figure 13(c); after 30 minutes of rainfall, the tunnel wall and the tunnel face are in a wet state. Under the action of the excavation disturbance, the tunnel face transits from a smooth to rough state continuously. At this time, a small amount of water seeps out from the tunnel face at times, which shows that the seepage channel in the tunnel-slope system is gradually formed during the tunnel excavation process, but the development is limited. Blocks and sand have fallen off from the vault and the arch shoulder of the tunnel, and the stability of the tunnel excavation section is gradually decreased, but the stability of tunnel lining structure support is still good. The face after the fourth excavation is shown in Figure 13(d). After 45 minutes of rainfall, the seepage channel inside the tunnel-slope system has further developed. The amount of water infiltration on the tunnel face is increasing, and the water quality is turbid. At this time, the phenomenon of falling blocks and sand is serious. The face after the fifth excavation is shown in Figure 13(e). After 1 h of rainfall, the tunnel wall and the tunnel face are wetter than before, and the tunnel face is uneven. At this time, the phenomenon of fall-

ing blocks and sand in the tunnel is becoming more and more serious, and the self-stability of the tunnel excavation section is decreasing continuously, but the tunnel lining structure support is good. The face after the sixth excavation is shown in Figure 13(f); the mud water mixture at the front section of the tunnel face continues to flow out, which seriously blocks the tunnel excavation and requires to be cleaned manually. This shows that the internal seepage channel of the tunnel-slope system has been formed and is still developing rapidly. At this time, the stability of the tunnel excavation section is bad, but the stability of the support of tunnel lining structure is still relatively stable.

3.1.3. *The Third Stage: The Development Stage of Tunnel Arch Collapse.* The face after the seventh excavation is shown in Figure 13(g). Under the continuous tunnel excavation and rainfall infiltration, some small-scale collapses occur in the tunnel at times. The self-stability of the tunnel excavation section is worse, but the stability of the support of tunnel lining structure is good. There are no falling blocks, sand, or collapses in the portal section, which is obviously different from that in the unsupported part. The tunnel face after the eighth

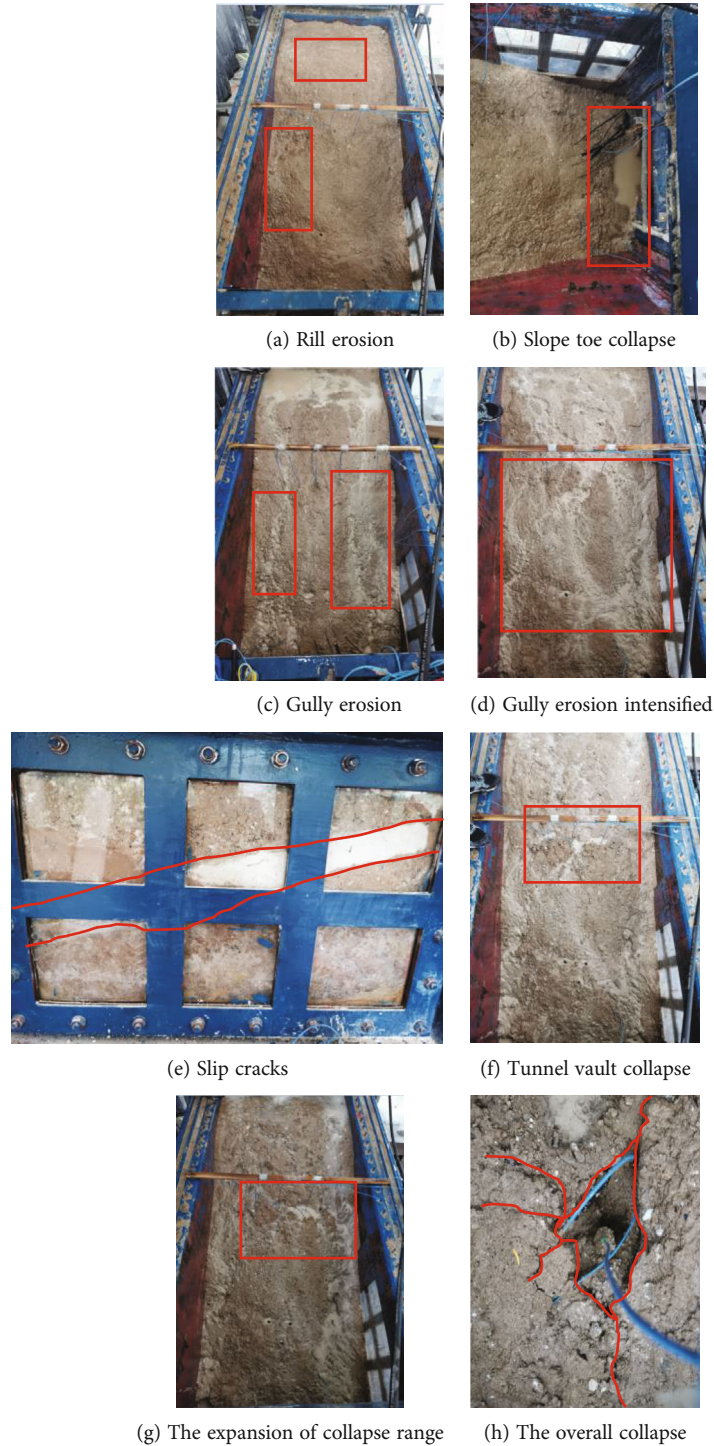


FIGURE 14: The analysis of the slope instability during rainfall.

excavation is shown in Figure 13(h); during the tunnel excavation, the collapse ranges of the tunnel face and tunnel vault are expanding constantly. The mud water mixture in the tunnel face gushes out continuously, the water quality is turbid, and the flow velocity is fast. The face of the ninth excavation is shown in Figure 13(i). During the excavation of the tunnel, the collapse ranges of the tunnel face and vault continue to expand. After about 5 min, an integral collapse occurred on the tunnel vault, with the shape of a quadratic parabola. The

rainwater mixed with collapses gushes out from the tunnel face constantly, and the water quality is turbid, as shown in Figure 13(j). After a few minutes, the water is clear. The total excavation footage is 47 cm, as shown in Figure 13(k). So far, the experiment is over.

3.2. The Analysis of the Slope Instability Process. In the early stage of rainfall, the water content of the slope is less. With the continuous infiltration of rainwater, the water content of

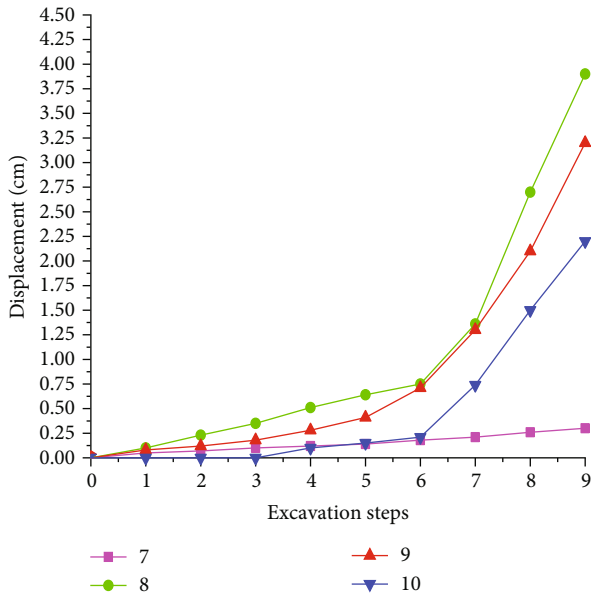


FIGURE 15: The changes of the displacement of the tunnel vault with excavation steps.

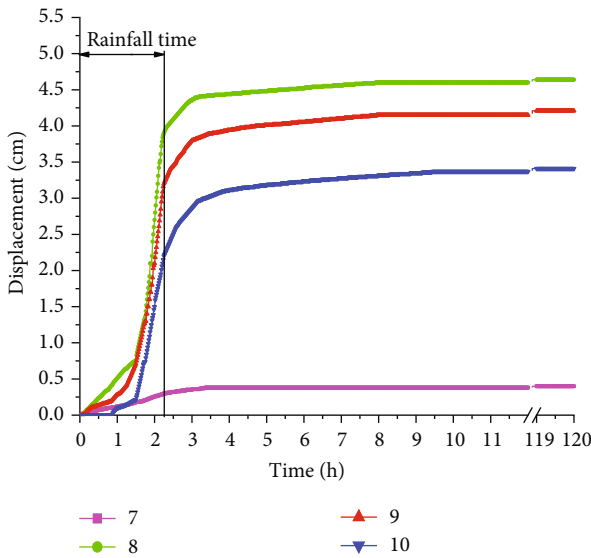


FIGURE 16: The changes of the displacement of the tunnel vault with time.

the slope increases continuously. However, due to the large amount of rainwater infiltration in the slope at the beginning, there is almost no obvious response. Besides, the tunnel excavation footage is short, and the excavation disturbance range is small. Therefore, the slope still maintains good stability.

After 30 minutes of rainfall (as shown in Figures 14(a) and 14(b)), the water content of the slope is still increasing. At this time, rill erosion occurs in the slope surface under the constant scouring effect of rainwater. There is also a small amount of water in front of the slope. In addition, there are a few discon-

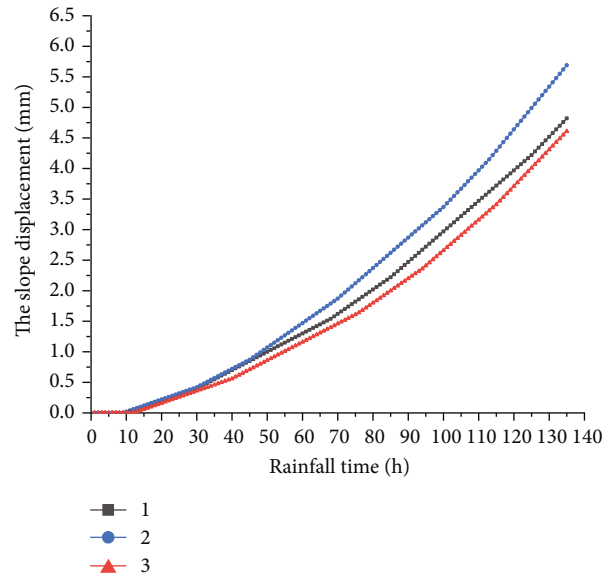


FIGURE 17: The changes of the slope displacement with rainfall time.

tinuous cracks on the tunnel vault, and the cracks are developing towards the direction of tunnel excavation. After 40 minutes of rainfall (as shown in Figure 14(c)), the infiltration of the slope gradually starts to decrease, and the water content of the slope tends to be stable. At this time, the slope surface forms gully erosion with a certain depth and width under the scouring effect of rainwater. There is also a small range of collapse at the foot of slope. After 60 minutes of rainfall (as shown in Figure 14(d)), the amount of water accumulated in the gullies is increasing, and the gullies gradually deepen under the continuous scouring effect of rainwater. After 75 minutes of rainfall (as shown in Figure 14(e)), the confluence of the surface flow is also obvious, and there are also a lot of slip cracks near the slip zone. At this time, the damage degree of the slope is developing rapidly.

After 105 minutes of rainfall (as shown in Figure 14(f)), partial settlement occurs in the tunnel vault, resulting in the formation of a puddle in the tunnel vault. Under the continuous excavation, the area of the water puddle is becoming larger and larger, and the amount of water accumulation is also increasing. After 115 minutes of rainfall (as shown in Figure 14(f)), a large amount of water and surface flow can be seen everywhere on the surface of the slope. There are more and more cracks near the slip zone. At this time, the surface of the slope is scoured and eroded seriously. In the later stage of rainfall (as shown in Figure 14(g)), the stability of the tunnel vault is extremely worse, and the collapse section is in the shape of a quadratic parabola and develops continuously to the postexcavation section. Finally, under the action of rainfall infiltration and excavation disturbance, the tunnel vault collapses as a whole, and collapses gush out from the tunnel face continuously; so far, the experiment ends. The collapse range is 13 cm in length and 18 cm in width. Five days after the end of the rainfall, the collapse range is 17 cm in length and 22 cm in width.

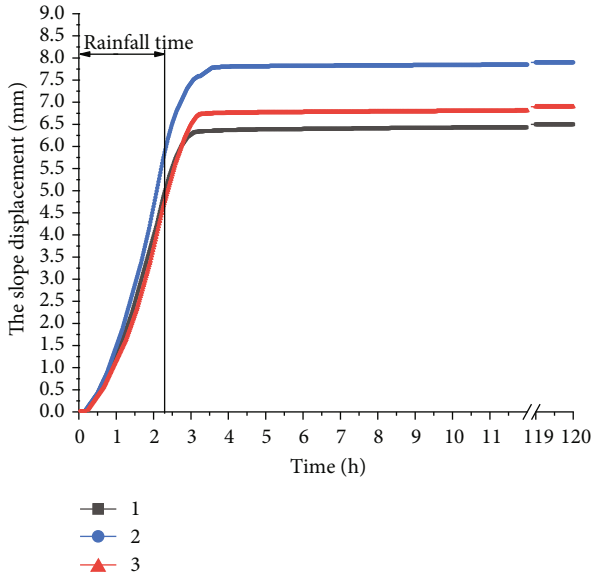


FIGURE 18: The changes of the slope displacement with time.

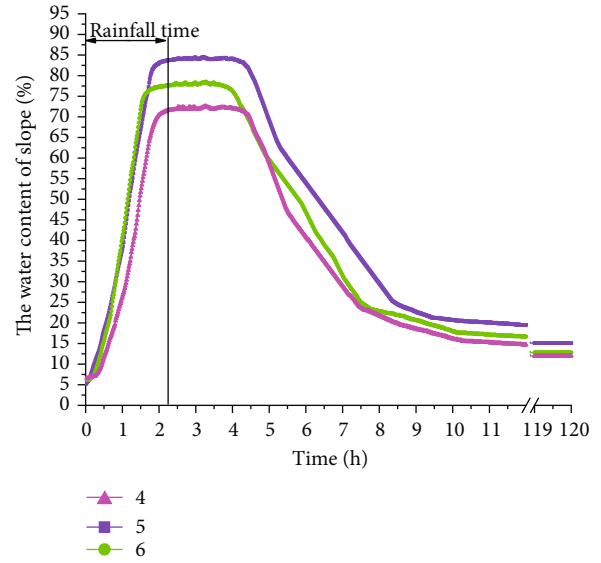


FIGURE 20: The changes of the lower slope water content with time.

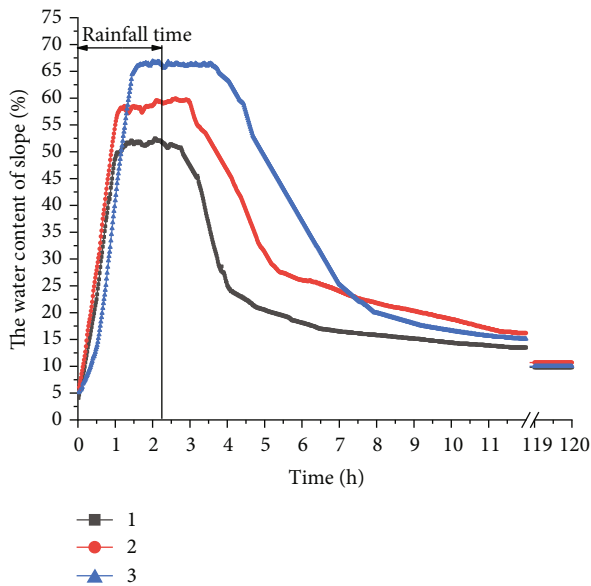


FIGURE 19: The changes of the upper slope water content with time.

4. The Analysis of Internal Change Laws in the Tunnel-Slope System during Rainfall

4.1. The Analysis of Displacement Changes of the Tunnel Vault. As can be seen from Figure 15, at the early stage of rainfall, rainfall infiltration has little impact on the tunnel stability, and the tunnel has good self-stability. Under the disturbance of tunnel excavation, the displacement of the tunnel vault has a slight change. With the continuous action of rainfall infiltration and tunnel excavation, the displacement of the tunnel vault is on the rise. When the tunnel is excavated to the sixth time, the phenomenon of falling blocks and sand on the vault of tunnel is becoming more and more serious, and the increasing rate of the tunnel vault displacement is accelerating. When

the tunnel is excavated to the seventh time, the tunnel vault collapses in a small range, and the displacement of the tunnel vault shows a rapid upward trend. In the later excavation process, the scope of the tunnel vault collapse is expanding, and the closer it is to the collapse surface, the more obvious the displacement growth trend. However, due to the existence of support structure at the tunnel entrance, the growth trend of displacement is slower than that of the excavation section.

As can be seen from Figure 16, after the end of rainfall, the displacement of the tunnel vault does not stop immediately but still maintains a rapid growth rate. It shows that the collapse and settlement of the tunnel vault induced by rainfall infiltration have the characteristics of hysteresis. A transient pressure arch is formed around the tunnel wall after the end of the rainfall for about two hours. At this time, the stresses of all sides form an equilibrium state, and the settlement of the tunnel vault also gradually becomes stable. Therefore, in the actual construction process of the tunnel, the tunnel lining should be done as soon as possible to make the surrounding rock and the support structure form a whole, to improve the safety of the tunnel excavation section. In addition, the corresponding drainage measures should be set up at the top of the tunnel vault to prevent leakage on the lining surface of the tunnel, which will reduce the structural strength of tunnel lining for a long time.

4.2. The Analysis of Slope Displacement Results. It can be seen from Figure 17 that in the early period of the rain, there is basically no obvious change in the slope displacement, but as the rainfall infiltration continues, the whole slope displacement shows a rising trend. In the process of the experiment, the front door of the slope is closed tightly, which limits the development of the front displacement of the slope to a certain extent. However, the displacement of the middle part of the slope changes the most due to the excavation disturbance. The growth trend of the displacement at the back and front of the slope is relatively slow, but the general rule is similar.

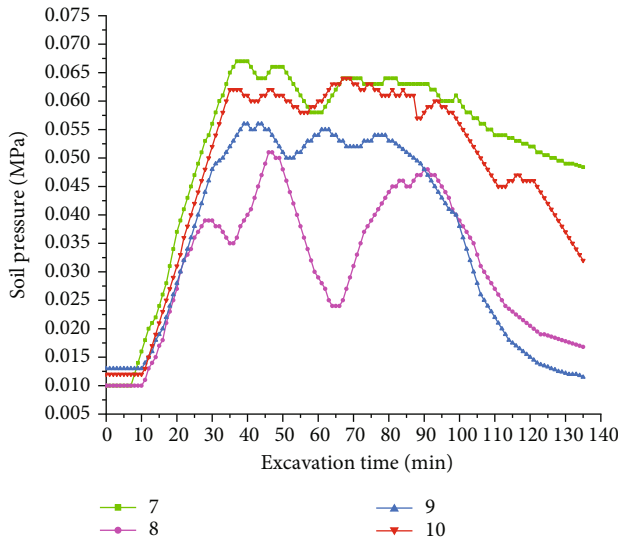


FIGURE 21: The changes of the soil pressure on the tunnel vault with rainfall time.

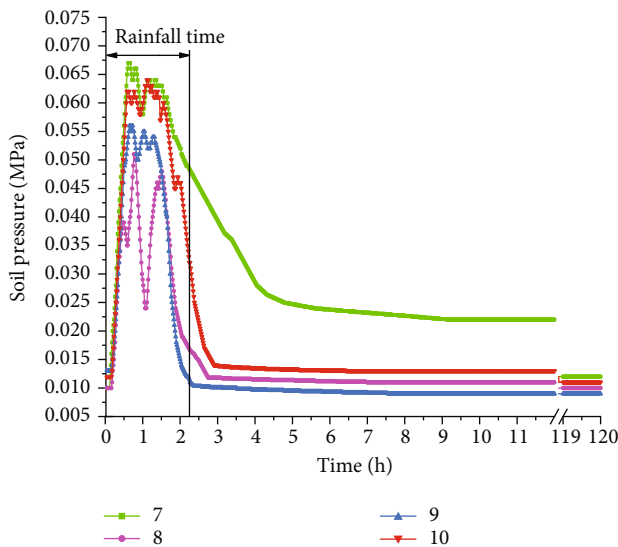


FIGURE 22: The changes of the soil pressure on the tunnel vault with time.

As can be seen from Figure 18, after the rainfall, the displacement of the slope does not stop developing but continues to keep rising. The result shows that the slope failure induced by the rainfall infiltration has the characteristics of hysteresis. The main reason is that under the effect of the long-term rainfall infiltration, the internal structure of the slope is loose, which makes the strength of the slope become more uneven; the integrity and stability of the slope further decrease, so that the displacement in slope increases in different degrees. After the rain stops for about 2 hours, the displacement in the slope gradually stabilizes.

Therefore, when the tunnel is excavated in the slope area, the slope must be reinforced in advance to prevent the creep deformation and even the overall collapse accident caused by tunnel excavation.

4.3. *The Analysis of Water Content Changes in the Tunnel-Slope System.* It can be seen from Figures 19 and 20 that the change trend of the water content at different depths of each soil layer in the slope is different in rainfall and after rainfall. In the early period of the rain, due to the fact that the rain seepage needs some time to accomplish, the water content of the upper layer of slope changes obviously and the response speed is fast. However, the water content in the lower layer of slope gradually increases after a period of rainfall infiltration, and the response speed is slow. After about 1 h of the rainfall, the water content at different depths of the slope reaches the peak value and tends to be stable gradually. The main reason is that the infiltration amount is larger than the runoff amount of the slope at the initial period of rainfall. With the continuous rainfall infiltration, when the infiltration amount and runoff amount of the slope gradually become stable, the water content of each layer in the slope does not continue to increase. After the rainfall, the water content in different depths of the slope will not immediately decrease but gradually decrease after a certain period of time, which has a certain degree of “hysteresis characteristics.” At the end of the rainfall for 1 h, the water content in the upper layer of the slope decreases rapidly because of the fast speed of rainwater loss. However, due to the slow rate of rainwater loss in the lower slope, the water content in the lower slope can remain relatively stable within 3 hours after the end of rainfall. With the continuous loss of rainwater, the runoff amount of rainwater is larger than the infiltration in the slope, resulting in a rapid downward trend of water content in the lower slope. After 8 hours of the rainfall, the water content of each soil layer finally tends to be the same.

In conclusion, the closer the rainwater infiltration to the slope surface, the faster the response speed and the more obvious the change range, but the shorter the retention time of the peak water content and the peak water content. Correspondingly, the further the rainwater infiltrate is to the slope, the slower the response speed and the longer the retention time of the peak water content. After the end of rainfall, the water content of each layer in the slope will not decrease immediately but gradually decrease after a period of rainfall, which is also one of the important reasons for the instability of the slope after the rain.

4.4. *The Analysis of Soil Pressure Changes in the Tunnel-Slope System.* As can be seen from Figure 21, in the early period of the rainfall, due to the fact that the impact of tunnel excavation is little, the soil pressure in various parts of the tunnel vault increases continuously under the action of rainwater infiltration. When the water content of the tunnel-slope system tends to be stable, the soil pressure in various parts of the tunnel vault also tends to be stable gradually. When the rainfall is about 50 minutes, the phenomenon of falling blocks and sand on the tunnel vault is serious, resulting in a significant decline of No. 8 earth pressure sensor near the collapse surface. Then, under the continuous infiltration of rainwater, the soil pressure of the tunnel vault shows a rising trend. When the rainfall is about 90 minutes, the stability of the tunnel-slope system is decreasing, the phenomenon of falling blocks and sand in the tunnel is becoming more and more serious, and even small-

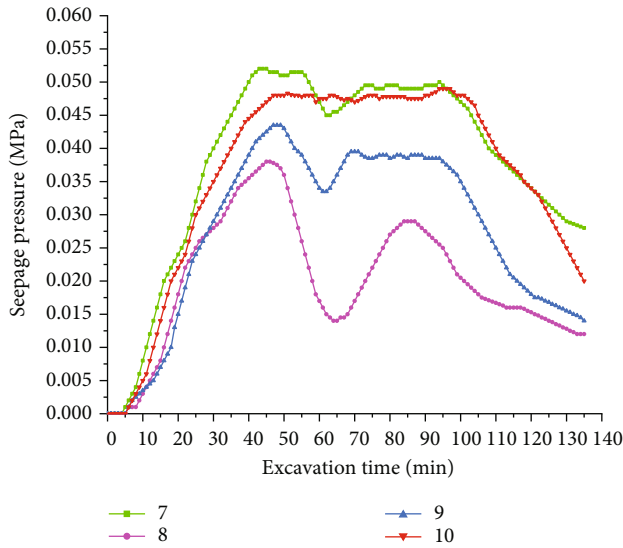


FIGURE 23: The changes of the seepage pressure on the tunnel vault with rainfall time.

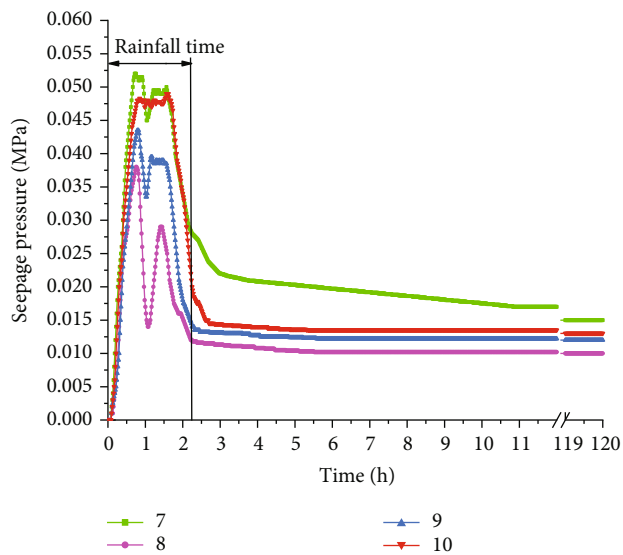


FIGURE 24: The changes of the seepage pressure on the tunnel vault with time.

scale collapses occur in some sections. At this time, the scope and the degree of collapse areas are expanding, resulting in the decreasing trend of the soil pressure in all sections of the tunnel vault. Finally, the overall collapse of the tunnel vault occurs, resulting in a cliff-like downward trend of soil pressure sensors.

As can be seen from Figure 22, after the rainfall stops, the soil pressure above the tunnel vault does not stop decreasing but continues to decrease with the expansion of the collapse scope and degree of the tunnel vault. After the rainfall stops for about 3 hours, the soil pressure around the tunnel vault gradually comes to stability. It shows that there is a hysteresis in the collapse of the tunnel vault induced by excavation under rainfall conditions, and it is very likely that it will occur after

rain when the collapse degree is the largest. However, the stability of the embedded lining is relatively good in the whole rainfall process, and there is no falling sand and collapse phenomenon, which plays an important role in supporting the excavation of the tunnel.

4.5. The Analysis of Seepage Pressure Changes in the Tunnel-Slope System. It can be seen from Figure 23 that the change trend of the seepage pressure and the soil pressure of the tunnel-slope system is similar in the whole rainfall process. In the early period of rainfall, due to the small disturbance of the tunnel excavation, the seepage pressure at all parts of the tunnel vault is rising and gradually tends to be stable under the continuous rainfall infiltration. When the rainfall is about 50 minutes, the phenomenon of falling blocks and sand in the excavation section of the tunnel vault occurs continuously, and even a small section of collapse has occurred, resulting in a temporary downward trend in the seepage pressure of the tunnel vault. After that, under the timely supply of rainwater, it shows a rising trend. When the rainfall is continuing for about 90 minutes, under the joint action of the rainfall infiltration and the tunnel excavation, the phenomenon of falling blocks, sand, and collapses of the tunnel vault is becoming more and more serious. At this time, the seepage pressure of the tunnel vault decreases continuously. During the later excavation of the tunnel, the collapse range extends from the tunnel excavation to the tunnel entrance section. The rainwater flows out from the entrance section constantly with collapses, resulting in a straight-line downward trend of seepage pressure sensors.

As can be seen from Figure 24, after the rainfall stops, the seepage pressure of the tunnel vault does not keep stable but continues to decrease obviously. The cause of this phenomenon is probably that after the rainfall stops, the collapse range of the tunnel vault continues to expand, and a large amount of rainwater flows out from the collapse surfaces and the cracks. After the rainfall stops for about 5 hours, seepage pressure sensors tend to be stable. It shows that the collapse and settlement of the tunnel vault induced by rainfall infiltration have hysteresis. The change laws are basically the same as that of the soil pressure sensors.

5. Conclusions

Through the large-scale physical model experiment, the influence of the excavation disturbance on the stability of the tunnel-slope under rainfall conditions is studied. The main conclusions are as follows:

- (1) The collapse process of the tunnel vault caused by tunnel excavation can be described as follows: tunnel excavation → gradual decline in self-stabilizing ability → falling blocks and sand → the internal seepage channel gradually develops → small scale collapse with the water seepage from the tunnel face → the amount of mud water mixture from tunnel face is increasing → the expansion of the collapse scope → the stability of the excavation section is very poor → the integral collapse of the excavation section in the form of a quadratic parabola → water inrush

from the tunnel face. And in the excavation process, the collapse degree of the first excavation section will expand with the continuous excavation of the second section; in other words, the influence and development of each excavation section are closely related. However, in the whole process of rainfall, the stability of the embedded part of tunnel portal lining is relatively good, and there are no collapse and falling sand. Therefore, in the construction process of the tunnel portal section in the slope area, tunnel lining support is particularly important.

- (2) The process of the slope instability caused by the rainwater infiltration can be described as follows: rainfall infiltration → rill erosion → slope toe collapse → gully erosion → gully erosion intensified → surface flow erosion → the partial excavation section collapse → slope instability slip → the integral excavation section collapse → the mud water mixture gushes from the tunnel face. Therefore, the slope failure develops gradually from the toe of the slope to the back slope under rainfall condition. The collapse failure of the slope toe and the upper surface of slope first occurs and then develops and gradually aggravates, finally causing the instability and sliding of the whole slope.
- (3) The influence of the rainfall infiltration on the tunnel-slope system is characterized by “accumulation.” In the early period of the rain, the influence of rainwater infiltration on the stability of the tunnel-slope system is small, but with the continuous rainfall infiltration, the tunnel-slope system will change obviously, and the influence will gradually increase until it is destroyed completely.
- (4) By analyzing the change laws of the tunnel-slope system such as displacement, water content, soil pressure, and seepage pressure, it can be concluded that the impact of the rainfall infiltration on the tunnel-slope system presents a certain degree of “hysteresis” characteristic, and the destruction process is gradual. This is one of the important reasons for the instability and destruction of the slope after rain.

Data Availability

The data used to support the findings of this study are available from the corresponding author upon request.

Conflicts of Interest

The authors declare that they have no conflicts of interest.

Acknowledgments

Financial supports from the National Natural Science Foundation of China (42272313), the Key Research and Development Program (Social Development) of Xuzhou City (KC21298), the scientific research project of China Railway Shanghai

Group Co., Ltd. (2022178), and the Open Research Fund of State Key Laboratory of Geomechanics and Geotechnical Engineering, Institute of Rock and Soil Mechanics, Chinese Academy of Sciences (Z020014), are sincerely acknowledged.

References

- [1] Y. C. Wang, Y. Q. Shang, X. H. Xu, Y. H. Xiao, and X. S. Yan, “Time and space prediction of collapse of loose wall rock at tunnel exit,” *Chinese Journal of Geotechnical Engineering*, vol. 32, no. 12, 2010.
- [2] M. Zhao, Y. Cheng, Z. Song et al., “Stability analysis of TBM tunnel undercrossing existing high-speed railway tunnel: a case study from Yangtaishan tunnel of Shenzhen metro line 6,” *Advances in Civil Engineering*, vol. 2021, Article ID 6674862, 18 pages, 2021.
- [3] N. Vlachopoulos, I. Vazaios, and B. M. Madjdabadi, “Investigation into the influence of excavation of twin-bored tunnels within weak rock masses adjacent to slopes,” *Canadian Geotechnical Journal*, vol. 55, no. 11, pp. 1533–1551, 2018.
- [4] Y. C. Wang, H. W. Jing, H. J. Su, and J. Xie, “Effect of a fault fracture zone on the stability of tunnel-surrounding rock,” *International Journal of Geomechanics*, vol. 17, no. 6, 2017.
- [5] N. Roy, R. Sarkar, and S. D. Bharti, “Prediction model for performance evaluation of tunnel excavation in blocky rock mass,” *International Journal of Geomechanics*, vol. 18, no. 1, p. 04017125, 2018.
- [6] F. Huang, H. Zhu, S. Jiang, and B. Liang, “Excavation-damaged zone around tunnel surface under different release ratios of displacement,” *International Journal of Geomechanics*, vol. 17, no. 4, p. 04016094, 2017.
- [7] P. Gattinoni and L. Scesi, “Landslide hydrogeological susceptibility of Maierato (Vibo Valentia, Southern Italy),” *Natural Hazards*, vol. 66, no. 2, pp. 629–648, 2013.
- [8] S. Miao, X. Hao, X. Guo, Z. Wang, and M. Liang, “Displacement and landslide forecast based on an improved version of Saito’s method together with the Verhulst-Grey model,” *Arabian Journal of Geosciences*, vol. 10, no. 3, pp. 1–10, 2017.
- [9] C. Duenser, K. Thoeni, K. Riederer, B. Lindner, and G. Beer, “New developments of the boundary element method for underground constructions,” *International Journal of Geomechanics*, vol. 12, no. 6, pp. 665–675, 2012.
- [10] Y. Wang, F. Geng, S. Yang, H. Jing, and B. Meng, “Numerical simulation of particle migration from crushed sandstones during groundwater inrush,” *Journal of Hazardous Materials*, vol. 362, pp. 327–335, 2019.
- [11] Y. Jing, R. G. Deng, Z. B. Zhong, K. T. Li, and C. P. Sun, “Stress and deformation laws and influence factors analysis of tunnel across the slope deformation zone,” *Chinese Journal of Rock Mechanics and Engineering*, vol. 35, no. S2, pp. 3615–3625, 2016.
- [12] J. Kumar and P. Bhattacharya, “Reducing the computational effort for performing linear optimization in the lower-bound finite elements limit analysis,” *International Journal of Geomechanics*, vol. 11, no. 5, pp. 406–412, 2011.
- [13] S. Alemdag, A. Kaya, M. Karadag, Z. Gurocak, and F. Bulut, “Utilization of the limit equilibrium and finite element methods for the stability analysis of the slope debris: an example of the Kalebasi District (NE Turkey),” *Journal of African Earth Sciences*, vol. 106, pp. 134–146, 2015.

- [14] S. G. Xiao, C. C. Xia, and D. P. Zhou, "One definition and analysis method of relaxation zone in cutting slope," *Journal of Tongji University*, vol. 33, no. 4, pp. 451–455, 2005.
- [15] H. M. Ma, "Discussion on problems of slope disaster and tunnel deformation," *Chinese Journal of Rock Mechanics and Engineering*, vol. 22, no. S2, pp. 2719–2724, 2003.
- [16] Z. P. Tao, *Study on Tunnel Deformation on Mechanism at Landslide Site and Disaster Predicting and Controlling*, Southwest Jiaotong University, 2003.
- [17] H. Wu, *Research on Deformation Mechanism and Control Technology of Tunnel-Landslide System*, China Academy of Railway Sciences, 2012.
- [18] A. Kaya, A. Akgün, K. Karaman, and F. Bulut, "Understanding the mechanism of slope failure on a nearby highway tunnel route by different slope stability analysis methods: a case from NE Turkey," *Bulletin of Engineering Geology and the Environment*, vol. 75, no. 3, pp. 945–958, 2016.
- [19] R. L. Baum, J. W. Godt, and W. Z. Savage, "Estimating the timing and location of shallow rainfall-induced landslides using a model for transient, unsaturated infiltration," *Journal of Geophysical Research: Earth Surface*, vol. 115, no. F3, 2010.
- [20] L. Henry and I. Hoe, "Centrifuge model simulations of rainfall-induced slope instability," *Journal of Geotechnical and Geoenvironmental Engineering*, vol. 138, no. 9, pp. 1151–1157, 2012.
- [21] S. Ganger, *Duzhengliang and Xiaoqiaochengzhi (Japanese). "Landslide and Slope Failure and Its Prevention and Control."*, Science Press, Beijing, 1980.
- [22] Z. P. Tao and D. P. Zhou, "Model test on deformation mechanism of tunnel at land-slide site," *Journal of Engineering Geology*, vol. 2003, no. 3, pp. 323–327, 2003.
- [23] H. G. Wu, X. Y. Chen, and H. Ai, "Research on the deformation mechanism model test of tunnel-landslide parallel system," *Journal of Railway Engineering Society*, vol. 33, no. 11, 2016.
- [24] H. G. Wu, X. Y. Chen, and H. Ai, "Research on the deformation mechanism model test of tunnel-landslide skew system," *Journal of Railway Engineering Society*, vol. 33, no. 9, 2016.
- [25] H. G. Wu, X. Y. Chen, and H. Ai, "Research on the force exerting mode model test of tunnel-landslide orthogonal system," *Journal of Railway Engineering Society*, vol. 3, 2016.
- [26] Z. H. G. Zhang, C. P. Zhang, B. B. Ma, J. F. Gong, and T. Ye, "Physical model test and numerical simulation for anchor cable reinforcements of existing tunnel under action of landslide," *Rock and Soil Mechanics*, vol. 39, no. S1, pp. 51–60, 2018.
- [27] J. Yin, R. G. Deng, K. T. Li, B. J. Chen, and C. H. P. Sun, "Stress and deformation of self-anchored reinforcement structures for landslide tunnels," *Chinese Journal of Rock Mechanics and Engineering*, vol. 35, no. 10, pp. 2062–2079, 2016.
- [28] J. B. Chen, "Experimental study on the influence of engineering disturbance on the tunnel-landslide orthogonal system," *Value Engineering*, vol. 36, no. 24, pp. 133–136, 2017.
- [29] H. Ai, H. G. Wu, and X. Y. Chen, "Research on the influence mechanism of rainfall for the tunnel-landslide orthogonal system without the supporting structure," *China Earthquake Engineering Journal*, vol. 39, no. 2, pp. 0213–0220, 2017.
- [30] Y. Gao, H. Wei, and B. Li, "Disaster evolution mechanism of rainfall-landslide-tunnel system: a case study of Yangjiawan tunnel of Fengxi highway in Chongqing," *Tunnel Construction*, vol. 42, no. 4, 2022.
- [31] L. Li, C. H. He, P. Geng, and D. J. Cao, "Study of shaking table model test for seismic response of portal section of shallow unsymmetrical loading tunnel," *Chinese Journal of Rock Mechanics and Engineering*, vol. 30, no. 12, pp. 2540–2548, 2011.
- [32] E. Yalcin, Z. Gurocak, R. Ghabchi, and M. Zaman, "Numerical analysis for a realistic support design: case study of the Komurhan tunnel in eastern Turkey," *International Journal of Geomechanics*, vol. 16, no. 3, 2016.
- [33] J. X. Wang, H. H. Zhu, Y. Q. Tang, L. S. Hu, P. Yang, and D. Wu, "Interaction between twin-arc tunnel and slope: twin-arc tunnel landslide," *China Civil Engineering Journal*, vol. 43, no. 1, pp. 103–107, 2010.
- [34] Y. Xing, P. H. S. W. Kulatilake, and L. A. Sandbak, "Stability assessment and support design for underground tunnels located in complex geologies and subjected to engineering activities: case study," *International Journal of Geomechanics*, vol. 19, no. 5, p. 05019004, 2019.
- [35] Q. Zhang, J. Wang, W. Wang, S. Bai, and P. Lin, "Study on slope stability due to the influence of excavation of the high-speed rail tunnel," *Geomatics, Natural Hazards and Risk*, vol. 10, no. 1, pp. 1193–1208, 2019.
- [36] P. Gattinoni, M. Consonni, V. Francani, G. Leonelli, and C. Lorenzo, "Tunnelling in landslide areas connected to deep seated gravitational deformations: an example in Central Alps (northern Italy)," *Tunnelling and Underground Space Technology*, vol. 93, article 103100, 2019.
- [37] L. Qin, *Analysis of Slope Stability Influenced by Tunnel Excavation: A Study of Reinforcement Measures*, Central South University, 2012.
- [38] H. Moriwaki, T. Inokuchi, T. Hattanji, K. Sassa, H. Ochiai, and G. Wang, "Failure processes in a full-scale landslide experiment using a rainfall simulator," *Landslides*, vol. 1, no. 4, pp. 277–288, 2004.
- [39] J. W. Hu, *The Stability Evaluation and Treatment Measures for the Daping No. III Landslide*, Chang'an University, 2013.
- [40] S. F. Wang, *Fengjie Daping Landslide in Chongqing City Stability Analyses and Government Plan Discussion*, Xi'an University of Science and Technology, 2008.
- [41] S. Sun and Y. Zhang, "Similarity criterion in physical simulation of rainfall and sheet flow," *Transactions of the Chinese Society of Agricultural Engineering*, vol. 28, no. 11, pp. 93–98, 2012.
- [42] Y. Wang, F. Chen, W. Sui, F. Meng, and F. Geng, "Large-scale model test for studying the water inrush during tunnel excavation in fault," *Bulletin of Engineering Geology and the Environment*, vol. 81, no. 6, 2022.
- [43] Y. C. Wang, Y. Liu, N. Zhao, and W. Jiang, "Investigation on the evolution mechanism of water and mud inrush disaster in fractured rock mass of mountain tunnel," *Geomatics, Natural Hazards and Risk*, vol. 13, no. 1, pp. 1780–1804, 2022.

Research Article

Superimposed Stress Calculation of Soil Underlying Anchor Beam considering Anisotropy and Strength Nonhomogeneity

Fei Xu ^{1,2}, Zhongshun Wang,¹ Liming Zhou ¹, Hemin Zheng,³ Bo Liu,⁴ Yuqiu Jiang,¹ and Daili Wang¹

¹Key Laboratory of Large Structure Health Monitoring and Control, Shijiazhuang Tiedao University, Shijiazhuang 050043, China

²School of Civil Engineering, Southwest Jiaotong University, Chengdu 610031, China

³China Railway Design Group Co., Ltd., Tianjin 300308, China

⁴School of Civil Engineering, Beijing Jiaotong University, Beijing 100044, China

Correspondence should be addressed to Liming Zhou; ming@stdu.edu.cn

Received 6 April 2022; Revised 29 June 2022; Accepted 22 August 2022; Published 10 September 2022

Academic Editor: Yang Yu

Copyright © 2022 Fei Xu et al. This is an open access article distributed under the Creative Commons Attribution License, which permits unrestricted use, distribution, and reproduction in any medium, provided the original work is properly cited.

Prestress anchor beams are an important reinforcement method for underground engineering and rock slopes, and they are crucial for maintaining the stability of civil engineering structures. In this study, the computational formula of superimposed stress of soil underlying an anchor beam was proposed in this paper, based on the assumption that the anchor beam is completely rigid and the prestress of the anchor cable is acting on soil in the form of a strip uniform load. By considering the anisotropy and strength nonhomogeneity of the saturated soft clay, the failure envelopes of the soil and the maximum effective depth underlying the anchor beam were obtained by the D-P yield criterion suitable for soft clay analysis. Furthermore, the experimental comparisons with the previous findings were used to validate the proposed approach. The proposed method was valid to assess the maximum effective depth. Considering the influence of the factors on the failure envelopes of soil, a parametric study was carried out to optimize the design of the prestressed anchor cable. The findings of this study provide a theoretical basis for designing prestressed anchor cables; these can also be used to predict the response of prestressed anchor cables as well as to optimize the design of the cables, such as the anchorage length of cable and grouting radius.

1. Introduction

Slope stability is a crucial issue in the field of geotechnical engineering; it is principally influenced by the properties of geological discontinuities of slope, and various approaches have been proposed for the slope stability analysis [1–4]. Du et al. [1] proposed a new method to evaluate slope stability in large open-pit mines based on a comprehensive investigation of the geometry and shear strength of the geological discontinuities; the results were in good agreement with field observation. Tang et al. [2] proposed a formula for calculating the safety factor of rock slope considering the effect of locked sections. Yuan et al. [3] studied the laws of slope displacement and the changing positions of a sliding surface during the filling process by using the finite element software PLAXIS. Chen et al. [4] proposed a new modified strength

reduction method to calculate the decay law of slope strength by applying the respective reduction factors in a strength reduction technique. In recent decades, anchors have become one of the popular methods for slope reinforcement; in particular, prestressed anchor cables have been extensively applied in geotechnical engineering. By installing prestressed anchor cables, the self-bearing capacity of rock and soil can be fully mobilized, and the forces acting on the supporting structure can be optimized [5]. Therefore, “anchor cable rigid beam” systems are becoming popular; prestressed anchor cables are also essential for reinforcement projects such as high slopes and deep foundation pits, as presented in Figure 1.

In the past several decades, many studies have analyzed the behaviors of prestressed anchor cables by using various methods such as theoretical analyses [6–8], model tests



(a)

(b)

FIGURE 1: Application of prestressed anchor cable: (a) used in a high slope and (b) used in a deep foundation pit.

[9–11], and numerical simulations [12–16]. Wang et al. [9] conducted pull-out tests for anchor cables for revealing the failure mechanisms and the constitutive relation; for anchorage segments, the failure mechanism displayed the pulling failure at first, followed by pulling and shearing failures. Yang et al. [12] studied the variation of tension in prestressed anchor cables based on field monitoring; they summarized the variation features of anchor tension considering the install positions on a single anchor pile, anchoring strata, and locations on the plane of the foundation pit. Wu et al. [17] conducted shaking table tests to investigate the seismic response of a slope reinforced by prestressed anchor cables and double-row antisliding piles, and they revealed that the reinforced slope had good overall stability. Sun et al. [18] proposed a large deformation anchor cable support system and used 3DEC software and a series of field tests to study the effect of applying an NPR anchor cable support system, showing that the NPR anchor cable support system achieved good results in tunnel engineering. Yuan et al. [19] established a similar method to simulate anchors in the combined structure and derived the inherent internal force and algorithmic tangent stiffness of the anchor model, revealing that the nonlinearity of the anchor was mainly caused by the interface failure and anchor yielding. Contemporary studies have mainly focused on a homogeneous and isotropic homogeneity stratum without considering the effect of load dispersion induced by the anchor beam. Few studies have calculated superimposed stress and the plastic failure zone of soil underlying the anchor beam, especially in terms of the saturated soft clay considering the anisotropy and strength nonhomogeneity.

Saturated soft clay has high permeability, large deformation, high compressibility, anisotropy, and strength nonhomogeneity. Thus, soil cohesive force considerably influences the direction of the maximum principal stress, and it varies at different soil depths [20, 21] (described in detail in Section 3.1).

In this study, the anchor beam is assumed to be completely rigid, a prestressed anchor cable is applied to soil in the form of uniform load, and the computational formula of the superimposed stress of soil underlying the anchor

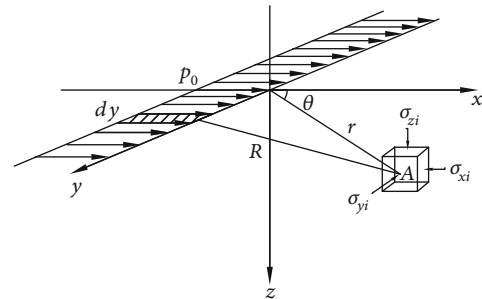


FIGURE 2: Superimposed stress of soil underlying the anchor beam induced by a horizontal line load.

beam is proposed. Considering the anisotropy and strength nonhomogeneity of saturated soft clay, the plastic failure envelopes of soil and the maximum effective depth underlying the anchor beam are obtained using the D-P yield criterion. To evaluate the validity of the proposed method, the results of the maximum effective depth are compared with those presented in previous studies. Good agreement is observed between the results of this study and those of previous studies, which indicates the validity of the proposed method. Finally, to optimize the design of the prestressed anchor cable, a parametric study is conducted by analyzing the influence of anisotropy on the plastic failure envelopes.

2. Superimposed Stress of Soil Underlying the Anchor Beam

As described by Huang [22] and He [23], the distribution of foundation stress derived from the elastic theory is in line with that obtained from the finite element method, demonstrating that the influence of the distribution of foundation stress induced by the nonlinearity, layered distribution, and plastic deformation of soil can be considered negligible. Therefore, in this study, it is assumed that the superimposed stress of soil underlying an anchor beam can be calculated using the elastic theory. It is assumed that the anchor beam is perfectly rigid, and the prestress of the anchor cable acting on the rigid beam is considered equivalent to a uniformly

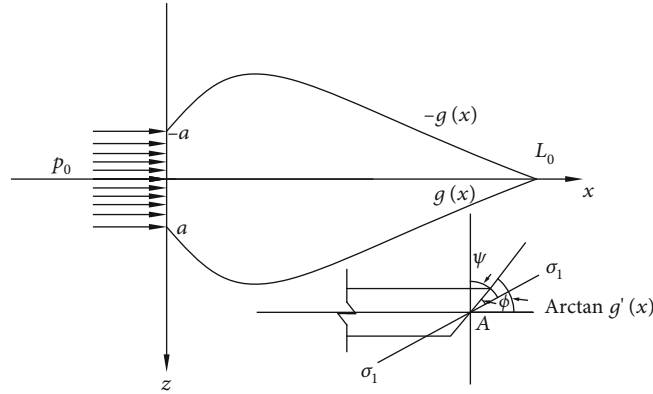


FIGURE 3: Calculation model of failure envelopes of soil underlying the anchor beam by horizontal line load.

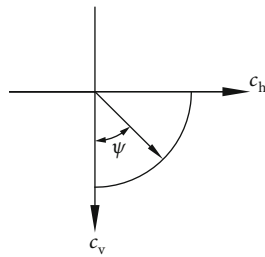


FIGURE 4: Anisotropy of soil.

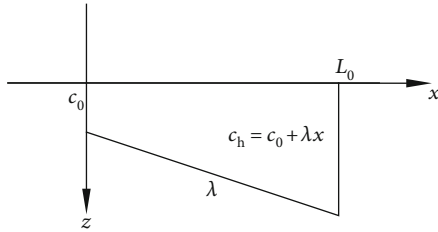


FIGURE 5: Nonhomogeneity of soil.

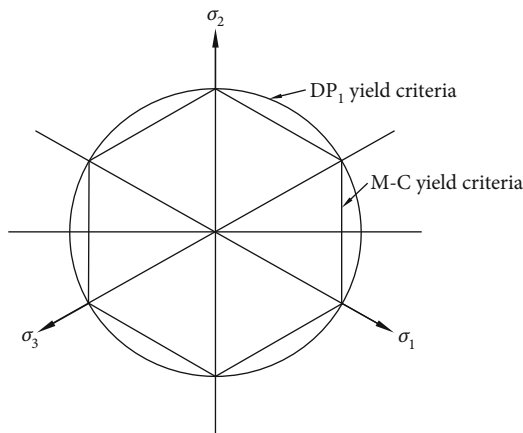


FIGURE 6: Yield curves of M-C and DP1 yield criteria in the π plane.

distributed strip load. The simplified calculation model of the load acting on the beam is shown in Figure 2.

Using the method of Melan integration [24], when the horizontal line load p_0 is applied to soil through the origin of coord-

inate (Figure 2), the superimposed stress acting at an arbitrary point A of soil underlying the anchor beam can be obtained using

$$\sigma_{xi} = \frac{2p_0x^3}{\pi[x^2 + g^2(x)]^2}, \quad (1)$$

$$\sigma_{zi} = \frac{2p_0xg^2(x)}{\pi[x^2 + g^2(x)]^2}, \quad (2)$$

$$\tau_{(xz)i} = \frac{2p_0x^2g(x)}{\pi[x^2 + g^2(x)]^2}, \quad (3)$$

$$\tau_{(xy)i} = 0, \quad (4)$$

$$\tau_{(zy)i} = 0. \quad (5)$$

Based on the general Hooke's law and plane strain assumption, the shear strain, ε_{yi} , can be expressed as

$$\varepsilon_{yi} = 0. \quad (6)$$

According to Equations (1)–(6), the normal stress along the Y-axis, σ_{yi} , can be calculated using

$$\sigma_{yi} = \mu(\sigma_{zi} + \sigma_{xi}) = \mu \left[\frac{2p_0g^2(x)}{\pi[x^2 + g^2(x)]^2} + \frac{2p_0x^3}{\pi[x^2 + g^2(x)]^2} \right] = \frac{2p_0x\mu}{\pi[x^2 + g^2(x)]}, \quad (7)$$

where σ_{xi} and σ_{zi} are the normal stress along the directions of X - and Z-axes, respectively; τ_{xy} , τ_{yz} , and τ_{zx} are the shear stress on the XY, YZ, and ZX surfaces, respectively; p_0 is the horizontal line load; $g(x)$ is the function of the failure envelopes of soil; and μ is Poisson's ratio.

The width of the anchor beam is assumed to be equal to $2a$ (see Figure 3). Integrating Equations (1)–(6) along the direction of the anchor beam width, the values of σ_x , σ_z , τ_{xz} , τ_{xy} , and τ_{zy} can be computed as given in

$$\sigma_x = \sum_{i=1}^n \sigma_{xi} = \int_{-a}^a \frac{2p_0x^3}{\pi\{x^2 + [g(x) - h]^2\}^2} dh, \quad (8)$$

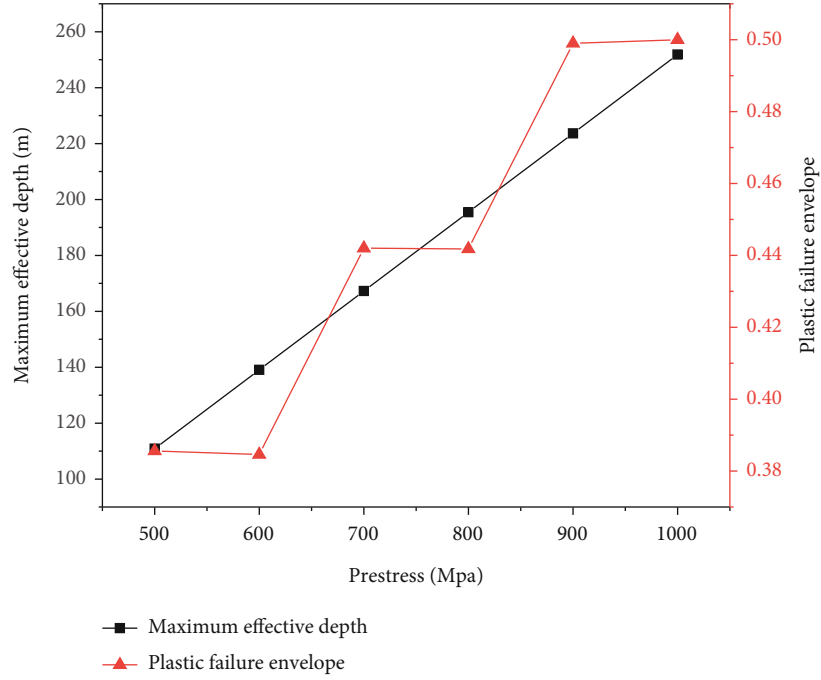


FIGURE 7: Failure envelopes of soil under different prestress p_0 values.

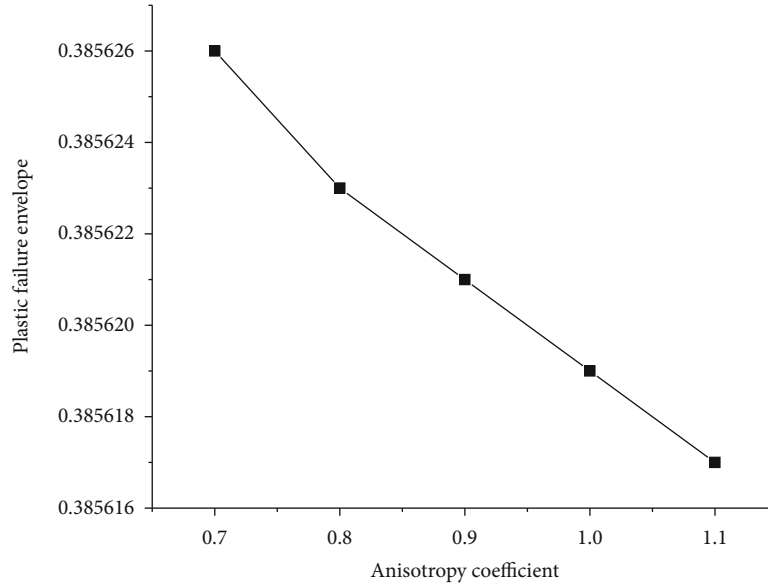


FIGURE 8: Failure envelopes of soil under different anisotropy coefficients ρ .

$$\sigma_z = \sum_{i=1}^n \sigma_{zi} = \int_{-a}^a \frac{2p_0 x [g(x) - h]^2}{\pi \{x^2 + [g(x) - h]^2\}^2} dh, \quad (9) \quad \tau_{yz} = 0. \quad (13)$$

$$\sigma_y = \sum_{i=1}^n \sigma_{yi} = \int_{-a}^a \frac{2p_0 x \mu}{\pi \{x^2 + [g(x) - h]^2\}^2} dh, \quad (10)$$

$$\tau_{xz} = \sum_{i=1}^n \tau_{(xz)i} = \int_{-a}^a \frac{2p_0 x^2 [g(x) - h]}{\pi \{x^2 + [g(x) - h]^2\}^2} dh, \quad (11)$$

$$\tau_{xy} = 0, \quad (12)$$

3. Failure Envelopes of Soil and the Maximum Effective Depth Underlying the Anchor Beam

3.1. *Anisotropy and Strength Nonhomogeneity of Soil.* The angle of internal friction, φ , and the cohesive force, c , can be used to predict soil strength. For nonhomogeneous and anisotropic soil, following the suggestion of [25], φ is assumed to be constant, and c is assumed to be nonhomogeneous and anisotropic [26]. As described in [27], the value of φ can be assumed to be 35° .

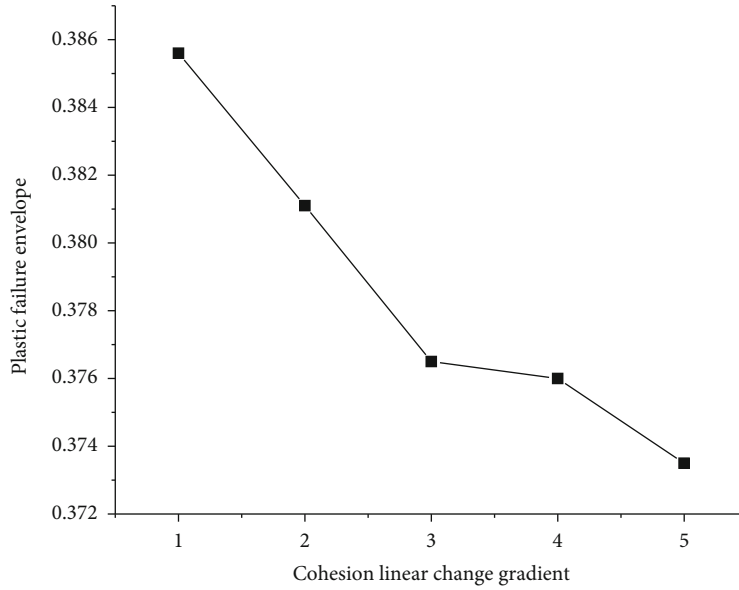


FIGURE 9: Failure envelopes of soil under different nonhomogeneity parameters λ .

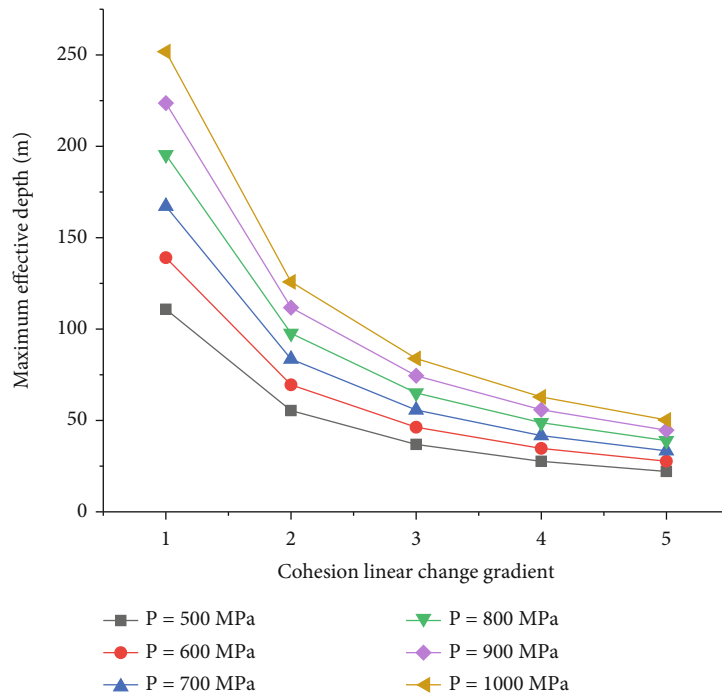


FIGURE 10: Maximum effective depth of soil under different nonhomogeneity parameters λ .

According to Casagrande and Carillo [28], for anisotropic clay soil, the cohesive force of saturated and undrained clay soil, c_ψ , can be obtained using

$$c_\psi = c_h + (c_v - c_h) \cos^2 \psi, \quad (14)$$

$$\psi = \frac{\pi}{2} - \arctan g'(x) + \phi, \quad (15)$$

where c_h and c_v are the cohesive forces along the X- and Y-axes, respectively (Figure 4).

The coefficient of anisotropy, ρ , can be expressed as

$$\rho = \frac{c_h}{c_v}, \quad (16)$$

where the value of ρ is in the range 0.50–1.33. When the value of ρ is 1.00, soil can be assumed to be isotropic [26].

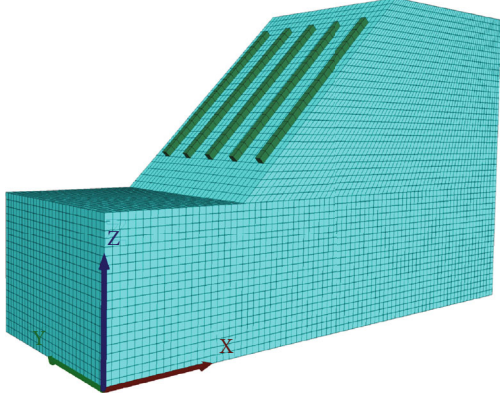


FIGURE 11: Numerical model sketch.

Substituting Equation (16) into Equation (14), we obtain

$$c_\psi = c_h \left(1 + \frac{1-\rho}{\rho} \cos^2 \psi \right). \quad (17)$$

For saturated and undrained clay soil, the strength varies linearly with increase in depth [29–31]. As shown in Figure 5, the cohesive force in the horizontal direction c_h can be expressed using

$$c_h = c_0 + \lambda x, \quad (18)$$

where λ is the gradient of linear variation of the cohesive force and x is the value of depth along the axis direction of the cable.

Substituting Equations (17) and (18) into Equation (14), we obtain

$$c_\psi = (c_0 + \lambda x) \left(1 + \frac{1-\rho}{\rho} \cos^2 \psi \right). \quad (19)$$

3.2. Failure Envelopes of Soil. The Drucker-Prager yield criterion, which is typically used as the modified model of the Mohr–Coulomb yield criterion, and a nonassociative flow rule were used herein [32]. This linear perfectly elastic–plastic yield criterion can be used to capture the shear-compression failure of soft clay with a small friction angle. In this study, the DP1 yield criterion [33] is used (Figure 6), and the yield function can be expressed as

$$F(\sigma) = f(I_1, J_2) = \alpha I_1 + \sqrt{J_2} - \kappa = 0, \quad (20)$$

$$I_1 = \sigma_x + \sigma_y + \sigma_z, \quad (21)$$

$$J_2 = \frac{1}{6} \left[(\sigma_x - \sigma_y)^2 + (\sigma_y - \sigma_z)^2 + (\sigma_z - \sigma_x)^2 + 6(\tau_{xy}^2 + \tau_{yz}^2 + \tau_{zx}^2) \right], \quad (22)$$

$$\alpha = \frac{2 \sin \varphi}{\sqrt{3}(3 - \sin^2 \varphi)}, \quad (23)$$

$$\kappa = \frac{6c_\psi \cos \varphi}{\sqrt{3}(3 - \sin^2 \varphi)}. \quad (24)$$

Substituting Equations (8)–(13) into Equations (21) and (22), we obtain

$$I_1 = (1 + \mu) \int_{-a}^a \frac{2p_0 x}{\pi \{x^2 + [g(x) - h]^2\}^2} dh, \quad (25)$$

$$J_2 = \int_{-a}^a \frac{4p_0^2 x^2}{3\pi^2 \{x^2 + [g(x) - h]^2\}^4} \{x^4(1 - \mu + \mu^2) + [g(x) - h]^4 \cdot (1 + \mu^2) + 2x^2[g(x) - h]^2\} dh, \quad (26)$$

where I_1 is the first invariant of the stress tensor and J_2 is the second principal invariant of the stress deviator tensor.

Substituting Equations (23)–(26) into Equation (20), we obtain

$$\begin{aligned} & \frac{3 - \sin^2 \varphi}{2 \sin \varphi} \sqrt{\int_{-a}^a \frac{x^2 \{x^4(1 - \mu + \mu^2) + [g(x) - h]^4(1 + \mu^2) + 2x^2[g(x) - h]^2\} dh}{\{x^2 + [g(x) - h]^2\}^2}} \\ & + (1 + \mu) \int_{-a}^a \frac{x dh}{\{x^2 + [g(x) - h]^2\}^2} = \frac{3c_\psi \pi}{2p_0 \tan \varphi}. \end{aligned} \quad (27)$$

3.3. Maximum Effective Depth. Considering the symmetry, when the value of z presented in $g(x)$ is 0, the maximum effective depth along the axial direction of cable L_0 can be obtained using Equation (34).

When the value of z is 0, the boundary conditions can be expressed as follows:

$$z = g(x) = g'(x) = 0, \quad (28)$$

$$\cos \psi = 0 \quad (\psi = 90^\circ). \quad (29)$$

Then, we obtain

$$\sigma_{x0} = \frac{2p_0 x^3}{\pi} \int_{-a}^a \frac{1}{(x^2 + h^2)^2} dh = \frac{2p_0}{\pi} \left(\arctan \frac{a}{x} + \frac{xa}{x^2 + a^2} \right), \quad (30)$$

$$\sigma_{z0} = \frac{2p_0}{\pi} \int_{-a}^a \frac{xh^2}{(x^2 + h^2)^2} dh = \frac{2p_0}{\pi} \left(\arctan \frac{a}{x} - \frac{xa}{x^2 + a^2} \right), \quad (31)$$

$$\sigma_{y0} = \mu(\sigma_{x0} + \sigma_{z0}) = \frac{4p_0 \mu}{\pi} \arctan \frac{a}{x}, \quad (32)$$

$$\tau_{(xz)0} = \tau_{(zy)0} = \tau_{(yx)0} = 0. \quad (33)$$

TABLE 1: Material properties of the model.

Material	Density ρ (kg/m ³)	Young's modulus E (MPa)	Poisson's ratio λ	Cohesion c (kPa)	Friction ϕ (°)
Soft clay	2000	50	0.15	30	20
Anchor beam	2500	25000	0.2	3000	50

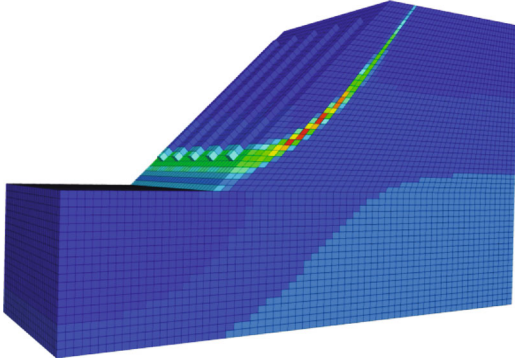


FIGURE 12: Initial equilibrium state of the slope.

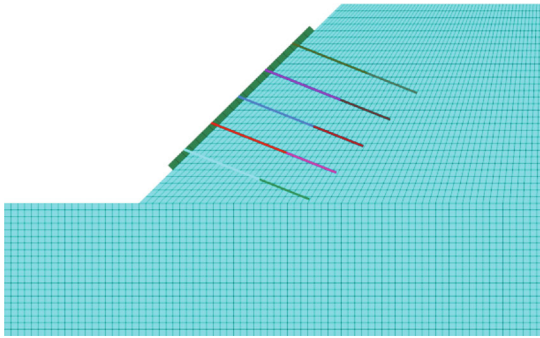


FIGURE 13: Slope model with cables.

Substituting Equations (30)–(33) into Equation (20), we obtain

$$\frac{3 - \sin^2 \varphi}{4 \sin \varphi} \sqrt{(1 - 2\mu)^2 \arctan^2 \frac{a}{x} + \frac{3x^2 a^2}{(x+a)^2} + (1 + \mu) \arctan \frac{a}{x}} = \frac{3c_0 \pi}{4p_0 \tan \varphi}. \quad (34)$$

The maximum effective depth, L_0 , can then be computed using Equation (34).

4. Parametric Study

To analyze the influence of parameters considered in the proposed method on the plastic failure envelopes of soil and the maximum effective depth underlying the anchor beam, a further parametric study was conducted. The value of beam width, $2a$, was adopted as 1 m; the value of Poisson's ratio, μ , of saturated soft clay was considered as 0.5; the value of initial horizontal cohesive strength, c_0 , was assumed to be 30 kPa; and the value of the angle of internal friction φ was set to 20°. Considering the complexity of Equations (27)

and (34), mathematical software Mathematica and Fortran 95 were used to compute the results.

4.1. Influence of Prestress on the Failure Envelopes. In this experiment, λ was set to 1, ρ was set to 1, and cable prestress, p_0 , was considered to be in the range 500–1000 kPa, with increment steps of 100 kPa. Figure 7 shows that the failure envelopes of soil increase with increase in the value of prestress, p_0 . The variation law of the maximum effective depth also follows the same trend.

4.2. Influence of Anisotropy on the Failure Envelopes. To analyze the influence of anisotropy on the plastic failure envelopes, λ was set to 1, and the cable prestress, p_0 , was set to 500 kPa. Figure 8 shows that the failure envelopes of soil only slightly influence ρ , increasing it from 0.7 to 1.1. Thus, the shear strength of soil decreased with increase in the value of ρ , and there were small increments in the failure envelopes of soil.

4.3. Influence of Nonhomogeneity on the Failure Envelopes. To analyze the influence of nonhomogeneity on the failure envelopes, ρ was set to 1, and the prestress, p_0 , of the cable was set to 500 kPa. Figure 9 shows that the plastic failure envelopes of soil decreased as λ increased from 1 to 5, with increments of 1. Thus, the shear strength of soil increased with increase in λ .

The value of ρ was set to 1, and the value of cable prestress, p_0 , was in the range 500–1000 kPa, with increments of 100 kPa. Figure 10 shows that the maximum effective depth of soil underlying the anchor beam increased with increase in the value of p_0 and decreased when λ increased from 1 to 5, with increments of 1. The influence of the coefficient of anisotropy, ρ , on the failure envelopes and the maximum effective depth of soil subjected to higher stress was larger than that under the influence of lower stress.

In general, based on the clarification of the influence of parameters p_0 , ρ , and λ on the plastic failure envelopes and the maximum effective depth of soil, a simple method can be provided to predict the response of the prestressed anchor cable and to optimize cable design parameters, such as the anchorage length of cable and grouting radius.

5. Verification through Numerical Simulation

To verify the critical parameters of the equations presented in Section 3, a simple model of slope and cable was built using Flac3d software. The slope was analyzed by considering the cable prestress, p_0 , the coefficient of anisotropy, ρ , and the linear gradient of cohesive force, λ .

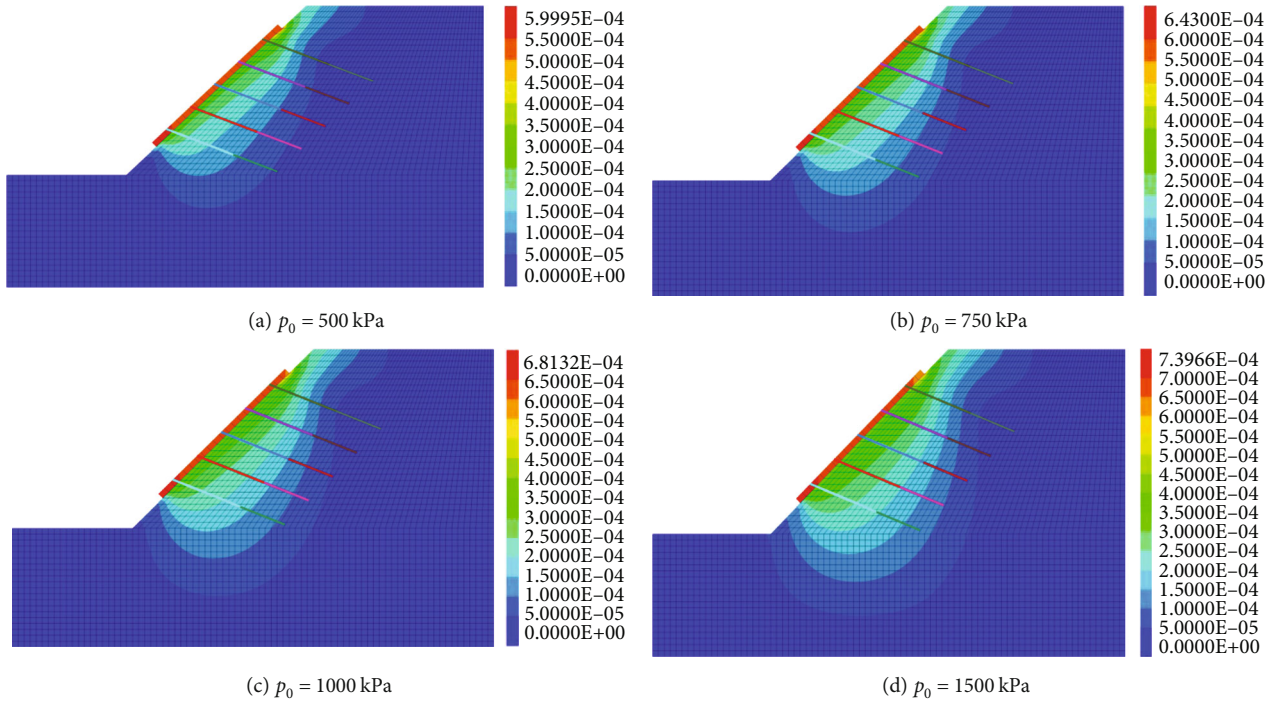


FIGURE 14: The displacement nephogram of the slope under different prestresses.

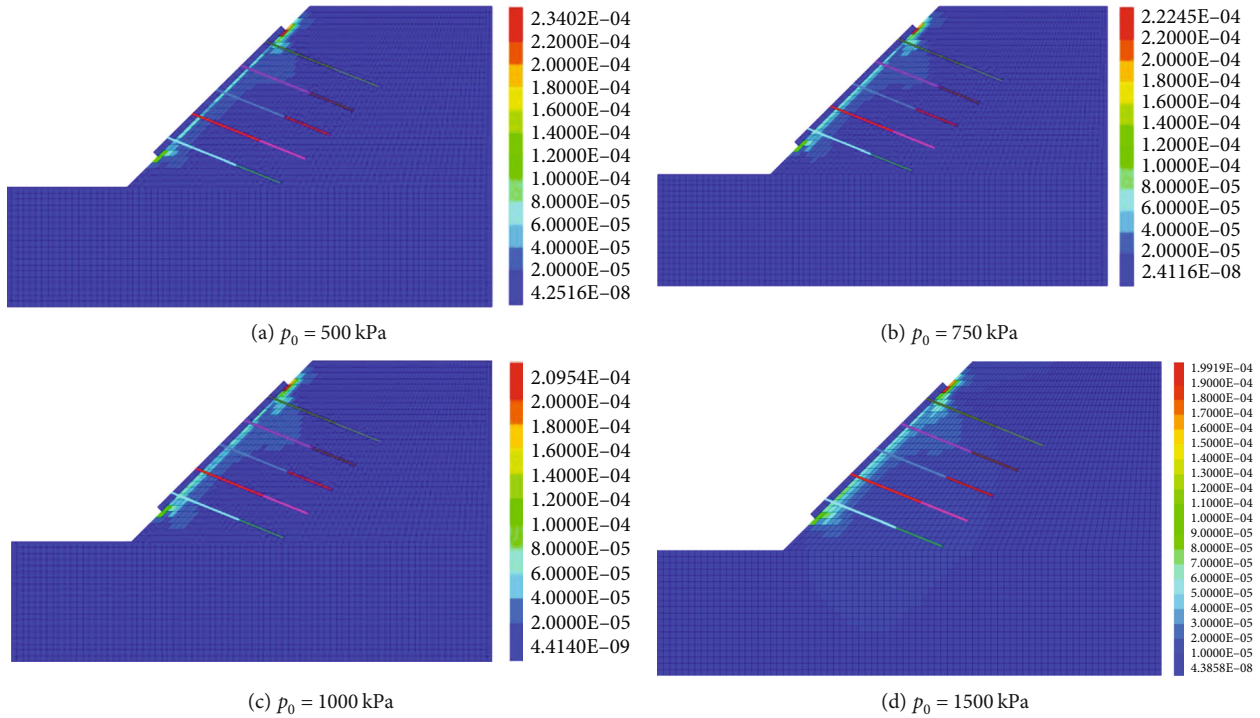


FIGURE 15: Maximum shear strain.

5.1. Modeling and Loading Cases. The brick element was used to simulate the slope, and the cable element was used to simulate the anchor beams. The dimensions of the slope model were length = 80 m, width = 30 m, and height = 50 m; the toe of the slope was 30 m high. Five anchor beams were

set on the slope surface with dimensions of 26 m × 1 m × 1 m . The function of the beam was to distribute the prestress evenly on the slope. The bottom of the slope was fully restrained, and normal restraint was applied at the four vertical surfaces. The slope model is illustrated in Figure 11.

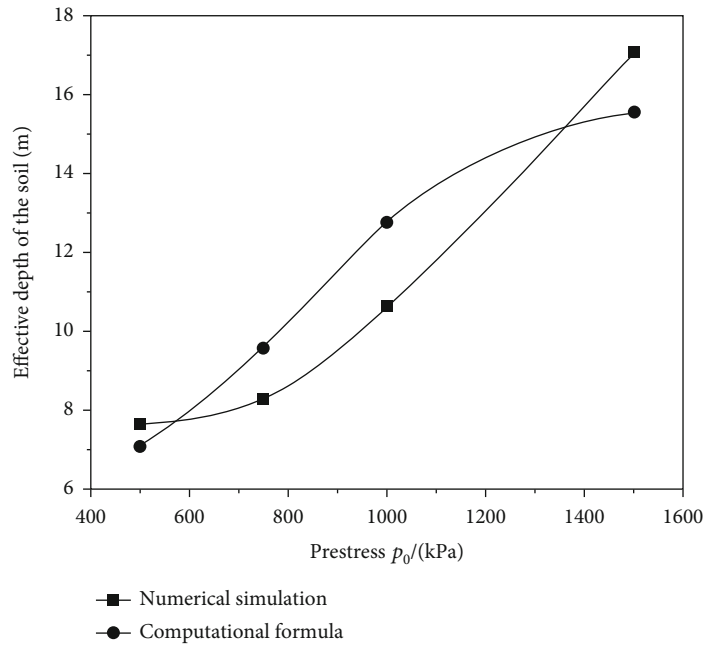


FIGURE 16: Maximum effective depth underlying the anchor beam.

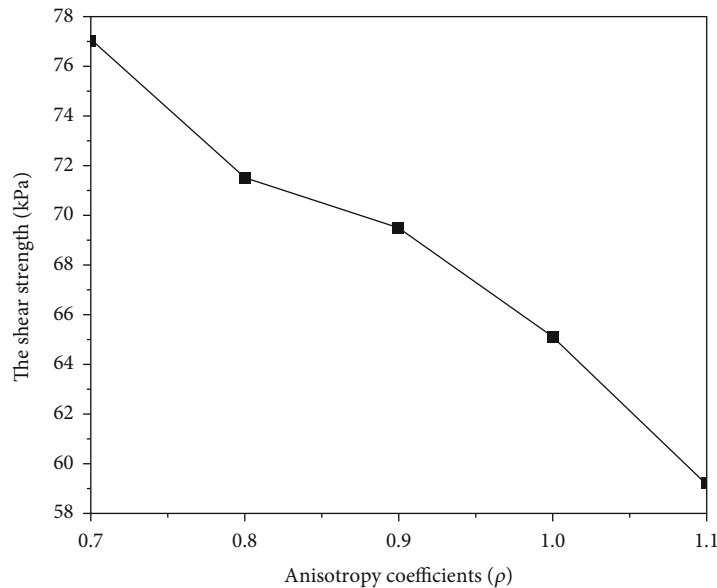


FIGURE 17: The variation in shear strength of soil with different anisotropy coefficients.

For soil of the slope, the Drucker-Prager ideal elastic-plastic stress-strain model was adopted, along with the Mohr-Coulomb constitutive model for anchor beams. Combined with the values suggested in Code and practical engineering, the properties of slope and beams were identified (listed in Table 1).

To ensure agreement between the behavior of the calculation model and real-time projects, an initial ground stress equilibrium is necessary. The factor of safety of the slope was 1.28, indicating sufficient stability. The initial state is shown in Figure 12. After the first equilibrium, elements

such as prestress cables and the interface between beams and slope were built. The cables were set through the beams using the built-in structural element (length = 20 m, interval = 4 m, and inclination angle = 22°) of Flac3d software. The prestress cable comprised a free section (length = 12 m) and an anchorage section (length = 8 m). The anchorage part was divided into eight parts for high calculation accuracy. Young's modulus of the cable was 200 GPa, the cross-sectional area was 0.00176 m², grout perimeter was 0.15 m, grout cohesion was 5.0 × 10⁶ N/m, grout stiffness was 1.0 × 10⁷ N/m², grout friction was 33°,

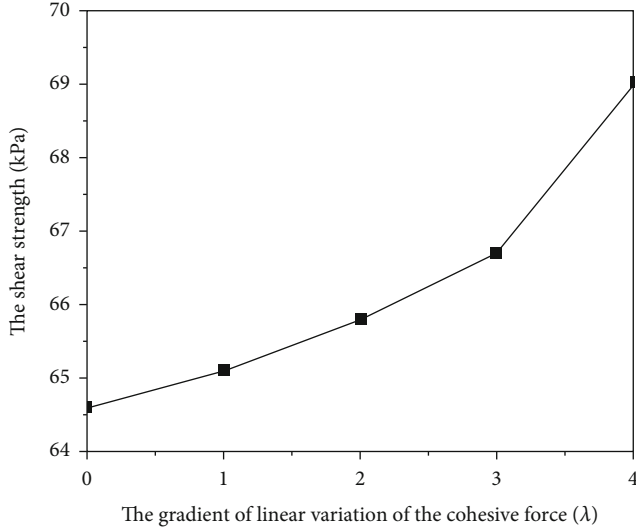


FIGURE 18: Variation in shear strength with the cohesion gradient.

and yield tension was 1×10^5 kN; the slope model with cables is shown in Figure 13.

To verify the theoretical formulas, the prestress of cables, p_0 , the anisotropy coefficient of saturated soft clay, ρ , and the linear gradient of cohesive force, λ , were considered successively to obtain the failure response of the prestressed cables. Thus, three cases were carried out in the numerical simulation, presented below.

Case 1. ρ was set to 1, and λ was set to 0. p_0 was set to 500 kPa, 750 kPa, 1000 kPa, and 1500 kPa.

Case 2. λ was set to 0, and p_0 was set to 500 kPa. ρ was increased from 0.7 to 1.1, with increments of 0.1.

Case 3. ρ was set to 1, and p_0 was set to 500 kPa. The value of λ was increased from 0 to 4, with increments of 1.

5.2. Calculation Results. For the three cases, the critical parameters were specifically concerned, and the failure responses of the cables were obtained, which were comparable with the theoretical formulas.

In Case 1, the shear strain indicated the slide state of the slope, and the maximum effective depth of soil underlying the anchor beam was obtained. Figure 14 shows the variation of soil displacement when the cables were subjected to different prestresses. Clearly, displacement increased with increase in prestress, and the affected area also increased (Figure 15). Therefore, the deformation response increased with increase in cable prestress.

To verify the effectiveness of the proposed calculation method, in this section, the calculation results are compared with the numerical simulation results. From the results of the computational formula, Equation (34), and the numerical simulation, as shown in Figure 16, the variation of the effective depth of soil showed similar trends; the effective depth increased with increase in prestress. As shown in Figure 16, the slope of the curve in numerical simulation

was relatively small when the pretension was <1000 kPa, and the effective depth increased sharply to 1500 kPa. This was attributed to the five cables working simultaneously in the numerical simulation; however, we only focused on one cable in the computational formula method. At a small value of pretension, the five cables coworked under the action of the anchor beam, and they were not fully functional. At a sufficiently large value of pretension, the cables were exploited; the effective depth of soil was determined to be slightly larger than the computational formula.

In Case 2, the variation in shear strength of soil with different anisotropy coefficients was obtained. The shear strength of soil was equal to the shear stress. Equation (16) illustrates the relationship between the cohesion of soil in the horizontal and vertical directions. Equation (17) shows the cohesive force of the saturated and undrained clay soil; c_ψ was influenced by the anisotropy coefficient of soil. Therefore, assuming that the cables were subjected to a prestress of 500 kPa, the displacement and stress responses of the slope were obtained. Figure 17 shows that the shear strength of soil decreased with increase in the value of ρ . This is because the cohesive force of the clay, c_ψ , decreased with increase in the value of ρ , showing an obvious influence on the strength of soil.

In Case 3, the variation in shear strength with the cohesion gradient was obtained. The strength of saturated and undrained clay soil varies linearly with depth [25–27]. According to Equation (19), when the anisotropy coefficient was 1, the cohesive force of soil increased with increase in the value of λ and the depth along the cable. As shown in Figure 18, the shear strength of soil increased with increase in the coefficient of anisotropy.

Thus, the influence of the parameters p_0 , λ , and ρ was investigated successively. The response of soil underlying the cable beam was also obtained. The results of numerical simulation verified that there is good agreement with the theoretical formulas proposed in Section 3.

6. Conclusions

Based on the assumption that an anchor beam is completely rigid and a prestressed anchor cable is applied to soil in the form of uniform load, this study presents an analysis on the responses of a prestressed anchor beam, considering nonhomogeneity and anisotropy of saturated soft clay. The computational formula of superimposed stress of soil underlying the anchor beam was proposed. Plastic failure envelopes of soil and the maximum effective depth underlying the anchor beam were obtained using the D-P yield criterion, which is typically used for soft clay analysis. The validity of the proposed method was checked for agreement with the findings of previous studies. Finally, a parametric study was conducted to analyze the influence on the plastic failure envelopes and the maximum effective depth of soil underlying the anchor beam, and an intuitive numerical simulation model was established for verifying the proposed equations. Some new findings are summarized as follows:

The plastic failure envelopes of soil increased with increase in the prestress and anisotropy coefficient, and it

decreased with increase in the gradient of linear variation in cohesive force.

The maximum effective depth of soil underlying the anchor beam increased with increase in the prestress and decreased with increase in the gradient of linear variation in cohesive force. The anisotropy coefficient had a greater influence on the failure envelopes as well as on the maximum effective depth of soil at higher prestress.

The shear strength of soil decreased with increase in the anisotropy coefficient and increased with increase in the gradient of cohesive force.

Comparing the results of the computational formula and numerical simulation, there were similar variations in the effective depth of soil, that is, it increased with increase in the prestress. Because of the coworking effect of the five cables in the numerical simulation, the effective depth of soil was smaller than that calculated using the computational formula when the pretension was <1000 kPa. With increase in pretension, the cables gradually functioned, and the effective depth of soil increased sharply and was finally larger than that of the computational formula.

The proposed method and the study results can help optimize cable design parameters such as anchorage length of the cable and grouting radius.

Data Availability

All data, models, and code generated or used during the study appear in the submitted article.

Conflicts of Interest

The authors declare that there is no conflict of interest regarding the publication of this paper.

Acknowledgments

The authors gratefully acknowledge the financial support offered by the National Natural Science Foundation of China (52078311); Young Talent Top Project of Hebei Province (BJ2020055); Hebei Provincial Natural Science Foundation of China (E2019210356); Natural Science Foundation for Youths of Hebei Province of China (E2021210055); Science and Technology Research Project of Colleges and Universities in Hebei Province (Grant Number: ZD2022073); State Key Laboratory for GeoMechanics and Deep Underground Engineering, China University of Mining and Technology (SKLGDUEK1916); China Postdoctoral Science Foundation (2019M663553); Key Laboratory of Large Structure Health Monitoring and Control (KLLSHMC1903); Shenzhen Science and Technology Innovation Program (KQTD20180412181337494) and Innovation and Entrepreneurship Training Program for College Students (S202210107051).

References

- [1] S. G. Du, C. Saroglou, Y. F. Chen, H. Lin, and R. Yong, "A new approach for evaluation of slope stability in large open-pit mines: a case study at the Dexing copper mine, China," *Environmental Earth Sciences*, vol. 81, no. 3, p. 102, 2022.
- [2] Y. Tang, H. Lin, Y. X. Wang, and Y. L. Zhao, "Rock slope stability analysis considering the effect of locked section," *Bulletin of Engineering Geology and the Environment*, vol. 80, no. 9, pp. 7241–7251, 2021.
- [3] B. X. Yuan, Z. H. Li, Z. L. Su, Q. Z. Luo, M. J. Chen, and Z. Q. Zhao, "Sensitivity of multistage fill slope based on finite element model," *Advances in Civil Engineering*, vol. 2021, Article ID 6622936, 13 pages, 2021.
- [4] Y. F. Chen, H. Lin, R. H. Cao, and C. Y. Zhang, "Slope stability analysis considering different contributions of shear strength parameters," *International Journal of Geomechanics*, vol. 21, no. 3, article 04020265, 2021.
- [5] L. K. Cheng, J. L. Fan, J. Han, and J. P. Xu, *Rock-Soil Anchor*, China Architecture and Building Press, Beijing, 2003.
- [6] F. Delhomme, G. Debicki, and Z. Chaib, "Experimental behaviour of anchor bolts under pullout and relaxation tests," *Construction and Building Materials*, vol. 24, no. 3, pp. 266–274, 2010.
- [7] F. Delhomme and G. Debicki, "Numerical modelling of anchor bolts under pullout and relaxation tests," *Construction and Building Materials*, vol. 24, no. 7, pp. 1232–1238, 2010.
- [8] C. A. You and Y. B. Zhan, "Distributing law and analysis of stresses at anchoring sections of prestressed cables," *Chinese Journal of Rock Mechanics and Engineering*, vol. 24, no. 6, pp. 925–928, 2005.
- [9] S. R. Wang, Y. H. Wang, J. Gong, Z. L. Wang, Q. X. Huang, and F. L. Kong, "Failure mechanism and constitutive relation for an anchorage segment of an anchor cable under pull-out loading," *Acta Mechanica*, vol. 231, no. 8, pp. 3305–3317, 2020.
- [10] Q. P. Xia, J. P. Gao, L. C. Chen, and A. T. Wang, "Distribution of soil pressure on back of suspension anchor retaining wall," *Chinese Journal of Highway and Transportation Research and Development*, vol. 36, no. 7, pp. 47–52, 2019.
- [11] X. Fu, J. J. Zhang, and L. R. Zhou, "Shaking table test of seismic response of slope reinforced by combination of anti-slide piles and multi-frame foundation beam with anchor cable," *Rock and Soil Mechanics*, vol. 38, no. 2, pp. 462–470, 2017.
- [12] Z. P. Yang, S. Q. Li, Y. Yu, X. R. Liu, and Y. X. Hu, "Study on the variation characteristics of the anchor cable prestress based on field monitoring in a foundation pit," *Arabian Journal of Geosciences*, vol. 13, no. 23, p. 1269, 2020.
- [13] J. C. Gu, Z. Q. Ming, and J. Shen, "Field testing study on load distribution of inner-anchor segment of prestress anchorage cable," *Chinese Journal of Rock Mechanics and Engineering*, vol. 17, pp. 251–256, 1998.
- [14] Q. W. Xu, C. A. You, and H. H. Zhu, "Research on 3D numerical simulation of prestressed anchor cable and its anchoring mechanism," *Chinese Journal of Underground Space and Engineering*, vol. 1, no. 2, pp. 214–218, 2005.
- [15] X. L. Ding, Q. Sheng, and J. Han, "Numerical simulation testing study on reinforcement mechanism of prestress anchorage cable," *Chinese Journal of Rock Mechanics and Engineering*, vol. 21, no. 7, pp. 980–988, 2002.
- [16] P. Yu and Y. Yu, "Test study on prestressed anchor rope in landslide," *The Chinese Journal of Geological Hazard and Control*, vol. 7, no. 1, pp. 59–63, 1996.
- [17] Z. J. Wu, Z. J. Wang, J. W. Bi, X. Fu, and Y. Yao, "Shaking table test on the seismic responses of a slope reinforced by prestressed anchor cables and double-row antisliding piles," *Shock and Vibration*, vol. 2021, Article ID 9952380, 13 pages, 2021.

- [18] X. Sun, B. Zhang, L. Gan, Z. Tao, and C. Zhao, "Application of constant resistance and large deformation anchor cable in soft rock highway tunnel," *Advances in Civil Engineering*, vol. 2019, Article ID 4347302, 19 pages, 2019.
- [19] Y. H. Yuan, M. Xiao, and J. T. Chen, "A method for simulating stress distribution along fully grouted anchor," *Rock and Soil Mechanics*, vol. 39, no. 5, pp. 1908–1961, 2018.
- [20] M. S. Huang, H. L. Qin, and Y. C. Guo, "Upper bound solution for bearing capacity of nonhomogeneous and anisotropic clay foundation," *Chinese Journal of Rock Mechanics and Engineering*, vol. 27, no. 3, pp. 511–518, 2008.
- [21] H. L. Qin, Y. J. Wang, Z. D. Tang, and S. K. Ma, "Upper bound solutions for bearing capacity of smooth rigid strip foundations on anisotropic and non-homogeneous clay," *Rock and Soil Mechanics*, vol. 32, no. 2, pp. 611–616, 2011.
- [22] Y. H. Huang, "Finite Element Analysis of Nonlinear Soil Media," in *Proc. of the Symposium on Application of FEM in Civil Engineering*, pp. 663–685, New York, ASCE, 1969.
- [23] S. M. He, "Modified layer-summation based on elastoplastic theory," *Rock and Soil Mechanics*, vol. 24, no. 1, pp. 81–92, 2003.
- [24] X. F. Wu, G. F. Li, and J. H. Luo, "Stress formula of soil under horizontal line load," *Natural Science Journal of Hainan University*, vol. 30, no. 3, pp. 219–224, 2012.
- [25] K. Y. Lo, "Stability of slopes in anisotropic soils," *Journal of the Soil Mechanics and Foundations Division*, vol. 91, no. 4, pp. 85–106, 1965.
- [26] W. F. Chen, *Limit Analysis and Soil Plasticity*, Elsevier Science, The Netherlands, 1975.
- [27] A. A. Al-karni and M. A. Al-shamrani, "Study of the effect of soil anisotropy on slope stability using method of slices," *Computers and Geotechnics*, vol. 26, no. 2, pp. 83–103, 2000.
- [28] A. Casagrande and N. Carillo, "Shear failure of anisotropic materials," *Journal of Boston Society of Civil Engineers*, vol. 31, no. 4, pp. 74–81, 1944.
- [29] S. Gourvenec and M. Randolph, "Effect of strength nonhomogeneity on the shape of failure envelopes for combined loading of strip and circular foundations on clay," *GEN*, vol. 53, no. 6, pp. 575–586, 2003.
- [30] R. E. Gibson, "The analytical method in soil mechanics," *Geotechnique*, vol. 24, no. 2, pp. 115–140, 1974.
- [31] A. W. Skempton, "The pore-pressure coefficient in saturated soils," *Geotechnique*, vol. 10, no. 4, pp. 186–187, 1960.
- [32] P. E. Li and Y. Q. Yin, "Modification of Drucker-Prager criterion in tensile shear region," *Chinese Journal of Rock Mechanics and Engineering*, vol. 29, no. S1, pp. 3029–3033, 2010.
- [33] X. H. Chu and Y. J. Xu, "Studies on transformation from M-C criterion to Drucker-Prager criterions based on distortion energy density," *Rock and Soil Mechanics*, vol. 30, no. 10, pp. 2985–2990, 2009.

Research Article

Head-On Dynamic Manifestations in the Roadway Driving with Small Coal Pillar under the Influence of Roof Drainage: A Case Study from Uxin Banner

Yunhai Cheng ¹, Fenghui Li ², Xiufeng Zhang,³ Chao Wang,⁴ and Gangwei Li²

¹National Engineering Laboratory of Coalmine Backfilling Mining, Shandong University of Science and Technology, Taian 271000, China

²School of Mining Engineering, Anhui University of Science and Technology, Huainan 232000, China

³Coal Burst Prevention and Control Research Centre, Shandong Energy Group Co., Ltd., Jinan 250000, China

⁴Yankuang Energy Group Co., Ltd., Zoucheng 273500, China

Correspondence should be addressed to Fenghui Li; ahlifenghui@163.com

Received 3 April 2022; Revised 27 July 2022; Accepted 2 August 2022; Published 23 August 2022

Academic Editor: Yang Yu

Copyright © 2022 Yunhai Cheng et al. This is an open access article distributed under the Creative Commons Attribution License, which permits unrestricted use, distribution, and reproduction in any medium, provided the original work is properly cited.

In the Uxin Banner area of the Inner Mongolia Autonomous Region, mines that have experienced rock bursts have all been affected by the presence of confined water in the roof strata. Strong mine pressure appears in the working face with about 30 m wide coal pillar in this area, and the research and practice of prevention and control of rock burst by small coal pillar are carried out. Mining-related events linked to the preservation of small coal pillars in the 2-2 coal seam of this region, and studies of the phenomenon, have shown that head-on rock bursts occur during gob-side roadway driving at the edge of the drained area, making it necessary to identify the sources of pressure triggering the events, to determine the related threshold criteria, and to identify methods to reduce the occurrence and magnitude of the rock burst events. This study used the gob-side entry driving in the drained area of the 2202 auxiliary haulage roadway of a mine as a case study. The paper built a structural and computational model for overburdens (including the drained stratum) before mining disturbance, based on the theory for a continuously distributed Winkler elastic foundation. The models used and developed in our study were used to identify, quantify, and describe the changes to stress and the transfer of stress during the drainage process. On the basis of the effects of drainage stress induced by the gob-side entry driving, we outlined a method for ranking the level of rock burst hazard associated with the areas in and adjacent to the drained area. The level of rock burst hazard associated with the entry driving could be arranged in descending order as follows: parallel boundary > vertical boundary > undrained area > drained area. Stress threshold criteria for head-on ejection were also proposed in the paper, namely, (1) the occurrence (or not) of coal ejection during loading and (2) the critical stress for the occurrence of ejection. Field monitoring indicated that microseismic events and energy are mainly concentrated in the driving region parallel to the boundary of the drained area. We concluded that head-on large-diameter borehole destressing would effectively reduce the likelihood of a rock burst occurrence.

1. Introduction

All mines susceptible to rock bursts in the Uxin Banner area of the Inner Mongolia Autonomous Region (China) are mines with complex hydrogeological conditions. In these mines, water confined in the roof strata affects the behavior of the

rock and hence the safety risks associated with the mining activities [1]. The mines are located within the Ordos Basin, with the coal seams hosted within the Jurassic Yan'an Formation. This formation is positioned between the older Fuxian Formation below and younger Zhiluo Formation above. The Yan'an Formation has been divided stratigraphically into five

subunits, namely, Y1, Y2, Y3, Y4, and Y5. The most important coal seam in the Yan'an Formation for mining purposes is the 2-2 coal seam.

The mining of the 2-2 coal seam in the Yan'an Formation is affected by water stored in the overlying Zhiluo Formation and the section of the Yan'an Formation above this coal seam. The occurrence of the water in the overlying strata is irregular over short distances [2–5]. Rock burst prevention practices, such as roof water drainage for small coal pillars, have further complicated the ground stress environment of the gob-side roadway. In the gob-side roadways, in drained areas of a mine, head-on ejection of coal has occurred multiple times, some of which have resulted in injuries to mine workers.

Many scholars have explored the relationship between the stress transfer induced by borehole drainage (or water inrush) and the rock bursts in roadways not subject to current mining activity. Shu et al. [6, 7] proposed that roof drainage modifies the physicochemical properties of aquifers, damaging them in the process. By using a method based on the principle of superposition for load analysis, they suggested that rock bursts could be induced by drainage through holes drilled during drive development (non-gob-side).

Li et al. [8–10] postulated that superposition between the step-up belt formed by drainage of confined water in the roof strata and the relatively greater bearing stress can lead to rock bursts. On this basis, they built a model for estimating roof confined water drainage and stress transfer. This model enabled them to show that the stress transfer could be caused by drainage. Using experimental methods, they discovered that water reduced the strength of the coal and argued that the weakening of the surrounding rock strength would increase the rock burst risk.

Wang et al. [11, 12] proposed a rock burst inducement mechanism dependent on “strong disturbance-drainage” in the high-intensity working face of the area of roof subject to drainage. They also developed models for estimating post-drainage and advanced bearing pressures, respectively. They tested their proposed inducement mechanism by carrying out field-based microseismic monitoring and numerical simulation. Based on the results of the studies, they proposed preventative measures for controlling the rate stopping development in the drained area.

The effect of roof drainage on rock bursts along a roadway and at a working face has also been investigated. However, gob-side driving differs from both solid entry driving, and working face stopping, in that gob-side entry driving, is carried out after stress redistribution. The stress redistribution could be attributed to the release of water pressure through drainage holes, or gob fissures. Gob-side entries are susceptible to rock bursts, and hence, the stress field characteristics of rock strata in close proximity to gob-side entries are of critical importance for rock burst hazard assessment [13, 14]. In addition, roof drainage, coal pillar width, coal pillar damage (the energy rate can be used to reflect the plastic failure of coal [15]), and roof fracture characteristics affect the nature of the stress field in rocks subject to gob-side entries [16–20].

References [6–12] have described how roof drainage-related stress in strata affects the occurrence of rock bursts in solid entry driving and stopping entries. However, they did not describe head-on coal bursts and rock bursts along roadways with small coal pillars. Furthermore, the ejection phenomena (e.g., spalling and rock bursts) that occur along the roadways with small coal pillars in other domestic mining areas have been rarely reported. In this context, research should be carried out to clarify the risks associated with the gob-side entry driving of small coal pillars subject to drainage.

This study used the elastic foundation beam model (based on the principle of load superposition) for roof drainage to analyze the changes to roof drainage stress during gob-side driving conditions. This paper also provides a description of how the stresses in the rock in these conditions can be assessed using a rock burst risk ranking for various roadway areas and introduces a rock burst reduction measure, namely, head-on large-diameter borehole placement to prevent (or mitigate) head-on-related rock burst risks.

2. Evolution of Roof Drainage Stress

The exploitation of coal seam resources causes the loss of groundwater [21]. On the damage of rock strata caused by drainage engineering for prevention and control of water inrush, Li et al. [8–10] focused their research on the effect of water on the lithology of coal. Shu, Wang et al., and Miao et al. [6, 22, 23] also examined the effect of water on the lithology of rocks. These studies showed that water played a major role in the weakening of coal and rocks. However, their conclusions were based on comparisons of the lithology of coal or rock samples before and after soaking in water. Zhao et al. used COMSOL Multiphysics software (version, COMSOL Inc., <https://www.comsol.com/>) to run simulations and model the damage and deformation caused by overburden and the loss of water from aquifers during mining. They found that seepage did not change the value of the rock parameters in the rock mechanics module [24]. Before drainage, a significant amount of time would have passed during which the nature of physicochemical reactions between the water and rock strata would have been relatively stable. The weakening of strata in this context differs from that taking place when dry sandstone is soaked in water, namely, during the relatively short periods typically associated with experiments. Therefore, in order to address the limitations associated with this modelling-based approach, we should take into account the weakening of rock physico-mechanical properties by mining-induced drainage.

Stress transfer is essentially a result of movement in rock strata. The scope of drainage stress transfer and the degree of stress concentration are directly related to the movement in the strata subjected to the drainage. Before the mining of an adjacent working face in gob-side entry driving, the pattern and degree of stress distribution caused by drainage can be determined using the elastic foundation beam model. The analysis is based on values obtained for movement and the measured specific pressure drop induced by overburden drainage.

After roof water drainage, the roof stratum above the drained area (the medium-fine sandstone stratum in our case study) can be regarded as a double-clamped beam, the length of which is related to the distance of the stratum away from the drained stratum. That is, the longer the distance of the stratum away from the drainage stratum, the greater the length of the beam. The load applied on the double-clamped beam was determined by deducting the stress transferred by the underlying relatively weak stratum from the water pressure drop after drainage.

The disturbance-related stress induced by drainage is borne jointly by the rocks in and outside the area that has been drained. Before the working face is mined, boreholes are drilled for drainage purposes into the two aquifers (i.e., Zhiluo Formation and Yan'an Formation). The drained stratum is located outside the plastic zone of the roadway, with the stratum in the drained area treated as an elastomer. References [8, 12] also treat the stratum in the drained area as an elastomer [8, 12]. The load borne by the elastic bearing zone was assumed to be a uniformly distributed load σ_e , with the rocks in and outside the drained area equated to a continuously distributed Winkler foundation model. The overlying stratum was treated as a double-clamped beam [25, 26], as shown in Figure 1. A simplified three-component mechanical model, based on the characteristics of the rocks (a) in the drained area, (b) the rocks outside the drained area, and (c) the overlying stratum, is shown in Figure 2.

The origin of the coordinates O was located at the edge of the drained area. The coordinate system was set up using the exterior of the drained area as the positive x -axis and roof deflection function $w(x)$ as the unknown quantity, where σ_e denoted the uniformly distributed load borne by the overlying stratum, k_n denoted the response modulus of the foundation in the drained area, and k_w denoted the response modulus of the foundation outside the drained area.

According to the basic principles of elasticity mechanics, the relationship between the strain and stress borne by the rocks in the drained area can be expressed using the following formula:

$$\varepsilon = \frac{\sigma}{E_n}, \quad (1)$$

where E_n denoted the elastic modulus of the rocks in the drained area.

Following Winkler's hypothesis [27], the relationships between the roof deflection function $w(x)$ with load σ_e and foundation pressure $p(x)$ can be expressed as

$$\frac{EI d^4 w(x)}{dx^4} = \sigma_e - p(x), \quad (2)$$

where EI denotes the bending strength of a random beam section, E denotes the elastic modulus, and I denotes the sectional moment of inertia.

The deflection w of a random point on the foundation is directly proportional to the pressure p applied at this point:

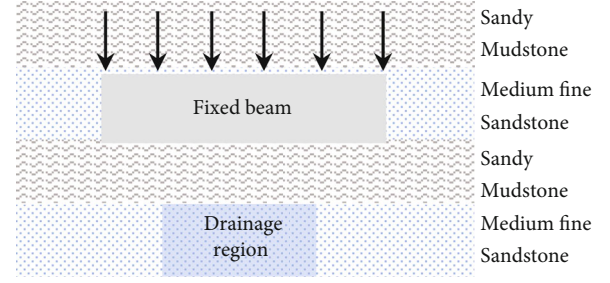


FIGURE 1: Fixed beam model of rock above drainage area.

$$k = \frac{p(x)}{w(x)}, \quad (3)$$

where k denotes the response modulus of the foundation, $p(x)$ denotes the specific pressure borne by the foundation, and $w(x)$ denotes the deflection value of the foundation.

The deflection equation for the overlying stratum in the drainage area can therefore be expressed as

$$\frac{EI d^4 w(x)}{dx^4} = \sigma_e - k_n w(x). \quad (4)$$

After defining the characteristic constant $\alpha = \sqrt[4]{k_n/EI}$, we have

$$\frac{d^4 w(x)}{dx^4} + 4\alpha^4 w(x) = \frac{\sigma_e}{EI}. \quad (5)$$

By solving the above equation, we obtain the following general solution:

$$w(x) = \sigma_e/k_n + d_1 e^{\alpha x} \cos(\alpha x) + d_2 e^{\alpha x} \sin(\alpha x) + d_3 e^{-\alpha x} \cos(\alpha x) + d_4 e^{-\alpha x} \sin(\alpha x), \quad (6)$$

where constants d_1 , d_2 , d_3 , and d_4 are undetermined parameters, while the roof deflection equation $w(x)$ can be used to determine the boundary and continuity conditions. The stress values for corresponding positions can be calculated by using the elastic moduli k_n and k_w of the strata in and outside the drained area and the roof deflection equation.

$$\sigma = kw(x). \quad (7)$$

The relationship between the maximum deflection of the beam and the compressive deformation of the drainage stratum can be assigned to one of two patterns:

- (1) The "M" stress distribution pattern when the maximum deflection of the beam is no greater than the compressive deformation of the drainage stratum (Figure 3(a))
- (2) The irregular wave-like stress distribution pattern when the theoretical maximum deflection of the

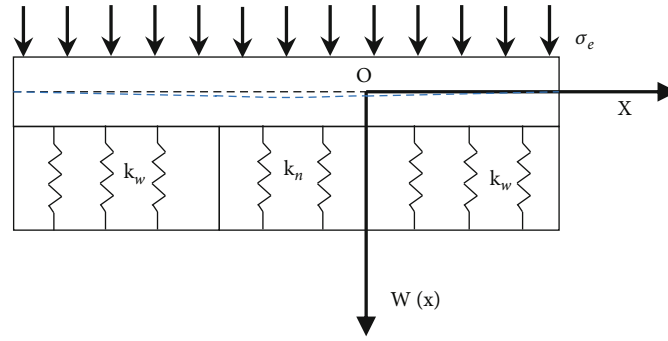


FIGURE 2: Mechanical model of roof in drainage area.

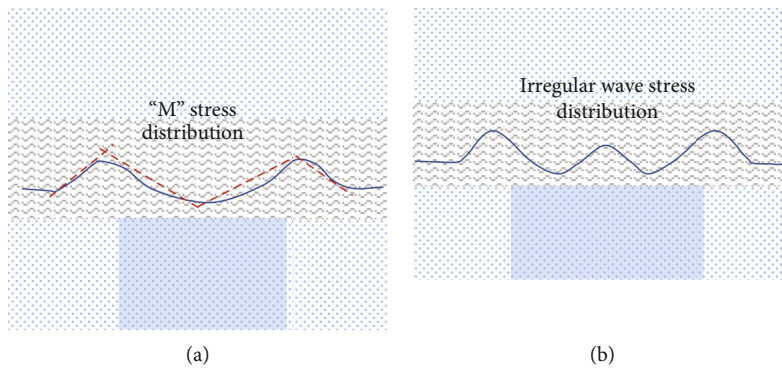


FIGURE 3: Schematic diagram of stress distribution of different drainage zone widths.

beam is greater than the compressive deformation of the drainage stratum (Figure 3(b))

We propose that when the theoretical maximum deflection of the beam is greater than the compressive deformation of the drainage stratum, the stratum in the middle of the drained area can still support the overlying stratum, giving rise to stress transfer similar to that in the case of gob compaction. In certain conditions, the stress restoration zone in Figure 3(b) may form a platform-type stress distribution (Figure 3(b)). In this paper, a drainage stress transfer model is built using the “M” stress distribution pattern as an example.

Before drainage, the vertical stress is uniformly distributed in the water-rich stratum. After drainage, the decline in the water pressure in the drained area weakens its supporting effect in the overlying stratum and causes the stratum above the drained area to subside. As a result, the vertical stress in the drained area is transferred outwards, giving rise to a low-stress zone in the drained area and a high-stress zone adjacent to it (Figure 4).

The elevated stress zone formed in this way affects the distribution of stress in the coal in the drained area. The path of stress transfer, indicated by the green-dotted arrow in Figure 4, shows the downward transfer of stress in accordance with a certain stress dispersion angle. The stress increment curve, indicated by the green solid curve in Figure 4, represents the change in stress in the coal seam.

These results are consistent with the findings of earlier studies. We therefore concluded that the morphology of the edge of the drained area and the relative spatial relationship between the roadway and the edge of the drained area affected the level

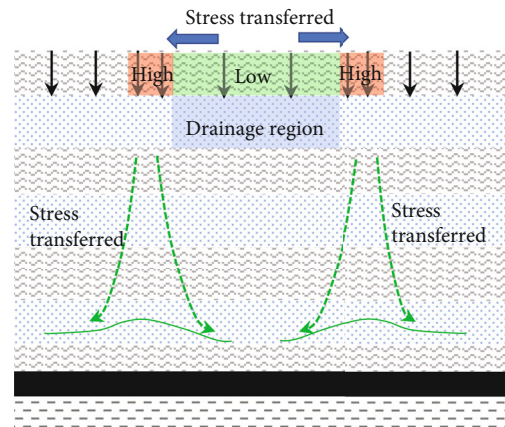


FIGURE 4: Stress transfer model after drainage.

of rock burst risk caused by entry driving. This finding was corroborated by (1) the concentration of microseismic events in the concave angle area of the drained area (reference [12]) and (2) the concentration of microseismic events in the driving region parallel to the edge of the drained area (Figure 5).

3. General Relationship between the Drained Area and the Gob-Side Entry Area

The overburdens at the gob boundary rotate and subside form a structure supported by one fulcrum on the coal wall and another on the gangue. The multilayer spatial structure

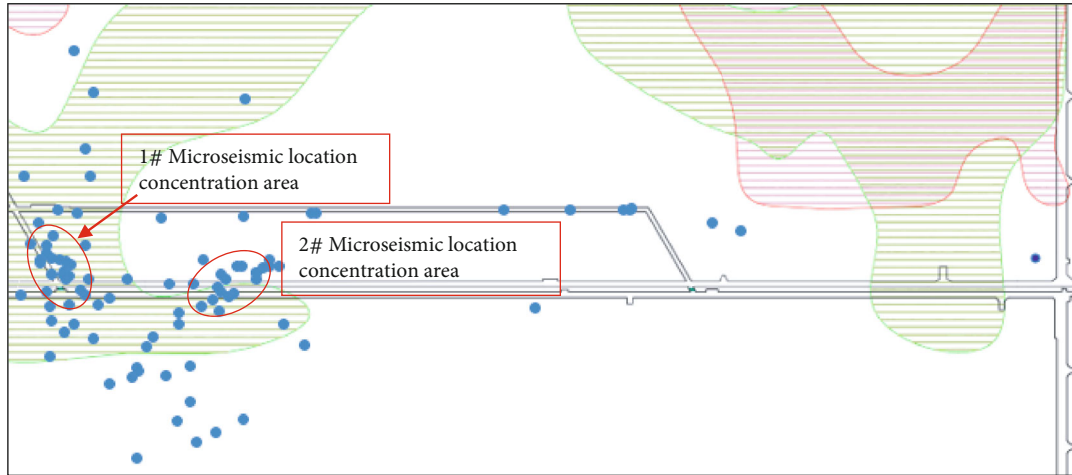


FIGURE 5: Distribution of microseismic events during the period of the 2202 auxiliary transport roadway excavation.

produces a stress increment in coal via the fulcrum on the coal wall [28].

The positional relationship between the drained area and the gob-side entry has three potential scenarios:

- (1) The gob-side entry is located in the postdrainage low pressure zone
- (2) The gob-side entry is located in the drained area with a pressure gradient between the drained (low pressure) and undrained (higher pressure) areas (i.e. coal seam)
- (3) The gob-side entry is unaffected by the drained area

After the drained area has been subjected to mining activity at the working face, the fissures in the fissure zone become drainage channels. While the elastic foundation beam model is no longer applicable to a drained area affected by mining, there is no fundamental change in the stress transfer laws in the drained area. That is, a low-stress zone still takes shape in the drained area, and a high-stress zone still forms at the boundary of the drained area [11].

After mining activity has taken place at the working face, the lateral stress present is as shown by the black-dotted curve in Figure 6. When the gob-side entry is in the post-drainage low pressure zone, the stress originally acting on the gob-side driving region on the solid coal wall side is transferred by the drained area to the boundary of the drained area. As a result, the stress level at the gob-side driving position drops below the lateral stress experienced in the undrained area, as indicated by the solid black curve in Figure 6.

In contrast, when the gob-side entry is in the postdrainage zone with a pressure gradient, the stress originally acting on the postdrainage low pressure zone is transferred by the drained area, partially to the gob-side driving region. This partial stress transfer produces a stress increment in the gob-side driving region, causing the stress level of the gob-side driving region to increase, as indicated by the solid black curve in Figure 7.

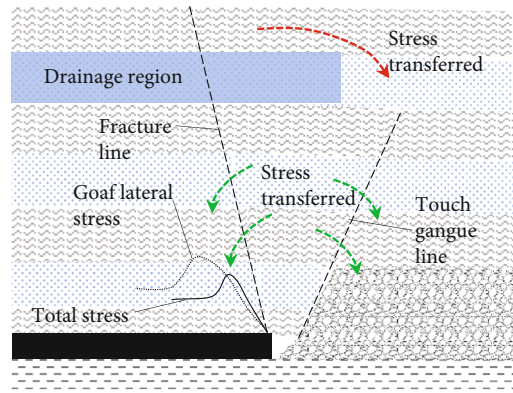


FIGURE 6: Stress evolution of roadway along goaf located in drainage depressurization area.

4. Mechanism and Criteria for Head-On Rock Bursts

Head-on rock bursts are closely related to the physico-mechanical properties and stress state of coal. Roof drainage affects the stress state in the coal. This section describes the effect of roof drainage on the stress state and the stress-induced mechanism for head-on rock bursts in gob-side driving due to roof drainage.

4.1. Rock Burst Risk Ranking for Various Roadway Areas. Regardless of chambers or crosscuts, the stress increment concentration coefficient for the effect of the gob on gob-side entry driving was consistent. If the stress increment concentration coefficient is λ , the stress at the position where the roadway is located becomes

$$\sigma_1 = (1 + \lambda)\gamma H, \quad (8)$$

where σ_1 denotes the stress in the surrounding rock due to gob-side entry driving; λ denotes the stress increment concentration coefficient for the surrounding rock produced by the gob-side entry driving, set as 0.5 (i.e., lateral stress concentration coefficient = 0.3 and driving stress

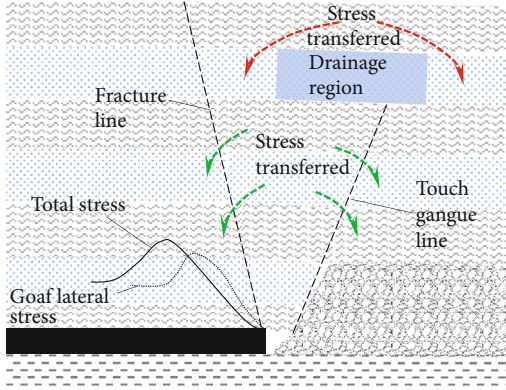


FIGURE 7: Stress evolution of roadway along goaf located in drainage pressurization area.

concentration coefficient = 0.2); γ denotes the bulk density of the stratum, set as $2,500 \text{ kg/m}^3$; and H denotes the burial depth of the roadway.

When gob-side entry driving is affected by roof drainage, the specific effect varies with the positional relationship between the driving face and the drained area. We assumed that the stress increment concentration coefficient and stress reduction concentration coefficient of the drained area had the same value and that the stress concentration coefficient was z . Driving in the water-rich zone (WRZ), driving in the water-poor zone (WPZ), and driving along the water-rich zone boundary (WRZB) are affected by roof drainage stress redistribution and gob lateral stress in different ways. In the case of driving along the WRZB, the effects of roof drainage stress redistribution and gob lateral stress are mutually enhanced via superposition. Driving in the WPZ is affected by gob lateral stress alone. In the case of driving in the WRZ, roof drainage stress redistribution and gob lateral stress are mutually weakened via superposition, and roof drainage stress redistribution weakens the effect of gob lateral stress on the gob-side driving roadway.

$$\sigma_2 = (1 + \lambda + z)\gamma H, \quad (9)$$

$$\sigma_3 = (1 + \lambda - z)\gamma H, \quad (10)$$

where σ_2 denotes the stress in the surrounding rock in the gob-side entry driving at the edge of the drained area, σ_3 denotes the stress in surrounding rock in the gob-side entry driving in the drained area, and z denotes the stress increment concentration coefficient for surrounding rock produced by drainage, with a mean value set at 0.2 [7].

The rock burst risks for the three roadway areas can be ranked in descending order according to the stress levels in different regions of the areas subject to gob-side driving, with the stress at the edge of the drained area > the undrained area > the drained area.

Due to the superposition of roof drainage stress and gob lateral stress, the stress level exceeds the stress threshold at which rock bursts occur in coal, at the working face of areas subject to gob-side driving. Rock bursts therefore occur in the areas where gob-side driving takes place.

4.2. Stress Criterion for Head-On Rock Bursts. For the prediction of rock burst hazards in mining engineering, “coal stress >1.5 times the integrated compressive strength” has been used as the stress threshold for assessing the level of rock burst hazard [29].

There is obvious zonation based on mining stress in the head-on direction of drive development, namely, a destressing zone (simulation results indicate that close to the coal wall, the stress vertical to the axial direction of the roadway is less than 4 MPa), a stress concentration zone, and an in situ stress zone [30]. Head-on ejection occurs near the head-on coal wall, within the destressing zone. The results in our study indicate that the widely used threshold value of 1.5 times the integrated compressive strength of the rock is probably not suitable for use as the critical stress for assessing the likelihood of a rock burst occurring near the coal wall.

Ejection is similar to tunnel rock bursts. The index used to predict rock bursts in tunnels is based on the ratio of rock uniaxial compressive strength to ground stress. That is, when the ratio is greater than 5, no rock burst occurs; when the ratio is between 2.5 and 5, mild or moderate rock bursts occur; and when the ratio is less than 2.5, severe rock bursts occur [31]. That is to say, the stress-strength ratios of 0.2 and 0.4 are taken as thresholds for assessing the level of the rock burst hazard (i.e., no rock burst hazard, mild to moderate rock burst hazard, and severe rock burst hazard). There are also studies that use 0.15, 0.2, 0.3, or 0.34 as the threshold value [32].

In uniaxial or triaxial compression tests on coal samples, the stresses under which ejection occurs generally exceed $0.6 \sigma_c$. In a total of 15 tests, the stresses have exceeded $0.6 \sigma_c$ in 13 tests (with $0.25 \sigma_c$ and $0.45 \sigma_c$ each occurring once) [33–36].

On the basis of the above analysis, the stress criterion for assessing the presence of ejection near the coal wall can be obtained from outburst susceptibility tests, including (1) the occurrence (or not) of coal ejection during loading and (2) the critical stress for the occurrence of ejection.

5. Engineering Cases

5.1. Engineering Background. The 2-2 coal seam is the primary mineable coal seam in most mines in the Uxin Banner. The safe and efficient mining of the 2-2 coal seam offers an important guarantee for mine output. When the auxiliary haulage roadway of the 2202 working face of a mine is driven at the edge of the drained area, there can be frequent coal bursts, and drill rods can jam in destressing boreholes and drill cutting holes. In particular, in the case of driving within II in Figure 8, coal ejection occurs, accompanied by head-on coal ejection, coal bursts, and massive amounts of coal dust.

The auxiliary haulage roadway of the 2202 working face is the roadway for gob-side driving, located 5 m away from the 2201 gob and 300 m away from the 2202 belt conveyor haulage roadway. At a site 80 m away from the auxiliary haulage roadway of the 2202 working face, there is an auxiliary haulage roadway for the 2201 working face, which is

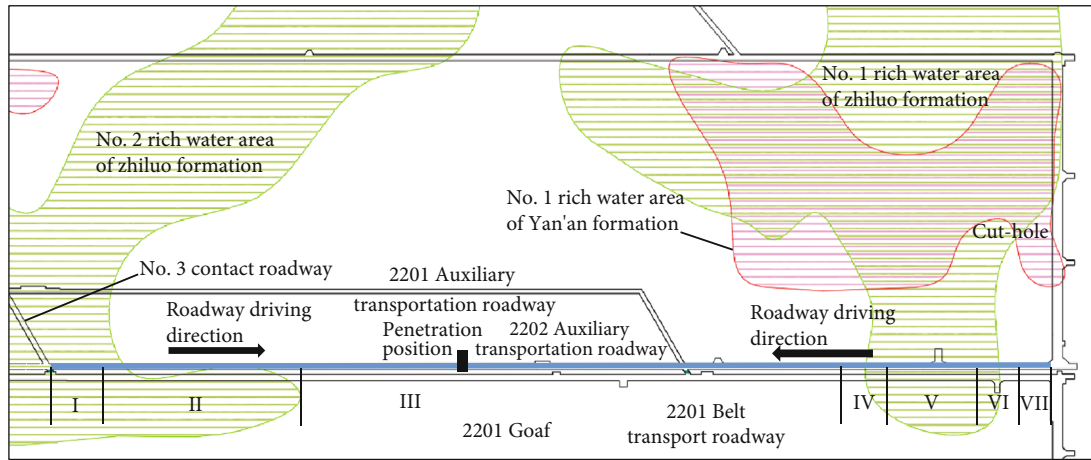


FIGURE 8: Spatial relationship of the roadway (the blue line is 2202 auxiliary transport roadway).

TABLE 1: Composite columnar section of the 2202 working face.

Strata	Thickness (m)	Comment
Medium-fine sandstone	12.91	The relative water-rich anomaly region of the Zhiluo formation
Sandy mudstone	12.45	
Medium-fine sandstone	13.56	The relative water-rich anomaly region of the Yan'an formation
Sandy mudstone	13.90	
Medium-fine sandstone	11.56	The relative water-rich anomaly region of the Yan'an formation
Sandy mudstone	6.87	
2-2 coal seam	6.50	

connected via the #3 crosscut. The crosscut intersects with the auxiliary haulage roadway of the 2202 working face.

The coal seam of the 2202 working face has a floor elevation of 516-521.3 m (average = 518.7 m) and a ground elevation of 1,249.8-1,250.4 m (average 1,250.1 m). The mean burial depth of the working face is 731.4 m. The coal seam has a simple structure and is unaffected by faults, folds, or other geological structures. The dip angle of the coal seam is 0-4° (average = 2°).

Distribution of roof water: the relatively water-rich strata of the Yan'an and Zhiluo Formations are located above the 2-2 coal seam, as shown in Figure 8. The area filled with green horizontal lines is the relatively water-rich Zhiluo Formation, while that filled with red horizontal lines is the relatively water-rich Yan'an Formation. Entry driving proceeds at one end from #3 crosscut towards the open offcut and at the other end from the open-off cut towards #3 crosscut, as illustrated in Figure 8. Depending on the specific effect of the drained area in the Zhiluo Formation on stress in driving, the spatial relationship between the drained area and driving is divided into four types (i.e., driving parallel to the edge of the drained area, driving vertically to the edge of the drained area, driving in the drained area, and driving in the undrained area), which are connected at the positions indicated in Figure 8.

As shown in Figure 8, on the basis of the relationship between entry driving and the drained area (with the point of intersection between the 2202 auxiliary haulage roadway

and the #3 crosscut being the origin), the roadway is divided into seven areas: I (0-45 m), II (45-250 m), III (250-782 m), IV (782-842 m), V (842-913 m), VI (913-973 m), and VII (973-996 m). To be more specific, I and V involve driving in the drained area; II involves driving parallel to the edge of the drained area; III and VII involve driving in the undrained area; and IV and VI involve driving vertically to the edge of the drained area.

The composite columnar section is shown in Table 1. Above the 2-2 coal seam, there is an intercalated sequence of sandy mudstone and medium-fine sandstone. The roof of the 6.5 m thick coal seam is a 6.87 m thick layer of sandy mudstone, and the basic roof is a 11.56 m thick layer of medium-fine sandstone. The relatively water-rich Yan'an Formation is located in the medium-fine sandstone layer of the basic roof. When the 2202 auxiliary haulage roadway is driven between the #3 crosscut and the open-off cut, the relatively water-rich Yan'an Formation is not involved. The relatively water-rich Zhiluo Formation is located 58.34 m above the 2-2 coal seam. The height of the diversion fissure zone of the mine is 21 times the mining height, namely, $6.5 \text{ m} \times 21 = 136.5 \text{ m}$, which is far greater than the distance from the relatively water-rich Zhiluo Formation in the mine to the 2-2 coal seam.

5.2. Rock Burst Risk Prediction for Gob-Side Entry. By analyzing the stress transfer of the drained area and the spatial relationship between the drained area and the gob, we were

able to predict that there are different rock burst risks associated with the different areas in the driving of the 2202 auxiliary haulage roadway. The roadway area can be divided into four areas, in order to predict rock burst risk, namely, drives in the drained area, drives in the undrained area, vertical drives to the edge of the drained area (i.e., stopes), and drives parallel to the edge of the drained area.

The driving of the 2202 auxiliary haulage roadway is mainly affected by roof drainage-related stress redistribution, gob lateral stress, and coal cutting in the 2201 auxiliary haulage roadway. The distribution of the gob lateral stress field is related to the distance away from the gob. The 2201 gob and the 2201 auxiliary haulage roadway exert the same effect on the driving of various areas of the 2202 auxiliary haulage roadway. In areas where coal pillar width varies due to chambers or crosscuts, gob lateral stress has a differential effect on the driving of the 2202 auxiliary haulage roadway. In entry driving, microseismic events are triggered in areas affected by chambers or crosscuts.

The roadway parallel to the edge of the drained area is located along the length of the high-stress zone. Compared with roadways driven perpendicular to the edge of the drained area (which only passes through the high-stress zone), roadways driven parallel to the edge of the drained area are more dangerous. In combination with the analysis in Section 3, the seven areas can be ranked as follows in descending order of rock burst risk, namely, II > IV, VI > III, VII > I, and V.

5.3. Field Monitoring. Many microseismic events are observed in the driving of the 2202 auxiliary haulage roadway. In particular, it is difficult to identify the distribution of microseismic events in the #1 and #2 seismic focus concentration areas marked in Figure 5. Microseismic events occurring in the driving of the 2202 auxiliary haulage roadway are screened, while those with an energy level above 10^4 joules are marked on the mining engineering plan, as shown in Figure 5.

The microseismic events shown in Figure 5 are concentrated in two areas. The areas marked by red ellipses are the #1 and #2 seismic focus concentration. The emergence of the #1 seismic focus concentration area is mainly attributable to the #3 crosscut. In the opening and initial driving stage of the 2202 auxiliary haulage roadway, driving disturbance affects the #3 crosscut, resulting in microseismic focus concentration in the vicinity of the #3 crosscut. The emergence of the #2 seismic focus concentration area is due to roof drainage, especially in the overlapping area between the edge of the drained area and the roadway.

While the distribution of microseismic events indicates the degree of roadway disturbance, it is also useful to analyze the information collected from microseismic monitoring work. For this statistical analysis, we selected the microseismic events that were recorded within 40 m, either side of a 10 segment of the roadway. Microseismic energy describes the statistical distribution of individual events in relation to the amount of energy released. Descriptive statistics were calculated for these microseismic events. In Figures 9 and 10, the point of intersection between the 2202 auxiliary haul-

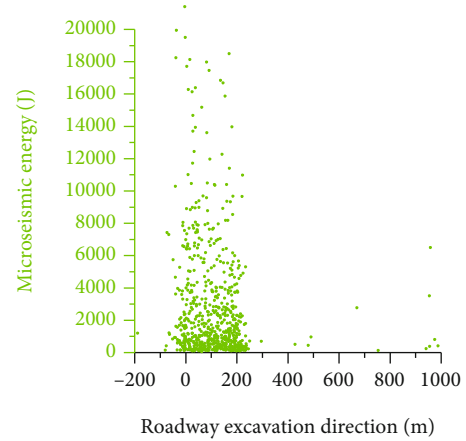


FIGURE 9: The distribution of microseismic energy along roadway excavation direction.

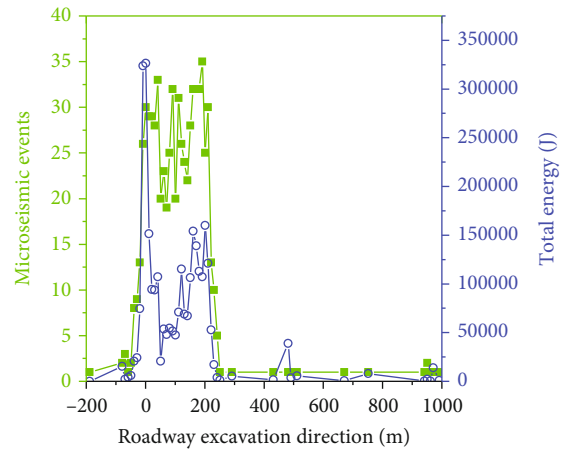


FIGURE 10: The distribution of the number of microseismic events and total energy along roadway excavation direction.

age roadway and the #3 crosscut is taken as the origin and the open-off cut direction of the working face as the positive x -axis.

The concentrated distribution of individual event energy, event count, and total energy was observed between -40 and 240 m, with both individual event energy and event count displaying a uniform distribution. However, the distribution of total energy displayed obvious regularities. At 0 m, there was a maximum peak in total energy, which could be attributed to the roadway opening having disturbed the original balance of the rock surrounding the #3 crosscut. From 50 to 100 m, there was a dip in the magnitude of the total energy values. This implied that the area was unaffected by the #3 crosscut and only slightly affected by proximity to the edge of the drained area. From 50 to 210 m, there was an obvious rise in the total energy released by microseismic events, as the edge of the drained area gradually approached the roadway, with entry driving affected by the edge of the drained area to an increasingly large degree. From 210 to 240 m, both event count and total energy decline rapidly, and entry driving is separated from the edge of the drained area and enters the drained area.

5.4. *Monitoring and Destressing.* Head-on monitoring methods include the monitoring of microseismic events and drill cutting. Large-diameter boreholes were used for destressing purposes. Monitoring plans and destressing measures were implemented in the field to effectively mitigate the occurrence of stress release-related events, such as rock bursts.

5.4.1. *Monitoring Plans*

(1) *Microseismic Monitoring.* The microseismic monitoring system adopted for the mine could cover all the mining areas of the mine. In the driving of the 2202 auxiliary haulage roadway, analysis was performed on all microseismic monitoring data related to roadway driving, including microseismic frequency, energy, their distribution characteristics, and patterns of variation.

(2) *Drill Cutting Monitoring.* Two boreholes (with a pitch of 1 m and a diameter of 42 mm) were arranged head-on and drilled vertically into the coal wall. Drill cutting holes were 15 m in depth. The safe distance for drill cutting monitoring was 5 m.

5.4.2. *Destressing Measures.* Local destressing measures generally include blasting destressing, injection/hydraulic fracturing, and large-diameter borehole destressing. Large-diameter boreholes, characterized by simple operation and strong adaptability to head-on operating conditions during driving, were selected for head-on distressing purposes. The boreholes used for the head-on destressing of the driving face had a diameter of 150 mm and a depth of ≥ 30 m and were located at least 0.5 m above the roadway floor. Cyclic construction was carried out, with the belt of destressing protection at least 10 m in width.

6. Conclusions

This paper developed a model for assessing the rock burst hazard induced by roof drainage in gob-side driving. This model for the drained stratum overburden was based on the theory for a continuously distributed Winkler elastic foundation. It was used to analyze the link between the relatively water-rich anomalies in the Yan'an and Zhiluo formations and the lateral stress field of the stope adjacent to gob-side entry driving-related activities. The model could be used to describe the mechanism by which the composite stress in the water-bearing stratum triggers head-on rock bursts during drive development.

- (1) According to calculations based on the theory of a continuously distributed Winkler elastic foundation, a zone with a pressure gradient develops at the edge of the drained area postdrainage, and a low pressure zone forms in the drained area
- (2) The spatial relationship between the drained area and the gob-side entry driving generally covers the following scenarios: the gob-side entry is located in the postdrainage low pressure zone; the gob-side

entry is located in the postdrainage zone with a pressure gradient; or the drained area affects the stress state, level of rock burst risk, and dynamic manifestations of the driving region

- (3) By combining the characteristics of the ejections observed in the mines, with the ejections observed in the laboratory, it can be concluded that the stress criteria for assessing the occurrence of ejection phenomena should include the following:
 - (a) The occurrence (or not) of coal ejection during loading
 - (b) The critical stress threshold required for an ejection to be triggered
- (4) On the basis of the spatial relationship between the drained area and the drive for the 2202 auxiliary haulage roadway, roadway drives can be divided into seven areas and four types. The driving region parallel to the edge of the drained area constitutes a key area for the prevention of head-on rock bursts. In this scenario, if the monitoring of microseismic events and drill cutting are combined with the implementation of head-on large-diameter borehole destressing measures, mining should be able to take place safely

While drainage is the external cause of ejections (e.g., rock bursts), the physicomaterial properties of coal represent the internal cause. In future research, we will explore how the physicomaterial properties of coal affect rock burst phenomena in the Uxin Banner.

Data Availability

Data available on request.

Conflicts of Interest

The authors declare that there is no conflict of interest regarding the publication of this paper.

Acknowledgments

This research is supported by the National Natural Science Foundation for Young Scientists of China (Grant No. 52004004).

References

- [1] B. C. Shi and Y. Li, "Inner Mongolia Coal Mine Safety Supervision Bureau Ordos Supervision Branch," in *How to Break the Dilemma of "Rock Burst"*, China Coal News, 2021.
- [2] J. Yang and X. Ding, "Dewatering and depressurizing effect of roof water in deep buried coal seam of Shaanxi and Inner Mongolia contiguous area," *Safety in Coal Mines*, vol. 34, no. 6, pp. 35–39, 2013.

- [3] X. Y. Liang, J. Yang, and Z. G. Cao, "Characteristics and sedimental control of mine water outflow in Hujirt mining area," *Coal Geology & Exploration*, vol. 48, no. 1, pp. 138–144, 2020.
- [4] G. Chen, *Study on the Deep Transfer and Storage Mechanism of Mine Water in the Eastern Margin of Ordos Basin*, China University of Mining and Technology, 2020.
- [5] Y. H. Wang, *Research on Characteristics of Water Gushing and Mining Technology in Xiaojihan Coal Mine*, China University of Mining and Technology, 2019.
- [6] C. X. Shu, *The Mechanism and Prevention of Rock Burst Occurrence at Water-Rich Working Face of Depth Mine in the Adjacent Area of Shaanxi and Inner Mongolia*, University of Science and Technology Beijing, 2018.
- [7] C. X. Shu, F. X. Jiang, and Q. D. Wei, "Mechanism and treatment of rockburst induced by drainage in roadways in deep coal mines," *Journal of Mining & Safety Engineering*, vol. 35, no. 4, pp. 780–786, 2018.
- [8] D. Li, *Mechanism and Control Techniques of Rockburst Disasters in Deep Mines with Thick Topsoil and Confined Water-Bearing Roofs*, University of Science and Technology Beijing, 2018.
- [9] D. Li, F. X. Jiang, C. W. Wang, Z. J. Tian, Y. Wang, and J. H. Liu, "Study on the mechanism of rockburst induced by water inrush from deep," *Chinese Journal of Rock Mechanics and Engineering*, vol. 37, no. S2, pp. 4038–4046, 2018.
- [10] D. Li, F. X. Jiang, Y. Chen et al., "Mechanism of rockburst induced by "dynamic-static" stress effect in water-rich working face of deep well," *Chinese Journal of Geotechnical Engineering*, vol. 40, no. 9, pp. 1714–1722, 2018.
- [11] B. Wang, S. T. Zhu, Q. D. Wei, Y. S. Gu, Z. C. Li, and B. Zhang, "Mechanism and prevention measures of rock burst rapid mining face of roof drainage area," *Safety in Coal Mines*, vol. 51, no. 7, pp. 205–209, 2020.
- [12] B. Wang, F. X. Jiang, S. T. Zhu et al., "Investigating on the mechanism and prevention of rock burst induced by high intensity mining of drainage area in deep mines," *Journal of China Coal Society*, vol. 45, no. 9, pp. 3054–3064, 2020.
- [13] Y. H. Cheng, F. X. Jiang, Z. F. Hu, and J. K. Lin, "Prevention and control of coal burst on gob-side entry in deep coal seam with fully mechanized sublevel caving mining," *Chinese Journal of Rock Mechanics and Engineering*, vol. 35, pp. 3000–3007, 2016.
- [14] Z. Q. Wang, P. Wang, L. Shi et al., "Research on prevention of rock burst based on stress analysis of surrounding rock of gob-side entry," *Journal of China University of Mining and Technology*, vol. 49, no. 6, pp. 1046–1056, 2020.
- [15] Y. Xue, J. Liu, P. G. Ranjith, Z. Zhang, F. Gao, and S. Wang, "Experimental investigation on the nonlinear characteristics of energy evolution and failure characteristics of coal under different gas pressures," *Bulletin of Engineering Geology and the Environment*, vol. 81, no. 1, p. ???, 2022.
- [16] J. F. Pan, S. H. Liu, J. M. Gao, X. K. Sun, Y. X. Xia, and Q. Wang, "Prevention theory and technology of rock burst with distinguish dynamic and static load sources in deep mine roadway," *Journal of China Coal Society*, vol. 45, no. 5, pp. 1607–1613, 2020.
- [17] Y. D. Jiang, H. H. Song, Z. Q. Ma, B. J. Ma, and L. T. Gao, "Optimization research on the width of narrow coal pillar along goaf tunnel in tectonic stress zone," *Journal of China Coal Society*, vol. 43, no. 2, pp. 319–326, 2018.
- [18] L. I. Xue-Hua, L. Shun, Y. A. O. Qiang-Ling, and Q. U. Qun-Di, "Control principle and its application of rock burst in roadway driving along goaf with outburst-proneness surrounding rocks," *Journal of Mining & Safety Engineering*, vol. 29, no. 6, pp. 751–756, 2012.
- [19] G. Han, L. M. Dou, Y. Zhang, X. D. Li, Q. Wang, and Y. L. Lyu, "Influence mechanism and prevention technology of dynamic manifestation of roadway along goaf," *Journal of Mining & Safety Engineering*, vol. 38, no. 4, pp. 730–738+748, 2021.
- [20] J. Wang, J. Q. Jiang, G. B. Li, and H. Hu, "Exploration and numerical analysis of failure characteristic of coal pillar under great mining height longwall influence," *Geotechnical and Geological Engineering*, vol. 34, no. 2, pp. 689–702, 2016.
- [21] Y. Xue, J. Liu, X. Liang, S. Wang, and Z. Ma, "Ecological risk assessment of soil and water loss by thermal enhanced methane recovery: numerical study using two-phase flow simulation," *Journal of Cleaner Production*, vol. 334, article 130183, 2022.
- [22] Y. L. Wang, J. X. Tang, J. Jiang, Z. Y. Dai, and G. J. Shu, "Mechanical properties and parameter damage effect of malmsstone under chemical corrosion of water-rock interaction," *Journal of China Coal Society*, vol. 42, no. 1, pp. 227–235, 2017.
- [23] S. J. Miao, M. F. Cai, and D. Ji, "Damage effect of granite's mechanical properties and parameters under the action of acidic solutions," *Journal of China Coal Society*, vol. 41, no. 4, pp. 829–835, 2016.
- [24] C. Zhao, D. Jin, H. Wang, Q. Wang, S. Wang, and Y. Liu, "Construction and application of overburden damage and aquifer water loss model in medium-deep buried coal seam mining in Yushen mining area," *Journal of China Coal Society*, vol. 44, no. 7, pp. 2227–2235, 2019.
- [25] Q. S. Li and C. Zhang, "Damage conduction model of high intensity mining in western mining area based on conservation of mining space and its application," *Journal of Mining & Safety Engineering*, vol. 38, no. 1, pp. 1–8, 2021.
- [26] H. Y. Pan, S. G. Li, T. W. Zhang, and H. F. Lin, "Composite key stratum module of Winkler foundation and its mechanical properties," *Journal of Central South University (Science and Technology)*, vol. 43, no. 10, pp. 4050–4056, 2012.
- [27] Y. Q. Long, *Calculation of Beam on Elastic Foundation*, People's Education Press, Beijing, 1981.
- [28] H. Shi and F. X. Jiang, "Study on abutment pressure rule of overlying strata spatial structures based on microseismic monitoring," *Chinese Journal of Rock Mechanics and Engineering*, vol. 27, pp. 3274–3280, 2008.
- [29] F. X. Jiang, C. X. Shu, and C. W. Wang, "Impact risk appraisal of stope working faces based on stress superimposition," *Chinese Journal of Rock Mechanics and Engineering*, vol. 34, no. 12, pp. 2428–2435, 2015.
- [30] S. H. Longyong, W. A. Kai, Q. I. Qingxin, and Z. H. Lang, "Stress field evolution characteristics and coal-gas outburst hazard evaluation model of the heading face in coal roadway," *Journal of Mining & Safety Engineering*, vol. 34, no. 2, pp. 259–267, 2017.
- [31] Y. B. Li, *Road Tunnel Brittle Rock Burst Mechanism and Simulation Research*, University of Science and Technology Beijing, 2015.
- [32] J. J. Zhang and B. J. Fu, "Rockburst and its criteria and control," *Chinese Journal of Rock Mechanics and Engineering*, vol. 27, no. 10, pp. 2034–2042, 2008.

- [33] J. Lu, G. Z. Yin, H. Gao et al., "True triaxial experimental study of disturbed compound dynamic disaster in deep underground coal mine," *Rock Mechanics and Rock Engineering*, vol. 53, no. 5, pp. 2347–2364, 2020.
- [34] J. Y. Fan, D. Y. Jiang, Z. H. Ouyang, T. Yang, J. Chen, and W. H. Liu, "Material-instability rock burst criteria based on the theory of strain gradient plasticity," *Journal of China Coal Society*, vol. 43, no. 11, pp. 2959–2966, 2018.
- [35] D. W. Yin, S. J. Chen, W. B. Xing, D. M. Huang, and X. Q. Liu, "Experimental study on mechanical behavior of roof-coal pillar structure body under different loading rates," *Journal of China Coal Society*, vol. 43, no. 5, pp. 1249–1257, 2018.
- [36] X. B. Wang, W. T. Hou, Y. S. Pan, and W. Dong, "Experiments of strain localization processes of coal specimens in uniaxial compression based on the digital image correlation method," *Journal of China Coal Society*, vol. 43, no. 4, pp. 984–992, 2018.

Research Article

Impact of Depressurizing Boreholes on Energy Dissipation in Deep Roadway

Meng Wang,^{1,2} Zhixue Li,¹ Yalong Xu¹ ,¹ Zhenhua Li¹ ,¹ Ruifu Yuan,¹ Hongchao Zhao,³ and Guodong Li³

¹School of Energy Science and Engineering, Henan Polytechnic University, Jiaozuo, China

²State Collaborative Innovation Center of Coal Work Safety and Clean-Efficiency Utilization, Jiaozuo, China

³School of Geology and Mining Engineering, Xinjiang University, Urumchi, China

Correspondence should be addressed to Yalong Xu; yalong_xu2021@126.com

Received 8 March 2022; Accepted 28 June 2022; Published 16 July 2022

Academic Editor: Jianyong Han

Copyright © 2022 Meng Wang et al. This is an open access article distributed under the Creative Commons Attribution License, which permits unrestricted use, distribution, and reproduction in any medium, provided the original work is properly cited.

Depressurizing borehole drilling is an effective approach to control the large deformation of deep roadway. It can transfer the high stress in the proximity of the roadway into the deep stable rock masses. However, it should be noted that the borehole drilling will inevitably cause the secondary damage to roadway. To determine the parameters of depressurizing boreholes, the degree of the secondary damage must be evaluated properly. Given that the rock mass failure is an unstable phenomenon driven by energy, it is of great use to reveal the disturbing impact of depressurizing boreholes on the roadway stability from the angle of energy dissipation. This is much more consistent with the failure nature of rock mass. Hence, an integrated method of laboratory test, numerical simulation, and theoretical analysis was used to study the disturbing effect of depressurizing boreholes on roadway energy dissipation. The equations of elastic energy and dissipated energy of rock cell grid were derived based on the energy principle and finite-difference algorithm, which was implemented into FLAC^{3D} software by the FISH language. The numerical stress-strain and dissipated energy-strain curves of rock samples were verified by experimentally obtained data, and the whole deformation path from roadway excavation to instability was back-analyzed by the dissipated energy evolution. Based upon the energy model, the ratio of borehole diameter D to row spacing R (D/R) was selected as the variable to analyze the influence of borehole parameters on the depressurizing effect. The varying D/R leads to three depressurizing states: insufficient depressurization, sufficient depressurization, and overdepressurization. Increasing D/R will make the roadway transfer from insufficient depressurization to sufficient depressurization and finally to overdepressurization. The sufficient depressurizing state could be realized by adjusting the borehole D/R value, which is of great use to the roadway control. The D/R values of 1 : 6 to 1 : 2 were proposed for the test roadway, and $D/R = 1 : 6$ was applied in the field test, which achieved a well roadway control effect.

1. Introduction

In China, lots of coal mines have successively shifted into the deep mining with the increase of mining intensity [1]. Compared to the shallow coal seam mining, the mechanical behaviors of coal/rock masses at deep depth changes fundamentally. As a result, the roadway is prone to nonlinear large deformation, which leads to the rock burst, coal and gas outburst, or other dynamic disasters in serious cases [2–4]. The instability events still occur in coal mines even when measures were implemented in the field, including increasing

support strength and repairing large deformed roadway more times [5–8]. Hence, how to effectively control the deep roadway stability is still a major issue that affects the safety of recovering the deep coal resources [9].

Scholars pointed out that the stress, lithology, and support are the three main factors affecting the stability of deep roadways [10–13]. Previous studies on roadway control mainly focused on the latter two factors, lithology and support. Measures which focused on these two factors were applied, such as excavating the roadway in the rocks with high strength [14] or using the high-strength support to

control roadway deformation [15]. However, roadway failure that still emerges as the high stress is ignored [16]. The stress transfer technology, later also referred to as depressurization, was invented to reduce the impact of high stress [17]. This approach transfers the high stress around the roadway surface into the deeper stable rock masses by artificially weakening the bearing capacity of surface rocks [18]. The stress transfer technology has been widely applied in roadways subject to complex conditions, such as deep roadways, dynamic roadways, and soft rock roadways. Field tests showed that the stress transfer technology could make the roadway more stable than other control methods [19].

In China, stress transfer (depressurization) technology is classified into two categories according to its constructing locations, including depressurizing outside the roadway (DOR) and depressurizing inside the roadway (DIR) [20]. The frequently-used DOR technologies, such as tunneling the depressurizing roadway and mining of the depressurizing coal seam, produce a more favorable depressurizing effect than DIR (e.g., drilling boreholes [21], cutting trenches [22], and blasting for loosening [23]). However, an additional roadway or advancing face needs to be developed when using DOR technology, which is faced with issues of large amount of works and high costs. In fact, the DIR has been used more widely than DOR [24]. The depressurizing borehole belongs to the frequently used DIR technology. Compared to other depressurizing technologies, it has two advantages except for the high-stress transfer [25–29]: (1) boreholes could provide a compensation space for the deformation of rock masses, which decreases the roadway radial displacement. (2) Borehole drilling can be performed via mechanized operations, which is more safe and cost-effective. Hence, many existing literatures have presented studies on depressurizing boreholes. For example, Gao et al. used three-dimensional cables and depressurizing boreholes to control the roadway stability for the soft and thick coal seam [30]. Liu et al. controlled the large deformation of deep roadway using the depressurizing boreholes [31]. Wang et al. developed a composite technology, including depressurizing boreholes and bolt-grouting support, to control the high-stress roadway, and achieved a great success in field test [32].

The depressurizing boreholes have been widely used in the field, but inevitably, it has limitations. Most of the existing studies are focused on the stress transfer, and they lack the analysis of deformation control and roadway stability [20]. These make it difficult to quantitatively evaluate the depressurizing degree of roadway and to help design the borehole parameters. The borehole diameter D and row spacing R were considered as the key variables affecting depressurizing degree. These two parameters affect each other, and the interaction between these two parameters needs to be considered to achieve the optimum borehole parameters. However, the interaction was frequently ignored during the determination of the borehole parameters [33].

In the authors' previous studies, we tried to evaluate the depressurizing degree from the angle of stress transfer and deformation control of the roadway. The main problem is that it is difficult to evaluate the stress transfer effect of the

depressurizing boreholes [32, 33]. In addition, using two indexes (stress and deformation) to evaluate the depressurizing effect complicated the analytical process. Given that the energy evolution occurs during the roadway deformation, energy dissipation in the surrounding rocks will be enhanced by drilling depressurizing boreholes [34, 35]. Analyzing the depressurizing degree from the view of energy dissipation can simplify the analytical process, as it can consider the stress and deformation at the same time. In this study, the energy equations were implemented into FLAC^{3D} software, and the disturbing effect of depressurizing boreholes on roadway stability was discussed from the view of energy dissipation. The influence of borehole diameter and row spacing on the damage degree of the surrounding rocks was revealed, which can provide guidance for the design of depressurizing borehole parameters.

2. Development and Application of Energy Models

2.1. Development of the Energy Model in FLAC^{3D}. The stress redistribution will occur after roadway excavation. Assuming that the process occurs in a closed system without the outside energy exchange, part of the energy generated by the stress redistribution is stored in the surrounding rocks as elastic energy, while the other part is consumed along the roadway deformation. The higher the damage degree of rock masses becomes, the lesser the elastic energy remains, and the more the energy is dissipated [36, 37]. Hence, based on the energy conservation and FLAC^{3D} difference operation principle, the expressions of elastic energy and dissipated energy can be derived according to the stress-strain relationship of rock elements. The specific calculation steps were given in the following.

In FLAC^{3D}, if the stress σ_i^I at time t and total strain increment $\Delta\varepsilon_i$ at time Δt were given, the new stress σ_i^N of cell grids could be solved at time $t + \Delta t$ [38]. Assuming that the Δt corresponds to the time-steps m , the formula of the total energy increment is described as

$$\Delta W_z = \sigma_i \Delta \varepsilon_i \quad (i = 1, 2, 3), \quad (1)$$

where i represents the three directions of the space rectangular coordinate system, and σ_i is the element stress corresponding to time-steps m , which can be represented by the average stress $\bar{\sigma}_i$ of the cell grids before and after the numerical operation. Then, the formula can be expressed as

$$\bar{\sigma}_i = \frac{1}{2} (\sigma_i^I + \sigma_i^N) \quad (i = 1, 2, 3). \quad (2)$$

Note that the m value is smaller and the element energy calculated by formula (1) is more accurate. By comparing numerical calculation with theoretical calculation, when $m \leq 20$, the error of them is controlled within 5%, so the value of m in the study is 20. Supposing that the time-step m is a computing loop, the total input energy of the cell grids after n loops can be written as

$$W_z = \sum_0^n \Delta W_z. \quad (3)$$

If the attenuation of postpeak elastic modulus E was ignored, the elastic energy accumulated in the cell grids can be calculated by the following formula:

$$W_e = \frac{1}{2} \sum_0^n \frac{\sigma_i^2}{E} \quad (i = 1, 2, 3). \quad (4)$$

Subtracting formula (4) from formula (3), the dissipative energy formula of cell grids can be obtained as

$$W_d = \sum_0^n \Delta W_z - \frac{1}{2} \sum_0^n \frac{\sigma_i^2}{E} \quad (i = 1, 2, 3). \quad (5)$$

The three variables, σ_i^I , σ_i^N , and $\Delta\varepsilon_i$, can be captured by the indicator functions in FLAC^{3D} [38]. Hence, equations (1) to (5) can be easily realized in FLAC^{3D} by the inbuilt FISH language. The implementing processes are given in Figure 1. Firstly, the numerical model is established and the rock mass parameters are determined. The end-step Q and the loop-step m can be defined, and the initial stress σ_i^I of each cell grid is captured before the operation. Then, the operation is started and the new stress σ_i^N and strain increment $\Delta\varepsilon_i$ are captured again after time-steps m . After that, the elastic energy and dissipated energy are calculated by equations (4) and (5). The whole loop will continue until the end-steps Q . Finally, the energy nephograms of the cell grids are achieved.

2.2. Application of the Energy Model

2.2.1. Engineering Background. The coal transporting main roadway (see the blue thick line in Figure 2) in the Sanhejian coal mine of Xuzhou Mine Group was selected as the engineering background. The roadway is connected to the -700 m west main roadway in the east and adjacent to the F1-1 fault in the south, where the north side is the gobs. The buried depth of the test roadway is about 800 m, and the total length is 1442 m. The main apparent lithology along the roadway is fine sandstone and siltstone (see the borehole columnar section at the lower-right corner of Figure 2). Fine sandstone accounts for about 75% of the total roadway length. According to the in situ stress test, the maximum principal stress along the roadway is gravity stress, and the horizontal stress is about 80% of the gravity stress [39]. The roadway was developed in the form of a straight wall with a semicircular arch roof with a section size (width \times height) of 5.0 m \times 4.0 m. Rock bolts with row spacing of 800 mm \times 800 mm were adopted after excavation.

The location at 400 m away from the roadway opening (see the red solid point in Figure 2) was selected for the field monitoring, because this location was outside of the influence of the fault and mining activities. The roadway deformation at the measure point is shown in the top-left pictures in Figure 2. The large deformation mainly occurred in the roadway floor and two ribs, where the maximum con-

vergences exceeded 1000 mm. The transportation work of the roadway has been interrupted by the large deformation, which requires renovation.

2.2.2. Simulation of the Rock Mechanics Test Based on the Energy Model. To calibrate the numerical simulation results, the experimental tests subject to 6 different confining stresses of 0 MPa, 5 MPa, 10 MPa, 15 MPa, 20 MPa, and 25 MPa were carried out in the laboratory. The test results were detailed in Ref. 40. The objective of this section is to verify the energy model using the experimentally obtained results. The size of numerical rock samples was in the diameter of 50 mm and in the height of 100 mm, which is the same as the laboratory test (see Figure 3(a)). The rock parameters obtained from the laboratory test were implemented into the model [40]. The bottom boundary of the model was fixed, the confining pressure was applied to the side boundary, and the axial displacement was applied to the upper boundary to simulate the loading. After that, the energy codes given in Section 2.1 were called to perform the calculation.

To simplify the analysis, the test with confining pressure of 5 MPa was selected and used here [40]. It can be seen from Figure 3(b) that the power generated by the loading stress was stored inside rock samples as elastic energy when the rock samples were in the prepeak stage, and at the same time, the dissipated energy remained at a very small value (almost zero). Once the rock samples entered the postpeak phase, the dissipated energy increased dramatically until it reached the residual stage where the dissipated energy gradually leveled off. The stress-strain and dissipated energy-strain curves obtained from the numerical simulation were in the high agreement with the experimental results. Since the elastic modulus E is assumed to be constant when calculating energy, there is no energy attenuation before the peak. The focus of this paper is on the description of postpeak failure. Therefore, this hypothesis has no influence on postpeak failure of rock mass. However, it should be noted that if the prepeak compaction and plastic deformation must be analyzed, the effect of elastic modulus E on prepeak energy change needs further consideration.

2.2.3. Simulation of Roadway Deformation Based on the Energy Model. A roadway simulation was also carried out to verify the applicability of the energy model in the analysis of engineering problems. The model size was 60 m in length (X axis), 40 m in width (Y axis), and 60 m in height (Z axis). The stress boundaries, roadway section size, and supporting parameters were consistent with the field case. The strain-softening Mohr-Coulomb criterion was used in the model. It should be noted that the rock mass parameters need to be verified before the simulation. For the sake of simplification, the fine sandstone section exposed in the test roadway is taken as the research object, because this section accounts for about 75% of the total roadway length. The strength properties of the rock samples were converted to those of the rock masses using RocLab software, which were assigned to the model as the initial parameters. Afterwards, the optimal parameters of rock masses were determined by

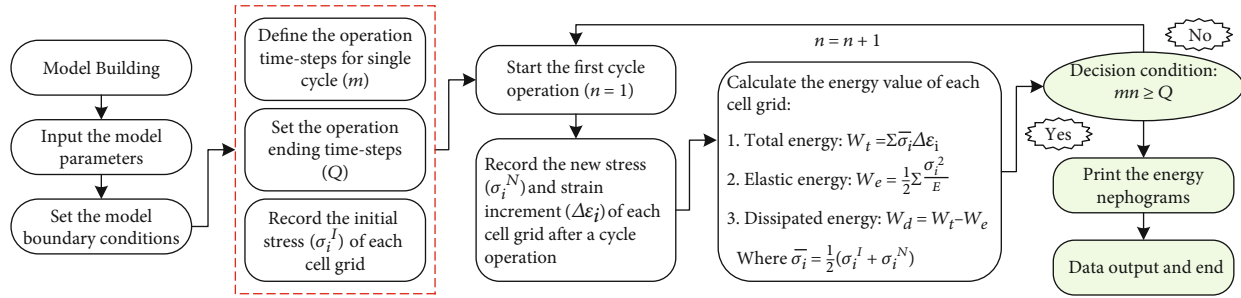


FIGURE 1: Flow chart of cell grid energy calculation in FLAC^{3D}.

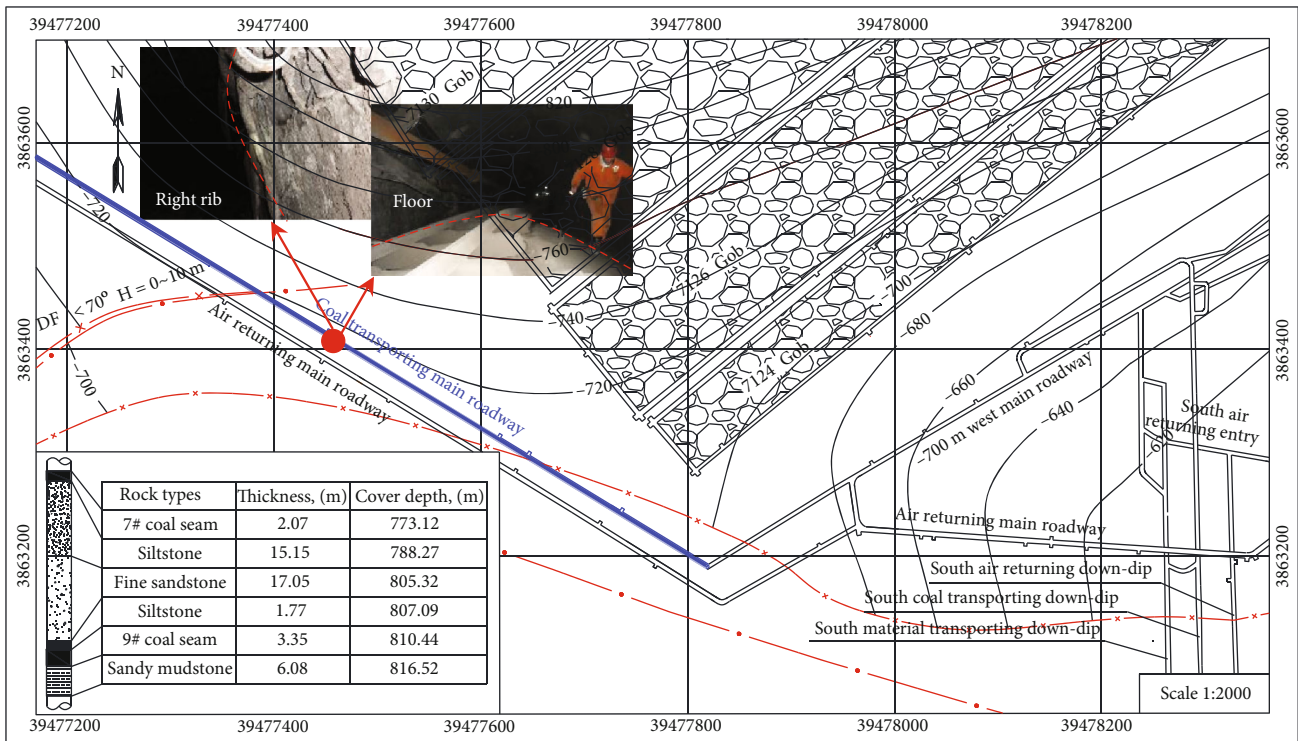


FIGURE 2: Layout of the test site in the Sanhejian coal mine. The lower-left corner gives the borehole columnar section of the test roadway. The thick blue line represents the test roadway position. The red solid point is the location where these roadway deformation photos were taken.

comparing with roadway failure ranges in the field. The calibrated parameters of the rock masses are given in Table 1.

In Figures 4(a) and 4(b), the dissipated energy density (DED) and the distribution cloud of the plastic zone are given, respectively. The vertical stress distribution of roadway ribs is shown in the curve of Figure 4(b). By comparing Figure 4(a) with Figure 4(b), the stress peak of the roadway wall is 7.5 m away from the center point of the roadway, and the expansion range of roadway dissipated energy is basically the same as the plastic zone. The roadway deformation path and main failure positions could be revealed by the dissipated energy evolution; however, it cannot be realized with the plastic zone analysis.

Analysis from Figure 4, the maximum principal stress of roadway is the gravity stress, and the stress concentration after excavation will be generated in the two ribs. The con-

centrated stresses cause the rib large deformation; meanwhile, they will intensify the floor extrusion flow when the stress was transferred to the floor [41]. In other words, the elastic energy accumulations caused by stress redistributions in roadway ribs provided a sustained power for the ribs and floor deformation.

For the test roadway, drilling the rib depressurizing boreholes is the effective approach to control its large deformation, because the depressurizing boreholes will absorb the rib deformation and also prevent the high stress from transferring to the roadway floor. However, attention should be paid to the depressurizing degree of roadway as a reasonable depressurizing degree plays a vital role in the control effect. Considering that the borehole diameter D and row spacing R are the main factors affecting the roadway depressurizing degree, in the following sections, the energy

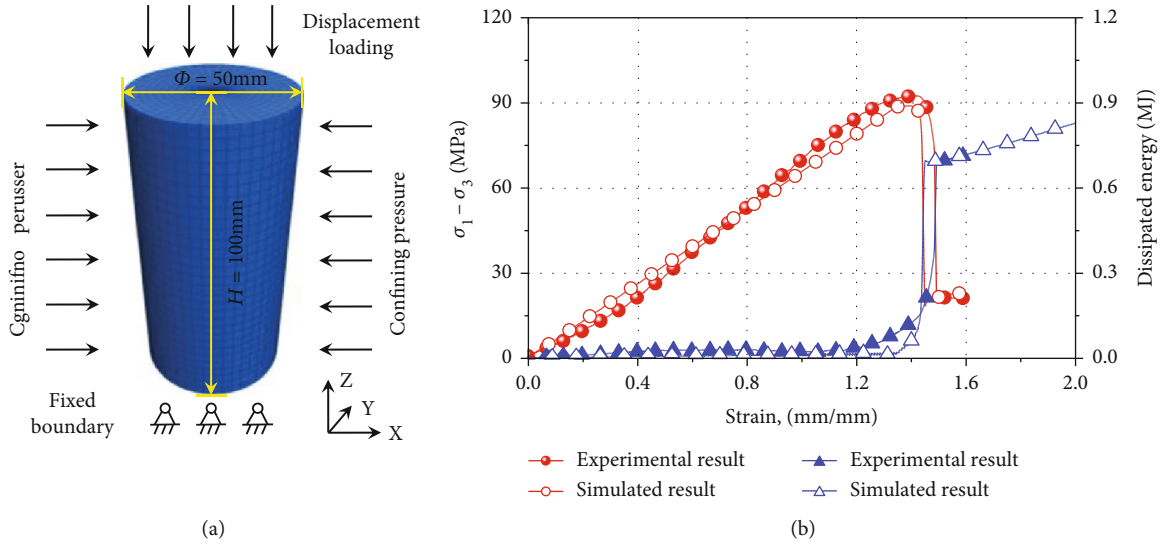


FIGURE 3: Comparisons between the numerical simulation and laboratory test. (a) Represents the numerical model of rock samples. (b) Gives the stress-strain and dissipated energy-strain curves obtained from numerical modeling and laboratory test, respectively.

TABLE 1: Calibrated parameters of the rock masses.

Prepeak	Elasticity modulus E (GPa)	Poisson ratio μ	Cohesion c (MPa)	Internal friction angle φ ($^\circ$)	Tensile strength σ_t (MPa)
	2.09	0.26	3.61	30.36	0.4
	Plastic strain ϵ^{ps}	0.01	0.02	0.5	1
Postpeak	Cohesion c (MPa)	2.61	1.60	0.32	0.32
	Internal friction angle φ ($^\circ$)	30.72	24.64	23.14	23.14

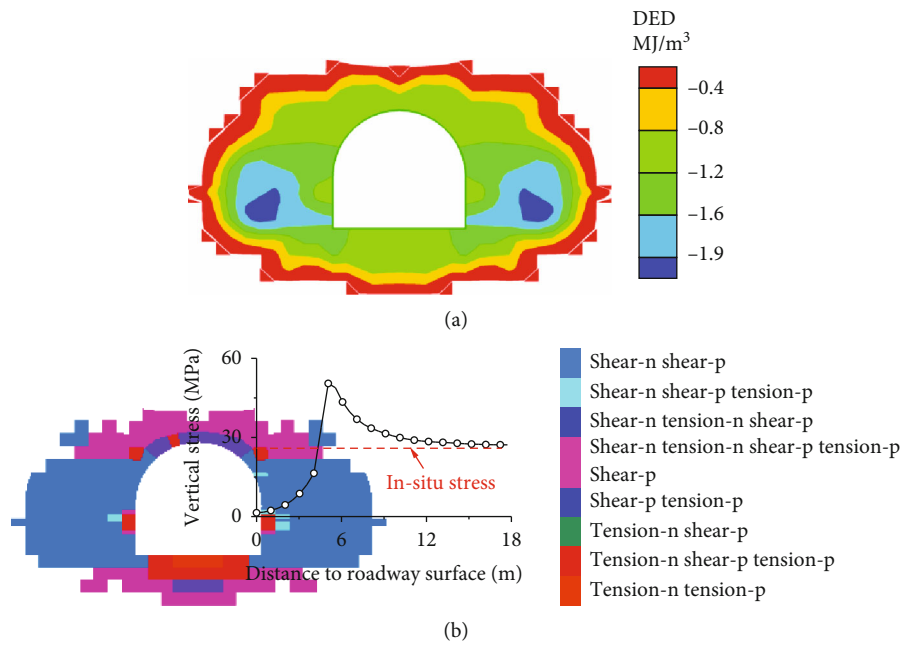


FIGURE 4: Numerical simulation results. (a) and (b) represent the evolvements of roadway dissipated-energy density (DED) and plastic zone, respectively. The curve in (c) is the vertical stress distribution of the roadway ribs.

model will be used to discuss the influence of D and R on the roadway stability.

3. Impact of Depressurizing Boreholes on Roadway Energy Dissipation

3.1. Model Setup of the Depressurizing Boreholes. Drilling depressurizing boreholes aims to release the elastic energy inside the roadway ribs. To facilitate the boreholes excavating, the rib meshes of the numerical model established in Section 2.2.3 were modified by HyperMesh software. In the modified model (see Figure 5), the boreholes were placed in the Y direction with a minimum row spacing (R) of 0.6 m, while each row (Z direction) contains up to four horizontal boreholes with 0.6 m interspacing (I). Four possible values, 100 mm, 200 mm, 300 mm, and 400 mm (see Figure 5(a)), were considered for the borehole diameters (D). These pretreating can realize the borehole excavation under the different schemes of R , I , and D . Note that the interspacing was fixed as 1.2 m due to the fact that it is difficult to drill multiple rows of boreholes in the circumferential direction. The parameters and boundary conditions of the rock masses were similar to those of the above model in Section 2.2.3.

3.2. Numerical Simulation Schemes. Ref. 32 pointed out that the borehole length affected the movement distance of the peak-stress zone, and it should be determined to penetrate the stress concentration area. In addition, a maximum of two rows of borehole generally could be constructed in the roof, rib, or floor, because of the limitation of roadway size and construction equipment [33]. Hence, the borehole diameter D and row spacing R were chosen as variables to carry out this study, while the borehole interspacing I was fixed as 1.2 m [33] (see Figure 5(a)), and the borehole length was determined as 9 m because the stress concentration area distributed in the range of 4 to 9 m from the roadway surface (see Figure 4(b)). Considering the correlation between borehole diameter D and row spacing R , the D/R ratio was used to design the simulation schemes as shown in Table 2. By the numerical simulation, borehole excavation with different D/R was carried out at the same time with roadway excavation. After excavation of roadway and boreholes, time-step control numerical simulation is used.

3.3. Simulation Results of the DED Distributions with Different D/R . Figures 6(a)–6(f) show the dissipated energy density (DED) distributions of roadway under different D/R ratios. As shown in Figure 6, when $D/R = 2 : 3$ and $1 : 2$, the peak values of DED distribute at the boundary of depressurizing zone (borehole excavation area), and DED has a larger magnitude. Once the D/R is less than $1 : 2$, the DED peaks locate in the middle of neighboring boreholes. As the D/R decreases, the interplay between the neighboring boreholes decreases and the DED profile eventually changes from the state of “single peak value” to the “double peak values,” and the peak value of the DED gradually decays. When $D/R < 1 : 6$, the influence range of neighboring boreholes cannot superimpose, and

the DED distribution generated by each borehole exists in an isolated state. Those indicate that a smaller D/R could lead to smaller energy dissipation and less depressurizing influence.

The DED values extracted from the central location of neighboring boreholes with different D/R ratios are shown in Figure 7. For the roadway without boreholes (see Figure 4(a) and blue curve in Figure 7), the evolution range of DED reaches 5 m from the roadway surface with the peak value of 2.5 MJ/m^3 . When $D/R = 1 : 10$ and $1 : 8$, the depressurizing boreholes have a slight influence on the roadway energy dissipation. Once the $D/R > 1 : 8$, the DED extended range increases sharply. For instance, when $D/R = 1 : 6$, the DED extended range increases to 9 m. Afterwards, the DED range gradually levels off with the further increase of the D/R ratio, as the designed borehole length of 9 m limits the roadway depressurizing range.

Increasing the D/R ratio would dramatically affect the DED within the effective depressurizing area (9 m from the roadway surface). As the D/R increases from $1 : 6$ to $2 : 3$, the DED peak value increases initially and then decreases afterwards. The peak values of DED for $D/R = 1 : 6$, $1 : 4$, $1 : 2$, and $2 : 3$ are 4.01 MJ/m^3 , 8.43 MJ/m^3 , 9.22 MJ/m^3 , and 8.30 MJ/m^3 , respectively. The larger the D/R is, the closer the DED peak is to the roadway surface, which indicates that a higher depressurizing degree will occur. Once D/R increases to certain critical values (e.g., $2 : 3$), the elastic energy stored in the surrounding rock would reduce significantly because it is subject to serious damage, which will result in the attenuation of DED values. Those cases are extremely dangerous for roadway control, as it is difficult to maintain the stability of fractured rock masses once they lost the bearing capacity.

In the above analysis (as shown in Figure 7), the DED distributions in the direction paralleled to borehole drilling (X axis) were grasped. In the following, discussions on DED distributions between neighboring boreholes along the roadway excavation (Y axis) will be carried out. As shown in Figure 4(b), the peak stress is located at 5 m from the roadway surface, approximately located in the middle of borehole length. The characteristic stress position (peak stress, $X = 7.5 \text{ m}$ in Figure 5) was selected as the study object, and the DED data between neighboring boreholes is shown in Figure 8.

As shown in Figure 8, when $D/R = 2 : 3$, the DED distribution exhibits approximately a straight line, which means a higher energy dissipation with the magnitude of 7.5 MJ/m^3 . When D/R decreases to $1 : 2$, the DED distributing curve has a “single peak value” of about 8.85 MJ/m^3 . Once $D/R < 1 : 2$, the DED curves change from “single peak value” to “double peak values” and distribute symmetrically along the neighboring borehole center. In addition, the DED peak value decreases with the decreasing D/R , implying the attenuations of the depressurizing degree. Note that when $D/R = 1 : 8$ and $1 : 10$, the DED curves have a “zero value section,” and its length increases with the decreasing D/R . The “zero value section” indicates the presence of the undisturbed region between the neighboring boreholes due to the lack of interplay.

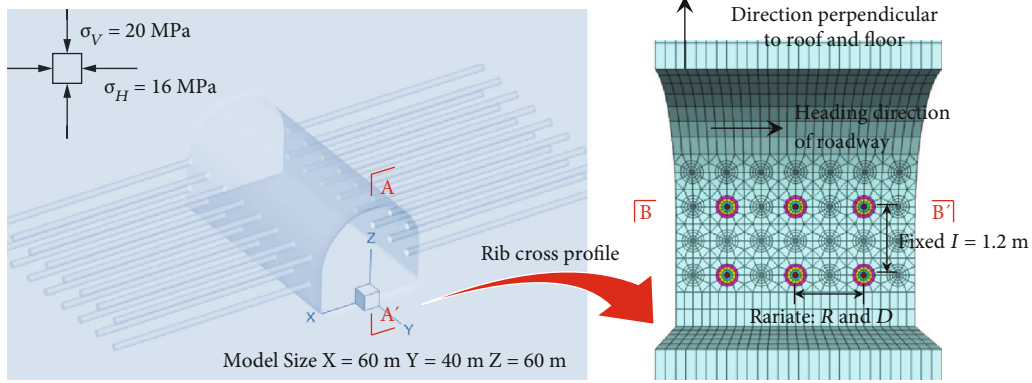


FIGURE 5: Numerical model containing depressurizing boreholes in FLAC^{3D}. (a) Illustrates the cross section of one rib along the longitude direction of roadway. The distance between the neighboring boreholes in the heading direction of roadway was defined as row spacing R , while that in the direction perpendicular to the roof and floor was termed as interspacing I . The interspacing I was fixed as 1.2 m, while D and R were chosen as the variables in this study. D and R will be constructed according to the design schemes.

TABLE 2: Simulation schemes for the depressurizing boreholes.

Constants	Orientation Horizontal boreholes drilled in ribs		Length 9 m	Interspacing 1.2 m		
Simulation schemes	I	II	III	IV	V	VI
D/R	2 : 3	1 : 2	1 : 4	1 : 6	1 : 8	1 : 10
Diameter	400 mm	300 mm	300 mm	300 mm	300 mm	300 mm
Row spacing	600 mm	600 mm	1200 mm	1800 mm	2400 mm	3600 mm

Note that the simulation results without boreholes were regarded as a reference for comparison.

Based on the characteristics of the DED distributing curves in Figures 7 and 8, the three depressurizing states could be summarized: (1) Insufficient depressurization. When $D/R < 1 : 6$, the depressurizing boreholes partially disturbed the roadway surrounding rock, which causes the existence of “zero value section” of DED curves. (2) Sufficient depressurization. When $1 : 6 \leq D/R \leq 1 : 2$, the influence area of boreholes could cover the entire depressurizing range, and the DED maintains a higher magnitude. (3) Overdepressurization. When $D/R > 1 : 2$, the DED in roadway ribs is almost a straight line, and its peak value inversely decreases, which is harmful to the roadway control.

3.4. Simulation Verifications for the Depressurizing Degree Classification. In Section 3.3, the depressurizing states were classified into three categories: insufficient depressurization, sufficient depressurization, and overdepressurization based on the characteristics of DED curves. The rationality of the corresponding D/R to the three depressurizing states will be justified from the angle of using relief borehole drilling to control the roadway deformation. Figures 9 and 10 give the displacement curves of ribs and floor under various D/R ratios, respectively. For the sake of simplification, the roof control by boreholes was not considered because the large deformation of roadway primarily occurs in the ribs and floor.

As shown in Figure 9, prior to depressurizing borehole drilling, the rib convergences mainly occur in the range of

0 to 5 m from the roadway surface. For instance, the rib convergences are 305 mm, 199 mm, and 3 mm at the locations of 0 m, 1.5 m, and 6 m distancing from roadway surface (see the first columns of Figures 9(a)–9(c)), respectively. The rib convergence within the scope of 5 m significantly decreases after the borehole drilling, but its amplitude reduction has the following differences: (1) when $1 : 6 \leq D/R \leq 1 : 2$, the rib convergence in the 5 m scope decreases with the increase of D/R , while the deformation beyond 5 m away from roadway surface slightly increases due to the borehole drilling. (2) When $D/R < 1 : 6$, the rib surface convergence has almost no differences compared to that without boreholes, because the low borehole density is insufficient to absorb the deformation of the surrounding rock mass. (3) When $D/R = 2 : 3$, the rib convergence becomes larger than that of $D/R = 1 : 2$, which is caused by the overdepressurization.

As shown in Figure 10, the depressurizing borehole drilling could effectively control the floor deformation. For roadways without boreholes, the convergences that occurred at the floor surface and 3 m below are 288 mm and 86 mm, respectively. For roadways with boreholes, the convergence at the floor surface remains in the range of 150 mm to 193 mm, and it decreases with the increasing D/R . On the contrary, the increase of D/R leads to the slightly larger deformation of rock mass at 3 m below the floor surface. The essence of drilling rib boreholes to control floor heave is that the boreholes cut off the transferring paths of elastic energy stored in

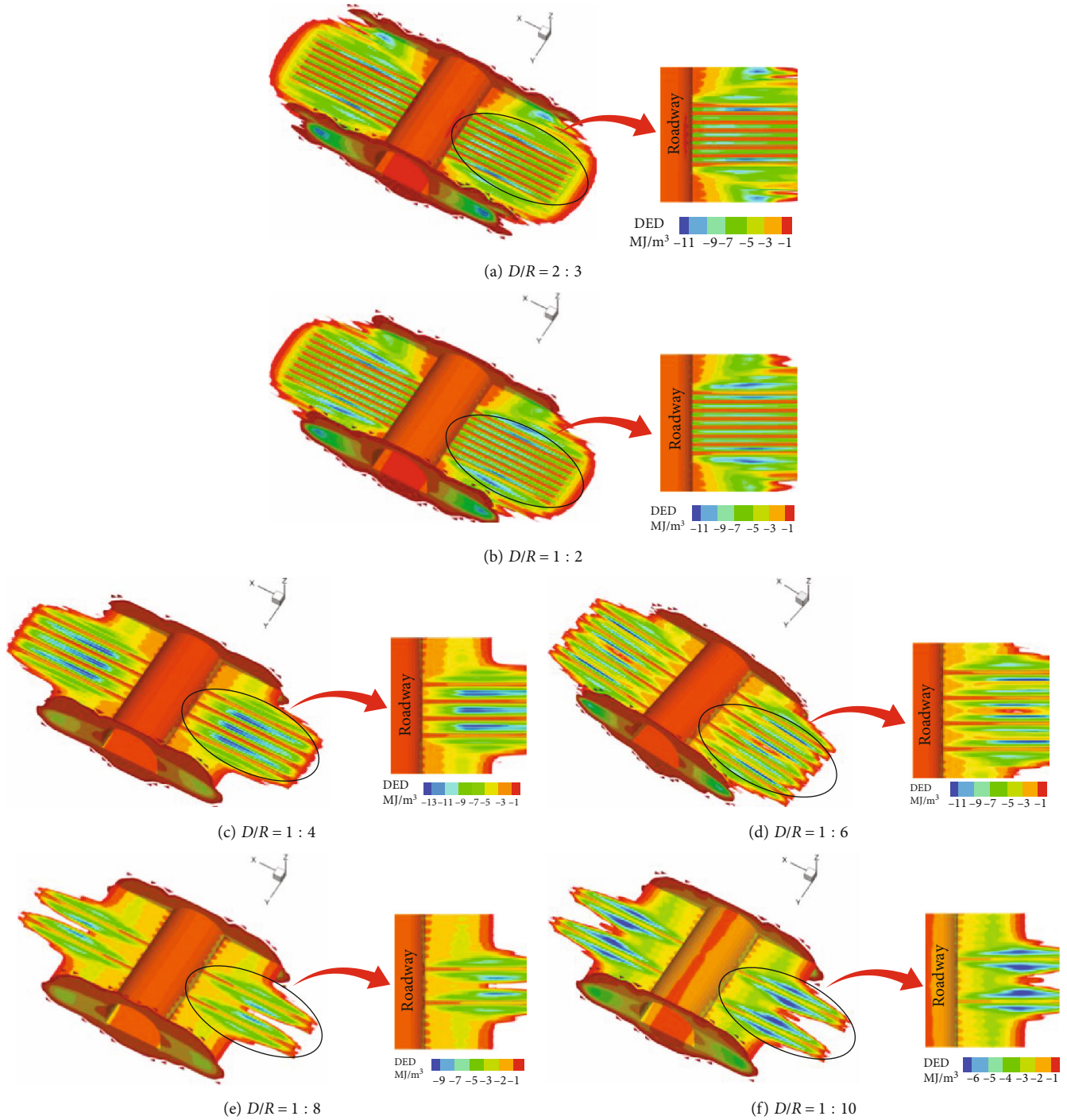


FIGURE 6: Dissipated energy density (DED) distributions of roadway under different borehole D/R ratios. Note that the data were obtained from the profile as shown in B-B' of Figure 5(a).

the ribs. The floor extrusion flow can be alleviated after the floor rock mass lost the power source, which results in the floor deforming continuously.

Based on the above analysis, the insufficient depressurization and overdepressurization could not improve the roadway stability. The former has a limited impact on the roadway control, while the latter could result in larger deformation. The roadway could be effectively controlled only when the sufficient depressurization is used. The depressur-

izing degree classification by the DED distribution is justified from the view of the roadway deformation control. For the test roadway, the D/R which can be used to control its large deformation could be defined as $1 : 6 \leq D/R \leq 1 : 2$.

3.5. Verifications of the Field Application. For the test roadway, the accumulations of elastic energy in both ribs were the main reason causing the roadway large deformation, and the depressurizing borehole drilling aims to increase

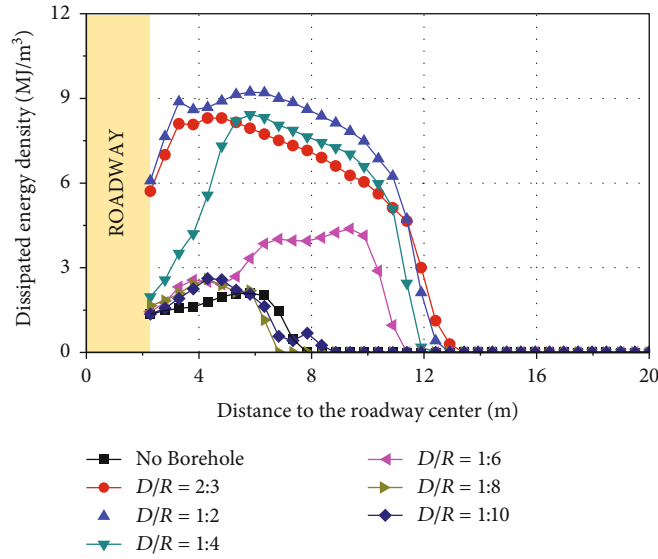


FIGURE 7: DED distributing curves between the neighboring boreholes in X direction under different D/R ratios. The data were extracted from the B-B' section in Figure 5(a).

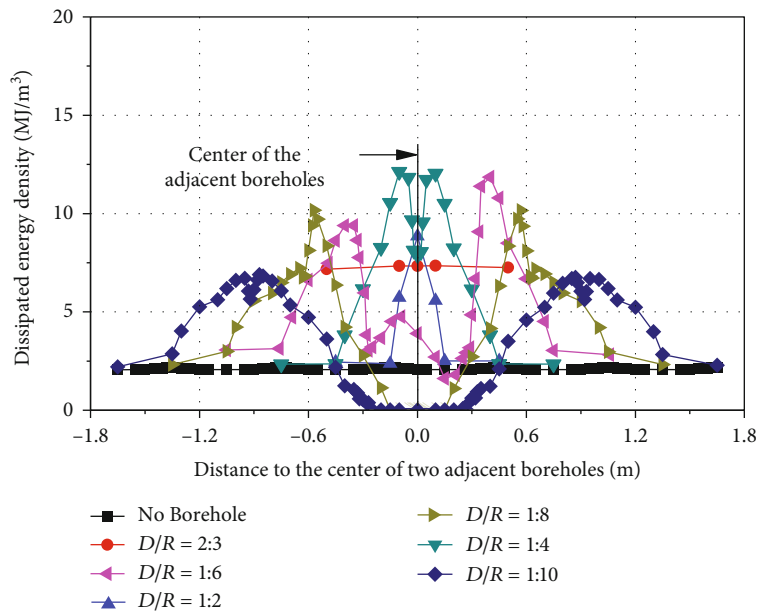


FIGURE 8: DED distributing curves between the neighboring boreholes at $X = 7.5$ m in Y direction under different D/R ratios. The data were extracted from the B-B' section in Figure 5(a). The "0" point indicates the midpoint of the circle center line of the adjacent boreholes.

the energy dissipation in the ribs. The reasonable D/R values were identified as $1 : 6 \leq D/R \leq 1 : 2$. In the Sanhejian coal mine, the available drilling rig could perform the maximum borehole diameter of 150 mm. Hence, the borehole row spacing was designed as 900 mm by the relation of borehole diameter and row spacing corresponding to the sufficient depressurization ($150 \text{ mm} \times 6 = 900 \text{ mm}$). Two boreholes were drilled in each row of roadway ribs with the interspace of 900 mm and length of 9 m. Figure 11 shows the comparison of the roadway deformation before and after depressurization. The deformation that occurred in roadway

ribs and floor after depressurization was only 40% of that without boreholes.

Note that the upper limit of the D/R value (1:6) corresponding to sufficient depressurization was used to determine the borehole row spacing. The purpose of doing this is to prevent the overdepressurization. If the roadway is in insufficient depressurization, extra boreholes could be conducted to increase the depressurizing degree. However, once the roadway enters into the overdepressurization, the excessive deformation will make it extremely difficult to maintain the stability of roadway.

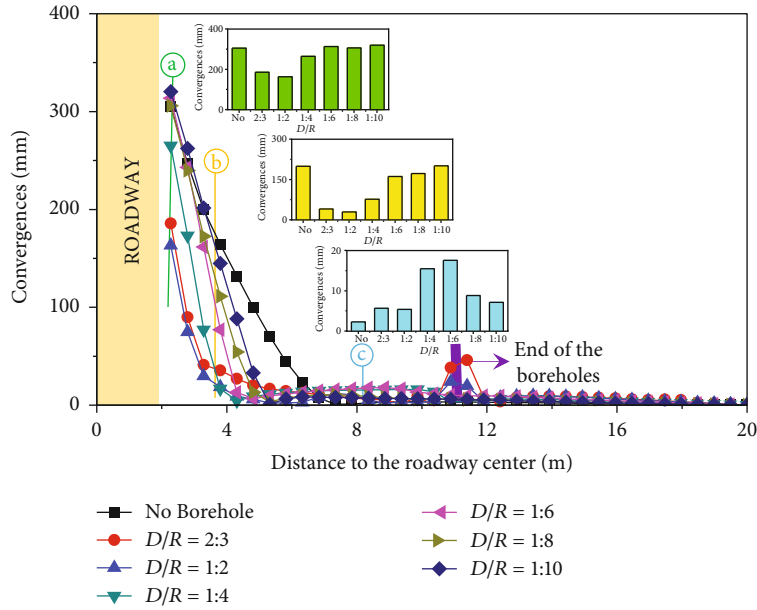


FIGURE 9: Rib convergence curves under the different borehole D/R ratios. (a-c) Represents the rib convergence at the locations of 0 m, 1.5 m, and 6 m distancing from the rib surface, respectively.

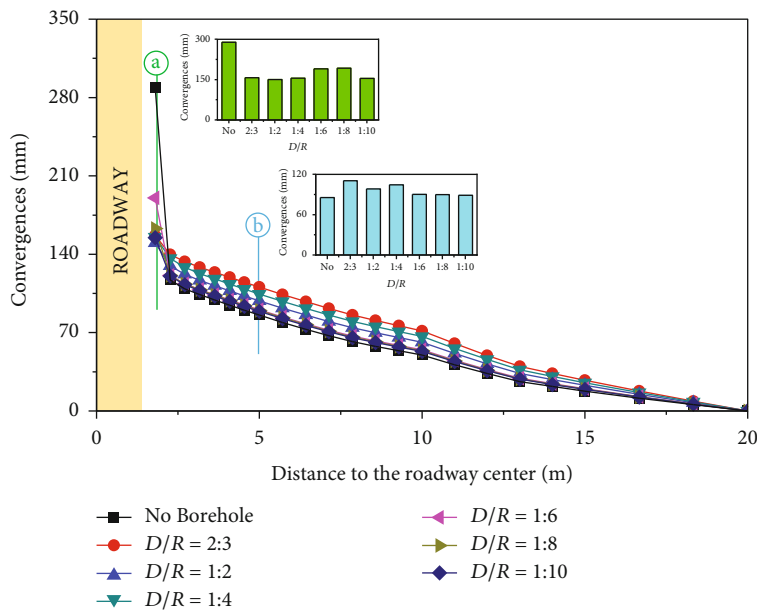


FIGURE 10: Floor convergence curves under the different borehole D/R ratios. (a) and (b) give the rib convergence that occurred in the locations of 0 m and 3 m from the floor surface, respectively.

3.6. *Discussions.* The energy dissipation of roadway could be adjusted by changing the diameter and row spacing of depressurizing boreholes. The borehole diameter should be determined prior to the row spacing, because its value is controlled by the drilling rig power. Once the diameter is determined, the row spacing of boreholes can be obtained based upon the D/R ratio. Increasing the D/R , the depressurizing state of roadway will be transferred from insufficient depressurization to sufficient depressurization and finally

to overdepressurization. The ideal depressurizing effect can be achieved only when a reasonable D/R value is selected.

In this study, only the row-by-row pattern of the depressurizing boreholes is considered in the present study. Other patterns of the boreholes, for example, staggered or triangular layouts, may also be employed to reduce roadway convergence. The future study with different borehole D/R and layouts will be conducted in order to reach the maximum technical and economic benefits.

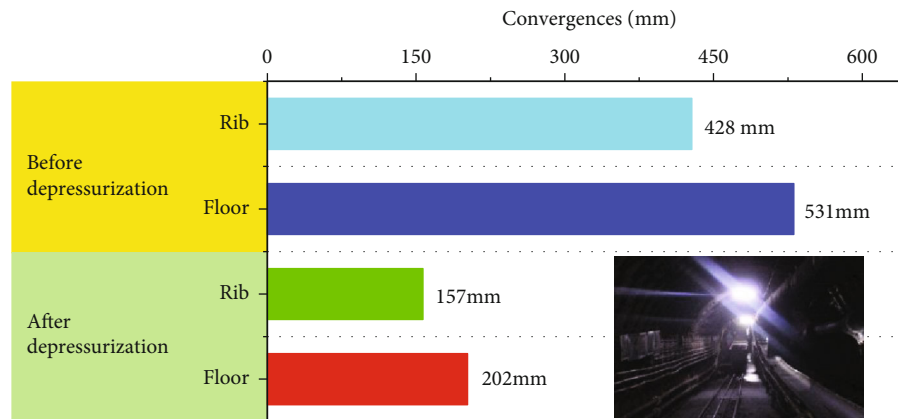


FIGURE 11: Comparison of the roadway deformation before and after depressurization. The photograph at the lower-right corner shows the roadway maintenance with drilling depressurizing boreholes.

In addition, the parameters of depressurizing boreholes are determined by dissipative energy distribution of rock mass and are verified by field test and numerical simulation which better verified the accuracy of borehole parameters. When borehole parameters are designed, the displacement check can be simplified and only from the energy evolution curve of adjacent boreholes, which saves a great deal of time than using stress and displacement bivariate analysis. Compared with the previous research work (Ref. 32), the borehole parameters determined by dissipative energy are more accurate than those determined by stress.

4. Conclusions

This study makes an attempt to reveal the impact of relief hole drilling on the roadway stability from the view of energy dissipation, which provides a basis for the determination of borehole parameters. The conclusions obtained are shown in the following.

- (1) Based on the energy principle and finite-difference algorithm, the formulas of elastic energy and dissipated energy of rock cell grid were derived and were implemented in the $FLAC^{3D}$ software by FISH language. The main roadway in the Sanhejian coal mine was chosen as the engineering background. The numerical model was calibrated by the stress-strain and dissipated energy-strain curves of rock samples. Additionally, the deformation paths from roadway excavation to instability were modeled using the dissipated energy evolution
- (2) The ratio of borehole diameter to row spacing (D/R) was selected as the variable to study the influence of borehole parameters on the energy dissipation and stability of roadway. It was concluded that there are three depressurizing states, insufficient depressurization, sufficient depressurization, and overdepressurization, due to the different D/R . By increasing the D/R , the depressurizing state will be transferred from insufficient depressurization to sufficient depressuri-

zation and finally to overdepressurization. If the roadway is in the insufficient depressurization, a depressurizing blind section where DED equals to zero appears between the neighboring boreholes. When the roadway is in the overdepressurization state, the roadway deformation will increase, which is harmful for the roadway maintenance. A reasonable D/R plays an important role in controlling the large deformation of deep roadway

- (3) The D/R ratios of 1:6 to 1:2 are suggested for the test roadway, and the D/R of 1:6 was applied in the field application. The monitoring results showed that the deformation occurred in roadway ribs and floor after depressurization was only 40% of that without boreholes. The depressurizing borehole drilling is capable of controlling the stability of roadway

Data Availability

The data used to support the findings of this study are available from the corresponding author upon request.

Conflicts of Interest

The authors declare that they have no known competing financial interests or personal relationships that could have appeared to influence the work reported in this paper.

Acknowledgments

The authors are grateful for the financial support from the National Natural Science Foundation of China (contract nos. 51704098 and 52174074), the Science Foundation for Outstanding Youth of Henan Province (contract no. 222300420048), and the Project Supported by the Distinguished Young Scholars Foundation of Henan Polytechnic University (contract no. J2021-4).

References

- [1] W. J. Yu, W. J. Wang, X. Y. Chen, and S. H. Du, "Field investigations of high stress soft surrounding rocks and deformation control," *Journal of Rock Mechanics and Geotechnical Engineering*, vol. 7, no. 4, pp. 421–433, 2015.
- [2] X. B. Li, C. J. Li, W. Z. Cao, and M. Tao, "Dynamic stress concentration and energy evolution of deep-buried tunnels under blasting loads," *International Journal of Rock Mechanics and Mining Sciences*, vol. 104, pp. 131–146, 2018.
- [3] Z. L. Li, X. Q. He, L. M. Dou, D. Z. Song, and G. F. Wang, "Numerical investigation of load shedding and rockburst reduction effects of top-coal caving mining in thick coal seams," *International Journal of Rock Mechanics and Mining Sciences*, vol. 110, pp. 266–278, 2018.
- [4] W. Shen, G. Shi, Y. Wang, J. Bai, R. Zhang, and X. Wang, "Tomography of the dynamic stress coefficient for stress wave prediction in sedimentary rock layer under the mining additional stress," *International Journal of Mining Science and Technology*, vol. 31, no. 4, pp. 653–663, 2021.
- [5] Q. Li, R. Yang, J. Li, W. He, and Z. Wen, "Strength and cost analysis of new steel sets as roadway support project in coal mines," *Advances in Materials Science and Engineering*, vol. 2018, Article ID 3927843, 9 pages, 2018.
- [6] S. W. Liu, D. Y. He, and M. X. Fu, "Experimental investigation of surrounding-rock anchoring synergistic component for bolt support in tunnels," *Tunnelling and Underground Space Technology*, vol. 104, article 103531, 2020.
- [7] G. J. Wu, W. Z. Chen, S. P. Jia et al., "Deformation characteristics of a roadway in steeply inclined formations and its improved support," *International Journal of Rock Mechanics and Mining Sciences*, vol. 130, p. 104324, 2020.
- [8] S. Q. Yang, M. Chen, H. W. Jing, K. F. Chen, and B. Meng, "A case study on large deformation failure mechanism of deep soft rock roadway in Xin'An coal mine, China," *Engineering Geology*, vol. 217, pp. 89–101, 2017.
- [9] H. Wagner, "Deep mining: a rock engineering challenge," *Rock Mechanics and Rock Engineering*, vol. 52, no. 5, pp. 1417–1446, 2019.
- [10] H. P. Kang, "Support technologies for deep and complex roadways in underground coal mines: a review," *International Journal of Coal Science & Technology*, vol. 1, no. 3, pp. 261–277, 2014.
- [11] X. F. Guo, Z. Q. Zhao, X. Gao, X. Y. Wu, and N. J. Ma, "Analytical solutions for characteristic radii of circular roadway surrounding rock plastic zone and their application," *International Journal of Mining Science and Technology*, vol. 29, no. 2, pp. 263–272, 2019.
- [12] K. P. Yu, F. Y. Ren, R. Puscasu, P. Lin, and Q. G. Meng, "Optimization of combined support in soft-rock roadway," *Tunnelling and Underground Space Technology*, vol. 103, p. 103502, 2020.
- [13] J. Chen, P. Liu, L. Liu et al., "Anchorage performance of a modified cable anchor subjected to different joint opening conditions," *Construction and Building Materials*, vol. 336, p. 127558, 2022.
- [14] H. P. Kang, J. Lin, and M. J. Fan, "Investigation on support pattern of a coal mine roadway within soft rocks — a case study," *International Journal of Coal Geology*, vol. 140, no. 15, pp. 31–40, 2015.
- [15] R. Peng, X. R. Meng, G. M. Zhao, Z. H. Ouyang, and Y. M. Li, "Multi-echelon support method to limit asymmetry instability in different lithology roadways under high ground stress," *Tunnelling and Underground Space Technology*, vol. 108, p. 103681, 2021.
- [16] J. Xie, M. Gao, R. Zhang, S. Li, Q. Tan, and Z. Qiu, "Lessons learnt from measurements of vertical pressure at a top coal mining face at Datong tashan mines, China," *Rock Mechanics and Rock Engineering*, vol. 49, no. 7, pp. 2977–2983, 2016.
- [17] T. Goto, Y. Ishijima, S. Kinoshita, and N. Oda, "Effectiveness of relief boring in case of Akabira Colliery," *Journal of the Japan Institute of Metals and Materials*, vol. 93, no. 1068, pp. 75–81, 1977.
- [18] F. Cheng, A. Chen, D. Wu, X. Tang, and S. Chunhui, "Numerical simulation of cracking failure and weakening law of roadway surrounding rock under high stress," *Shock and Vibration*, vol. 2021, Article ID 7236077, 11 pages, 2021.
- [19] C. J. Hou, X. Y. Wang, and J. B. Bai, "Basic theory and technology study of stability control for surrounding rock in deep roadway way," *International Journal of Mining Science and Technology*, vol. 50, no. 1, pp. 1–12, 2021.
- [20] C. Hou, "Ground control of roadway. Xuzhou, China (in Chinese)," 2013.
- [21] S. Zhang, Y. Li, B. Shen, X. Sun, and L. Gao, "Effective evaluation of pressure relief drilling for reducing rock bursts and its application in underground coal mines," *International Journal of Rock Mechanics and Mining Sciences*, vol. 114, no. 2, pp. 7–16, 2019.
- [22] D. Yang, X. Wang, Y. Wang, H. An, and Z. Lei, "Experiment and analysis of wedge cutting angle on cutting effect," *Advances in Civil Engineering*, vol. 2020, Article ID 5126790, 16 pages, 2020.
- [23] A. G. Yardimci and M. Karakus, "A new protective destressing technique in underground hard coal mining," *International Journal of Rock Mechanics and Mining Sciences*, vol. 130, p. 104327, 2020.
- [24] X. Cheng, G. M. Zhao, Y. M. Li, X. R. Meng, and Q. Y. Tu, "Key technologies and engineering practices for soft-rock protective seam mining," *International Journal of Mining Science and Technology*, vol. 30, no. 6, pp. 889–899, 2020.
- [25] H. Liu, Y. Cheng, J. Song, Z. Shang, and L. Wang, "Pressure relief, gas drainage and deformation effects on an overlying coal seam induced by drilling an extra-thin protective coal seam," *International Journal of Mining Science and Technology*, vol. 19, no. 6, pp. 724–729, 2009.
- [26] Z. L. Li, L. M. Dou, W. Cai, G. F. Wang, Y. L. Ding, and Y. Kong, "Roadway stagger layout for effective control of gob-side rock bursts in the longwall mining of a thick coal seam," *Rock Mechanics and Rock Engineering*, vol. 49, no. 2, pp. 621–629, 2016.
- [27] J. Xie, J. Xu, and F. Wang, "Mining-induced stress distribution of the working face in a kilometer-deep coal mine—a case study in Tangshan coal mine," *Journal of Geophysics and Engineering*, vol. 15, no. 5, pp. 2060–2070, 2018.
- [28] B. Lin, J. Zhang, C. Shen, Q. Zhang, and C. Sun, "Technology and application of pressure relief and permeability increase by jointly drilling and slotting coal," *International Journal of Mining Science and Technology*, vol. 22, no. 4, pp. 545–551, 2012.
- [29] X. L. Yang, G. C. Wen, T. K. Lu et al., "Optimization and field application of CO₂ gas fracturing technique for enhancing CBM extraction," *Natural Resources Research*, vol. 29, no. 3, pp. 1875–1896, 2020.

- [30] M. Gao, N. Zhang, C. Guo, and L. Dou, "Mechanics and practice of combined supporting technology of 3D anchor cable and unloading technology of wall of roadway," *Chinese Journal of Geotechnical Engineering*, vol. 27, no. 5, pp. 587–590, 2005.
- [31] H. Liu, Y. He, J. Xu, and L. Han, "Numerical simulation and industrial test of boreholes destressing technology in deep coal tunnel," *Journal of China Coal Society*, vol. 32, no. 1, pp. 33–37, 2007, (in Chinese).
- [32] M. Wang, D. J. Zheng, W. L. Shen, X. Y. Wang, and W. F. Li, "Depressurizing boreholes for mitigating large deformation of the main entry," *Energy Science & Engineering*, vol. 8, no. 4, pp. 1404–1417, 2020.
- [33] M. Wang, X. Y. Wang, and T. Q. Xiao, "Borehole destressing mechanism and determination method of its key parameters in deep roadway," *Journal of China Coal Society*, vol. 42, no. 5, pp. 1138–1145, 2017.
- [34] Z. P. Zhang, H. P. Xie, R. Zhang et al., "Deformation damage and energy evolution characteristics of coal at different depths," *Rock Mechanics and Rock Engineering*, vol. 52, no. 5, pp. 1491–1503, 2019.
- [35] H. Xie, "Research framework and anticipated results of deep rock mechanics and mining theory," *Advanced Engineering Sciences*, vol. 49, pp. 1–16, 2017.
- [36] Z. Zhang and F. Gao, "Confining pressure effect on rock energy," *Chinese Journal of Rock Mechanics and Engineering*, vol. 34, pp. 1–11, 2015.
- [37] J. Cho, P. Martin, and L. W. Poon, "The older they are, the less successful they become? Findings from the Georgia Centenarian Study," *Journal of Aging Research*, vol. 2012, Article ID 695854, 8 pages, 2012.
- [38] Itasca Consulting Group Inc, *FLAC3D 5.0 Manual*, ICG, Minneapolis, 2010.
- [39] H. Kang, J. Lin, X. Zhang, and Y. Wu, "In-situ stress measurements and distribution laws in Lu'an underground coal mines," *Rock and Soil Mechanics*, vol. 31, no. 3, pp. 827–831, 2010.
- [40] M. Wang, Z. Song, D. Zheng, W. Shen, P. Gou, and S. Wei, "FLAC^{3D} in the development and application of energy dissipation of rock model," *Journal of coal*, vol. 46, no. 8, pp. 2565–2573, 2021.
- [41] S. Cicek, I. B. Tulu, M. V. Dyke, T. Klemetti, and J. Wickline, "Application of the coal mine floor rating (CMFR) to assess the floor stability in a central Appalachian coal mine," *International Journal of Mining Science and Technology*, vol. 31, no. 1, pp. 83–89, 2021.

Research Article

A New Bayesian Network Model for the Risk Assessment of Water Inrush in Karst Tunnels

Yingchao Wang ^{1,2}, Yang Liu ¹, Zhaoyang Li,² and Wen Jiang²

¹State Key Laboratory for Geomechanics and Deep Underground Engineering, China University of Mining & Technology, Xuzhou, Jiangsu 221116, China

²State Key Laboratory of Geomechanics and Geotechnical Engineering, Institute of Rock and Soil Mechanics, Chinese Academy of Sciences, Wuhan 430071, China

Correspondence should be addressed to Yingchao Wang; wangyingchao@cumt.edu.cn and Yang Liu; tb19220012b4@cumt.edu.cn

Received 22 December 2021; Accepted 30 April 2022; Published 14 June 2022

Academic Editor: Tao Chen

Copyright © 2022 Yingchao Wang et al. This is an open access article distributed under the Creative Commons Attribution License, which permits unrestricted use, distribution, and reproduction in any medium, provided the original work is properly cited.

Water inrush seriously restricts the safe construction of a karst tunnel. Once it occurs, it will cause serious consequences such as economic loss and casualties. Due to the complexity of an underground environment, it is difficult to calculate the probability of karst tunnel water inrush. Therefore, it is of great engineering significance to establish an effective risk assessment model. Based on the Bayesian theory, interpretation structure model, and generative adversarial network, a Bayesian network risk assessment model is established. The results show that firstly, twelve indexes selected can not only characterize the karst tunnel water inrush but also are easy to be counted, which effectively improves the accuracy of the Bayesian risk assessment model. Secondly, the Bayesian network risk assessment model overcomes the shortcomings of other risk assessment models that rely too much on geological data and improves the accuracy through massive data training. Thirdly, the corresponding noninrush samples are generated by the generative adversarial network and analytic hierarchy process, which effectively solve the problem of an unbalanced database. Finally, the Bayesian network risk assessment model is applied to the DK490+373 section of the Shangshan Tunnel. The assessment model is operable, effective, and practical, and it is also suitable for the situation of incomplete index statistics.

1. Introduction

In recent years, with the development of underground engineering, the scale and difficulty of tunnel construction in China have leapt to the number one in the world. China, with an expanse territory, complex topography, climatic condition, and abundant karst landform, complex environment leads to water inrush disasters that frequently occur during the construction of underground engineering. According to statistics, water inrush accounts for about 40% of all kinds of disasters and nearly 50% of tunnel water inrush disasters are directly or indirectly caused by the karst landform, which seriously affects the safety of underground engineering construction, causing massive

casualties and economic losses. Water inrush also leads to collapse, surface subsidence, water resources depletion, and other secondary disasters. Figure 1 shows the situation of water inrush in the Yesangaun Tunnel. On the 5th of August, 2007, water inrush occurred during the excavation and the quantity reached $15.1 \times 10^4 \text{ m}^3/\text{d}$, resulting in 10 deaths and half a year's delay of construction [1]. Therefore, it is of great engineering significance to establish an effective risk assessment model for water inrush probability and disaster consequences.

A long time ago, many experts and scholars have realized the danger of water inrush and which is easy to occur during the excavation in a karst stratum. In 1970s, for the first time, the British scholar Wilson J.L. [2] summarized



FIGURE 1: Situation of water and mud inrush in the Yesangaun Tunnel [1].

the water inrush law of karst landform. Subsequently, in terms of theoretical research, scholars have carried out research on the disaster-causing mode and mechanism of water inrush in the karst tunnel through fluid mechanics, groundwater dynamics, rock mechanics, and fracture mechanics [3–6]. In addition, numerical simulation, experiment, and other methods are also introduced into the study about water inrush of the karst tunnel [7–13] carried out research on the occurrence mechanism, failure modes, and main influencing factors of water inrush in karst tunnels. Li et al. [14] divided the source of water inrush into three categories, cavity, fissure, and pipeline according to the type of karst structure, and pointed out that the development of disaster source was controlled by various factors such as geographic and geomorphic conditions and rock strata dip angle.

Based on the research about water inrush in a karst tunnel, the water inrush mechanism of the karst tunnel is complex and there are many influencing factors, which seriously affect the safety of underground engineering construction. Therefore, it is of great engineering significance to establish an effective risk assessment model for water inrush. The research about water inrush in the karst area lays a good foundation for the development of the water inrush risk assessment model of the karst tunnel. Based on the research about water inrush in a karst tunnel, the idea of risk assessment was firstly introduced into engineering in 1983 [15] and the first risk assessment model was established. Subsequently, three-dimensional reticulated exploration, GIS, case analysis, advanced geological prediction, Dempster-Shafer (D-S) evidence theory, microseismic monitoring technology, MFIM, TOPSIS, and other theories have been introduced into the risk assessment model [16–23].

In 1992, for the first time, Nilsen [24] implemented the risk assessment in the construction of a subsea tunnel and established the corresponding risk assessment model. Subsequently, Kampmann et al. [25] further extended the risk assessment method to the construction of subway engineering and formulated corresponding risk control measures. Weiss and Vig [26] extended the idea of risk assessment to the preliminary engineering design. Wang et al. [27, 28] introduced the efficiency coefficient method and analytical

comparison method into the risk assessment model, which improved the calculation efficiency. Hou et al. [29] combined the AHP method and coefficient of variation method to the comprehensive weight and introduced the ideal point method.

At present, the risk assessment model has proved its effectiveness in underground engineering construction. However, most of the risk assessment models used for water inrush are based on detailed geological data and clear disaster causes. The complexity of the tunnel geological environment and the uncertainty of each index are ignored. Without detailed geological data as support, the accuracy of assessment model will be greatly reduced. And underground engineering itself has great fuzziness, and geological data collection is very difficult. Therefore, a new risk assessment model based on the Bayesian network theory is established, which effectively overcomes these problems. Bayes' theory has its origins in Bayes' 1763 work. The essence of Bayesian theory is to determine the mutual influence among various factors through data training and measured by probability, which can dynamically control the probability from the "macrolevel [30]". Therefore, the Bayesian theory is often used in engineering risk assessment models. Kool et al. [31] used the Bayesian theory to advance the procedure of hindcasting of levee failures and verified the dam failure near Breitenhagen in Germany. Zhao et al. [32] proposed a Bayesian method to effectively develop regional correlation models to estimate the runoff distance. This method systematically integrates the sparse data collected in a specific region and the prior knowledge embedded in the existing relevant models in other regions. The method is illustrated by examples and numerical examples. In order to better understand groundwater dynamics and improve the reliability of model prediction, Yin et al. proposed a Bayesian multi-model uncertainty quantification framework to explain the model parameter uncertainty in complex alluvial groundwater modeling. The method is applicable to the agricultural intensive Mississippi River alluvial aquifer (mraa) in Northeast Louisiana. Wu et al. proposed an integrated model based on dynamic hazard scenario identification (DHSI), Bayesian network (BN) modeling, and risk analysis for risk assessment of urban public utility tunnels. The worst-case

scenario of urban utility tunnel accidents is identified by DHSI and modelled by BN. In 2014, for the first time, the Bayesian network was applied to the risk assessment model of tunnel construction. Hu [33] applied the Bayesian network to the stability assessment of the tunnel and proved the validity of his risk assessment model by monitoring displacement and stress.

Compared with other assessment models, the Bayesian risk assessment model established in this paper can accurately predict the water inrush of a karst tunnel through massive data training under the condition of incomplete geological data and unknown disaster cause. The selected evaluation indexes are more in line with the characteristics of the karst tunnel. In order to solve the problem that the Bayesian risk assessment model needs massive data training, for the first time, the idea of the generative adversarial network and the principle of the analytic hierarchy process are used to solve the problem of unbalanced database. The Bayesian network theory is of great theoretical significance to the risk assessment and disaster prevention of tunnel water inrush and to guide the safe and economic construction of a karst tunnel.

2. The Construction of the Bayesian Network Model

2.1. The Basic Principle of the Bayesian Network. Bayesian network is a probabilistic graph model that consists of nodes, directed arrows, and conditional probability table. Nodes represent random variables in the network, directional arrows represent the relationship between nodes, and conditional probability tables represent the degree of mutual influence between nodes. The Bayesian network has the following advantages: the statistical data are quantitatively evaluated, and the final results are determined according to the interval membership degree of each node. As the accumulation of statistical data, model evaluation can become more and more accurate without changing the original topology diagram. Be able to combine expert experience with training data.

The mathematical formula and the expression of conditional independence criterion of the Bayesian network are shown in formula (1) [34]:

$$P(M|N=a) = \frac{P(M)P(N=a|M)}{P(N=a)}. \quad (1)$$

In the formula, $P(M|N=a)$ is the posterior probability, which is the probability of M occurring when a new value of N is known as a ; $P(M)$ is the prior probability, the probability of M before considering the new value of N , which is obtained by historical data; $P(N=a|M)$ is the likelihood of M , calculated from historical data; $P(N=a)$ is the probability that N is a .

2.2. Model Building Method. The widely used hybrid modeling method is adopted to build the model. The hybrid

TABLE 1: Risk classification of formation lithology.

Risk classification	$t = \sum A_i B_j$	Definition
I	>0.254	Strong karst stratum
II	0.104~0.254	Moderate karst stratum
III	0.042~0.104	Weak karst stratum
IV	<0.042	Nonsolute stratum

modeling method can integrate the influence relationship between the variables from experience into the data training without unnecessary causality, which can greatly improve the learning efficiency. The main steps of the hybrid modeling method are as follows. Firstly, representative evaluation factors of karst tunnel water inrush are selected and classified according to the risk classification. Secondly, the corresponding interpretation structure model is constructed and the evaluation index is processed hierarchically according to the influence relationship. Thirdly, according to the causality diagram method, the causal relationship of each node is modified.

2.3. Selection of Evaluation Indexes. The influencing factors of water inrush in a karst tunnel can be summarized into geological factors, hydrological factors, and anthropogenic factors, through reviewing the relevant literature on the risk assessment of water inrush in a karst tunnel [5, 27, 28]. Six evaluation indexes are selected from geological factors, including topography and geomorphology, attitude of rocks, formation lithology, unfavorable geology, interlayer fissures, and contact zones of dissolvable and insoluble rock. Two evaluation indexes are selected from hydrological factors, including the groundwater level and rainfall. Two evaluation indexes are selected from anthropogenic factors, including construction disturbance and support measures. Water inrush probability and water inrush quantity are selected as the output of the model. Detailed introduction and risk classification of each evaluation index are shown as follows.

2.3.1. Formation Lithology S_1 . The formation lithology mainly refers to the solubility of rock. In references [27, 28], $t = \sum A_i B_j$ is defined for risk classification. Among them, A_i represents solubility (weak solubility, moderate solubility, and strong solubility) and B_j represents the proportions of solute rock in total rock (0–20%, 20%–40%, 40%–60%, and 60%–100%); see Table 1.

2.3.2. Unfavorable Geology S_2 . Unfavorable geology usually refers to the water-storing structure in a karst landform, such as cavity, underground river, and karst pipeline. In this paper, risk classification of unfavorable geology is carried out according to the on-site expert assessment, as shown in Table 2 [28].

2.3.3. Topography and Geomorphology S_3 . Karst landform is formed by the erosion and deposition of soluble rock by groundwater. Due to the special geological condition of karst

TABLE 2: Risk classification of unfavorable geology.

Risk classification	Definition
I	High risk: large-sized water-storing structure exists
II	Moderate risk: medium-sized water-storing structure exists
III	Low risk: small-sized water-storing structure exists
IV	No risk: no water-storing structure exists

TABLE 3: Risk classification of topography and geomorphology.

Risk classification	The proportion of negative relief (%)	Definition
I	>60	Strong water storage capacity
II	30~60	Moderate water storage capacity
III	10~30	Weak water storage capacity
IV	<10	Terrible water storage capacity

landform, plenty of groundwater is accumulated in negative landform, which provides water for water inrush. In reference [35], the proportion of negative landform in the area is used to classify the risk, as shown in Table 3.

2.3.4. *Groundwater Table S_4* . The quantitative analysis of groundwater table risk classification is the premise of accurate risk assessment [36]. Distance h between the groundwater table and the tunnel floor is used to classify the risk, as shown in Table 4.

2.3.5. *Rainfall S_5* . According to the rainfall division of meteorology, rainfall in 24 hours l (mm) is used to classify the risk. Because different types of karst tunnels have different response times to rainfall, the time range is set as one week, that is, as long as the rainfall reaches light rain once within a week, the rainfall of this week can be identified as light rain, as shown in Table 5 [29].

2.3.6. *Attitude of Rock S_6* . The attitude of rocks can indirectly affect the recharge, runoff, and discharge capacity of groundwater. In this paper, the dip angle is used to classify the risk, as shown in Table 6 [36].

2.3.7. *Inter-Layer Fissure S_7* . The development degree of interlayer fissure represents the activity of groundwater. In reference [29], the development degree of interlayer fissure is used to classify the risk, as shown in Table 7.

2.3.8. *Contact Zone of Dissolvable and Insoluble Rock S_8* . The contact zone of dissolvable and insoluble rock [5] is a necessary condition for the formation of the underground water-storing structure. The degree of contact zone development is used to classify the risk, as shown in Table 8.

TABLE 4: Risk classification of contact zones of the groundwater table.

Risk classification	h (m)	Definition
I	≥ 60	High risk: high water pressure and large instantaneous water inrush quantity
II	30~60	Moderate risk
III	0~30	Low risk
IV	<0	No risk

TABLE 5: Risk classification of rainfall in a week.

Risk classification	l (mm)	Definition
I	>50	Rainstorm, high risk
II	25~50	Heavy rain, middle risk
III	10~25	Moderate rain, low risk
IV	<10	Light rain or no rain, no risk

TABLE 6: Risk classification of the attitude of rock.

Risk classification	Attitude of rocks ($^\circ$)	Definition
I	25~65	Strong water conductivity
II	10~25/65~80	Moderate water conductivity
III	80~90	Weak water conductivity
IV	0~10	Terrible water conductivity

TABLE 7: Risk classification of interlayer fissures.

Risk classification	Definition
I	The fissure is strongly developed
II	The fissure is generally developed
III	The fissure is poorly developed
IV	The fissure is almost undeveloped

TABLE 8: Risk classification of contact zones of dissolvable and insoluble rock.

Risk classification	Definition
I	Strongly conducive to the development of large karst structures
II	Generally conducive to the development of large karst structures
III	Poorly conducive to the development of large karst structures
IV	Almost not conducive to the development of large karst structures

2.3.9. *Excavation Disturbance S_9* . Different excavation methods are used to classify the risk, as shown in Table 9 [37].

2.3.10. *Support Measures S_{10}* . The support measures of the tunnel are divided into two steps: preliminary support and

TABLE 11: Subgrading of the karst tunnel water irruption quantity.

Subgrading	I	II ₁	II II ₂	II ₃	III ₁	III III ₂	IV	V
Water irruption quantity (m ³ /h)	≥10000	7000~10000	4000~7000	1000~4000	550~1000	100~550	10~100	≤10

TABLE 12: Relationship between indexes of karst tunnel water inrush.

S ₁	S ₂	S ₃	S ₄	S ₅	S ₆	S ₇	S ₈	S ₉	S ₁₀	S ₁₁	S ₁₂	
	A	A	A	C	A	A	A	C	A	A	C	S ₁
		C	C	C	B	B	B	C	C	A	A	S ₂
			A	C	C	A	A	C	C	A	A	S ₃
				B	B	B	C	C	C	A	A	S ₄
					C	C	C	C	C	A	A	S ₅
						C	A	C	C	A	A	S ₆
							A	C	A	A	A	S ₇
								C	C	A	C	S ₈
									A	A	A	S ₉
										A	A	S ₁₀
											C	S ₁₁
												S ₁₂

2.4.4. *Hierarchical Process.* In the accessibility matrix G , the indexes corresponding to the columns with the value of 1 in each row constitute the accessibility set $L(S_i)$ and the indexes corresponding to the rows with the value of 1 in each column constitute the reason set $Q(S_i)$. The necessary and sufficient condition for the variable set O_1 to be the top-level variable set is shown as follows:

$$L(S_i) = L(S_i) \cap Q(S_i). \quad (6)$$

After obtaining set O_1 , clear the rows and columns of the indexes corresponding to O_1 in the matrix G , then, get new matrix G , and then, follow the same method, according to formula (6) to get the set O_2 , by analogy O_3, \dots, O_n . And finally, form a multistage skeleton matrix structure.

According to the hierarchical process table and the relationship between each index, the interpretation structure model of karst tunnel water inrush risk assessment is shown in Figure 2.

2.5. *Correction of the Causality Chart.* The causality chart describes the causality among variables through charts, focusing on the results of different combinations of multiple input indexes. Since the interpretation structure model will ignore the skip-level relationship and the important relationship between various indexes, according to the reference, the interpretation structure model is further modified by the causality chart and the final Bayesian network model applied to the risk assessment for water inrush in the karst tunnel is obtained. Figure 3 shows the final Bayesian network model.

The new dotted arrows in Figure 3 are used to represent the interaction between each index.

3. The Data Training and Verification of the Bayesian Network Model

After the model is established, Netica software is used to train the model. Firstly, it is necessary to divide each index into interval grades to meet the input and output requirements of the network model; secondly, the engineering cases that can be used for Bayesian network data training need to be counted separately and the interval quantization processing should be carried out; finally, the consistency ratio (RCR) is used to evaluate the training of the model.

3.1. *Determine the Input and Output Types of Each Evaluation Index.* There are twelve indexes in this model, among which $S_1 - S_{10}$ are the input indexes and $S_{11} - S_{12}$ are the output indexes. The risk classification of the input index is divided into four grades. The output index water inrush probability is divided into two sections, yes and no, and the water inrush quantity is divided into 8 sections to further accurately calculate the disaster consequences. According to the classification of indexes, the intensity of each index is described in Tables 13 and 14.

3.2. *Training Specimen of the Network.* Bayesian network training requires plenty of data, but the existing databases are all water inrush cases and nonwater inrush cases are not included. If only the existing database is used for

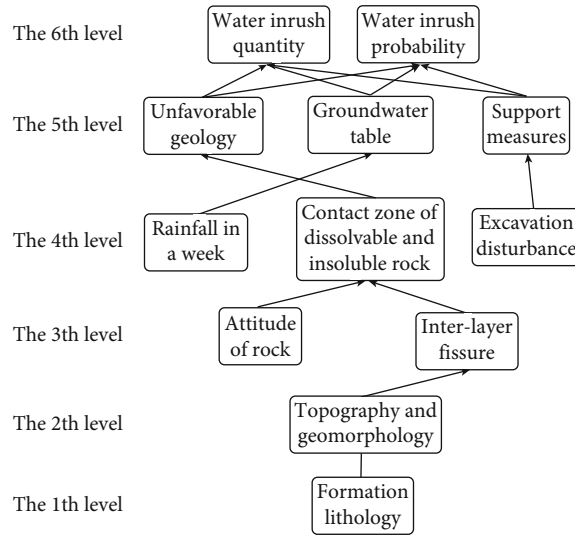


FIGURE 2: Interpretive structural model among factors of karst tunnel water inrush.

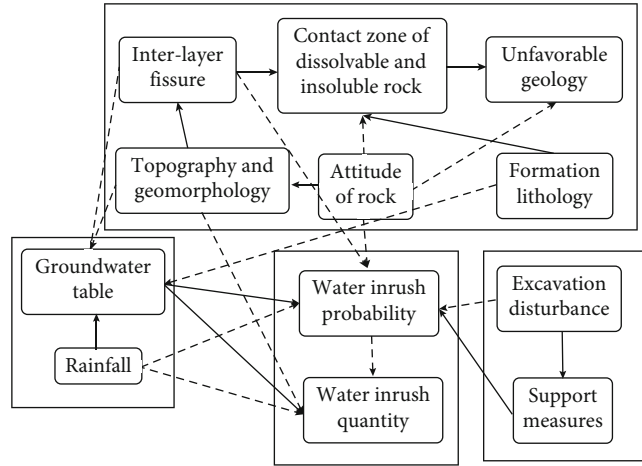


FIGURE 3: Bayesian network of karst tunnel water inrush.

TABLE 13: S_1 – S_{11} grading interval.

	Strong	Medium	Weak	None
S_1 – S_9	I	II	III	IV
S_{10}	IV	III	II	I
S_{11}		Yes		No
		Yes		No

The more reasonable the support measures of S_{10} , the lower the risk, so the expression is in contrary to that of the other input indexes.

network training, the sample will be extremely unbalanced. In order to realize the training of the model, based on the idea of generative adversarial network and analytic hierarchy process, some nonwater inrush cases are generated from water inrush cases to further enrich the database.

In essence, the generative adversarial network generates new data according to the existing data range or boundary conditions, which is mainly used to solve problems such as unbalanced database. The process of generating nonwater

inrush cases is as follows. Firstly, according to the existing data, $S_1, S_2, S_3, S_7, S_8, S_9$, and S_{10} are selected and weighted by the analytic hierarchy process and the indexes are quantitatively processed from 0 to 1. Secondly, value range of 0–1 can be obtained by summing the value of each index times the weight, which is denoted as the range of water inrush, that is, if the calculated result is within this range, water inrush disaster will occur. Thirdly, the lower limit of the water inrush range is selected as the boundary between

TABLE 14: S_{11} – S_{12} grading interval.

	Strong	Medium 1	Medium 2	Medium 3	Weak 1	Weak 2	None 1	None 2
S_{12}	I	II-1	II-2	II-3	III-1	III-2	IV	V

The water inrush quantity is divided into 8 sections corresponding to the subgrading of water irruption quantity in the previous paper.

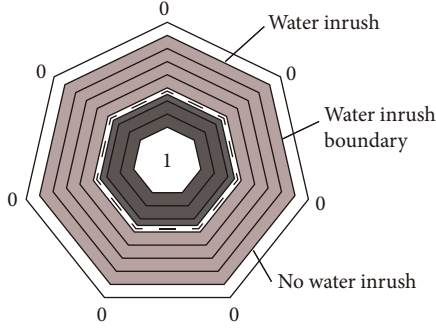


FIGURE 4: Generative adversarial network diagram.

water inrush and nonwater inrush. According to the one-to-one principle, the nonwater inrush range is obtained from the water inrush range. According to the same weight, it can be calculated backwards to get the corresponding quantitative value between 0 and 1 of each index. Finally, the corresponding grade of each index in nonwater inrush cases can be obtained by reverse mapping from the quantization value. The schematic diagram of the generative adversarial network is shown in Figure 4.

Figure 4 is a seven-sided shape, representing the seven selected indexes. The distance from the corner point to the center is 1, representing the quantitative range of 0–1. The dark-gray area represents the water inrush range, the light-gray area represents the nonwater inrush range, and the dotted line between the two areas represents the water inrush boundary. The judgment matrix constructed by the analytic hierarchy process, as shown in Table 15.

$$C = (0.159, 0.35, 0.07, 0.032, 0.237, 0.106, 0.046),$$

$$R_{CR} = \frac{I_{CI}}{I_{RI}} = 0.025 < 0.1. \quad (7)$$

R_{CR} represents the consistency ratio, and when it is less than 0.1, it represents that the consistency of the judgment matrix meets the requirements; I_{CI} represents the consistency index; I_{RI} represents the average random consistency index.

According to I (0.75–1), II (0.75–0.5), III (0.5–0.25), and IV (0–0.25) to quantify the various samples, 37 water inrush samples are selected from the database for quantitative process and the range of water inrush samples is 0.55–0.9 according to the calculation method of the above-introduced water inrush range. Select 0.5 as the water inrush boundary, and it can be concluded that the nonwater inrush range is 0.1–0.45. According to the reverse calculation method, the corresponding nonwater inrush cases can be

obtained. Finally, reverse quantitative processing and the risk classification of each index of the nonwater inrush cases can be obtained.

3.3. Bayesian Network Model Training and Verification Results. Figure 5 shows the training results of the Bayesian network model, and the probability table of each index after training is shown. Ten samples are selected from the database for verification. After verification, the accuracy for water inrush probability is 100% and that for predicting water inrush quantity is 90%.

4. Application of Bayesian Network Risk Assessment Model

The DK490+373 section of the Shanggaoshan Tunnel of the Chengdu-Guiyang Railway is selected to verify the feasibility of the model.

4.1. Engineering Background. The Shanggaoshan Tunnel of the Chengdu-Guiyang Railway is located in Qingzhen city, Guizhou province [38]. The maximum depth of the tunnel reaches 135 m. The average annual rainfall reaches 1000–1600 mm. The surrounding rock of the DK490+373 section is mainly composed of limestone, marl, and other carbonate rocks, and the overall dip angle of the rock layer is 5°–30°. Rock joints and fractures most are open and vertical.

4.2. The Determination of Input Indexes. According to the engineering data, the Bayesian network model is used to predict the water inrush risk of DK490+373 of the Shanggaoshan Tunnel under no-rain and heavy-rain conditions. Risk classification of each input index is shown in Table 16.

There is no accurate quantitative data to describe the topography and geomorphology, formation lithology. According to the description of engineering data and the risk classification of the index, it is considered as moderate risk. The overall dipping direction is 5°–30°; according to the abovementioned risk classification, the attitude of rocks is considered as moderate risk. The water storage structures in the tunnel area mainly are karst pipeline and small karst cave, which are classified as moderate risk. According to the engineering data, interlayer fissure is classified as moderate risk by qualitative description. The bench cut method is adopted in construction, and water inrush occurred without support, so it can be concluded that the construction disturbance is weaker than blasting but stronger than drilling. Due to the lack of support measure, it can be determined as high risk.

4.3. Prediction Result of the Bayesian Network Risk Assessment Model. Figure 5 shows the training result of the Bayesian network model. Input the values of the indexes in

TABLE 15: Overview of the value of each input index.

	Topography and geomorphology	Contact zones of dissolvable and insoluble rock	Formation lithology	Unfavorable geology	Interlayer fissure
No rainfall	II (medium)	*	II (medium)	II (medium)	II (medium)
Heavy rainfall	II (medium)	*	II (medium)	II (medium)	II (medium)
	Attitude of rock	Groundwater table	Rainfall in a week	Excavation disturbance	Support measures
No rainfall	II (medium)	*	IV (none)	II (medium)	IV (strong)
Heavy rainfall	II (medium)	*	II (medium)	II (medium)	IV (strong)

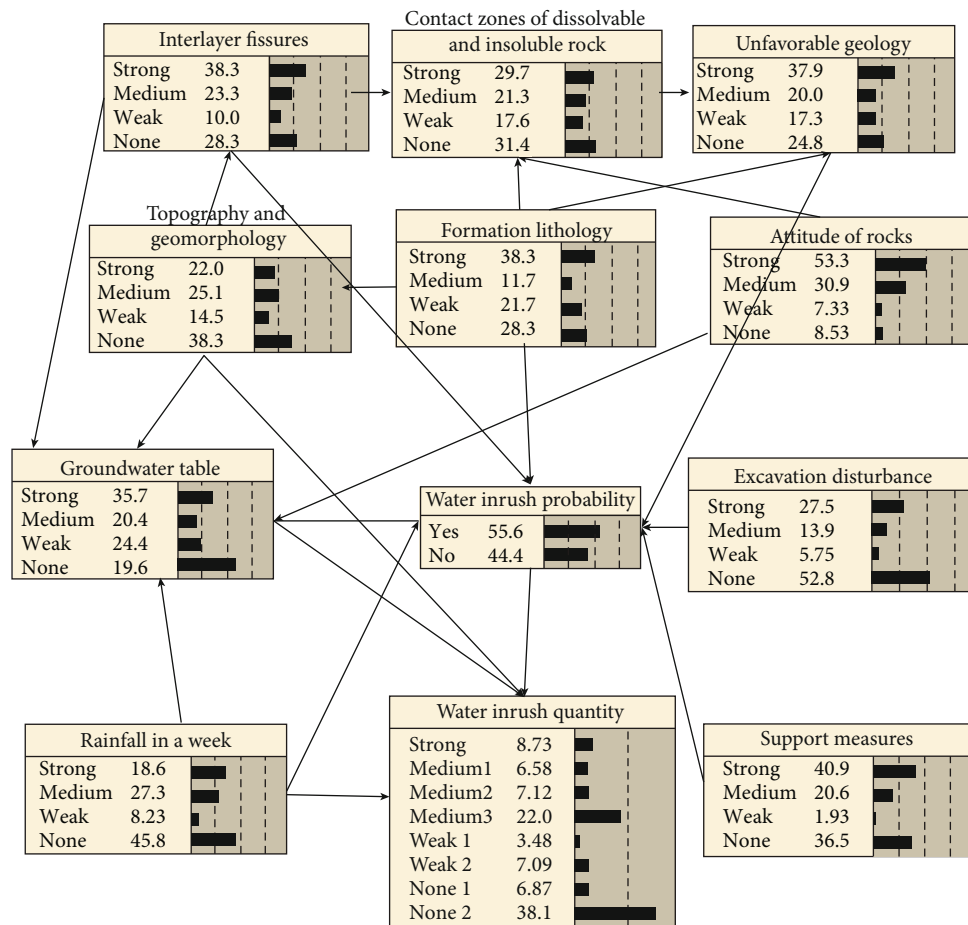


FIGURE 5: Bayesian network training results.

Table 16 in turn, and observe whether the final output is consistent with the reality. In the case of no rain or heavy rain, the prediction results of water inrush in the DK490 +373 section are shown in Table 17.

4.4. Realistic Water Inrush Situation. On the 23th of August, 2015, the exit section of the tunnel was excavated to DK490 +373 and a karst cave with diameter of 0.55 m was exposed at the right-side wall. Small-scale water inrush occurred immediately, and water inrush quantity reaches 226.8m³/h. After investigation, it was found that the exposed karst cave

was connected with the karst pipe, which resulted in the continuous small-scale water inrush. The geological profile of the section is shown in Figure 6. On the 28th of August, 2015, massive sustained rainfall (the rainfall in 24 hours reached 33.4 mm, which can be identified as heavy rain) occurred within the tunnel area, which caused large-scale water inrush disaster in the tunnel, with the water inrush quantity reaching 5005 m³/h.

4.5. Results Analysis. Under the condition of heavy rain or no rain, the prediction results of water inrush risk in section

TABLE 16: Overview of the value of each input index.

	Topography and geomorphology	Contact zones of dissolvable and insoluble rock	Formation lithology	Unfavorable geology	Interlayer fissure
No rainfall	II (medium)	*	II (medium)	II (medium)	II (medium)
Heavy rainfall	II (medium)	*	II (medium)	II (medium)	II (medium)
	Attitude of rock	Groundwater table	Rainfall in a week	Excavation disturbance	Support measures
No rainfall	II (medium)	*	IV (none)	II (medium)	IV (strong)
Heavy rainfall	II (medium)	*	II (medium)	II (medium)	IV

*The value of the index is unknown, such as contact zones of dissolvable and insoluble rock and groundwater table.

TABLE 17: Prediction and real result.

	Prediction result		Actual result	
	Probability of water inrush	Water inrush quantity	Whether water inrush occurs	Water inrush quantity
No rainfall	85.3%	100~550 m ³ /h	Yes	226.8 m ³ /h
Heavy rainfall	51.3%	4000~7000 m ³ /h	Yes	5005 m ³ /h

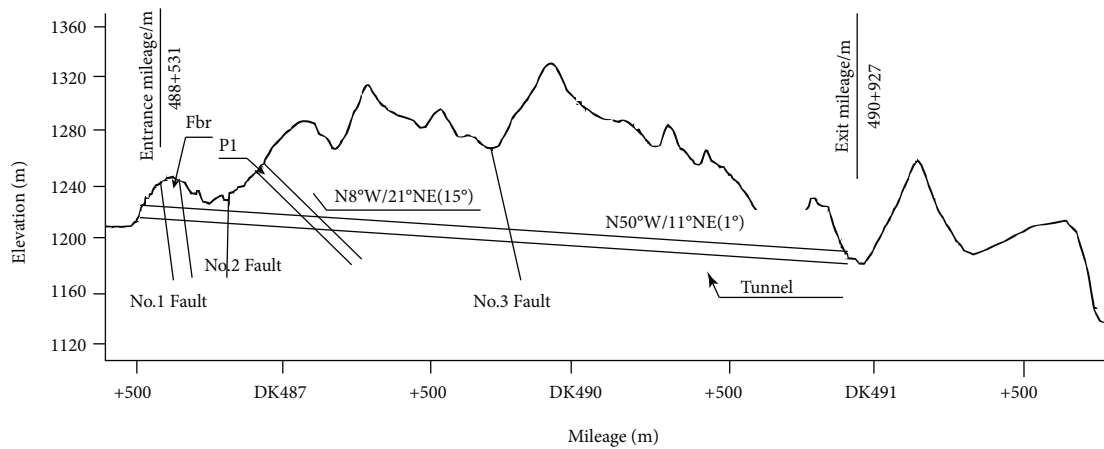


FIGURE 6: Geological section of Shanggaoshan Tunnel.

DK490+373 are completely consistent with reality. It can be seen from the results that this model is accurate and practical in predicting karst tunnel water inrush probability and quantity.

5. Conclusion

Based on the Bayesian theory, interpretive structure model, generative adversarial networks, and analytic hierarchy process, a new Bayesian network risk assessment model is established. The main conclusions are as follows:

Twelve indexes which can not only characterize the karst tunnel water inrush but also are easy to be counted are selected as the input and output indexes of the model, which summarizes the disaster-causing factors of karst tunnel water inrush comprehensively and effectively improves the accuracy of the Bayesian risk assessment model.

In view of the variability and complexity of the underground engineering environment, a new Bayesian network risk assessment model is established. The model overcomes the shortcomings of other risk assessment models that rely too much on geological data. Through massive data learning, it can carry out accurate risk assessment under the condition of incomplete geological data and unknown disaster cause.

Based on the idea of the generative adversarial network and principle of the analytic hierarchy process, the generation method of no water inrush samples is proposed for the first time, which can generate no water inrush sample from water inrush sample database, and effectively solved the problem of unbalanced database.

The Bayesian network risk assessment model is applied to the risk assessment of water inrush in the DK490+373 section of the Shanggaoshan Tunnel. The result shows that the model is operable, effective, practical, and also applicable to the case of incomplete index statistics. The prediction

results of water inrush risk are completely consistent with the realistic water inrush situation.

Data Availability

The data used to support the findings of this study are available from the corresponding author upon request.

Conflicts of Interest

The authors declare that they have no conflicts of interest.

Acknowledgments

Support provided by the open research fund of the State Key Laboratory of Geomechanics and Geotechnical Engineering, Institute of Rock and Soil Mechanics, Chinese Academy of Sciences (no. Z020014), the Key Research and Development Program (Social Development) of Xuzhou City (KC21298), and the National Natural Science Foundation of China (no. 41572263) are sincerely acknowledged.

References

- [1] D. Ma, *Study on Impact Mechanism of Deep Buried Karst to Tunnel Safety and the Treatment Technique*, [Ph.D. Thesis], Beijing Jiaotong University, 2012.
- [2] J. L. Wilson, "Characteristics of carbonate-platform margins," *American Association of Petroleum Geologists Bulletin*, vol. 58, no. 5, pp. 810–874, 1974.
- [3] L. P. Li, T. Lei, S. C. Li et al., "Risk assessment of water inrush in karst tunnels and software development," *Arabian Journal of Geosciences*, vol. 8, no. 4, pp. 1843–1854, 2015.
- [4] W. Lu, Z. Zhou, T. Liu, and Y. H. Liu, "Discrete element simulation analysis of rock slope stability based on UDEC," *Advanced Materials Research*, vol. 461, pp. 384–388, 2012.
- [5] Y. C. Wang, F. Geng, S. Q. Yang, H. Jing, and B. Meng, "Numerical simulation of particle migration from crushed sandstones during groundwater inrush," *Journal of Hazardous Materials*, vol. 362, pp. 327–335, 2019.
- [6] Y. C. Wang, H. W. Jing, H. J. Su, and J. Xie, "Effect of a fault fracture zone on the stability of tunnel-surrounding rock," *International Journal of Geomechanics*, vol. 17, no. 6, 2017.
- [7] N. Zhao, Y. C. Wang, B. Meng, and N. Luo, "Numerical simulation on the seepage properties of soil-rock mixture," *Advances in Materials Science and Engineering*, vol. 2018, Article ID 1859319, 10 pages, 2018.
- [8] S. V. Kuznetsov and V. A. Trofimov, "Hydrodynamic effect of coal seam compression," *Journal of Mining Science*, vol. 38, no. 3, pp. 205–212, 2002.
- [9] M. Salis and L. Duckstein, "Mining under a limestone aquifer in southern Sardinia: a multiobjective approach," *International Journal of Mining Engineering*, vol. 1, no. 4, pp. 357–374, 1983.
- [10] S. C. Li, C. L. Gao, and Z. Q. Zhou, "Analysis on the precursor information of water inrush in karst tunnels: a true triaxial model test study," *Rock Mechanics & Rock Engineering*, vol. 52, p. 2, 2019.
- [11] F. Chen, Y. C. Wang, W. Jiang, and S. H. Zheng, "Numerical simulation of ground movement induced by water and sand gushing in subway through fault based on DEM-CFD," *Computers and Geotechnics*, vol. 139, article 104282, 2021.
- [12] Y. C. Wang, F. Chen, X. Z. Li, X. Yin, F. Geng, and S. H. Zheng, "Experimental Investigation on Mass Loss Characteristics of Broken Rocks with Discontinuous Gradation," *International Journal of Geomechanics*, vol. 21, no. 9, p. 04021168, 2021.
- [13] Y. C. Wang, Z. Y. Li, H. W. Jing, Y. B. Li, and M. T. Wang, "Study on the seepage characteristics of deep buried tunnels under variable high-pressure water heads," *Bulletin of Engineering Geology and the Environment*, vol. 80, no. 2, pp. 1477–1487, 2021.
- [14] S. C. Li, P. He, L. P. Li et al., "Reliability analysis method of sub-classification of tunnel rock mass and its engineering application," *Rock and Soil Mechanics*, vol. 39, no. 3, pp. 967–976, 2018.
- [15] G. F. Salazar, *Stochastic and Economic of Adaptability in Tunneling Design and Construction*, Department of Civil Engineering, Massachusetts Institute of Technology, Cambridge, MA, USA, 1983.
- [16] G. Z. Ou, Y. Y. Jiao, G. H. Zhang, J. P. Zou, F. Tan, and W. S. Zhang, "Collapse risk assessment of deep-buried tunnel during construction and its application," *Tunnelling and Underground Space Technology*, vol. 115, no. Sep 2021, p. 104019, 2021.
- [17] Z. H. Peng, L. W. Chen, X. W. Hou, Q. H. Ou, J. Zhang, and Y. F. Chen, "Risk assessment of water inrush under an unconsolidated, confined aquifer: the application of Gis and information value model in the Qidong coal mine, China," *Earth Science Informatics*, vol. 14, no. 4, pp. 2373–2386, 2021.
- [18] W. F. Tu, L. P. Li, S. Cheng, D. Y. Chen, Y. C. Yuan, and Y. H. Chen, "Evolution mechanism, monitoring, and early warning method of water inrush in deep-buried long tunnel," *Geofluids*, vol. 2021, Article ID 2023782, 16 pages, 2021.
- [19] H. C. Yin, B. Xu, S. X. Yin, W. Z. Tian, H. Yao, and H. P. Meng, "Prevention of water inrushes in deep coal mining over the Ordovician aquifer: a case study in the Wutongzhuang Coal Mine of China," *Geofluids*, vol. 2021, Article ID 5208670, 13 pages, 2021.
- [20] J. N. Yin, F. T. C. Tsai, and S.-C. Kao, "Accounting for uncertainty in complex alluvial aquifer modeling by Bayesian multi-model approach," *Journal of Hydrology*, vol. 601, article 126682, 2021.
- [21] G. D. Zhang, Y. G. Xue, C. H. Bai, M. X. Su, K. Zhang, and Y. F. Tao, "Risk assessment of floor water inrush in coal mines based on Mfim-Topsis variable weight model," *Journal of Central South University*, vol. 28, no. 8, pp. 2360–2374, 2021.
- [22] J. Pearl, *Probabilistic Reasoning in Intelligent Systems: Networks of Plausible*, Morgan Kaufmann, 1988.
- [23] J. S. Wu, Y. P. Bai, W. P. Fang, R. Zhou, G. Reniers, and N. Khakzad, "An integrated quantitative risk assessment method for urban underground utility tunnels," *Reliability Engineering & System Safety*, vol. 213, article 107792, 2021.
- [24] B. Nilsen, A. Palmström, and H. Stille, "Quality control of a subsea tunnel project in complex ground conditions," in *Proceedings of the ITA World Tunnel Congress*, pp. 137–145, Oslo, NO, USA, 1992.
- [25] J. Kampmann, S. D. Eskesen, and J. W. Summers, "Risk assessment helps select the contractor for the Copenhagen Metro System," *Proceedings of the world tunnel congress 98 on tunnels and me-tortoises*, vol. 98, pp. 123–128, 1998.

- [26] E. H. Weiss and L. Vig, "Mediation-A proper tool for risk assessment in tunneling projects," in *Proceedings of the AITE-SITA 2001 world tunnel congress*no. 3, pp. 583–588, 2001.
- [27] Y. C. Wang, H. W. Jing, L. Y. Yu, H. J. Su, and N. Luo, "Set pair analysis for risk assessment of water inrush in karst tunnels," *Bulletin of Engineering Geology and the Environment*, vol. 76, no. 3, pp. 1199–1207, 2017.
- [28] Y. C. Wang, X. Yin, F. Geng, H. W. Jing, H. J. Su, and R. C. Liu, "Risk assessment of water inrush in karst tunnels based on the efficacy coefficient method," *Polish Journal of Environmental Studies*, vol. 26, no. 4, pp. 1765–1775, 2017.
- [29] D. S. Hou, X. Zhang, and L. Wang, "Risk evaluation of tunnel water inrush based on comprehensive weighting-TOPSIS method and its application," *Tunnel Construction*, vol. 37, no. 6, pp. 691–699, 2017.
- [30] J. L. Hu, X. W. Tang, and J. N. Qiu, "A Bayesian network approach for predicting seismic liquefaction based on interpretive structural modeling," *Georisk Assessment & Management of Risk for Engineered Systems & Geohazards*, vol. 9, no. 3, pp. 200–217, 2015.
- [31] J. J. Kool, W. Kanning, C. Jommi, and S. N. Jonkman, "A Bayesian hindcasting method of levee failures applied to the Breitenhagen slope failure," *Georisk-Assessment and Management of Risk for Engineered Systems and Geohazards*, vol. 15, no. 4, pp. 299–316, 2021.
- [32] T. Y. Zhao, J. Y. Lei, and L. Xu, "An efficient Bayesian method for estimating runout distance of region-specific landslides using sparse data," *Georisk-Assessment and Management of Risk for Engineered Systems and Geohazards*, vol. 16, no. 1, pp. 140–153, 2022.
- [33] X. Hu, *Risk Analysis for High-Speed Rail Karst Tunnel Based on the Bayesian Network*, [M.S. thesis], Hunan University Of Science And Technology, 2014.
- [34] X. W. Tang, J. L. Hu, and J. N. Qiu, "Identifying significant influence factors of seismic soil liquefaction and analyzing their structural relationship," *KSCE Journal of Civil Engineering*, vol. 20, no. 7, pp. 2655–2663, 2016.
- [35] S. C. Li, Z. Q. Zhou, L. P. Li, S. S. Shi, and Z. H. Xu, "Risk evaluation theory and method of water inrush in karst tunnels and its applications," *Chinese Journal of Rock Mechanics and Engineering*, vol. 32, no. 9, pp. 1858–1867, 2013.
- [36] L. P. Li, S. C. Li, J. Chen, J. L. Li, Z. H. Xu, and S. S. Shi, "Construction license mechanism and its application based on karst water inrush risk evaluation," *Chinese Journal of Rock Mechanics and Engineering*, vol. 30, no. 7, pp. 1345–1355, 2011.
- [37] X. Yin, J. X. Ye, and Y. C. Wang, "Analysis of water inrush mode and quantitative analysis of influence factors of deep buried karst tunnel," *Bulletin of Science and Technology*, vol. 34, no. 4, pp. 247–253, 2018.
- [38] Z. H. Fang, Y. Yang, and H. J. Ding, "Study on water gushing disease of karst pipeline in Shanggaoshan Tunnel of Chengdu-Guiyang Railway," *High Speed Railway Technology*, vol. 8, no. 4, pp. 70–73, 2017.

Research Article

A New Method of Seismic Source Parameter Estimation of a Locked-Segment Cracking Event

Bai-Cun Yang ¹, Jian-Xin Bai,¹ Yong-Ting Duan ^{2,3} and Cheng Cheng^{4,5}

¹School of Resources and Civil Engineering, Northeastern University, Shenyang 110819, China

²Key Laboratory of Ministry of Education on Safe Mining of Deep Metal Mines, School of Resources and Civil Engineering, Northeastern University, Shenyang 110819, China

³Key Laboratory of Liaoning Province on Deep Engineering and Intelligent Technology, Northeastern University, Shenyang 110819, China

⁴State Key Laboratory for Geomechanics and Deep Underground Engineering, China University of Mining and Technology, Xuzhou 221116, China

⁵School of Mechanics & Civil Engineering, China University of Mining and Technology, Xuzhou 221116, China

Correspondence should be addressed to Bai-Cun Yang; yangbaicun@mail.neu.edu.cn

Received 19 January 2022; Accepted 21 May 2022; Published 6 June 2022

Academic Editor: Mohammed Fattah

Copyright © 2022 Bai-Cun Yang et al. This is an open access article distributed under the Creative Commons Attribution License, which permits unrestricted use, distribution, and reproduction in any medium, provided the original work is properly cited.

Locked segments are widely present in the slip surface of large rock slopes and seismogenic faults of rock underground engineering. Each cracking occasion of the locked segment results in a seismic event. Accurate determination of the seismic source parameters of a locked-segment cracking event is crucial for the reliable evaluation of rock-mass stability associated with slopes and underground openings. The theoretical framework for calculating seismic source parameters in previous studies is mostly based on the stick-slip model, which is not applicable to describing the locked segment's damage process, and research on seismic source parameter estimation of a locked-segment cracking event is insufficient. Hence, based on the principle of energy conversion and distribution during the locked segment's damage process, we proposed an equation for the radiated seismic energy of a locked-segment cracking event. Using this equation, we established a mechanical relationship between the earthquake magnitude and the stress drop or shear strain increment (or maximum coseismic displacement) of a locked-segment cracking event. Typical case studies of rock slope and rock underground engineering showed that the proposed calculation method of seismic source parameters was reliable. In addition, this paper discusses the controversy surrounding the relationship between earthquake magnitude and stress drop. Relevant results lay a firm physical foundation to accurately calculate the seismic source parameters of a locked-segment cracking event and obtain detailed insights into the generation mechanism of the locked-segment cracking event.

1. Introduction

Many researchers [1–11] have recognized locked segments with high bearing capacity (determined both by scale and strength) and subjected to shear stress concentration, such as rock bridges, asperities, and blocks bound by faults, which are commonly found in the slip surface of large rock slopes and seismogenic faults of rock underground engineering (Figure 1). Cracking of the locked segment results in a seismic event, such as a slope-slip-induced earthquake (Figure 2) or a

mining-induced earthquake [5, 10–14]. Therefore, estimating the seismic source parameters of such cracking events is essential and includes the radiated seismic energy (earthquake magnitude), stress drop, and slippage. A better understanding of these parameters will help assess rock-mass stability associated with slopes and underground openings.

The radiated seismic energy of a locked-segment cracking event, transmitted in the form of seismic waves, is a fundamental parameter when assessing the locked segment's size and source characteristics. To estimate this energy, many stud-

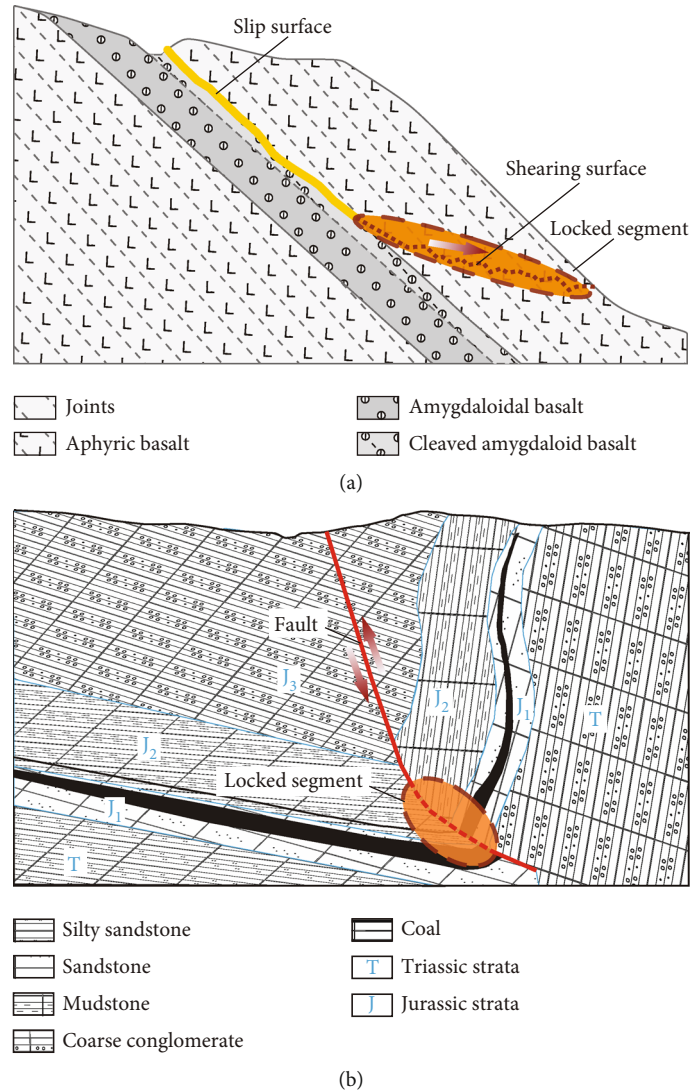
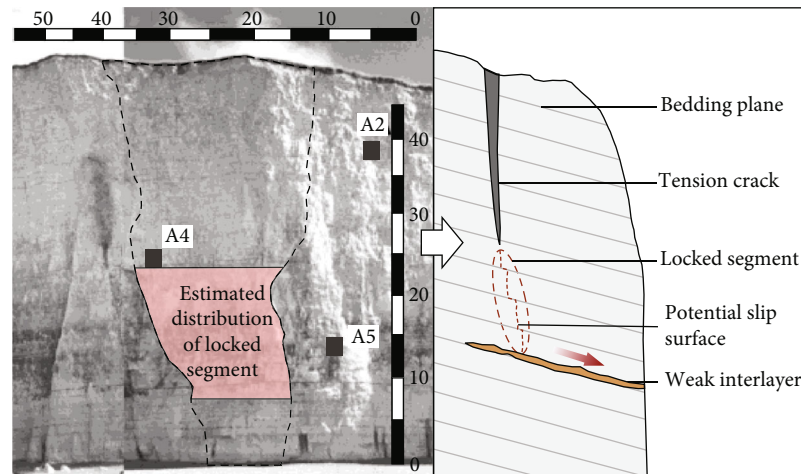


FIGURE 1: Conceptual model of locked segments in slip surface of rock slope (a) and seismogenic faults of rock underground engineering (b) (modified from Chen and Kong [15], Huang and Xu [16], Jiang et al. [17], and Song [18]).

ies have been conducted. For example, Savage and Wood [19] and Wyss and Molnar [20] presented an equation for the radiated seismic energy based on the theoretical framework of a stick-slip model. Kanamori [21] and Vassiliou and Kanamori [22] assumed that the average frictional stress equals the final stress to render the problem solvable. However, when the methods mentioned above were used in practical applications, especially in seismic source parameter estimation of the locked-segment cracking event, there was usually a significant error in the radiated seismic energy [13, 23]. This is due to the affected average frictional stress during the seismic rupture by many factors that cannot be treated as a constant. Moreover, the fracture surface energy produced by the cracking event is not considered in the previous methods. Rivera and Kanamori [24] presented an integral expression of radiated energy in finite faults, yet the formula is impractical due to its complex form. Anderson et al. [25] developed a self-consistent scaling model relating magnitude to surface rupture length, surface displacement, and rupture width for strike-slip faults and esti-

mated the earthquake magnitude from the fault length and slip rate under the assumption of a constant stress drop. Zang et al. [26] obtained the seismic source parameters near the northeast margin of Qinghai-Tibet Plateau using the joint inversion method. They found that the ratio of the apparent stress to the stress drop is greater in an earthquake with a lower local magnitude, suggesting that the seismic rupture is more sufficient and the radiation energy is relatively small. As mentioned above, all the theoretical framework of these studies is based on the stick-slip model. However, some studies [4, 6, 13] show that the stick-slip model is not applicable in describing the damage evolution process of the locked segment. Unfortunately, there is little research on the seismic source parameter estimation of a locked-segment cracking event. Thus, it is crucial to propose a new method to estimate the seismic source parameters of the locked-segment cracking event.

Unlike previous studies, to accurately estimate the source parameters of a locked-segment cracking event, we focused



□ Collapse boundary
 ■ Seismic station
 A4 Number of seismic station

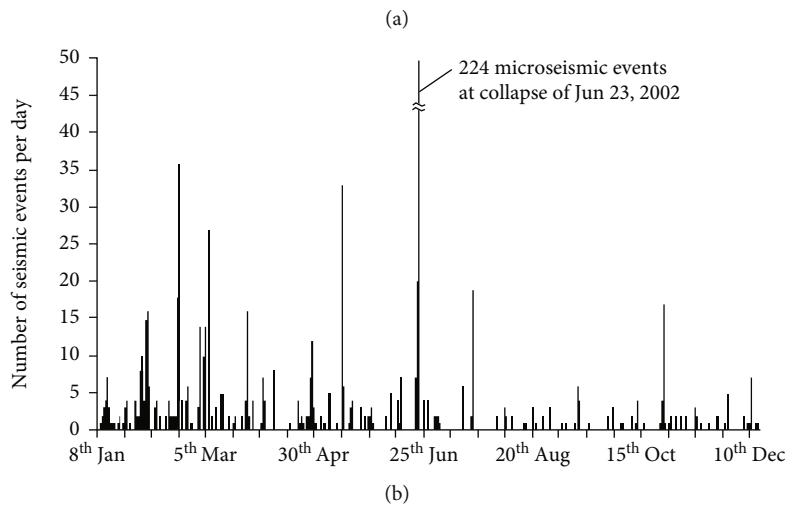


FIGURE 2: A rockcliff profile and its microseismic monitoring record at Mesnil-Val, Normand, NW France (modified from Senfaute et al. [12]): (a) trailing-edge slip surface after collapse and diagram of inferred profile before the collapse; (b) microseismic time-series recorded by A4 seismic station.

on the damage evolution characteristics of the locked segment under loading. We first formulated the principle of energy conversion and distribution during the locked segment's damage process. Then, we proposed an equation for the radiated seismic energy of the locked-segment cracking event. Using this equation, we established a mechanical relationship linking the stress drop, shear strain, or maximum coseismic displacement with the earthquake magnitude for a locked-segment cracking event. Finally, we presented two typical case studies of rock slope and rock underground engineering to verify our proposed method.

2. Method for the Seismic Source Parameter Estimation

2.1. Principle of Energy Conversion and Distribution during a Locked Segment's Damage Process. Loads (such as self-weight stress, tectonic stress, and engineering disturbance)

constantly provide elastic strain energy for deformation and failure of a locked segment. As the elastic strain energy stored in the locked segment accumulates to a certain extent, its damage initiates, which dissipates some elastic strain energy. When the applied stress reaches the locked segment's crack-initiation point, cracks propagate. Accompanying crack propagation is an inevitable drop in stress [13], as part of the elastic strain energy stored in the rock converts into dissipated energy, which mainly includes surface energy, friction-induced thermal energy, and radiated seismic energy (Figure 3).

According to Griffith's theory of crack propagation, crack propagation will stop when the driving force for crack propagation is equal to the crack propagation resistance. As illustrated in Figure 3, the crack starts to propagate when stress reaches point C, and a stress drop inevitably occurs. The mechanical effect or process of crack propagation leading to the stress drop is equivalent to the unloading of

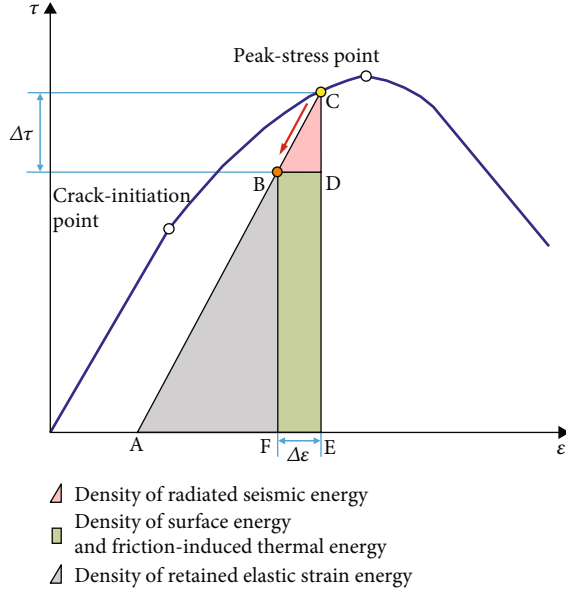


FIGURE 3: Conversion and distribution relationship of elastic strain energy density stored in a locked segment when a crack propagates (modified from Yang et al. [13]).

stressed rock along the CA path; when the stress drops to point B, an equilibrium between the resistance and the driving force is achieved, thereby the crack propagation is terminated. Based on the energy conservation principle, the elastic strain energy density stored in the locked segment before crack propagation ($S_{\Delta ACE}$) is equal to the sum of the elastic strain energy density ($S_{\Delta ABF}$, retained in the locked segment after crack propagation) and the dissipated energy density (S_{BCEF} , converted from the stored elastic strain energy). This S_{BCEF} is equal to the sum of the radiated seismic energy density (S_{ABCD}) and the density of both surface energy and friction-induced thermal energy (S_{BDEF}).

Based on the theoretical framework mentioned above, the elastic strain energy density, dissipated energy density, and radiated seismic energy density during crack propagation can be calculated as follows [27]. The dissipated energy density during crack propagation can be calculated according to the measured stress drop (unloading stress path), initial stress before the stress drop, and final stress after the stress drop, and its value is equal to the trapezoidal area S_{BCEF} shown in Figure 3. The elastic strain energy density stored before crack propagation can be calculated according to the stress-strain curve and the measured unloading stress path, and its value is equal to the triangular area $S_{\Delta ACE}$ shown in Figure 3. The elastic strain energy density stored after crack propagation can be calculated using the difference between the elastic strain energy density stored before crack propagation and the dissipated energy density during crack propagation, which is equal to the triangular area $S_{\Delta ABF}$ shown in Figure 3. The radiated seismic energy density during crack propagation can be calculated according to the measured unloading stress path, initial stress before the stress drop, and final stress after the stress drop, and its value is equal to the triangular area S_{ABCD} shown in

Figure 3. The calculation method of the energy conversion and distribution in a locked segment is given above, under the condition that the stress drop path is clear. The following calculation method of radiation seismic energy is proposed for the stress drop hardly obtained accurately.

2.2. Radiated Seismic Energy. Assuming that the strain in the locked segment is distributed uniformly, the unloading modulus is approximately equal to the shear elastic modulus [28, 29], and using the above-mentioned energy density relationship, we obtain the radiated seismic energy (E_r):

$$E_r = \frac{1}{2} V \Delta\tau \Delta\epsilon = \frac{1}{2} G V \Delta\epsilon^2 = \frac{1}{2} \frac{V \Delta\tau^2}{G}, \quad (1)$$

where V and G are the locked segment's volume and shear elastic modulus, respectively, and $\Delta\tau$ and $\Delta\epsilon$ are the stress drop and corresponding shear (slip) strain increment, respectively.

According to Equation (1), the earthquake magnitude (radiated seismic energy) depends on the locked segment's volume, the shear elastic modulus, and stress drop or strain increment of the cracking event. As the volume and the shear elastic modulus of the same locked segment can be considered constants, the earthquake magnitude is only related to the stress drop or strain increment of the cracking event generated from the same locked segment. Compared with the previous studies [19, 22, 24], the earthquake magnitude, expressed by Equation (1), has a definite physical meaning and a simple form.

In general, a stronger locked segment corresponds to a larger shear elastic modulus [13]; therefore, the earthquake magnitude is positively correlated with the bearing capacity of the locked segment. Since the bearing capacity of a locked segment is much greater than that of a nonlocked segment (usually between the locked segment and soft medium), the earthquake magnitude of a locked-segment cracking event is generally much greater than that of a non-locked-segment cracking event. Therefore, when using the micro-seismic detection data to analyze the damage and fracture process of the locked segment in slope or underground engineering, the small cracking events (usually the non-locked-segment cracking events) should be excluded.

2.3. Relationships Linking Stress Drop and Shear Strain Increment or Maximum Coseismic Displacement with Earthquake Magnitude. In accordance with previous research [30–32], the relationship between earthquake magnitude (M) and the radiated seismic energy (E_r) can be expressed as

$$\lg E_r = 1.5M + C_M, \quad (2)$$

where C_M is a constant.

Substituting Equation (1) into Equation (2) yields

$$M = 1.33 \lg \Delta\tau + 0.67 \lg \frac{V}{G} - 0.67C_M - 0.2 = 1.33 \lg \Delta\tau + C_{\Delta\tau} \quad (3)$$

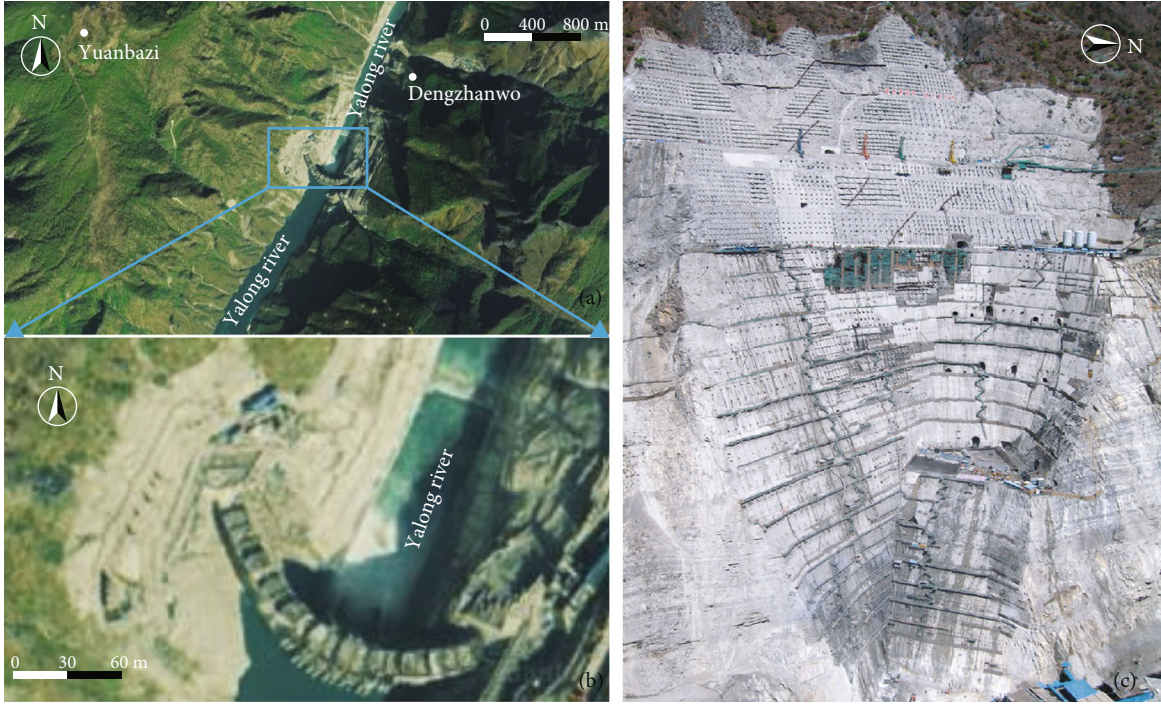


FIGURE 4: Overview pictures (captured from Google Earth) of the Jinping-1 dam site (a) and the left bank slope (b) and the photograph of the left bank slope after excavation (c) (modified from Xu et al. [36]).

TABLE 1: The source parameters of the twelve microseismic events that occurred along the key block.

Event number	Stress drop $\Delta\tau$ (Pa)	Moment magnitude M_W
1	$2.97E+04$	-3.3
2	$1.68E+05$	-2.2
3	$4.09E+05$	-1.8
4	$1.15E+05$	-2.0
5	$1.09E+05$	-2.2
6	$1.40E+05$	-1.9
7	$5.75E+05$	-1.1
8	$2.21E+05$	-1.8
9	$1.11E+05$	-2.0
10	$1.68E+05$	-2.6
11	$4.25E+05$	-1.6
12	$3.65E+05$	-1.7

or

$$M = 1.33 \lg \Delta\epsilon + 0.67 \lg GV - 0.67C_M - 0.2 = 1.33 \lg \Delta\epsilon + C_{\Delta\epsilon}, \quad (4)$$

where $C_{\Delta\tau}$ and $C_{\Delta\epsilon}$ are two constants for the cracking events of the same locked segment.

Alternatively, by substituting shear strain increment for maximum coseismic displacement (D) in Equation (4), we can get the mechanical relationship between the earthquake

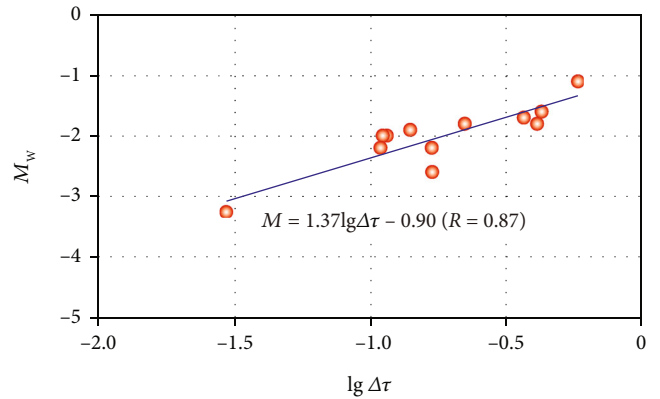


FIGURE 5: Relationship between the stress drop and the earthquake magnitude of the left bank slope of the Jinping-1 hydropower station. Red dots represent the twelve microseismic events that occurred along the locked segment.

magnitude and maximum coseismic displacement of a locked-segment cracking event as

$$M = 1.33 \lg D + C_D, \quad (5)$$

where C_D is a constant. Note that when using Equations (3)–(5) to estimate seismic source parameters of a locked-segment cracking event, the various magnitudes (such as local magnitude M_L , surface-wave magnitude M_S , and moment magnitude M_W) should be transformed into a uniform scale (usually is the moment magnitude M_W). Equations (3)–(5), though similar in the form to previous empirical relations [33, 34], are established on a firm



FIGURE 6: Overview picture of the Strathcona mine (captured from MinDat: <https://www.mindat.org/>).

TABLE 2: The source parameters of the seven mining-induced events of the Strathcona mine.

Event number	Stress drop $\Delta\tau$ (Pa)	Seismic moment M_0 (dyne-m)	Moment magnitude M_W
1	$2.1E+04$	$8.1E+19$	2.54
2	$1.4E+04$	$3.1E+19$	2.26
3	$5.0E+03$	$3.4E+18$	1.62
4	$2.0E+03$	$9.8E+17$	1.26
5	$1.0E+04$	$9.1E+18$	1.91
6	$1.2E+04$	$7.8E+19$	2.53
7	$2.2E+04$	$8.8E+19$	2.56

physical basis. In the following, we will test the reliability of the calculation method of the seismic source parameters via case studies.

3. Case Studies

3.1. Microseismic Activity on the Left Bank Slope of the Jinping-1 Hydropower Station. The Jinping-1 hydropower station is located at the sharp bend of Jinping on the Yalong River's middle reach, in Sichuan, China (Figure 4), situated within the slope transition zone from the Qinghai-Tibet Plateau to the Sichuan Basin [35]. Due to continuous excavations, 1,125 seismic events occurred at the left bank slope of the Jinping-1 hydropower station from June 2009 to May 2011 [36]. The rock mass outside the tension fissure zone and lamprophyre veins is a key block (locked segment) that controls the slope's deformation and stability [37]. Based on the measured source parameters (Table 1) of the twelve $M_W \geq -3.3$ microseismic events that occurred along the key block, a relationship between the stress drop and the earthquake magnitude (Figure 5) is fitted as

$$M = 1.37 \lg \Delta\tau - 0.90 \text{ (correlation coefficient} = 0.87). \quad (6)$$

It is seen from Figure 5 that a relatively good linear fit-

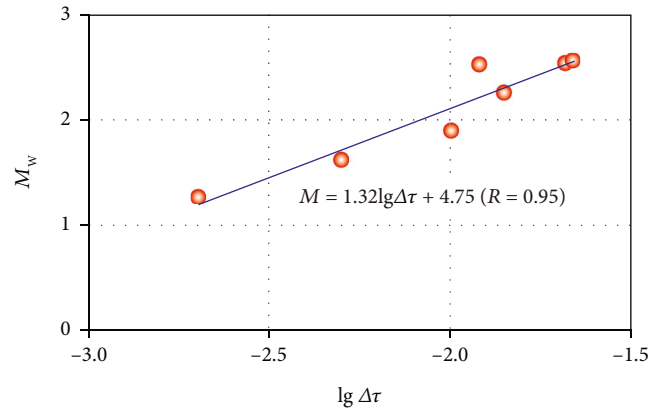


FIGURE 7: Relationship between the stress drop (in MPa) and the earthquake magnitude. Red dots represent seven events triggered by mining activity at the Strathcona mine.

ting result is obtained, where the slope (1.37) is close to the theoretical result of 1.33 in Equation (3). This case study demonstrates that the proposed calculation method of seismic source parameters of a locked-segment cracking event is reliable and could be used to estimate the seismic source parameters of a locked-segment cracking event in large rock slopes.

3.2. Microseismic Activity of the Strathcona Mine. The Strathcona mine is located in the town of Levack on the North Range of the Sudbury Basin, Canada (Figure 6). In June 1988, seven mining-induced events between depths of 640 and 825 m occurred over two days in the mine [38, 39]. Data analysis and underground observation confirmed that these events were mining-induced fault-slip earthquakes [38, 40]. Based on the source parameters (Table 2) of the seven events provided by Trifu et al. [39], we plotted the relationship between the stress drop and the earthquake magnitude (Figure 7) and derived a linear fitting:

$$M = 1.32 \lg \Delta\tau + 4.75 \text{ (correlation coefficient} = 0.95). \quad (7)$$

The slope of the good linear fitting result (1.32) is very

close to the theoretical result of 1.33 in Equation (3). This case study demonstrates that the proposed calculation method of seismic source parameters of a locked-segment cracking event is reliable, which could be used to estimate the seismic source parameters of a locked-segment cracking event in rock underground engineering.

4. Discussion

Whether the earthquake magnitude is related to the stress drop remains controversial and needs urgent clarification. Some scholars [41–45] believed that the earthquake magnitude is positively correlated with the stress drop. In contrast, others [46–49] held the opinion that there is no positive correlation between them. In addition, Shi et al. [50] and Jin et al. [51] accepted that the two parameters are positively correlated within a certain range of magnitudes. Based on Equation (1), the earthquake magnitude of a locked segment's cracking event is positively correlated with the stress drop if the cracking events (earthquakes) are generated from the same locked segment. It must be mentioned that the following points need to be noted in the statistical analysis of the relationship between the earthquake magnitude and the stress drop: (1) it should be distinguished whether earthquakes are the cracking events of the same locked segment, that is, the cracking events of the same locked segment is comparable using Equation (1); (2) small earthquakes are the main cracking events related to the nonlocked segment, so they should not be included in such statistical analysis.

5. Conclusions

Based on the energy conservation principle, a new method for the seismic source parameter estimation of the locked-segment cracking event was proposed, and then, it was verified by typical case studies of rock slope and rock underground engineering. The following conclusions were drawn:

- (1) Based on the principle of energy conversion and distribution in the locked segment's damage process, an equation for calculating the radiated seismic energy of a locked-segment cracking event (earthquake) was proposed. It can be concluded that the earthquake magnitude is only related to the stress drop or the strain increment of cracking events generated from the same locked segment
- (2) Using the equation for calculating the radiated seismic energy of a locked-segment cracking event, the mechanical relationships of the earthquake magnitude and the stress drop, and the earthquake magnitude and the shear strain increment (or maximum coseismic displacement) of a locked-segment cracking event were established
- (3) The proposed calculation method of seismic source parameters is validated using the measured data of the stress drop and the earthquake magnitude from two typical engineering cases. The results show that

this method is reliable and can be widely used in rock slope and rock underground engineering

Data Availability

The data used to support the findings of this study are included within the article.

Conflicts of Interest

The authors declare no conflict of interest.

Acknowledgments

This work was supported by the National Natural Science Foundation of China (42007243 and 42102309) and the Fundamental Research Funds for the Central Universities (N2001028).

References

- [1] K. Aki, "Asperities, barriers, characteristic earthquakes and strong motion prediction," *Journal of Geophysical Research*, vol. 89, no. B7, pp. 5867–5872, 1984.
- [2] P. Somerville, K. Irikura, R. Graves et al., "Characterizing crustal earthquake slip models for the prediction of strong ground motion," *Seismological Research Letters*, vol. 70, no. 1, pp. 59–80, 1999.
- [3] Y. Klinger, R. Michel, and G. C. P. King, "Evidence for an earthquake barrier model from $M_w \sim 7.8$ Kokoxili (Tibet) earthquake slip-distribution," *Earth and Planetary Science Letters*, vol. 242, no. 3–4, pp. 354–364, 2006.
- [4] S. Q. Qin, X. W. Xu, P. Hu, Y. Y. Wang, X. Huang, and X. H. Pan, "Brittle failure mechanism of multiple locked patches in a seismogenic fault system and exploration on a new way for earthquake prediction," *Chinese Journal of Geophysics*, vol. 53, no. 4, pp. 1001–1014, 2010.
- [5] S. Q. Qin, Y. Y. Wang, and P. Ma, "Exponential laws of critical displacement evolution for landslides and avalanches," *Chinese Journal of Rock Mechanics and Engineering*, vol. 29, no. 5, pp. 873–880, 2010.
- [6] B. C. Yang, S. Q. Qin, L. Xue, H. R. Chen, X. W. Wu, and K. Zhang, "A physical self-similarity law describing the accelerated failure behavior of rocks," *Chinese Journal of Geophysics*, vol. 60, no. 5, pp. 1746–1760, 2017.
- [7] H. R. Chen, S. Q. Qin, L. Xue, B. C. Yang, and K. Zhang, "Universal precursor seismicity pattern before locked-segment rupture and evolutionary rule for landmark earthquakes," *Geoscience Frontiers*, vol. 13, no. 3, article 101314, 2021.
- [8] D. Shaunik and M. Singh, "Bearing capacity of foundations on rock slopes intersected by non-persistent discontinuity," *International Journal of Mining Science and Technology*, vol. 30, no. 5, pp. 669–674, 2020.
- [9] X. F. Mei, N. F. Wang, G. T. Ma et al., "Deformation process and mechanism analyses of a rock slope based on long-term monitoring at the Pubugou Hydropower Station, China," *Geofluids*, vol. 2021, Article ID 6615424, 17 pages, 2021.
- [10] X. Q. Wang, F. Q. Gao, J. Z. Li, G. Y. Yuan, and L. Yang, "Realization method and influencing factors of excavation-induced slip for locked fault," *Journal of China Coal Society*, vol. 2021S2, pp. 1–9, 2021.

- [11] H. D. Liu, J. X. Chen, Z. F. Guo, D. D. Li, and Y. F. Zhang, "Experimental study on the evolution mechanism of landslide with retaining wall locked segment," *Geofluids*, vol. 2022, Article ID 7923448, 10 pages, 2022.
- [12] G. Senfaute, A. Duperret, and J. A. Lawrence, "Micro-seismic precursory cracks prior to rock-fall on coastal chalk cliffs: a case study at Mesnil-Val, Normandie, NW France," *Natural Hazards and Earth System Sciences*, vol. 9, no. 5, pp. 1625–1641, 2009.
- [13] B. C. Yang, S. Q. Qin, L. Xue, and H. R. Chen, "Energy conversion and allocation principle during the damage process of locked segment," *Journal of Northeastern University*, vol. 41, no. 7, pp. 975–981, 2020.
- [14] B. C. Yang, S. Q. Qin, L. Xue, and H. R. Chen, "The reasonable range limit of the shape parameter in the Weibull distribution for describing the brittle failure behavior of rocks," *Rock Mechanics and Rock Engineering*, vol. 54, no. 6, pp. 3359–3367, 2021.
- [15] Z. S. Chen and J. M. Kong, "A catastrophic landslide of Sept. 23, 1991 at Touzhaigou of Zhaotong, Yunnan province," *Mountain Research*, vol. 9, no. 4, pp. 265–268, 1991.
- [16] R. Q. Huang and Q. Xu, *Catastrophic Landslides in China*, Science Press, Beijing, 2008.
- [17] F. X. Jiang, Q. D. Wei, C. W. Wang et al., "Analysis of rock burst mechanism in extra-thick coal seam controlled by huge thick conglomerate and thrust fault," *Journal of China Coal Society*, vol. 39, no. 7, pp. 1191–1196, 2014.
- [18] L. S. Song, *Study on the Mechanism and Control Technology of Pressure Bump Induced by Mining near the Deep Thrust Fault*, Xi'an University of Science and Technology, China, 2014.
- [19] J. C. Savage and M. D. Wood, "The relation between apparent stress and stress drop. Bulletin of the seismological society of America," *Bulletin of the Seismological Society of America*, vol. 61, pp. 1381–1388, 1971.
- [20] M. Wyss and P. Molnar, "Efficiency, stress drop, apparent stress, effective stress, and frictional stress of Denver, Colorado, earthquakes," *Journal of Geophysical Research*, vol. 77, no. 8, pp. 1433–1438, 1972.
- [21] H. Kanamori, "The energy release in great earthquakes," *Journal of Geophysical Research*, vol. 82, no. 20, pp. 2981–2987, 1977.
- [22] M. S. Vassiliou and H. Kanamori, "The energy release in earthquakes," *Bulletin of the Seismological Society of America*, vol. 72, pp. 371–387, 1982.
- [23] R. Teisseyre and E. Majewski, *Earthquake Thermodynamics and Phase Transformations in the Earth's Interior*, Academic Press, San Diego, 2001.
- [24] L. Rivera and H. Kanamori, "Representations of the radiated energy in earthquakes," *Geophysical Journal International*, vol. 162, no. 1, pp. 148–155, 2005.
- [25] J. G. Anderson, G. P. Biasi, S. Angster, and S. G. Wesnousky, "Improved scaling relationships for seismic moment and average slip of strike-slip earthquakes incorporating fault-slip rate, fault width, and stress drop," *Bulletin of the Seismological Society of America*, vol. 111, no. 5, pp. 2379–2392, 2021.
- [26] Z. Yang, Y. X. Yu, L. Y. Meng, and Y. Y. Han, "Study on attenuation characteristics of seismic waves and seismic source parameters in the northeast margin of Qinghai-Tibet Plateau," *Seismology and Geology*, vol. 43, no. 6, pp. 1638–1656, 2021.
- [27] B. C. Yang, L. Xue, and Y. T. Duan, "Investigation into energy conversion and distribution during brittle failure of hard rock," *Bulletin of Engineering Geology and the Environment*, vol. 81, no. 3, pp. 1–12, 2022.
- [28] D. Huang, R. Q. Huang, and Y. X. Zhang, "Experimental investigations on static loading rate effects on mechanical properties and energy mechanism of coarse crystal grain marble under uniaxial compression," *Chinese Journal of Rock Mechanics and Engineering*, vol. 31, pp. 245–255, 2012.
- [29] C. Y. Liang, X. Li, S. X. Wang, S. D. Li, J. M. He, and C. F. Ma, "Experimental investigations on rate-dependent stress-strain characteristics and energy mechanism of rock under uniaxial compression," *Chinese Journal of Rock Mechanics and Engineering*, vol. 31, pp. 1830–1838, 2012.
- [30] B. Gutenberg and C. F. Richter, "Magnitude and energy of earthquakes," *Nature*, vol. 176, no. 4486, pp. 795–795, 1955.
- [31] T. C. Hanks and H. Kanamori, "A moment magnitude scale," *Journal of Geophysical Research*, vol. 84, no. B5, pp. 2348–2350, 1979.
- [32] G. L. Choy and J. L. Boatwright, "Global patterns of radiated seismic energy and apparent stress," *Journal of Geophysical Research*, vol. 100, no. B9, pp. 18205–18228, 1995.
- [33] S. J. Gibowicz, "Stress drop and aftershocks," *Bulletin of the Seismological Society of America*, vol. 63, no. 4, pp. 1433–1446, 1973.
- [34] D. L. Wells and K. J. Coppersmith, "New empirical relationships among magnitude, rupture length, rupture width, rupture area, and surface displacement," *Bulletin of the Seismological Society of America*, vol. 84, pp. 974–1002, 1994.
- [35] N. W. Xu, C. A. Tang, L. C. Li, Z. Zhou, and J. Y. Yang, "Micro-seismic monitoring and stability analysis of the left bank slope in Jinping first stage hydropower station in southwestern China," *International Journal of Rock Mechanics and Mining Sciences*, vol. 48, no. 6, pp. 950–963, 2011.
- [36] N. W. Xu, F. Dai, Z. Z. Liang, Z. Zhou, C. Sha, and C. A. Tang, "The dynamic evaluation of rock slope stability considering the effects of microseismic damage," *Rock Mechanics and Rock Engineering*, vol. 47, no. 2, pp. 621–642, 2014.
- [37] R. Q. Huang, F. Lin, and M. Yan, "Deformation mechanism and stability evaluation for the left abutment slope of Jinping I hydropower station," *Bulletin of Engineering Geology and the Environment*, vol. 69, no. 3, pp. 365–372, 2010.
- [38] T. I. Urbancic and R. P. Young, *Focal Mechanism and Source Parameter Studies of a m_N 1.8–2.7 Sequence of Mining-Induced Seismic Events Recorded during June, 1988, at the Strathcona mine, Sudbury, Canada*, Tech Trans Project Rep, Dept Geol Sci, Queen's University, Kingston, Canada, 1990.
- [39] C. I. Trifu, T. I. Urbancic, and R. P. Young, "Source parameters of mining-induced seismic events: an evaluation of homogeneous and inhomogeneous faulting models for assessing damage potential," *Pure and Applied Geophysics*, vol. 145, no. 1, pp. 3–27, 1995.
- [40] D. M. Morrison, "Rockburst research at Falconbridge's Strathcona mine, Sudbury, Canada," *Pure and Applied Geophysics*, vol. 129, no. 3–4, pp. 619–645, 1989.
- [41] K. Mayeda and W. R. Walter, "Moment, energy, stress drop, and source spectra of western United States earthquakes from regional coda envelopes," *Journal of Geophysical Research*, vol. 101, no. B5, pp. 11195–11208, 1996.
- [42] J. L. Hardebeck and E. Hauksson, "Static stress drop in the 1994 Northridge, California, aftershock sequence," *Bulletin of*

- Engineering Geology and the Environment*, vol. 87, pp. 1495–1501, 1997.
- [43] J. Mori, R. E. Abercrombie, and H. Kanamori, “Stress drops and radiated energies of aftershocks of the 1994 Northridge, California, earthquake,” *Journal of Geophysical Research*, vol. 108, no. B11, p. 2545, 2003.
- [44] Q. D. Ye, Z. F. Ding, S. W. Wang, D. X. Yu, and C. Zheng, “Determining the source parameters of the microearthquakes near the third borehole of the Wenchuan Earthquake Fault Scientific Drilling (WFSD-3) and its implications,” *Chinese Journal of Geophysics*, vol. 60, no. 7, pp. 2716–2732, 2017.
- [45] M. Qin, D. N. Li, H. Y. Zhang, Y. Gao, and J. Z. Jiang, “Research on inelastic attenuation Q-value, site response and source parameters in Yunnan Yingjiang Region,” *Journal of Seismological Research*, vol. 41, no. 4, pp. 583–594, 2018.
- [46] H. Kanamori and D. L. Anderson, “Theoretical basis of some empirical relations in seismology,” *Bulletin of Engineering Geology and the Environment*, vol. 65, pp. 1073–1095, 1975.
- [47] R. E. Abercrombie, “Earthquake source scaling relationships from -1 to 5ML using seismograms recorded at 2.5-km depth,” *Journal of Geophysical Research*, vol. 100, no. B12, pp. 24015–24036, 1995.
- [48] B. P. Allmann and P. M. Shearer, “Global variations of stress drop for moderate to large earthquakes,” *Journal of Geophysical Research*, vol. 114, no. B1, article B01310, 2009.
- [49] J. M. Liu, Q. Wang, J. Liu et al., “Research on stress drops and the focal mechanisms of the Xinyuan- Hejing $M_L 6.8$ earthquake sequences,” *Earthquake Research in China*, vol. 32, no. 1, pp. 28–39, 2016.
- [50] J. Shi, W. Kim, and P. G. Richards, “The corner frequencies and stress drops of intraplate earthquakes in the northeastern United States,” *Bulletin of Engineering Geology and the Environment*, vol. 88, no. 2, pp. 531–542, 1998.
- [51] A. Jin, C. A. Moya, and M. Ando, “Simultaneous determination of site responses and source parameters of small earthquakes along the Atotsugawa Fault zone, central Japan,” *Bulletin of Engineering Geology and the Environment*, vol. 90, pp. 1430–1445, 2000.

Research Article

Analysis of Settlement Induced by Shield Construction of the Metro Passing under Existing Buildings Based on the Finite Difference Method

Rui Wang¹, Bin Zhang,² and You Wang¹

¹School of Civil Engineering, Central South University, 410075 Changsha, China

²China Railway (Shanghai) Investment Group Co., Ltd., 200126 Shanghai, China

Correspondence should be addressed to You Wang; ywang1920@csu.edu.cn

Received 4 March 2022; Revised 15 April 2022; Accepted 5 May 2022; Published 28 May 2022

Academic Editor: Yang Yu

Copyright © 2022 Rui Wang et al. This is an open access article distributed under the Creative Commons Attribution License, which permits unrestricted use, distribution, and reproduction in any medium, provided the original work is properly cited.

A frequent problem when constructing metro tunnels is the uneven settlement of adjacent buildings, which results in huge economic losses. Due to shields causing the settlement of adjacent buildings, this study took the Nantong Metro Line 1 as the research object. The metro runs from the East Huancheng Road Station to the Nantong Intermediate People's Court Station and passes under the old residential area of the Community Sendadi-Huayuan building. Based on the settlement monitoring data, this study analyzed the impact of tunnel shield construction on the foundation settlement of adjacent buildings. The computational analysis of the shield tunnel was performed by numerical simulation, taking into account the upper building load and the construction disturbance to the surrounding rock. Afterward, the study summarized the law behind the settlement. The results show that when the boring machine was tunneling through sandy soil and silt rich in water, its head was prone to twisting due to soil disturbance and the dissipation of pore water, causing instability in the excavation process and eventual ground settlement. In the sandy strata, the relationship between foundation settlement caused by shield construction and time can be approximated as an exponential function in a certain area. The vibrations from shield excavation caused the foundations to vibrate for a short period of time. Therefore, the average settlement of buildings directly above the underpass reached 7 mm/d. Likewise, the tunneling shield caused a 1.5 mm settlement before passing under the building. It caused a peak settlement of 4.0 and 5.1 mm during and after passing under the buildings, respectively. The width of the settlement troughs of approximately 7D formed after the tunnel was excavated. Shield excavation placed the soil at the top of the excavation face in a state of tensile stress, causing tensile and shear damage to the soil and forming a local plastic zone.

1. Introduction

The tunnel boring machine is widely used in metro construction because it is safe and quick. More than half of the planned metro miles in China are constructed with this method [1, 2]. Most metros in China pass under busy areas. New metros are usually constrained by the complex surrounding environment and inevitably pass under existing metro tunnels, bridges, underground pipelines, and buildings. Therefore, shield construction must not only meet safety requirements but also ensure the stability of the surrounding buildings.

The impact of metro construction on buildings is mainly manifested in ground settlement caused by strata disturbance during shield excavation [3–5]. Most of the engineering practice shows that tunnel excavation disturbs the soil and surrounding rocks and disrupts the original equilibrium. Only after completing the tube lining, the surrounding strata gradually regain equilibrium [6–8]. At the end of the 20th century, González and Sagasetta and Yun et al. [9, 10] conducted research on the protection and control of adjacent buildings above shield tunnels and offered recommendations for practical control of buildings in all phases of tunnel construction. Afterward, Wang et al. [11] discussed the

theoretical method of applying the law of spatial and temporal effects of settlement to reflect surface subsidence below the Wuhan Metro. Based on the method of estimating ground settlement caused by mining, Peck [12, 13] concluded that the shape of ground settlement caused by tunnel construction in the direction perpendicular to the tunnel axis was similar to the normal distribution curve in probability theory. Peck's formula for calculating ground settlement is an essential theoretical basis for controlling ground settlement caused by tunnel excavation. In 1987, Sagaseta [14] also proposed a formula for three-dimensional ground settlement caused by tunnel excavation based on the assumption that the strata and isotropy are incompressible. These early theories based on engineering practice and theoretical analysis summarized the ground settlement pattern caused by tunnel construction and provided a rich theoretical framework for future studies to predict the structural response of surrounding buildings influenced by tunneling shield construction.

With the development of computer technology, numerical simulation has become a common means of geotechnical engineering research and has been used in shield tunnel research [15–17]. Liu et al. [18] investigated new tunnels passing under existing ones in conjunction with the Winkler's foundation model, considering the additional loads caused by tunnel excavation and the weakening effect of the foundation. Likewise, they investigated the loads and deformations of existing tunnels. Kan and Li and Zhang [19, 20] analyzed the settlement pattern of buildings produced by tunnel construction using the finite difference method (FDM). Godinho et al. [21–23] applied finite element calculation procedures combined with neural networks and other methods to investigate the environmental changes caused by tunnel excavation. In addition, they analyzed the changes and proposed corresponding prediction tools. At present, numerous studies have obtained a myriad of results in the research of shield tunnel construction under buildings. However, most of them were focused on new buildings with short time in use, strong integrity, and stability. Studies on shield tunnels passing under old residential areas are relatively rare because the buildings are used for a long time, old, and more sensitive to foundation deformation.

This study took the Nantong Metro Line 1 as the research object because it passes under the old residential area in the *Community Sendadi-Huayuan*. It conducted on-site settlement monitoring and numerical simulation to find out the settlement law of building foundations above the shield. In addition, it analyzed the distribution of pore pressure in sandy soil with high water content and the distribution characteristics of soil displacement and plastic zones.

2. Project Overview

Nantong Metro Line 1 is 39.46 km long, and it will have 28 underground stations. The study section is about 1.504 km long at a depth from 16.5 to 28.0 m. It was constructed along the road using the shield method; however, it passes under some old residential areas.

2.1. Engineering Geology. Nantong is located in the alluvial plain of the lower reaches of the Yangtze River in China. Within this area, the terrain is flat with elevation ranging from 4.0 to 6.0 m. *Nantong Metro Line 1* crosses two types of landforms, namely, the alluvial-marine reticulated and neo-deltaic plains. In particular, the area from *the East Huancheng Road* to *the Intermediate People's Court Station* belongs to the alluvial-marine reticulated plain. The geological profile of the study area is schematically shown in Figure 1. According to the survey results of the site, the Quaternary strata are over 200 m thick, and the soft soil layer is thick, as well. In this study, the soils were divided into five soil units from (1) to (5) and from top to bottom within the survey depth. In addition, the study included three subunits with more complex soil types and different properties. A water system with high water content in the thick layer of soft soil flows along the metro line. This layer of soft soil mainly constitutes powder clay, powder soil, powder fine sand, fine sand, and medium coarse sand. Among these, the powder fine sand is a well permeable stratum. The tunnel in this stratum mainly passes through sandy silt with silty sand, silty sand, sandy silt with silty clay, etc. Additionally, the upper and lower layers of soil also include sandy silt, silty clay with silty soil, and silty sand with silty soil.

2.2. Shield Construction Parameters. The study site is located in Chongchuan District in Nantong City, China. In this study, the Earth Pressure Balance (EPB) shield was used based on shield construction cases in the surrounding areas of Nantong. EPB construction technology is commonly used for excavating layers of soft soil. The constructed lines in Shanghai, Suzhou, Wuxi, Changzhou, and other areas used the EPB shield. Moreover, the tunnels in the mentioned areas pass through powder soil, while the ones in Nantong pass through powder and sandy soils. The speed of shield excavation was 40–45 mm/min (about eight rings per day). When an EPB shield was used, the soil warehouse pressure was continuously adjusted to a reasonable value in the first 100 m of the tunnel. The fluctuation of soil warehouse pressure was also controlled, amounting to less than 0.01 MPa during construction. The shield machine used in the study section was a China Railway Construction EPB shield machine (ZTE6410) with an excavation diameter of 6440 mm and a panel box spoke cutter. The main body of the shield is 8.5 m long, while the main body together with the supporting carriage in the back is 84 m long. The shield has a maximum rated torque of 5700 kN·m, a breakaway torque of 6300 kN·m, and a rated thrust of 4000 kN. During the construction of the study section, the work face pressure was between 260 and 270 Pa and the push force was between 14,000 and 16,000 kN, with a torque of less than 2500 kN·m. Furthermore, the cutter speed was between 1.0 and 1.2 rpm, the synchronous grouting pressure was between 400 and 500 Pa, and the grouting volume was greater than 5.5 m³ per ring. The amount of grease injected into each ring on the shield's end was greater than 35 kg. The longitudinal line of the shield was at 5‰ uphill. The width of the lining was 1200 mm, with an outer and inner diameter of 6200 and 5500 mm, respectively. For each advance of the shield, the

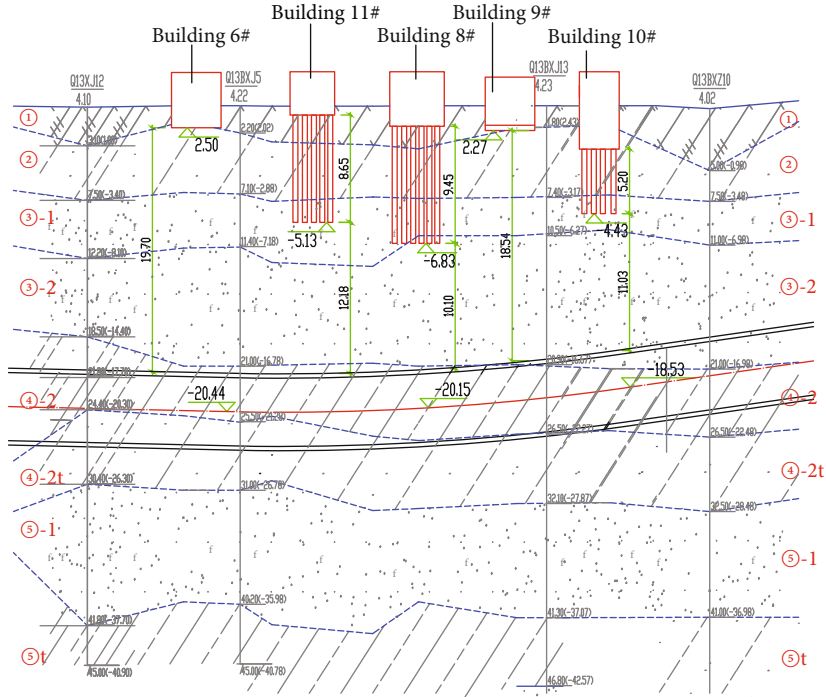


FIGURE 1: Geological profile of the study area.

unearted quantity was 39.2 m^3 in the left and 39.1 m^3 in the right line.

3. Settlement Observation and Analysis of Building Foundations

3.1. Setting the Points for Monitoring the Foundation Settlement. The line between the East Huancheng Road station and the Intermediate Court station passes below the buildings #3 to #7 and buildings #11 and #12 of the Sendadi Garden District. In the district, the residential buildings are 6-story high and old. The bottom part of the buildings' foundation was about 11.3 m away from the top of the tunnel. The tunnel construction caused loss and disturbance of soil, which subsequently induced ground settlement. Then, the settlement trough that formed inevitably caused the adjacent buildings to tilt. Based on the construction drawings and the *Technical Code for Urban Rail Transit Engineering Monitoring* (GB50911-2013) [24], the settlement and the tilt values of the houses along both sides of the line within 50 m had to be monitored during the excavation of the tunnel.

In particular, the average settlement of the foundation and the value of the settlement difference were monitored during excavation. The monitoring points were arranged so that buildings within 50 m from the tunnel centerline had them at the corners and on load-bearing structures. A total of 6 monitoring points, No. A to F, were set for each building. The arrangement of monitoring points is shown in Figure 2. Furthermore, the points were monitored 2 times a day, when the work face of the shield tunnel was located 20 m before and 50 m after passing the building, and once

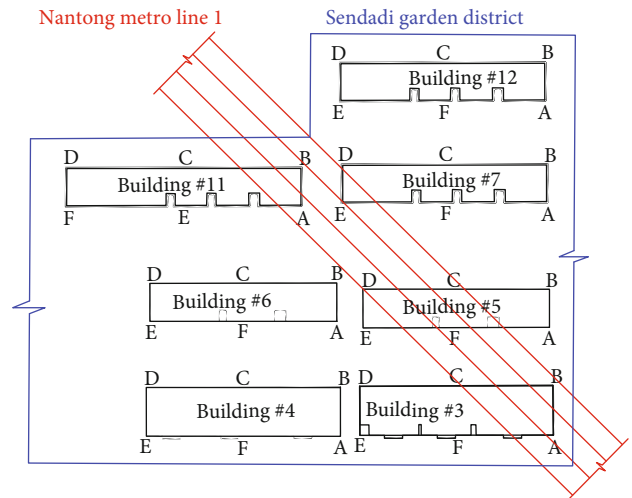


FIGURE 2: Layout of ground settlement monitoring points in the study area.

a week, when the heading face was located 50 m away after passing the building. The measurement accuracy was $\pm 0.5\text{ mm}$. Building monitoring control indicators should include the average settlement (20 mm), the average settlement rate ($2\text{ mm}\cdot\text{d}^{-1}$), and the maximum settlement rate ($3\text{ mm}\cdot\text{d}^{-1}$).

3.2. Results of Foundation Settlement Monitoring. Since the tunnel construction began, a total of seven residential buildings (#3 to #7 and #11 to #12) in the old residential area of Sendadi Garden District have been monitored for settlement for 3 months, that is, from April to July 2020. The tunnel passed under buildings #11, #7, #5, and #3 in sequence on

May 4, 2020. The time curve of the settlements was drawn according to the monitoring results in Figure 3.

After analyzing the monitoring data, it was found that the maximum settlement of the seven buildings occurred when the tunneling shield passed the first building (#11). The settlement value reached a maximum of 8.1 mm. When the monitoring was completed, it was found that the settlement of buildings #11, #12, #7, #6, #5, #4, and #3 were 8.42, 7.42, 4.87, 2.79, 7.39, 3.87, and 1.86 mm, respectively. The tilt of each building was calculated based on its geometry, the settlement differences between buildings, and the setup of the monitoring points. The tilt of buildings #11, #12, #7, #6, #5, #4, and #3 was 0.012%, 12 0.026%, 0.017%, 0.010%, 0.026%, 0.013%, and 0.006%, respectively. Moreover, the inclination of each building was less than 0.3% [24], and it was directed towards the metro line. These results indicate that the uneven settlement of the foundations was caused by the excavation of metro tunnel.

The monitoring curves in Figure 3 show that the effect of the shield construction on foundation settlement in the sandy strata can be approximated by fitting an exponential function over a specific period of time. The ground settlement caused by soil disturbance and the loss of strata caused by excavation gradually stabilized as the shield machine moved away from the monitoring points, and its increment gradually decreased until convergence. The average settlement curve is shown in Figure 4.

Furthermore, the average settlement value increased with time, as shown in Figure 4. Building #11 was the first to settle and stabilize, while buildings #3 and #4 began to settle at the end of June. This happened because the tunneling shield passed under building #11 first and #3 and #4 last. Additionally, no significant settlement occurred in the foundation of building #4. By the end of monitoring, the average settlement value of building #5 reached 7.09 mm. Figure 5 shows the average settlement rate of each building. According to Figure 5, the settlement rate of most foundations during shield tunneling was lower than the allowable value ($2 \text{ mm}\cdot\text{d}^{-1}$). However, the instantaneous settlement rate of some monitoring points exceeded the maximum control value ($3 \text{ mm}\cdot\text{d}^{-1}$), reaching $7 \text{ mm}\cdot\text{d}^{-1}$ at buildings #5 and #3. This indicates that the vibration from tunneling caused the foundations to vibrate for a short period, as well.

3.3. Analysis of Foundation Settlement. Shield construction causes ground settlement and disrupts the soil stress field around the surface of the excavation. According to shield machine and ground settlement monitoring data, it was found that the instability of the head was one of the causes of excessive soil disturbance around the tunnel during excavation. The unbalanced pressure distribution at the surface of the excavation was causing the instability of the head. Likewise, the pore water in the soil affected the pressure distribution on the surface of the excavation. Figure 6 shows the types of relative positions of the tunnels in regard to the buildings and the distribution of strata underneath the buildings. The shield machine mainly tunneled through sandy soil and silt mixing sand. The silt mixing sand layer contains diving, while sandy silt mixed with silty clay

contains pressurized water. When the shield tunnel encountered silty clay and sandy soil during construction, the pore water in the soil at the front of the shield machine head dissipated quickly. Its shear strength and the frictional resistance on the side of the shield sharply rose, so that the torque of the cutting-head and the total thrust immediately reached their limit, which eventually lead to the torsional instability of the shield head. In addition, quicksand and other phenomena quickly formed in silty clay and sandy soil under hydrodynamic force, which was also one of the reasons for the instability of the excavation. The attitude of the shield machine was adjusted before passing under buildings. Likewise, the shield machine was controlled to advance slowly when passing under buildings. The balance of the excavation face was strictly ensured, and the lining and grouting were reinforced in time after the shield passed under the buildings. Therefore, no significant settlement occurred in the neighboring buildings, and the differential settlement value did not exceed the limit.

Since the powder and sand soil hold pore water pressure and the burial depth of the head was between 2 and 5 m, the pressure of the soil chamber was adjusted to balance the pressure at the excavation face during tunneling. In addition, quality grouting was ensured by maintaining stable grouting pressure. The initial setting time of the slurry was also strictly controlled in combination with test section monitoring to avoid water seepage, sand gushing, and soil gushing from the rear of the shield machine. When the shield is excavated to the soft plastic state stratum of silty clay with silty soil, the soft plastic stratum of silty clay and soil has high water content, high compressibility, low strength, and an obvious thixotropic and rheological deformation under dynamic action. It is easy to reduce the strength of this soil, which increases the displacement of the stratum.

As the shield advanced towards the interface of soft and hard soil, the difference in the resistance between the layers of soil caused the soft soil layer to lose too much soil. As a result, the shield lost control in the vertical direction and the head of the shield deviated in the line direction. The instability of the ground also induces uneven settlement of the buildings.

In summary, the loss of strata, disturbance of the surrounding rock, and remodeling or reconsolidation of shear-damaged soils were the main causes of ground and foundation settlement. The tunnel between East Huancheng Road and the Intermediate People's Court station is mainly located in the sandy silt mixed with silty clay, which is locally interspersed in silty clay and situated in the silty clay mixed with silty soil. The ground settlement was relatively large when the shield machine passed through the soft and hard soils. The line was reinforced by grouting during shield construction to fill the voids between the lining and the surrounding rock, improve grouting quality, effectively control the ground settlement, and reduce the impact of shield construction on neighboring buildings.

4. Numerical Simulation of Shield Construction

Combining the investigation and settlement monitoring data, numerical simulation was conducted using *FLAC*^{3D}

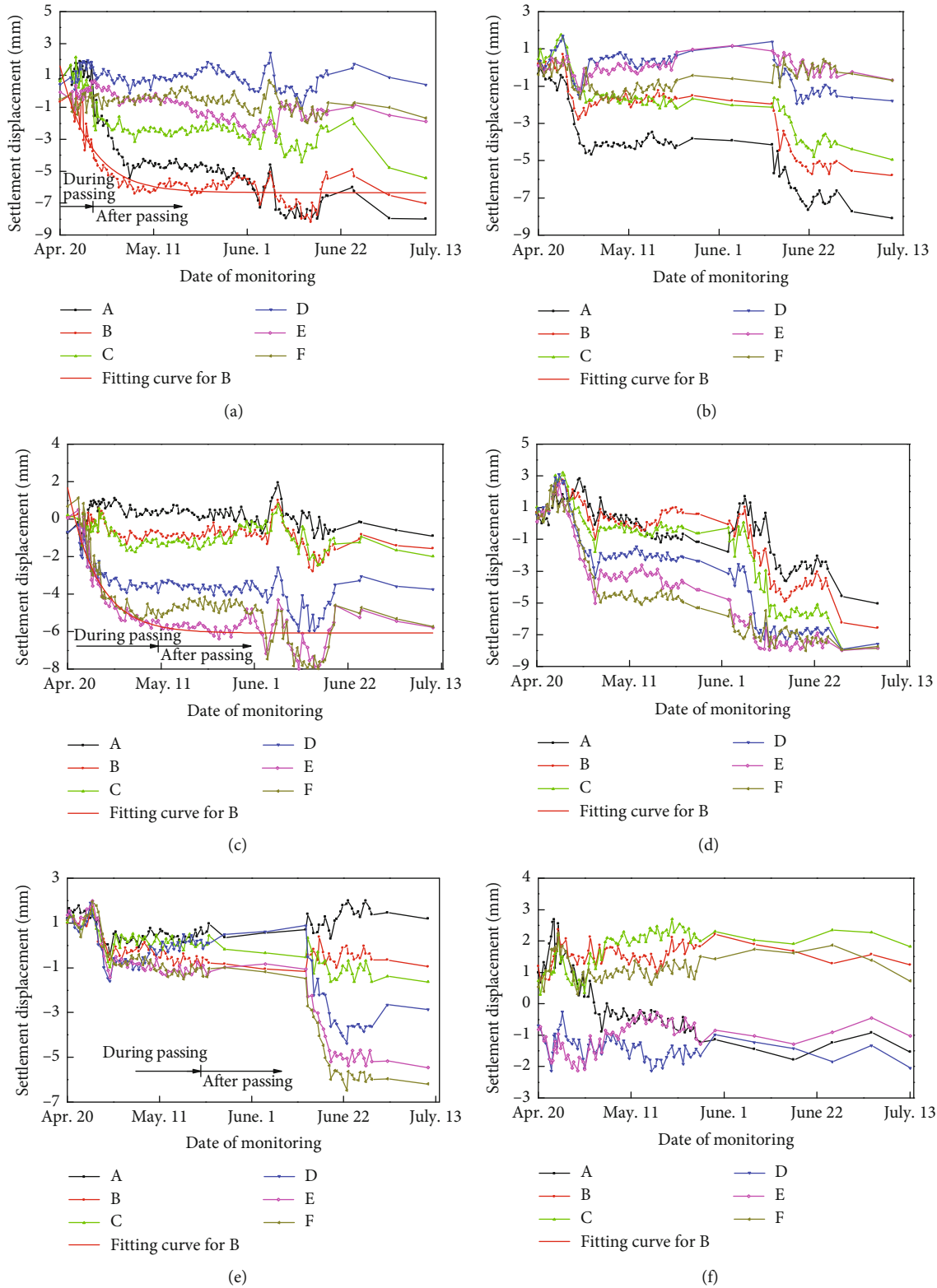


FIGURE 3: Continued.

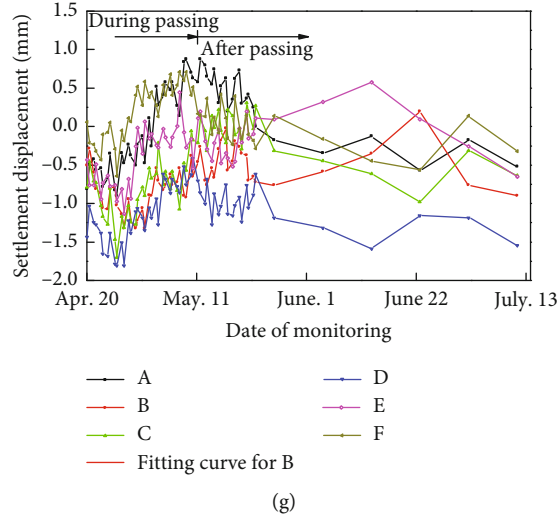


FIGURE 3: Settlement of the buildings of Sendadi Garden District: (a) building #11, (b) building #12, (c) building #7, (d) building #6, (e) building #5, (f) building #4, and (g) building #3.

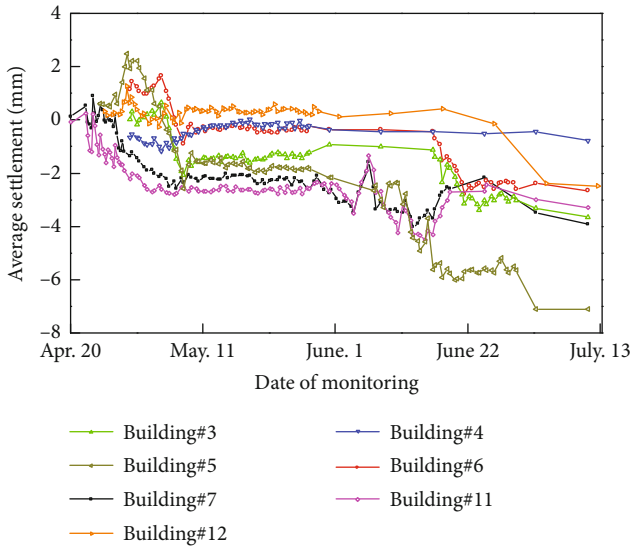


FIGURE 4: Average settlement of foundation of each building.

for the foundation settlement caused by the shield machine passing under buildings #3 to #7 and buildings #11 and #12. The distribution and development pattern of foundation subsidence was summarized to analyze the settlement effect of the tunnel construction on the adjacent foundations. In addition, the settlement laws of the ground surface were summarized and the plastic zones in each stratum analyzed to clarify the degree of disturbance shield tunneling caused and the influence it had on the surrounding environment.

4.1. Model Building and Parameter Determination. The scope of the calculation model was determined to be within the area of the two-lane tunnel passing through residential buildings #3 to #7 and buildings #11 to #12 in the residential area of the Sendadi Garden District. Affected by the construction of tunneling shield, the range of settlement troughs

was about 30 m on both sides of the tunnel center [19]. The average spacing between the centers of the two metro tunnels was 18.44 m when crossing the district. This study also considered the distribution width of the foundation of each building within the affected areas. The model was 196 m wide, 50 m high, and 174 m deep in the longitudinal direction. The tunnel diameter was 6.44 m, while the lining pipes on each section were 1 m long and 0.35 m thick. The height of the model depended on the influence of the excavation on the surrounding rock. A small model can produce the Saint-Venant's effect, while a large model can lead to too much mesh and make balancing difficult. In this study, the grid points of both the soil and the lining around the tunnel were encrypted when dividing the grid. The calculation model is shown in Figure 7.

The "excavation part" of the model was dug before the excavation. The material parameters of the corresponding soil layers were selected according to their location. Furthermore, the excavation of the model was realized by the intrinsic null model, while the soil layers were described by the Mohr-Coulomb model. The stratigraphy of the study area indicated that the soil contains clayey, chalk, and sand. The Mohr-Coulomb model is commonly used to describe shear damage in soils. In this study, the envelope of the model corresponded to the Mohr-Coulomb strength criterion. When the Mohr-Coulomb model is based on principal stresses σ_1 , σ_2 , and σ_3 and out-of-plane stresses σ_{zz} and used in FLAC^{3D}, the principal stresses and their directions can be obtained from the stress tensor and its components. The principal strain increment corresponding to the principal stress consists of an elastic and a plastic part:

$$\Delta e_i = \Delta e_i^e + e_i^p, i = 1, 3, \quad (1)$$

where Δe_i^e and Δe_i^p represent the strain increments in the elastic and plastic parts, respectively.

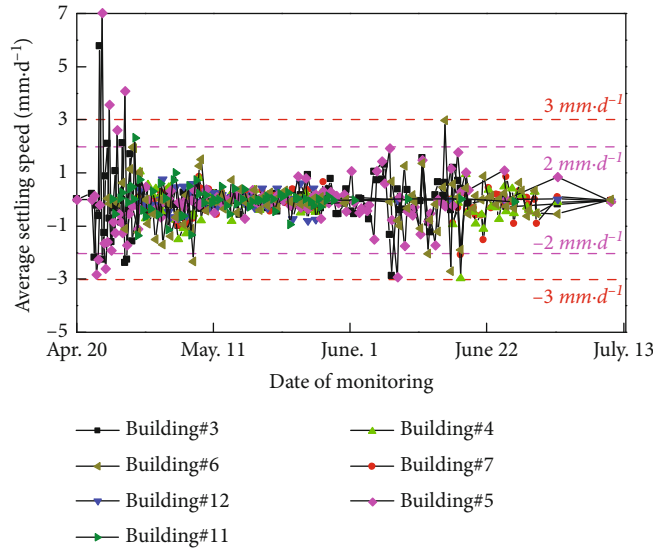


FIGURE 5: Average settlement rate of the foundation.

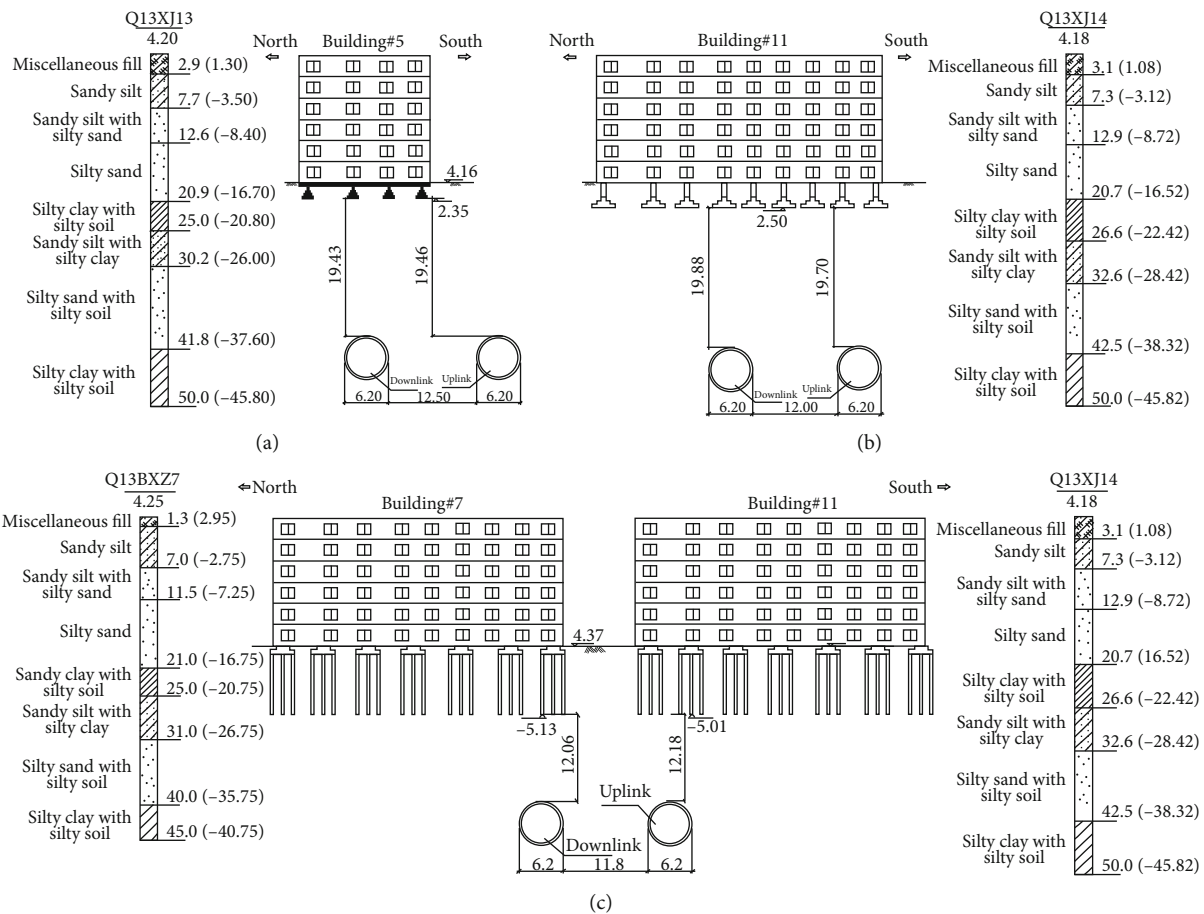


FIGURE 6: The type of tunnel underpass in the Sendadi Garden District (unit: m): (a) tunnel underneath #5, (b) tunnel underneath #6, and (c) tunnels under buildings #7 and #11.

The Mohr-Coulomb model is not able to account for the change effects in midmajor stresses when describing the mechanical behavior of sandy and chalky soils. In contrast,

the spatially mobilized plane (SMP) criterion better reflects the yielding behavior of soft soils. It also considers midprincipal stresses in a large and small principal stress space and

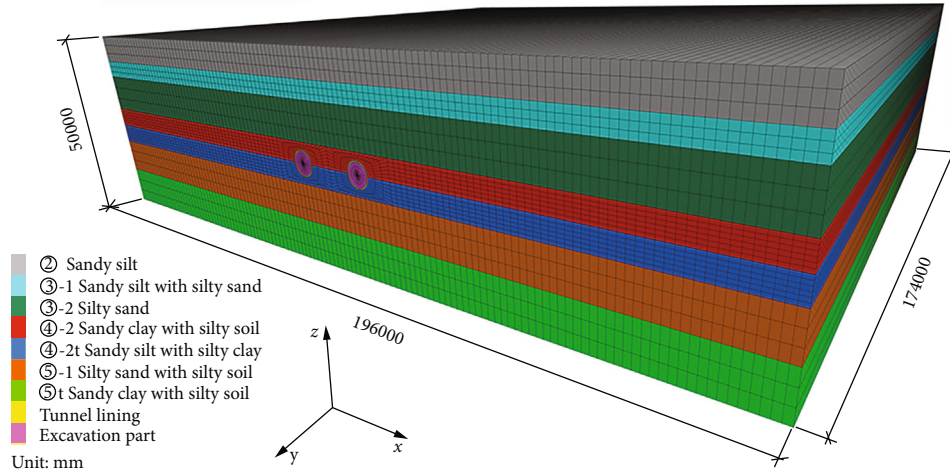


FIGURE 7: Computational model for shield tunneling (unit: mm).

constructs a 3D damage surface. However, this can only be achieved in $FLAC^{3D}$ by means of a customized constitutive model in secondary development.

Moreover, the tunnel lining was generated by the elastic model. The strength of the concrete was C50, and the elasticity modulus was 34.5 GPa. The properties of each soil layer and the linings are shown in Table 1. The values of each parameter were taken from the geotechnical investigation report of the study area. In addition, the ground surface of the residential area above the metro line was simplified to a horizontal surface.

When it comes to sandy soils with high water content and permeability, fluid-solid coupling in the soil must be considered when analyzing the impact of the excavation on the environment [25]. Tunnel excavation causes loss of volume and dissipation of pore water pressure, resulting in the deformation of the soil layer and ultimately affecting the permeability and mechanical properties of the soil. When the $FLAC^{3D}$ software was used, the seepage module was closed, and only mechanical calculations were conducted. When the mechanical calculations reached balance or a set number of calculation steps, the seepage module was opened and the fluid-solid coupling calculated. The fluid flow model was set with its head buried 3 m deep based on the soil-water characteristic curve and the results of the undrained triaxial test. The effective stresses of the soil around the tunnel changed as the seepage field changed due to excavation [26]. This paper selected the isotropic fluid model “f_liso” and set the segmented lining to a nonpermeable group during the calculation.

4.1.1. Boundary Conditions and Calculation Settings. The model sets normal velocity constraints on all surfaces, except the ground one, which was designated as a free boundary. The crustal stress had been balanced before the excavation was calculated. Because the tunnel was buried very deep, only the self-weight stress was considered and not the structural one. In reference to the *Load Code for Building Structures* (GB50009-2012) [27] and other related studies [20], the load of each building on the ground was simplified to a

vertical uniform load with a value of 105 kPa. After balancing the ground stress, the displacement is also zeroed. In addition, the ground settlement caused by the building load and tunneling was recalculated. During model calculation, every 3 m of the excavation site was lined and balanced once. The whole model was completed after 58 calculations of the excavation.

The numerical simulations considered the loss of strata caused by shield construction, simulated the settlement of building and the soil rebalancing after supporting the lining. Simulating the excavation-lining process in the computer was achieved by transforming the constitutive model of solid units from the Mohr-Coulomb to the null and then to the elastic model.

4.2. Analysis of Foundation Settlement

4.2.1. Pore Pressure and Distribution of Vertical Displacement. Figure 8 shows the contour of pore pressure when tunnel excavation reached 87 m. Each excavation of the tunnel disturbed the balance of pore pressure in the surrounding soil. As a result, water leaked at the excavation face and seeped into the unsupported areas of the tunnel, ultimately causing more displacement. Figure 8(a) shows the pore pressure contour when the segmental lining was not constructed yet. Due to the excavation, water seeped from the surrounding soil around the inner wall of the tunnel into the tunnel. Therefore, pore pressure in the inner wall of the tunnel was zero. Figure 8(b) shows that pore pressure in the soil recovered and the diving surface restabilized after the completion of the segmental lining. Furthermore, Figure 8(c) shows the longitudinal section of the model. According to the seepage vector in the soil, the water from the soil seeped into the working face, resulting in head difference. Pore pressure at the upper part of the working face was 50 kPa, while that at the lower part was 150 kPa.

Based on the simulation of Nantong Metro Line 1, the vertical displacement contour of the surface of the tunnel at different stages of tunnel construction is shown in Figures 9–10.

TABLE 1: The properties of each stratigraphic and tunnel lining.

Group		Thickness (m)	Weight (kN/m ³)	Shear (MPa)	Bulk (MPa)	Cohesion (kPa)	Friction (°)	Porosity	Permeability coefficient (cm/s)
Sandy silt		6.99	18.2	15.846	34.333	7.7	23.0	0.45	2.4e-5
Sandy silt with silty sand		4.48	18.5	22.596	48.958	4.7	27.8	0.37	9.8e-3
Silty sand		9.52	18.6	25.115	54.417	4.5	28.8	0.37	9.8e-3
Silty clay with silty soil		6.00	18.2	16.615	36.000	6.5	19.2	0.41	1.4e-5
Sandy silty with silty clay		4.00	18.0	11.827	25.625	8.1	18.4	0.41	9.1e-7
Silty sand with silty soil		9.00	18.6	23.115	50.083	3.5	27.3	0.4	3.6e-4
Silty clay with silty soil		10.01	18.0	11.827	25.625	8.1	18.4	0.4	3.6e-6
Tunnel lining	C50	0.35	25.0	14781.5	17267.3	—	—	—	—

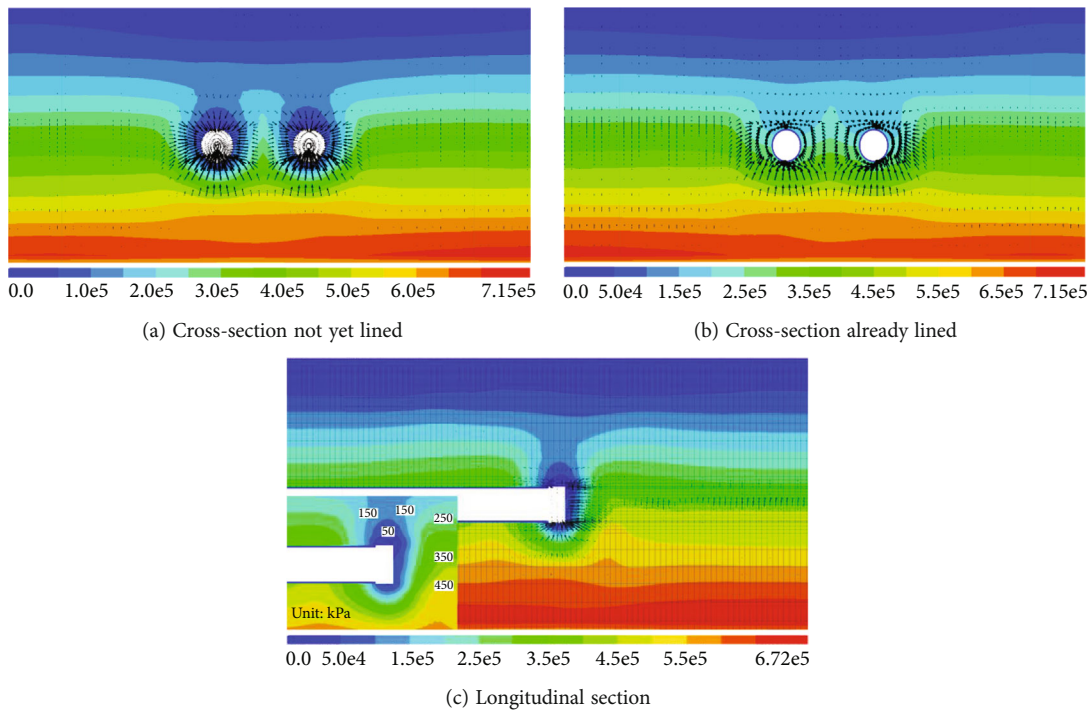


FIGURE 8: Contours of pore pressure distribution when excavated to 87 m (unit: Pa).

Figure 9 shows the trace of the ground settlement caused by excavation. The maximum settlement value in the tunnel occurred at the top of the excavation face at different stages as zero pore pressure did in the seepage field. According to the numerical simulation results, the ground settlement caused by the shield machine before passing under several buildings was about 1.5 mm when 30 m of the tunnel was excavated. However, the value of ground settlement when passing under the buildings was 4.0 mm after excavating

87 m. After passing under the buildings and excavating 174 m, the value was 5.1 mm. Figure 8 shows the settlement trough and displacement of the upper soil layer after tunneling. The impact area of lateral ground settlement was about 24.5 m on both sides of the tunnel.

Figure 11 shows the distribution of plastic zones in different excavation stages of the tunnel. Due to the disturbance of the original soil layer and the reduction of pore pressure at the top of the excavation face, the soil at the top of the

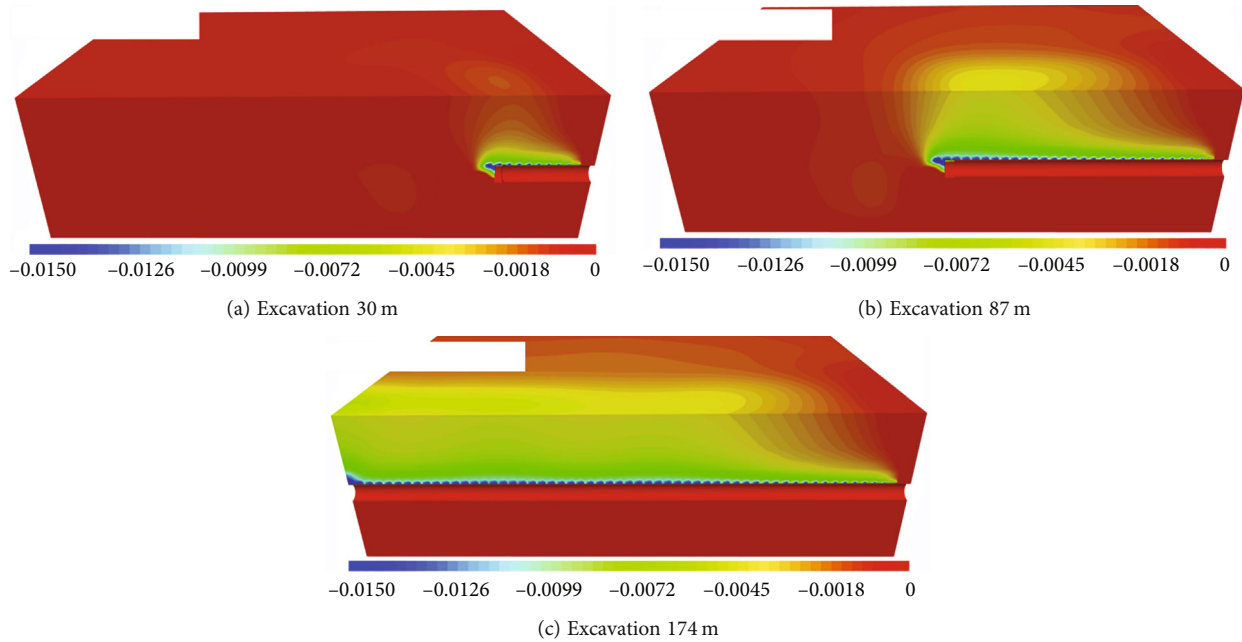


FIGURE 9: Tunnel vertical displacement contour at different shield tunneling stages (unit: m).

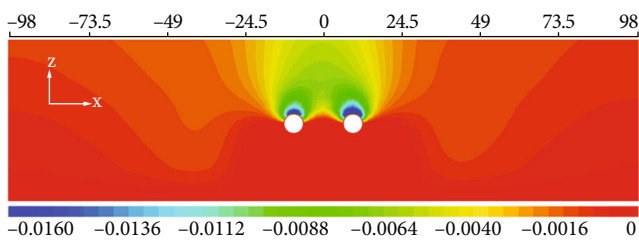


FIGURE 10: Contour of vertical displacement of stratigraphic cross-section (unit: m).

excavation face and the top of the tunnel was susceptible to subsidence, causing tensile stress in this part of the soil. As a result, tensile-shear damage occurred, and local plastic zones formed in the soil. In contrast, the bottom of the excavation face maintained high pore pressure. According to the effective stress principle, the stress in this part of the soil was relatively low and no plastic zones formed. Due to timely lining after the excavation, the plastic zone around the tunnel regained equilibrium after tensile-shear damage. It transformed into a shear strain zone after the completion of the lining. When the tunnel excavation was completed and the lining finished, the tensile and shear stress zones disappeared and only a layer of the shear strain zone remained. The lining support restabilized the soil around the tunnel while also converging the ground settlement.

4.2.2. Settlement Analysis. The dissipation of pore water pressure and the loss of volume in the soil layer eventually caused ground settlement, after which a settlement trough formed. Figure 12 shows the settlement trough curve based on the site monitoring data of the south side of building #4. The settlement curve of this section shows that the width

of the settlement trough was about $7D$ on both sides of the metro (D is the diameter of the tunnel excavation). The numerical simulation results showed that the maximum settlement of this section was 5.3 mm, while the settlement of the same section during site monitoring was 6.7 mm. However, the settlement distribution of both was consistent, which indicates that the numerical simulation results were valid. The reason for the errors between the two can be attributed to the fact that the values of the material parameters and the intrinsic model were difficult to fully restore. Likewise, the ground settlement was affected by a variety of complex factors, but only the excavation of the tunnel was considered in the numerical simulation process, so the calculated results were smaller than the field monitoring data.

Before calculating the model excavation, monitoring points were set up at the four corners and the center of the long side of buildings #3 to #7 and buildings #11 and #12 to monitor the settlement of their foundations. The location of each measurement point is shown in Figure 13. After the excavation, the upper soil layer settled downward during the excavation. However, the layer gradually stabilized and regained equilibrium after lining the shield tunnel. The monitoring curve of the foundation settlement of the seven main residential buildings in the Sendadi Garden District is shown in Figure 14.

The metro line slant passed under the residential neighborhood. The tunnels passed first underneath buildings #11 and #12. Building #7 was juxtaposed with building #11. Because building #12 was adjacent to tunnel and the tunnel did not pass directly under its foundation, the settlement of its foundation was small, and it recovered after tunnel lining was finished. Similarly, building #4 was less affected by the construction because the tunnel did not pass under it directly. According to Figure 14(a), points A and B of

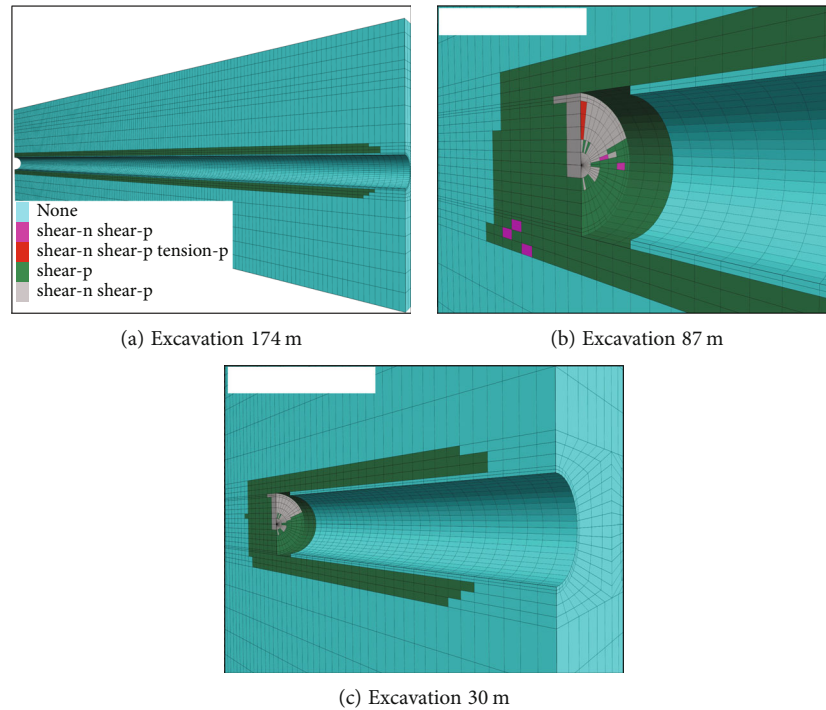


FIGURE 11: The plastic zone of tunnel surrounding rock in different stages.

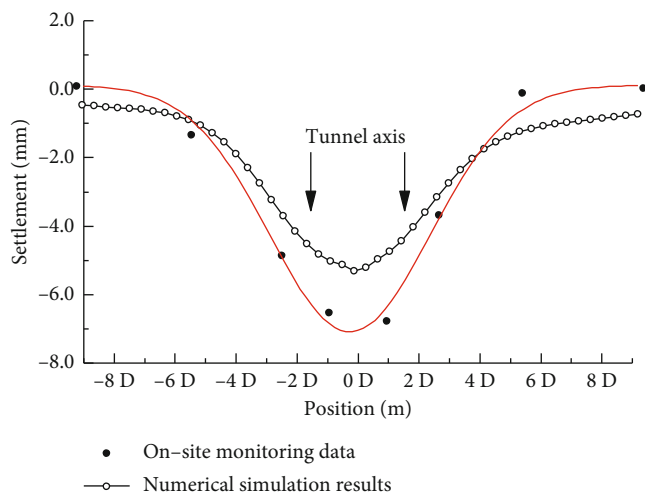


FIGURE 12: Surface settlement trough.

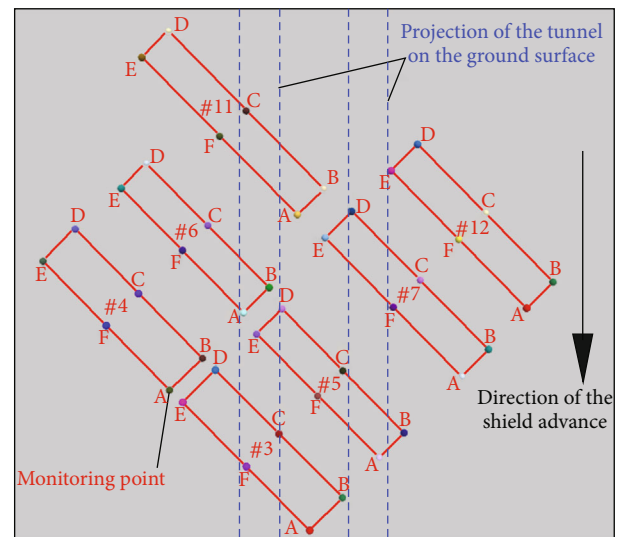


FIGURE 13: Layout of ground settlement monitoring points.

building #11 nearest to the tunnel were affected by its construction. However, the other points of building #11 were farther away from the tunnel and consequently less affected by the settlement. Therefore, the different results of the monitoring points revealed differential settlement. Similarly, monitoring points D and E of building #7, B of building #6, C, D, E, and F of building #5, and A, B, and C of building #3 were all close to the tunnel, so they were affected by the construction of the tunnel and suffered significant settlement unlike other points.

Macroscopic analysis of the monitoring curve in Figure 14 revealed that the foundation settlement of all buildings caused by tunnel construction was less than 4 mm. The settlement value of building #5 was the largest, i.e., 3.6 mm. With the completion of the tunnel lining, the ground settlement in the upper part of the tunnel gradually stabilized and even recovered, but some of the monitoring points on the foundations directly above the tunnel significantly fluctuated in settlement values. The settlement values

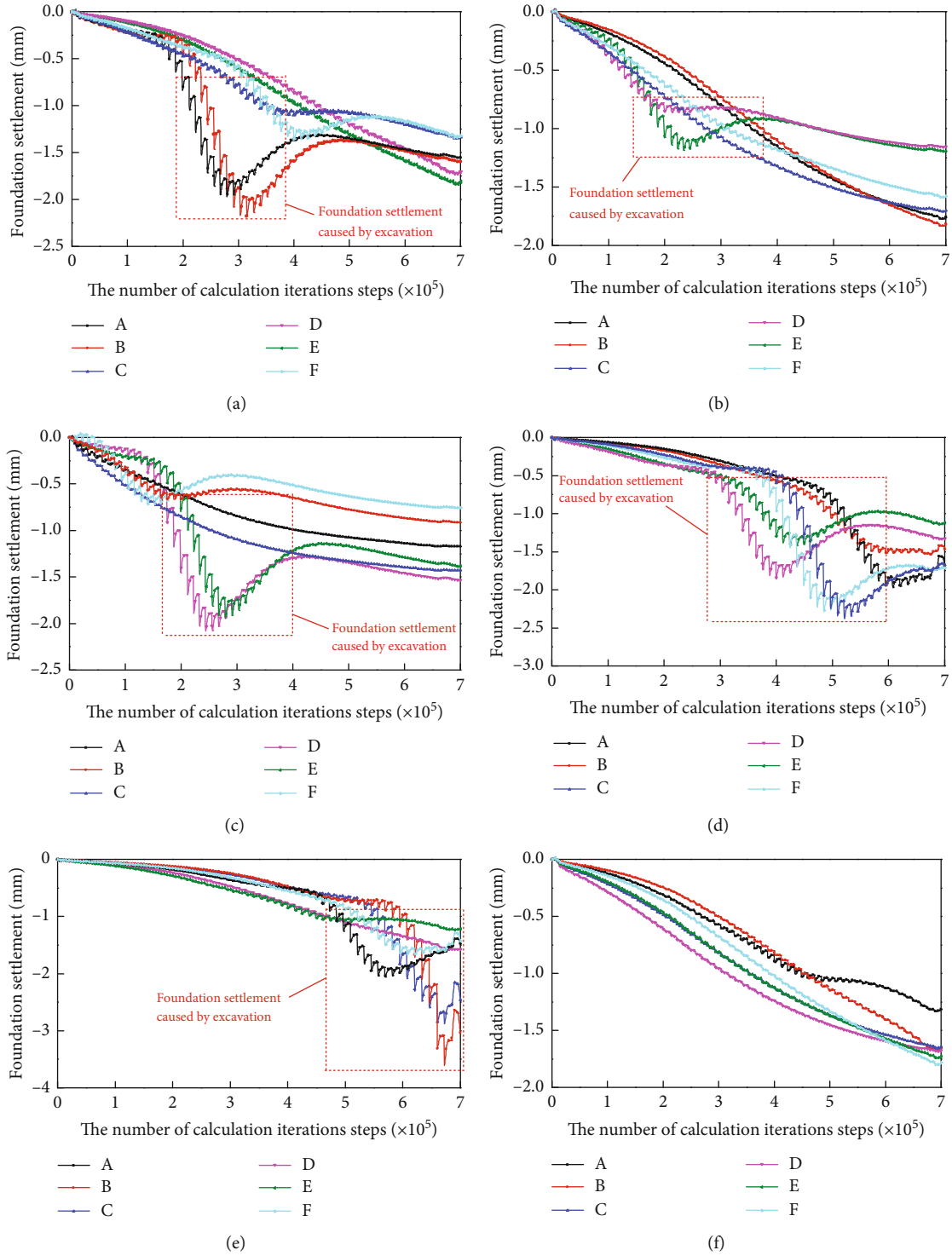


FIGURE 14: Continued.

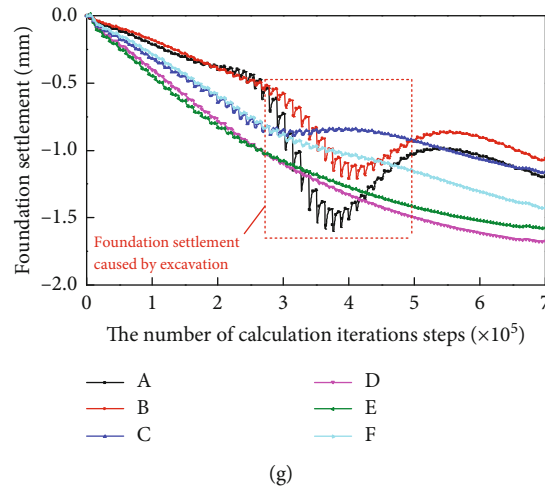


FIGURE 14: Settlement curves of the foundation: (a) building #11, (b) building #12, (c) building #7, (d) building #6, (e) building #5, (f) building #4, and (g) building #3.

of neighboring foundations during shield crossing were significantly greater than those registered by other monitoring points on the foundation of the same building.

5. Construction Proposals

Based on the actual construction of Nantong Metro Line 1, the settlement monitoring results, and numerical simulation calculations, the following recommendations are given for the different relative positions of the building and the tunnel when shield construction is passing under the neighboring buildings. Before passing under the buildings, the attitude of the shield machine should be adjusted. Then, the propulsion speed and the time and amount of correction should be reduced when passing under the buildings. The total push force should be controlled and disturbance in the surrounding soil avoided. The shield machine should also pass under the buildings no more than once. After passing under the buildings, shield tail grouting should be strictly controlled because it can reduce later settlement.

Furthermore, cutterhead should be inspected and replaced before passing under dense buildings. The discharge speed should be strictly controlled and adjusted in time according to the amount of soil lost during excavation. Similarly, grouting should be completed in time and its pressure controlled strictly. The grouting volume on each section of lining should be more than 6 m^3 . Grouting pressure should be more than 200 kPa.

The parameter control scheme during excavation can be determined by referring to the initial 100 m test section of the excavation and monitoring results. The specific construction parameters can be referred to as follows. The average advancement speed is controlled at 40~45 mm/min and the shield advances about 8 rings per day. The speed is more reasonable, so that the daily progress can be controlled at 8~12 rings. The pressure in the soil chamber is greater than 200 kPa to better balance the pressure at the excavation face, while the recommended value can be between 260 and

270 kPa. Thrust can be controlled between 14000 and 16000 kN, with torque less than 2500 kN·m. Cutter speed can be controlled at 1.0~1.2 r/min. The grouting pressure is controlled at 400 to 500 kPa, and the grouting volume is guaranteed to be not less than 5.5 m^3 per ring in reality.

6. Conclusions

- (1) When the shield tunnel was digging in sandy soil and silt, pore water in the soil in front of the cutter dissipated faster and its shear strength rose quickly. The frictional resistance at the side of the shield also rose quickly, so that the torque and total thrust of the cutter of the shield reached their limit, leading to an unstable shield machine
- (2) The vibrations caused by the shield in a short period of time resulted in the rapid settlement of the buildings. The average settlement rate for buildings directly above the shield reached 7 mm/d. The shield caused a maximum of 1.5 mm of settlement before it passed under the buildings. However, the peak settlement during and after the passage was 4.0 and 5.1 mm, respectively. The settlement troughs formed during tunnel excavation had a width of approximately 7D on one side
- (3) The excavation reduced the pore pressure at the top of the excavation face. This part of the soil was affected by tensile stress, causing the soil to suffer tensile-shear damage. In that soil, a local plastic zone formed, which eventually became a relatively large deformation. In contrast, the bottom of the excavation face still maintained large pore pressure. Based on the effective stress principle, this part of the soil suffered small stress, so no plastic zone was formed
- (4) When shield construction was carried out in sand with high water content, the settlement of the

adjacent buildings caused by the shield decreased with time according to the exponential law. When the shield passed under these buildings, their settlement eventually stabilized as the shield moved away

Data Availability

The data used to support the findings of this study are included within the article.

Conflicts of Interest

The authors declare that there are no financial and personal relationships with other people or organizations that can inappropriately influence our work and there is no professional or other personal interest of any nature or kind in any product, service, and/or company that could be construed as influencing the position presented in, or the review of, the manuscript entitled “Analysis of Settlement Induced by Shield Construction of the Metro Passing under Existing Buildings Based on the Finite Difference Method.”

Authors' Contributions

Rui Wang was responsible for the data curation, writing of the original draft, software, and visualization. Bin Zhang was responsible for the conceptualization, methodology, project administration, supervision, and investigation and wrote, reviewed, and edited the manuscript. You Wang was responsible for the resources, investigation, and project administration and wrote, reviewed, and edited the manuscript.

Acknowledgments

This work was supported by the NNSFC (National Natural Science Foundation of China) through project Grant Nos. 51778633 and 51308552 and 2020 Science and Technology Research and Development Plan Guiding Subjects of China Railway Corporation through project Grant Nos. 41 and 243.

References

- [1] Y. Cai, C. P. Zhang, and B. Min, “Analysis of ground deformation and failure induced by shallow tunneling with cavity in the overlying strata,” *Journal of the China Railway Society*, vol. 41, no. 9, pp. 118–127, 2019.
- [2] K. Cui and W. Lin, “Muck problems in subway shield tunneling in sandy cobble stratum,” *Polish Maritime Research*, vol. 23, no. s1, pp. 175–179, 2016.
- [3] K. L. Chen, H. N. Wu, W. C. Cheng, Z. Zhang, and J. Chen, “Geological characteristics of strata in Chongqing, China, and mitigation of the environmental impacts of tunneling-induced geo-hazards,” *Environmental Earth Sciences*, vol. 76, no. 1, p. 10, 2017.
- [4] C. C. Torres and C. Fairhurst, “Application of the convergence-confinement method of tunnel design to rock masses that satisfy the Hoek-Brown failure criterion,” *Tunnelling and Underground Space Technology*, vol. 15, no. 2, pp. 187–213, 2000.
- [5] A. R. Selby, “Tunnelling in soils-ground movements, and damage to buildings in Workington, UK,” *Geotechnical & Geological Engineering*, vol. 17, no. 3–4, pp. 351–371, 1999.
- [6] Y. Z. Xiang, H. L. Liu, W. G. Zhang, J. Chu, D. Zhou, and Y. Xiao, “Application of transparent soil model test and DEM simulation in study of tunnel failure mechanism,” *Tunnelling and Underground Space Technology*, vol. 74, pp. 178–184, 2018.
- [7] J. H. Shin, I. K. Lee, Y. H. Lee, and H. S. Shin, “Lessons from serial tunnel collapses during construction of the Seoul subway line 5,” *Tunnelling and underground space technology*, vol. 21, no. 3–4, pp. 296–297, 2006.
- [8] Y. Jiang, H. Yoneda, and Y. Tanabashi, “Theoretical estimation of loosening pressure on tunnels in soft rocks,” *Tunnelling and Underground Space Technology*, vol. 16, no. 2, pp. 99–105, 2001.
- [9] C. González and C. Sagaseta, “Patterns of soil deformations around tunnels. application to the extension of Madrid Metro,” *Application to the extension of Madrid Metro*, vol. 28, no. 6–7, pp. 445–468, 2001.
- [10] B. Yun, Z. H. Yang, and Z. W. Jiang, “Key protection techniques adopted and analysis of influence on adjacent buildings due to the bund tunnel construction,” *Tunnelling and Underground Space Technology*, vol. 41, no. 1, pp. 24–34, 2014.
- [11] Z. D. Wang, L. M. Jiang, and Y. Rao, “Estimation of ground settlement induced by shield tunnel excavation based on the time-space relationship,” *Journal of Civil and Environmental Engineering*, vol. 41, no. 1, pp. 62–69, 2019.
- [12] R. B. Peck, “Deep excavations and tunneling in soft ground,” in *7th International Conference on Soil Mechanics and Foundation Engineering, Mexico City, Mexico, State-of-the-Art, 1969* Mexico City.
- [13] P. B. Attewell, “Ground movements caused by tunnelling in soil,” in *Conference on Large Ground Movements and Structures*, pp. 812–948, London, 1978.
- [14] C. Sagaseta, “Analysis of undrained soil deformation due to ground loss,” *Geotechnique*, vol. 37, no. 3, pp. 301–320, 1987.
- [15] R. P. Chen, F. Y. Meng, Y. H. Ye, and Y. Liu, “Numerical simulation of the uplift behavior of shield tunnel during construction stage,” *Soils and Foundations*, vol. 58, no. 2, pp. 370–381, 2018.
- [16] Z. Wang, G. Li, A. Wang, and K. Pan, “Numerical simulation study of stratum subsidence induced by sand leakage in tunnel lining based on particle flow software,” *Geotechnical and Geological Engineering*, vol. 38, no. 4, pp. 3955–3965, 2020.
- [17] X. T. Wu and Z. W. Liu, “Numerical simulation of ground settlement caused by over-lapping tunnel shield construction and measures of stratum reinforcement,” *Journal of Physics: Conference Series*, vol. 1176, no. 5, p. 052070, 2019.
- [18] X. Liu, Q. Fang, D. Zhang, and Z. Wang, “Behaviour of existing tunnel due to new tunnel construction below,” *Computers and Geotechnics*, vol. 110, pp. 71–81, 2019.
- [19] C. Kan and J. J. Li, “Study on the influence of small clear distance tunnel with multiple arches on the foundation of adjacent high-rise buildings,” *Railway Construction Technology*, vol. 293, no. 2, pp. 77–81+102, 2018.
- [20] S. L. Zhang, *Impact Analysis of Earth Pressure Balance Shield Tunnel Construction on Existing Buildings in Beijing Metro*, China University of Geosciences, China, 2010, (in chinese).

- [21] L. Godinho, P. Amado-Mendes, A. Pereira, and D. Soares Jr., "A coupled MFS-FEM model for 2-D dynamic soil-structure interaction in the frequency domain," *Computers & Structures*, vol. 129, pp. 74–85, 2013.
- [22] Z. Xiang, G. Swoboda, and Z. Cen, "Identification of damage parameters for jointed rock," *Computers & Structures*, vol. 80, no. 16-17, pp. 1429–1440, 2002.
- [23] A. Zhang and Z. Ling, "RBF neural networks for the prediction of building interference effects," *Computers & Structures*, vol. 82, no. 27, pp. 2333–2339, 2004.
- [24] Ministry of housing and urban-rural development and P. R. China, *Technical Code for Urban Rail Transit Engineering Monitoring (GB50911-2013)*, China Building Industry Press, Beijing, 2013.
- [25] X. L. Lu, Y. C. Zhou, M. S. Huang, and F. Li, "Computation of the minimum limit support pressure for the shield tunnel face stability under seepage condition," *International Journal of Civil Engineering*, vol. 15, no. 6, pp. 849–863, 2017.
- [26] Y. T. Zhang, "Analysis of seepage field of highway tunnel excavation by finite difference method," *Applied Mechanics and Materials*, vol. 638-640, pp. 798–803, 2014.
- [27] Ministry of construction of the People's Republic of China and P. R. China, *Load Code for Building Structures (GB50009-2012)*, China Building Industry Press, Beijing, 2012.

Research Article

Identification of Mine Water Source Based on AHP-Entropy and Set Pair Analysis

Xianming Zhao , Zhimin Xu , and Yajun Sun 

School of Resources and Geosciences, China University of Mining and Technology, Xuzhou 221116, China

Correspondence should be addressed to Zhimin Xu; xuzhimin@cumt.edu.cn

Received 2 March 2022; Accepted 23 March 2022; Published 27 April 2022

Academic Editor: Constantinos Loupasakis

Copyright © 2022 Xianming Zhao et al. This is an open access article distributed under the Creative Commons Attribution License, which permits unrestricted use, distribution, and reproduction in any medium, provided the original work is properly cited.

After a water inrush disaster occurs in the mine production process, it is urgent to identify the source of water inrush and formulate corresponding countermeasures in the complex hydrogeological condition of coal mines. Therefore, accurate identification of mine groundwater source is one of the keys to prevent mine water disasters. According to the difference between the hydrochemical compositions of three aquifers in Chengjiao coal mine, six primary ions ($Na^+ + K^+$, Ca^{2+} , Mg^{2+} , SO_4^{2-} , Cl^- and HCO_3^-) were selected as the indexes for groundwater source identification. On this basis, a mathematical model for groundwater source identification was established by combining the analytic hierarchy process- (AHP-) entropy weight method and the set pair analysis (SPA) theory. Next, this model was used to identify the sources of 10 sets of water samples from the mine, and then, the identification results were compared with the results of conventional models established using Fisher discriminant analysis (FDA) and Bayes discriminant analysis (BDA) methods. The results show that the SPA-based model performs better in identifying the groundwater sources. Furthermore, the model was used to identify the source of water inflow in the No. 21304 panel. The analysis on identification results reveals that the area close to the F_{20} normal fault tends to receive water supply from the Ordovician limestone aquifer and the Taiyuan Formation limestone aquifer, so it should be regarded as a key area for water inrush prevention and control.

1. Introduction

China is the largest coal producer and consumer in the world. The coal mass production was 3.84 billion tons in 2020, and it kept increasing at the rate of about 0.9% according to the Energy Production Report (2020) released by the National Bureau of Statistics of China. At present, coal plays an important role in China's economic development, accounting for 62% and 68.5% of China's energy structure and energy consumption, respectively. However, water disasters happened frequently in the mining process due to complex hydrogeological conditions of Chinese coal mines [1]. Groundwater may inrush into the mine roadway suddenly when faults, mined-out space, and karst collapse columns are affected and broken during mining activities. The mine water inrush is ferocious, often engulfing the roadway in an instant and resulting in considerable casualties and economic losses. A total amount of 779 water disasters happened in China, which resulted in

enormous casualties (3,831 deaths) and economic losses in the period 2000-2020 [2]. After a water inrush disaster occurs in mine production processing, it is urgent to identify the source of water inrush and formulate the corresponding control measures, and varied control measures should be made out for the different aquifer conditions based on water richness. For aquifers with less water, the water inrush hazards could generally be eliminated through temporary water bin construction in low-lying areas or enough water pump installation. However, for those with rich water aquifers, water inrush hazards were often controlled by grouting into aquifer's fissures and transforming it into aquiclude or retaining water-resisting coal pillars [3]. In a word, rapid and accurate groundwater source identification is essential for reasonable selection and optimization of water control measures [4-6].

It is an essential step to reasonably determine the weight of each identification index in groundwater source identification [7-9]. While the above methods we mentioned

promoted the identification accuracy, they still have some restrictions to comply with, for instance, the certain random weight assignment and fuzzy indexes were generally generated based on artificial experiences. Researches that were conducted by using this method could neither overcome the complicacy and fuzziness of the multiaquifer system nor fully represent the hydrochemical characteristics of the aquifers and increase the inaccuracy of the identification results. In order to solve this problem, this paper combined the AHP- (analytic hierarchy process-) entropy weight method and the SPA (set pair analysis) theory to establish a new groundwater source identification model. To be specific, the objective weight was calculated based on information entropy, while the subjective weight was calculated by the means of AHP. Then, the two weights were combined for calculating a comprehensive weight for each identification index. This weighting method not only reflects the knowledge and experiences of experts but also avoids the subjectivity of traditional experience-based methods [10–12]. It is successful to ensure the scientific nature and comprehensiveness of the weight of mine water source identification indexes.

The SPA theory, proposed by a Chinese scholar named Keqin Zhao in 1989, is a systematic analysis method for uncertain issues [13, 14]. It has been applied in various fields, such as building sustainable performance [15], disease hazard [16], efficacy of medicine, tourism resources [17], urban ecosystem [18], information technology [19], water environment [20, 21], and water resource system [22]. It focuses on the relationship between the accurate and inaccurate features of two related data sets and establishes the relationship between them in a mathematical form, and this form could be identified by identity-discrepant-contrary coefficients. There generally exist several aquifers that are capable of supplying inrush water to be identified. These aquifers could hardly be identified accurately through a single index due to their significantly varied hydrochemical characteristics and obsolete boundaries. This problem could be effectively solved by SPA. A SPA theoretical mathematical model was established to promote the accuracy of groundwater source identification based on the characteristic values of water samples from potential aquifers.

In this work, a mathematical model for mine water source identification was proposed based on the analytic hierarchy process- (AHP-) entropy weight method and the set pair analysis (SPA) theory. In addition, water samples extracted from different aquifers in Chengjiao coal mine were screened for excluding abnormal data by the means of the Piper trilinear diagram and the cluster analysis. Finally, characteristic values of water samples from potential aquifers were determined. This practical study not only provides a positive reference for identifying groundwater sources but also lays an important foundation for optimizing water disaster prevention and control schemes.

2. Materials and Methods

2.1. The AHP-Entropy Weight Method. The AHP-entropy weight method, a weighting method that combines the

objective weight with the subjective weight, varied with the conditions of the object to be evaluated. It comprehensively considers subjective and objective situations to ensure the rationality of the assignment of index weight. The objective weight of each index was calculated by using the entropy weight method. According to the definition of entropy, the entropy of the j th ($j = 1, 2, \dots, n$) index could be expressed as

$$E_j = -\frac{\sum_{i=1}^m f_{ij} \ln f_{ij}}{\ln m}, \quad j = 1, 2, \dots, n, \quad (1)$$

where m is the total number of samples; n is the total number of indexes; $f_{ij} = v_{ij}/\sum_{i=1}^m v_{ij}$; v_{ij} is the quantity value of each index of each water source; and if $f_{ij} = 1$, then $f_{ij} \ln f_{ij} = 1$. The entropy weight value of the j th index could be calculated by

$$\delta_j = \frac{1 - E_j}{\sum_{j=1}^n (1 - E_j)}, \quad j = 1, 2, \dots, n. \quad (2)$$

The subjective weight of each index was obtained by means of AHP. First, the importance of indexes was compared to establish a judgment matrix. Meanwhile, the characteristic equation was solved:

$$AR = \lambda_{\max} R, \quad (3)$$

where λ_{\max} is the maximum eigenvalue of the judgment matrix A ; $R = (r_1, r_2, \dots, r_n)$ is the eigenvector of λ_{\max} . Then, the subjective weight vector of the j th index could be obtained after normalizing the eigenvector R :

$$\theta_j = \left(\frac{r_1}{\sum_{j=1}^n r_j}, \frac{r_2}{\sum_{j=1}^n r_j}, \dots, \frac{r_n}{\sum_{j=1}^n r_j} \right). \quad (4)$$

Finally, the comprehensive weight of the j th index could be determined by combining the objective weight with the subjective weight:

$$\omega_j = \frac{\delta_j \theta_j}{\sum_{j=1}^n \delta_j \theta_j}, \quad j = 1, 2, \dots, n. \quad (5)$$

2.2. The SPA Theory. SPA is a systematic analysis method to deal with the problem of uncertainty in nature. Its core idea is to use dialectical analysis (identity, discrepancy, and contradistinction) for describing the uncertainty of things, which means to describe the uncertainty with a certain degree of connection [23]. In the process of mine groundwater source identification, it is assumed that the degree of connection between the set U and the set V is expressed by μ , and the two sets constitute the set pair H , and $H = (U, V)$. The degree of connection μ could be expressed by a mathematical expression:

$$\mu = a + bi + cj. \quad (6)$$

Equation (6), referred to as the ternary degree of connection, is the basic formula of SPA. a , b , and c in the equation, commonly known as three components of the degree of connection, are the identity coefficients, the discrepant coefficient, and the contrary coefficient, respectively. In order to adapt to the complexity, ambiguity, and comprehensiveness of mine groundwater source identification, Equation (6) could be extended into

$$\mu = a + (b_1 + b_2)i + (c_1 + c_2)j = a + b_1i^+ + b_2i^- + c_1j^+ + c_2j^-, \quad (7)$$

where b_1 and b_2 are the coefficients of the water source type's left and right adjacent intervals; c_1 and c_2 are the coefficients of the water source type's secondary left and right adjacent intervals; $a + b_1 + b_2 + c_1 + c_2 = 1$, $i^- \in [-1, 0]$, $i^+ \in [0, 1]$, $j^+ = \{0, 1\}$, and $j^- = -1$. The intervals of mine groundwater source identification are interpreted in Figure 1. The whole identification interval was equally divided into three parts, namely, the water source type's membership interval (1/3 in total), the adjacent intervals (1/3 in total), and the secondary adjacent intervals (1/3 in total). That is, the left adjacent interval, secondary left adjacent interval, right adjacent interval, and secondary right adjacent interval account for 1/6 of the whole identification interval, respectively.

$$S_4 - S_1 = 2(S_3 - S_2), \quad (8)$$

where S_2 and S_3 are the lower and upper limits of a certain index in the water source type's membership interval, respectively; S_1 and S_4 are the lower and upper limits of this index in the water source type's adjacent intervals, respectively.

Assuming that the water sample to be evaluated is $X = [x_1, x_2, \dots, x_n]$, then the calculation formulas for the connection degree components of X 's p th index x_p ($p = 1, 2, \dots, n$) are displayed as

$$\mu = a + b_1i^+ + b_2i^- + c_1j^+ + c_2j^- = \begin{cases} \frac{S_3 - S_2}{S_3 - x_p} + \frac{S_2 - S_1}{S_3 - x_p}i^- + \frac{S_1 - x_p}{S_3 - x_p}j^- & x_p < S_1, \\ \frac{S_3 - S_2}{S_3 - x_p} + \frac{S_2 - x_p}{S_3 - x_p}i^- & S_1 \leq x_p < S_2, \\ 1 & S_2 \leq x_p < S_3, \\ \frac{S_3 - S_2}{x_p - S_2} + \frac{x_p - S_3}{x_p - S_2}i^+ & S_3 \leq x_p < S_4, \\ \frac{S_3 - S_2}{x_p - S_2} + \frac{S_4 - S_3}{x_p - S_2}i^+ + \frac{x_p - S_4}{x_p - S_2}j^+ & S_4 \leq x_p. \end{cases} \quad (9)$$

With the aid of the components of connection degree, the set pair trend between X and a certain water source type's identification interval could be calculated by

$$t = \frac{\sum_{p=1}^n \omega_p a}{\sum_{p=1}^n \omega_p (b_1 + b_2 + c_1 + c_2)}, \quad (10)$$

where ω_p is the comprehensive weight of X 's p th ($p = 1, 2, \dots, n$) index; t is the set pair trend. When $t > 1$, X and the water source type's identification interval share the same trend in the dialectical relationship; and the larger the value of t , the stronger the trend. Thus, X 's water source type could be determined by Equation (10).

3. The Geological Setting

3.1. Study Area. Chengjiao coal mine is located in Yongcheng City, Henan Province, China (Figure 2). Overall, the mine's high altitude is in the north and the west and lower in the south and the east. The surface water system is poorly developed, and vertical infiltration of atmospheric precipitation is the main source of groundwater supply here. The main mining coal seam, i.e., the II₂ coal seam, is located in the Lower Permian Shanxi Formation. The main sources of groundwater are the Shanxi Formation sandstone aquifer, the Taiyuan Formation limestone aquifer (in the upper section), and the Ordovician limestone aquifer. Besides, a fully developed fault destroys the continuity of the aquiclude and facilitates hydraulic connections between aquifers, which immensely impedes water control in the mine.

3.2. Major Hydrological Problem. The No. 21304 panel, whose plane position is exhibited in Figure 2, is the first mining face in the south wing of the mine. The F_{20} fault lies outside the panel, and its profile section is shown in Figure 2. Since the fault throw is greater than 400 m, the top surface of Ordovician limestone in the fault footwall rises to an elevation of about -510 m which is far higher than the current coal seam elevation (-880 m) of the panel. If the fault is able to conduct aquifers' water, Ordovician limestone water near the opposite and foot of the fault is likely to flow into the panel through the fractures and cracks and pose considerable threats to mining operation safety. Hence, the groundwater source is necessary to be identified accurately in the panel, so that the corresponding water control measures could be formulated to ensure safe mining in this region.

4. Results and Discussion

4.1. Establishment of an Identification Model. To identify the groundwater source accurately in the No. 21304 panel, the AHP-entropy weight method and the SPA theory were combined to establish an identification model through the NumPy library of Python software. Figure 3 shows the workflow of the identification model.

The specific steps are as follows:

Step 1. Sampling.

Hydrochemical characteristics, especially main ion contents ($Na^+ + K^+$, Ca^{2+} , Mg^{2+} , SO_4^{2-} , Cl^- , and HCO_3^-), are the basis of establishing a groundwater source identification model. In this study, a total of 47 water samples (1 to 47 in

	S_1	S_2	S_3	S_4
Secondary leftadjacent interval	Left adjacent interval	Water source type's membership interval	Right adjacent interval	Secondary right adjacent interval
1/6	1/6	1/3	1/6	1/6

FIGURE 1: Zoning interpretation of extended set pair.

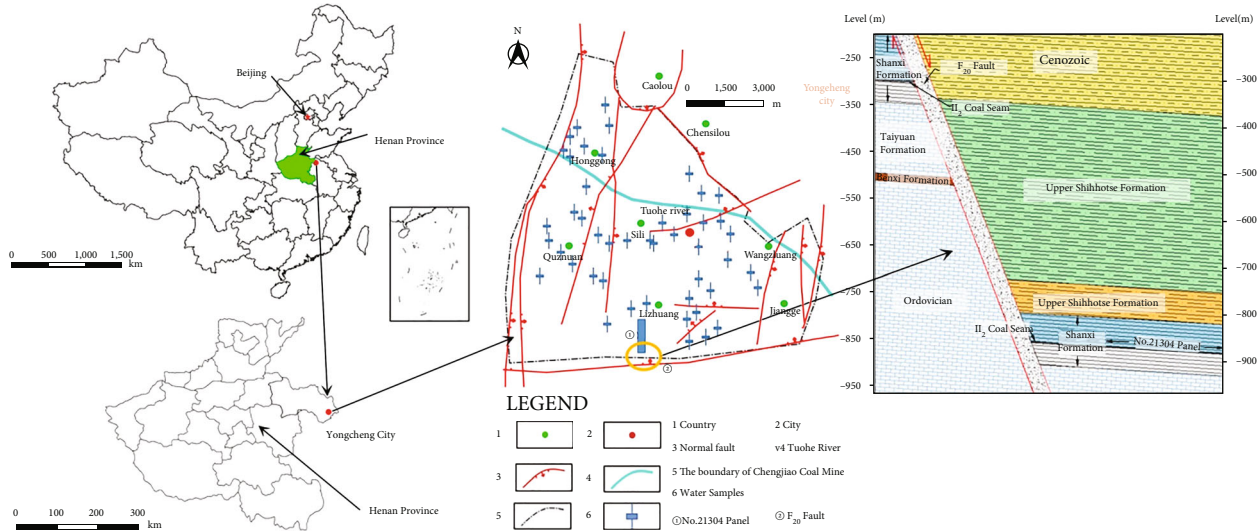


FIGURE 2: Location of Chengjiao coal mine and histogram of the No. 21304 panel.

Supplemental File) were extracted from different sampling sites of the three aquifers to establish the model.

Step 2. Exclusion of abnormal data.

The water samples were screened by means of the Piper trilinear diagram and the cluster analysis to exclude exceptional samples. In this way, the remaining ones could faithfully reflect the characteristic values of corresponding aquifers.

The Piper trilinear diagram, first proposed by Piper in 1944 [24], indicates the contents of six primary ions $Na^+ + K^+$, Ca^{2+} , Mg^{2+} , SO_4^{2-} , Cl^- , and HCO_3^- in a water sample. Corresponding analysis could be conducted according to the distributions of the six ions. The Piper trilinear diagram could illustrate the hydrochemical characteristics of groundwater through the relative compositions of the chemical components [25].

The Piper trilinear diagram was plotted based on the data of 47 water samples (Figure 4). As shown in Figure 4, the result demonstrated all water samples belong to $NaSO_4$ -type water, and the cationic compositions of the three water source types were quite different. Sample 10 (from the Ordovician limestone aquifer) and sample 45 (from the Shanxi Formation sandstone aquifer) have notably different hydrochemical characteristics, as marked by the red oval area.

The cluster analysis refers to the analysis process of grouping a set of physical or abstract objects into multiple classes composed of similar objects [26]. It classified the research objects (samples or indexes) according to their characteristics to exclude abnormal objects. Specifically, each

water sample is regarded as a vector comprising n indexes, and the space composed of n -dimensional vectors is approximated as the distance space [27]. Under the condition that other factors exert a limited effect, the groundwater samples from the same source or with the same hydrochemical characteristics could be classified into one category because of the relatively short distance between them, while those from different sources or with different hydrochemical characteristics could be classified into different categories.

In this paper, the cluster analysis was also conducted based on the data of 47 water samples (Figure 5). The cluster analysis results also reveal the distinct hydrochemical characteristics of samples 10 and 45 from the Piper diagram as those of other samples. This confirms that the two exceptional samples should be excluded from further analysis.

Step 3. Establishment of an index system.

With the contents of six ions $Na^+ + K^+$, Ca^{2+} , Mg^{2+} , SO_4^{2-} , Cl^- , and HCO_3^- in the water samples taken as the indexes, the index set named as $U = \{Na^+ + K^+, Ca^{2+}, Mg^{2+}, SO_4^{2-}, Cl^-, HCO_3^-\}$ is established.

The evaluation set of water source types for the identification model, i.e., $V = \{\text{Shanxi Formation sandstone water, Taiyuan Formation limestone water, and Ordovician limestone water}\}$, was established in accordance with the three water sources types (represented by I, II, and III, respectively).

Step 4. Weight assignments for the indexes.

The objective weights of the indexes were calculated based on the mass concentration data of six indexes $Na^+ + K^+$, Ca^{2+} ,

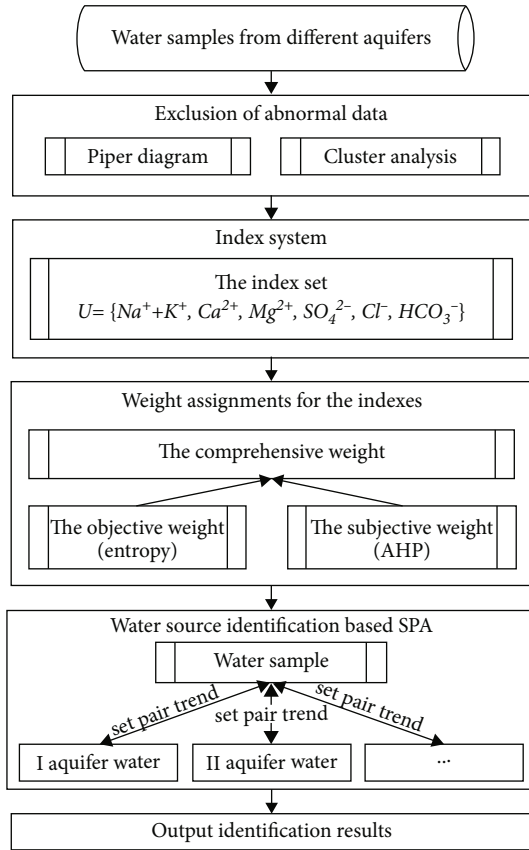


FIGURE 3: Workflow of identification of groundwater source.

Mg^{2+} , SO_4^{2-} , Cl^- , and HCO_3^- of the remaining 45 water samples (abnormal samples excluded). Next, the subjective weights and the comprehensive weights of the indexes were calculated through Equations (4) and (5) in the AHP-entropy weight method. The calculation results are listed in Table 1.

Step 5. Groundwater source identification based on SPA.

The box plot reflecting the mass concentration variations of various ions in different aquifers was drawn based on the remaining 45 water samples (Figure 6). The box plot is a statistical method that reflects the distribution characteristics of the original data [28]. The standard of response data characteristics of the box plot is based on the quartiles and the interquartile range. The quartiles have certain resistance. Up to 25% of the data could become arbitrarily far away without greatly disturbing the quartile. Using the upper and lower quartiles of the box plot as the water source discrimination interval could objectively reflect the hydrochemical characteristics of aquifers [29]. The upper quartile and lower quartile of the box plot are set as the lower limit S_2 and upper limit S_3 of a certain index in the water source type's membership interval, and then, the corresponding S_1 and S_4 were calculated through Equation (8). The results are given in Table 2.

Then, the components of connection degree and the set pair trends between each water sample and each water source type's identification interval could be calculated through Equations (9) and (10) in the SPA theory we men-

tioned above. The water source to which the sample belongs is determined by comparing the set pair trends.

4.2. Model Validation and Analysis. The established identification model was utilized to identify another 10 samples (W_1 to W_{10}) taken from Chengjiao coal mine for verifying its accuracy. The samples to be identified and the identification results are exhibited in Table 3. Shanxi Formation sandstone water, Taiyuan Formation limestone water, and Ordovician limestone water were represented by I, II, and III, respectively.

A comparison between the identification results and the actual water source types indicates that for all the 10 samples, the identification results and the actual situation were completely consistent, which means the model achieves 100% identification accuracy. However, the values of t_I and t_{II} in the set pair trends of water sample W_1 were very close, which will reduce the confidence of the final identification result. There are two possible reasons for this phenomenon: One is the water sample W_1 may come from mixed water of more than one aquifer, which leads to an increase in the connection degree between some indexes of multiple aquifers in the SPA-based identification model, then resulting in the similar set pair trends calculated. On the other hand, the model employs too few water samples in each aquifer as the basis to fully reflect the hydrochemical characteristics of the aquifer, therefore increasing the error of the identification results. Additionally, FDA and BDA were also employed for groundwater source identification and their identification accuracy rates were 70% and 80%, respectively. To sum up, the SPA-based identification model performed better in identifying the sources of water samples.

4.3. Determination of the Source of Water Inflow in No. 21304 Working Face. A water sample collected from the No. 21304 panel was identified by using the model established above. The sample and identification result are disclosed in Table 4.

According to the identification result, there is no doubt that the Ordovician limestone aquifer water was the major source of inflow of the No. 21304 panel and that the Taiyuan Formation limestone aquifer water may be highly related to the inflow water. However, there is only a minuscule chance that the Shanxi Formation sandstone aquifer water relates to the inflow.

It is assumed that the three aquifers all contribute to water inflow in the No. 21304 panel to further verify the accuracy of the above identification results in this paper. According to the principle that the content of each ion component of the mixed solution is constant, the element composition and content remain unchanged after the water of the three water source types is mixed to form mine water. The migration of groundwater is accompanied by ion exchange, which will lead to the alternating adsorption of $Na^+ + K^+$ and $Ca^{2+} + Mg^{2+}$ by rocks, resulting in the change in the concentration of Na^+ , K^+ , Ca^{2+} , and Mg^{2+} in water [30]. Meanwhile, the content of HCO_3^- in water is also easily affected by other ions and pH. However, SO_4^{2-} and Cl^- whose contents are less affected by other ions and pH will not be

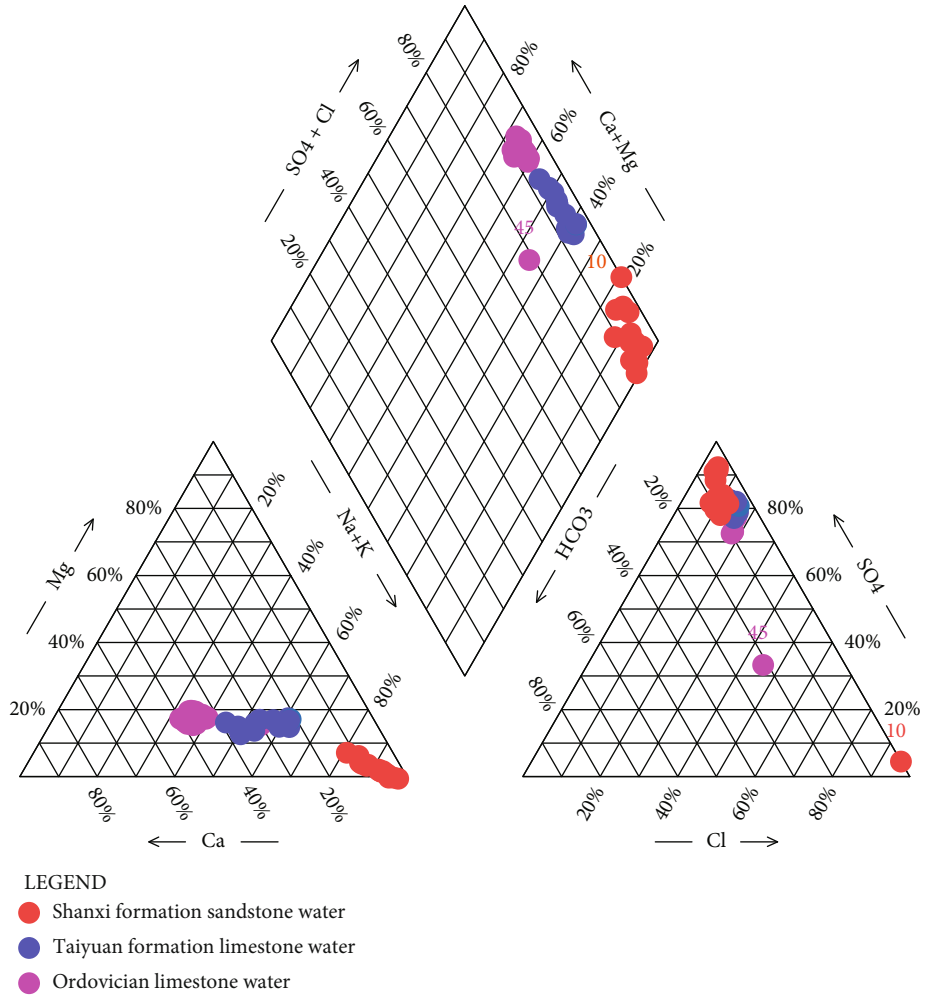


FIGURE 4: Piper diagram of water samples from different aquifers.

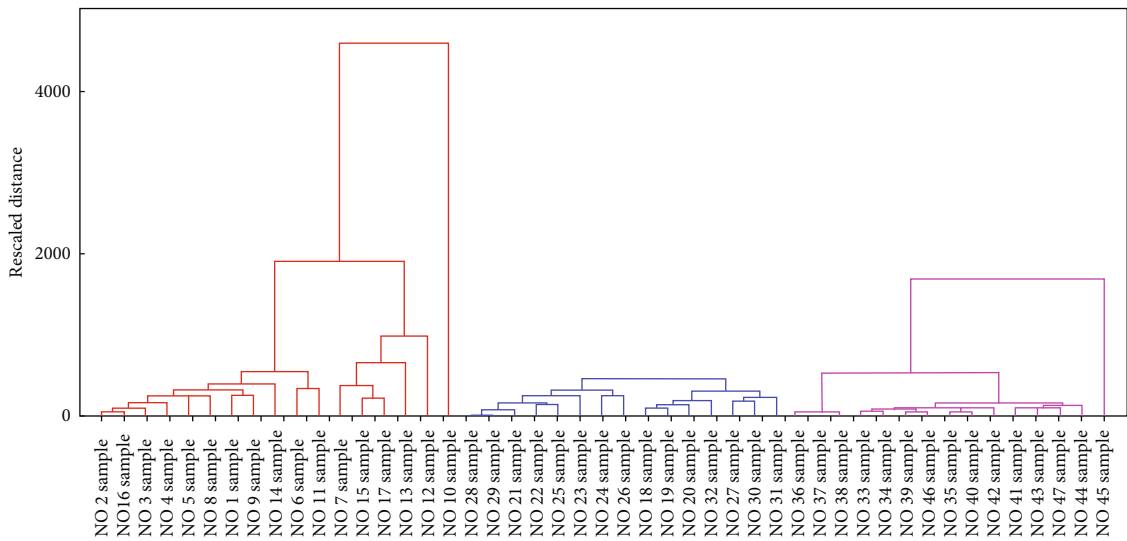


FIGURE 5: Cluster analysis of water samples (red: Shanxi Formation sandstone aquifer; blue: Taiyuan Formation limestone aquifer; pink: Ordovician limestone aquifer).

TABLE 1: Weights of the indexes.

Weights	K^+Na^+	Ca^{2+}	Mg^{2+}	SO_4^{2-}	Cl^-	HCO_3^-
Objective weights	0.27	0.31	0.23	0.07	0.05	0.07
Subjective weights	0.17	0.16	0.18	0.22	0.17	0.10
Comprehensive weights	0.27	0.29	0.25	0.09	0.06	0.04

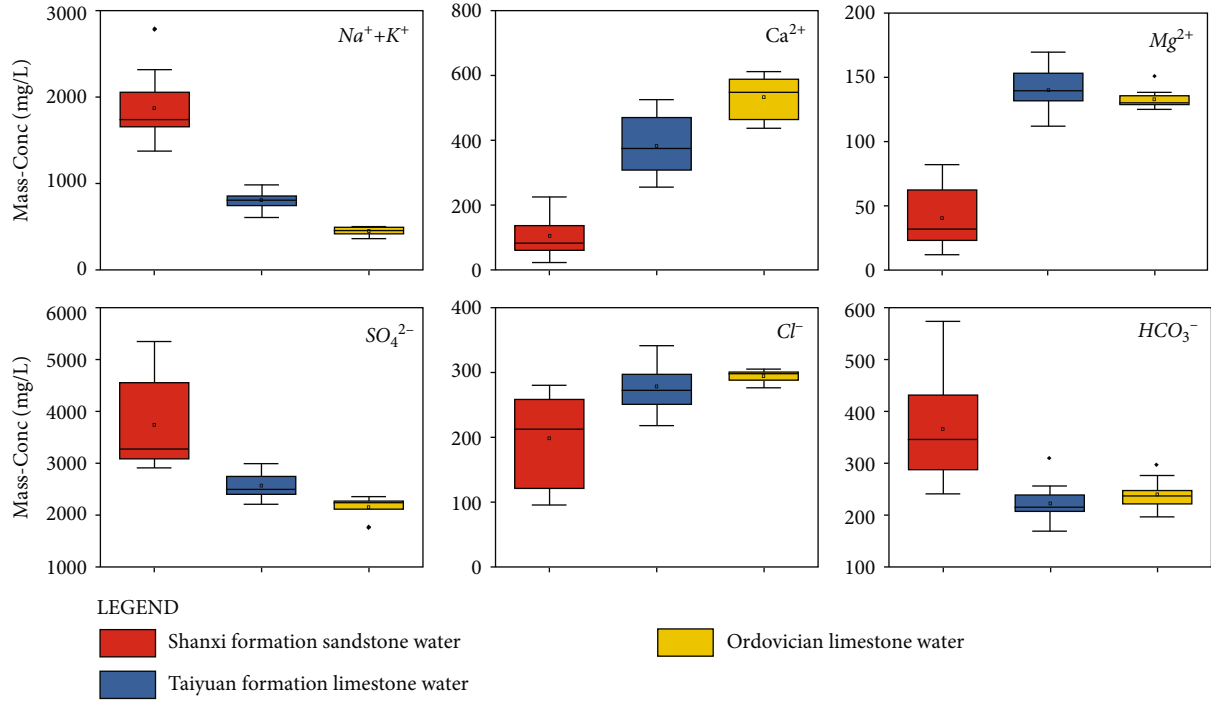


FIGURE 6: Box plot of six indexes.

TABLE 2: Limits of six indexes.

Water source type	Index	S_1	S_2	S_3	S_4
Shanxi Formation sandstone aquifer	K^+Na^+	1479.68	1662.08	2026.88	2209.28
	Ca^{2+}	24.83	62.29	137.21	174.66
	Mg^{2+}	5.74	23.04	57.65	74.95
	SO_4^{2-}	2439.16	3092.57	4399.39	5052.79
	Cl^-	61.15	125.85	255.25	319.95
	HCO_3^-	220.27	289.45	427.81	497.00
Taiyuan Formation limestone aquifer	K^+Na^+	706.51	756.47	856.37	906.32
	Ca^{2+}	231.38	309.55	465.90	544.07
	Mg^{2+}	123.43	131.67	148.16	156.40
	SO_4^{2-}	2280.57	2427.19	2720.43	2867.05
	Cl^-	238.30	257.90	297.11	316.71
	HCO_3^-	196.68	209.94	236.46	249.72
Ordovician limestone aquifer	K^+Na^+	392.21	427.21	497.22	532.22
	Ca^{2+}	413.88	471.30	586.15	643.58
	Mg^{2+}	124.78	128.27	135.25	138.74
	SO_4^{2-}	2066.11	2134.70	2271.86	2340.44
	Cl^-	286.12	290.69	299.84	304.41
	HCO_3^-	210.88	222.50	245.73	257.34

TABLE 3: Samples to be identified and identification results.

Sample	Sample data (unit: mg/L)						Set pair trend			SPA	FDA	BDA	Actual
	K^+Na^+	Ca^{2+}	Mg^{2+}	SO_4^{2-}	Cl^-	HCO_3^-	t_I	t_{II}	t_{III}				
W_1	1534.83	267.14	92.77	2465.36	255.39	248.86	2.77	2.08	0.67	I	I	II	I
W_2	1347.93	225.41	83.18	3155.16	274.12	307.89	3.06	1.34	0.47	I	I	I	I
W_3	1357.54	237.65	121.67	3311.33	129.75	266.59	2.37	1.33	0.79	I	I	II	I
W_4	706.30	360.78	120.02	2247.41	273.34	232.90	1.18	6.78	1.87	II	II	II	II
W_5	721.84	263.88	113.11	2047.28	274.74	235.00	1.38	4.29	1.15	II	II	II	II
W_6	780.75	202.24	109.31	1977.25	243.05	170.69	1.72	3.58	0.75	II	II	II	II
W_7	865.56	342.14	112.99	2572.35	276.51	200.18	1.32	9.90	0.99	II	II	II	II
W_8	484.00	463.51	118.59	2018.03	285.37	164.10	0.97	3.15	5.75	III	II	III	III
W_9	510.40	579.82	134.19	2316.10	297.78	257.41	0.94	3.57	23.19	III	II	III	III
W_{10}	565.56	493.56	127.58	2272.08	286.93	269.62	1.03	4.14	8.27	III	II	III	III

TABLE 4: Samples of No. 21304 working face and identification results.

Sample of No. 21304 working face (unit: mg/L)						Set pair trend		
K^+Na^+	Ca^{2+}	Mg^{2+}	SO_4^{2-}	Cl^-	HCO_3^-	t_I	t_{II}	t_{III}
542.00	524.31	143.42	2217.55	296.72	206.74	0.89	4.57	5.73

adsorbed in rock mass and soil, so they are relatively stable ions in groundwater. Based on this premise, the mass balance equation of SO_4^{2-} and Cl^- could be established to calculate the relative proportion of the sources of water inflow.

$$\begin{bmatrix} 369.1 & 278.1 & 305.6 \\ 3537.7 & 2560.6 & 2037.3 \\ 1 & 1 & 1 \end{bmatrix} \begin{bmatrix} m_I \\ m_{II} \\ m_{III} \end{bmatrix} = \begin{bmatrix} 296.7 \\ 2217.6 \\ 1 \end{bmatrix}, \quad (11)$$

where m_I , m_{II} , and m_{III} are the proportions of the Shanxi Formation sandstone aquifer water, the Taiyuan Formation limestone aquifer water, and the Ordovician limestone aquifer water of total panel inflow, respectively.

Solving Equation (11) yields $m_I = 0.0042$, $m_{II} = 0.3325$, and $m_{III} = 0.6633$. The results show that the Ordovician limestone aquifer water accounts for 66.33% of total water inflow, while the Taiyuan Formation limestone aquifer and the Shanxi Formation sandstone aquifer water account for 33.25% and 0.42% of water inflow, respectively. This is basically consistent with the results of the groundwater source identification model based on the AHP-entropy weight method and the SPA theory, so the results of the model are reliable.

Specific water inrush controlling measures should be formulated for the three aquifers due to their varying water abundances. Although the Shanxi Formation sandstone aquifer is the closest to the II_2 coal seam, its maximum unit water inflow is only 0.07 L/s-m. Considering its poor water abundance, its threat of water disaster could generally be

eliminated through measures such as temporary water bin construction in low-lying areas and water pump installation. In contrast, the Taiyuan Formation and the Ordovician limestone aquifer possess abundant water, with their maximum unit water inflows being 2.87 L/s-m and 3.56 L/s-m, respectively. As a result, their water disasters are often controlled by measures such as aquiclude grouting reinforcement and water-resisting coal pillar retention.

Accordingly, the Ordovician limestone aquifer water was the major source of inflow of the No. 21304 panel. In the follow-up production, the area of the No. 21304 panel that is close to the F_{20} fault should be regarded as the focus of attention. In this area, safer and stricter mining methods, as well as more reliable and effective prevention and control measures, such as aquiclude reinforcement by grouting and water-resisting coal pillar retention, should be adopted to ensure production safety in the panel.

5. Conclusions

The identification of mine groundwater source is a complex problem. Under the influences of multiple factors, it is difficult to identify the groundwater sources accurately in the coal mining processing. Quick and accurate identification of mine groundwater source is of great significance to the prevention and control of water inrush accidents in coal mines. Thus, a reliable method is urgently needed to solve this problem.

In this study, the hydrochemical characteristics of water sources from different aquifers in Chengjiao coal mine were determined by means of the Piper trilinear diagram and the cluster analysis, and ions in the groundwater were analyzed

by combining the AHP-entropy weight method and the SPA theory. On the basis of the analysis results, a mine groundwater source identification model was established, and the identification reliability of the model was verified. The verification results were showed that the model based on the AHP-entropy weight method and the SPA theory performs better in identifying the groundwater source compared with those established using FDA and BDA methods.

After systematical analysis of the established model, the source of water inflow in the No. 21304 panel was identified, and the primary source was revealed. The analysis on the identification results reveals that the area close to the F_{20} fault tends to receive water supply from the Ordovician limestone aquifer and the Taiyuan Formation limestone aquifer, so it should be regarded as the key area for mine water inrush prevention and control.

Data Availability

The data used to support the findings of this study are included within the article.

Conflicts of Interest

The authors declare no conflict of interest.

Acknowledgments

This work was supported by the Chengjiao Coal Mine in Henan Province, China. This research was financially supported by the National Key Research and Development Program of China (No. 2019YFC1805400), the National Nature Science Foundation of China (42172272), the Fundamental Research Funds for the Central Universities (No. 2020ZDPY0201), and the National Science Foundation of China (No. U1710253).

Supplementary Materials

The tables of 47 water samples from different aquifers (Line 187), classification function coefficients of the FDA method (Line 272), and classification function coefficients of the BDA method (Line 272) are in the supplementary files. (*Supplementary Materials*)

References

- [1] P. Bukowski, "Water hazard assessment in active shafts in upper Silesian coal basin mines," *Environment*, vol. 30, no. 4, pp. 302–311, 2011.
- [2] B. Luo, Y. Sun, Z. Xu et al., "Damage characteristics and mechanism of the 2017 groundwater inrush accident that occurred at Dongyu coalmine in Taiyuan," *Water*, vol. 13, no. 3, p. 2021, 2021.
- [3] H. Yin, C. Zhao, Y. Zhai et al., "Application of comprehensive support techniques to roadway tunneling in vicinity of Ordovician carbonate confined aquifers under complicated tectonic conditions," *Carbonates and Evaporites*, vol. 35, no. 4, 2020.
- [4] D. Dong, Z. Chen, G. Lin, X. Li, R. Zhang, and Y. Ji, "Combining the fisher feature extraction and support vector machine methods to identify the water inrush source: a case study of the Wuhai mining area," *mine water and the Environment*, vol. 38, no. 4, pp. 855–862, 2019.
- [5] G. Vizintin, M. Veselic, A. Bombac, E. Dervaric, J. Likar, and Z. Vukelic, "The development of a "drive-in" filters dewatering system in the Velenje coal mine using finite-element modeling," *Acta Geotechnica Slovenica*, vol. 6, no. 1, pp. 50–63, 2009.
- [6] F. Hu, M. Zhou, P. Yan et al., "Selection of characteristic wavelengths using SPA for laser induced fluorescence spectroscopy of mine water inrush," *Spectrochimica Acta Part A: Molecular and Biomolecular*, vol. 219, pp. 367–374, 2019.
- [7] Y. B. Du, Y. S. Zheng, G. Wu, and Y. Tang, "Decision-making method of heavy-duty machine tool remanufacturing based on AHP-entropy weight and extension theory," *Journal of Cleaner Production*, vol. 252, 2020.
- [8] M. Peters and S. Zelewski, "Pitfalls in the application of analytic hierarchy process to performance measurement," *Management Decision*, vol. 46, no. 7, pp. 1039–1051, 2008.
- [9] G. D. Wu, K. F. Duan, J. Zuo, X. B. Zhao, and D. Z. Tang, "Integrated sustainability assessment of public rental housing community based on a hybrid method of AHP-entropy weight and cloud model," *Sustainability*, vol. 9, 2017.
- [10] Z. An and L. R. Song, "Research on the role of AHP- entropy method in the identification and evaluation of China tariff source risk," *Journal of Intelligent & Fuzzy Systems*, vol. 34, no. 2, pp. 1053–1060, 2018.
- [11] Z. K. Ding, M. L. Zhu, Z. Z. Wu, Y. B. Fu, and X. Liu, "Combining AHP-entropy approach with GIS for construction waste landfill selection-a case study of Shenzhen," *International journal of environmental research and public health*, vol. 15, no. 10, 2018.
- [12] G. Z. Feng, S. Y. Lei, Y. J. Guo, B. Meng, and Q. F. Jiang, "Optimization and evaluation of ventilation mode in marine data center based on AHP-entropy weight," *Entropy*, vol. 21, no. 8, 2019.
- [13] Y. Cao, Y. Cao, H. Zhou, H. Zhou, J. Wang, and J. Wang, "An approach to interval-valued intuitionistic stochastic multicriteria decision-making using set pair analysis," *International Journal of Machine Learning and Cybernetics*, vol. 9, no. 4, pp. 629–640, 2018.
- [14] C. Wei, X. Dai, S. Ye, Z. Guo, and J. Wu, "Prediction analysis model of integrated carrying capacity using set pair analysis," *Ocean & Coastal Management*, vol. 120, pp. 39–48, 2016.
- [15] Y. Liu, "Assessment of building sustainable performance based on set pair analysis (SPA)," *Materials Research*, vol. 255–260, pp. 94–98, 2011.
- [16] T. Chong, S. Yi, and C. Heng, "Application of set pair analysis method on occupational hazard of coal mining," *SAFETY SCIENCE*, vol. 92, pp. 10–16, 2017.
- [17] Q. Wei and Z. J. Zhao, "Research on evaluation of coastal city water sports tourism resources based on set pair analysis," *Journal of Coastal Research*, vol. 115, pp. 190–192, 2020.
- [18] M. R. Su, Z. F. Yang, and B. Chen, "Set pair analysis for urban ecosystem health assessment," *Communications in Nonlinear Science and Numerical Simulation*, vol. 14, no. 4, pp. 1773–1780, 2009.
- [19] K. Kumar, K. Kumar, H. Garg, and H. Garg, "Connection number of set pair analysis based TOPSIS method on intuitionistic fuzzy sets and their application to decision making," *Applied Intelligence*, vol. 48, no. 8, pp. 2112–2119, 2018.
- [20] Y. C. Liu, C. S. Wang, Y. T. Chun, L. X. Yang, W. Chen, and J. Ding, "A novel method in surface water quality assessment

- based on improved variable fuzzy set pair analysis,” *International Journal of Environmental Research and Public Health*, vol. 16, no. 22, 2019.
- [21] J. Zhang, Y. Li, C. Liu et al., “Application of set pair analysis in a comprehensive evaluation of water resource assets: a case study of Wuhan City, China,” *Water*, vol. 11, no. 8, 2019.
- [22] F. S. Yang, C. J. Xu, X. M. Huang, and J. R. Shao, “Improved set pair analysis model for urban water security assessment,” *Advanced Materials Research*, vol. 1065, pp. 2903–2908, 2015.
- [23] G. He, K. Bao, W. Wang, Y. Zhu, S. Li, and L. Jin, “Assessment of ecological vulnerability of resource-based cities based on entropy-set pair analysis,” *Environmental Technology*, vol. 42, pp. 1–11, 2021.
- [24] P. Li, Y. Zhang, N. Yang, L. Jing, and P. Yu, “Major ion chemistry and quality assessment of groundwater in and around a mountainous tourist town of China,” *Exposure and Health*, vol. 8, no. 2, pp. 239–252, 2016.
- [25] N. Subba Rao, B. Ravindra, and J. Wu, “Geochemical and health risk evaluation of fluoride rich groundwater in Sattenapalle region, Guntur district, Andhra Pradesh, India,” *Human and ecological risk assessment: An international journal*, vol. 26, no. 9, pp. 2316–2348, 2020.
- [26] N. Subba Rao, A. Dinakar, B. K. Kumari, D. Karunanidhi, and T. Kamalesh, “Seasonal and spatial variation of groundwater quality vulnerable zones of Yellareddygudem watershed, Nalgonda District, Telangana State, India,” *Archives of environmental contamination and toxicology*, vol. 80, no. 1, pp. 11–30, 2021.
- [27] Y. Chen, S. Zhu, and S. Xiao, “Discussion on controlling factors of hydrogeochemistry and hydraulic connections of groundwater in different mining districts,” *Natural Hazards*, vol. 99, no. 2, pp. 689–704, 2019.
- [28] N. S. Rao, A. Dinakar, M. Sravanthi, and B. K. Kumari, “Geochemical characteristics and quality of groundwater evaluation for drinking, irrigation, and industrial purposes from a part of hard rock aquifer of South India,” *Environmental Science and Pollution Research*, vol. 28, no. 24, pp. 31941–31961, 2021.
- [29] J. Zhang and D. Yao, “Hydrogeochemical characteristics of coal mine based on box-plot and its application in water inrush source identification,” *Part A, Recovery, utilization, and environmental effects*, pp. 1–14, 2020.
- [30] H. Zhang, G. Xu, X. Chen, and A. Mabaire, “Hydrogeochemical evolution of multilayer aquifers in a massive coalfield,” *Environmental Earth Sciences*, vol. 78, no. 24, 2019.

Research Article

Roadway Deformation and Control under Multidisturbed Secondary High Stress

Xiaoguang Sun,¹ Haibin Wang,² Xiaofang Wo ,^{3,4} Zhimeng Sun,⁵ Wenliang Sun,² and Chungue Li⁶

¹Xuzhou Cumt Backfill Technology Co., Ltd, Xuzhou Jiangsu 221116, China

²Huaneng Lingtai Shaozhai Coal Industry Co., Ltd, Pingliang, Gansu 272000, China

³School of Mines, China University of Mining and Technology, Xuzhou, Jiangsu 221116, China

⁴Key Laboratory of Deep Coal Resource Mining of the Ministry of Education, China University of Mining and Technology, Xuzhou, Jiangsu 221116, China

⁵Honghui No.1 Coal Mine of Gansu Jingyuan Coal Industry and Electricity Power Co., Ltd, Baiyin, Gansu 273000, China

⁶Xinjiang Institute of Engineering, Urumqi, Xinjiang 830000, China

Correspondence should be addressed to Xiaofang Wo; ts21020053a31tm@cumt.edu.cn

Received 13 January 2022; Revised 13 March 2022; Accepted 29 March 2022; Published 16 April 2022

Academic Editor: Lei Wang

Copyright © 2022 Xiaoguang Sun et al. This is an open access article distributed under the Creative Commons Attribution License, which permits unrestricted use, distribution, and reproduction in any medium, provided the original work is properly cited.

Aiming at the serious deformation and failure of mining roadway under the condition of high secondary stress in Xuchang Coal Mine, Shandong Province, the deformation law of surrounding rock under the influence of high secondary stress in the original support belt transport roadway was analyzed by the method of field measurement and numerical simulation, and the control scheme of surrounding rock was put forward. According to the actual site conditions of 3318 working face belt transport drift in Xuchang Coal Mine, this paper proposed a new bolt-net support technology scheme with high strength, high stiffness, and asymmetric characteristics and obtained through numerical simulation analysis: (1) when the 3318 working face begins to mining, the distribution of the maximum principal stress in the surrounding rock of the roadway changes from weak symmetry to strong asymmetry, especially the maximum principal stress in the surrounding rock of the two sides; (2) the superposition effect of leading abutment pressure, lateral abutment pressure, and fault structure has a strong influence on the distribution of the maximum principal stress of roadway surrounding rock. The field industrial test shows that the deformation of the surrounding rock at different parts of the belt transport roadway is significantly reduced after the implementation of the double-height asymmetric bolting support. Among them, the deformation of the roof decreases from 630 mm to 185 mm, the deformation of the left wall decreases from 550~620 mm to 150~170 mm, and the deformation of the right wall decreases from 600 mm to less than 180 mm. The nonuniform deformation degree of the top side is within 1~1.13, indicating that the anchor mesh composite bearing structure is uniformly deformed as a whole, and the overall bearing capacity of the structure is realized.

1. Introduction

After long-term mining, some coal mines in China have entered the middle and later stage of mine life cycle, mining areas with simple occurrence conditions are basically completed, and most of the remaining mining areas are mining areas with strong geological structure influence, the occurrence conditions of coal seams are complex, and geological structures such as faults are developed [1–5]. For this part

of the mine, the coal roadway is strongly affected by the fault geological structure, and its surrounding rock maintenance is difficult, so it is always in a difficult situation of repeated repair [6–10]. Because most of the working face is surrounded by existing goaf, the roadway of the working face is always within the strong influence range of the lateral bearing pressure of the goaf [11]. Under the superposition influence of the geological structure and the fixed supporting pressure of the adjacent working face, the roadway has been

repaired many times before the working face is mined and has always been subject to the long-term effect of secondary high stress caused by multiple disturbances [12–16]; when the working face is mined, the mining roadway within a certain range ahead of the working face will have strong deformation.

Aiming at the problem of large deformation of surrounding rock caused by repeated disturbance of deep buried soft rock roadway, some scholars have constructed the stress coupling numerical model of roadway excavation stress field and working face mining stress field, the research shows that the increase or decrease of stress caused by adjacent coal seam mining is less than 15%, and the simple stress change will not lead to the overall failure of roadway support or large deformation of surrounding rock; after repeated disturbance, the mechanical properties of roadway surrounding rock are significantly reduced, which makes it develop from elastic-plastic deformation to loose deformation [17–20]; in view of the serious deformation and damage of the mining roadway under the influence of multiple mining in the close coal seam, taking Cuijiazhai coal mine as a typical case, some scholars analyzed the reasonable position of the mining roadway under the influence of mining and determined that the relative horizontal distance between the mining roadway and the residual coal pillar in the upper coal seam should be greater than 25 m, and the width of the roadway pillar in the working face should be 20 m; the technical scheme of bolt-net cable combined support is put forward [21, 22]; some scholars take the 11271 haulage roadway of Zhaogu No. 1 coal mine as an example; aiming at the problem of large deformation of the roadway under the influence of high stress, weak surrounding rock, and strong mining, scholars analyze and conclude that the main reason for large deformation and failure of surrounding rock of 11271 haulage roadway is that the existing support parameters are unreasonable. Based on the principle of high prestress and prestress diffusion guided by the action mechanism of bolt cable coordinated support and strong side support, the original support scheme is optimized [23–27]; in view of the serious problem of surrounding rock fragmentation and deformation caused by multiple mining in the mining roadway with double roadway layout, taking the auxiliary transportation roadway of Dongliang coal industry 3101 face as an example, some scholars analyzed the direct inducement leading to the destruction of surrounding rock and put forward the “three high” strengthening surrounding rock control technology based on the full section high-strength lengthened anchor rod of roadway+high-strength prestressed anchor cable+high-strength anchor mesh [28–30]. In view of the influence of fault structure on the original rock stress of transportation roadway in working face, some scholars take 3318 working face of Xuchang Coal Mine as an example, analyze and obtain the roadway stress distribution law under the superposition of goaf lateral abutment pressure, adjacent working face abutment pressure, and fault structure, and reveal the stability characteristics of roadway surrounding rock under the action of multiple perturbation stresses [31]. Although Chinese scholars have done a lot of theoretical and practical research on this type of subject,

many different factors lead to the deformation of surrounding rock of this kind of mine roadway, so we still need to do a lot of research and exploration [32–36].

By carrying out the technical problems of roadway surrounding rock support under the superposition effect of multiple factors such as fault structure, goaf lateral supporting pressure, and advanced mining stress in this working face, this paper is aimed at deeply analyzing the surrounding rock stability characteristics of this kind of roadway, revealing its surrounding rock failure mechanism, guiding the bolt mesh support design and optimization of this kind of roadway, achieving the ultimate goal of no expansion, and repairing during the roadway service period [37–41]. This study has theoretical and practical significance for maintaining the safety of roadway surrounding rock.

2. Project Overview

Xuchang Coal Mine is one of the main production mines of Shandong Energy Zibo Mining Group. It is located in the northeast of Jining City. The roadway is arranged in the coal seam and excavated along the coal seam floor. The relative ground elevation within the roadway excavation range is about +40 m, the underground elevation is about -320 m, and the maximum buried depth of the roadway is about 360 m. The belt transport roadway of 3318 working face adopts a rectangular section, the net section area of the roadway is 14.88 m², the net width is 4800 mm, and the net height is 3100 mm. The direct roof of the coal seam is medium-grained sandstone, with a thickness of 7.80~9.15 m, with an average of 8.98 m; the basic roof is siltstone, with a thickness of 1.60~9.97 m, with an average of 8.36 m; the immediate floor is mudstone, with a thickness of 0~2.8 m, with an average of 0.52 m; the hard floor is siltstone with a thickness of 0~2.75 m and an average of 1.54 m. The engineering background of Xuzhuang Coal Mine is shown in Figure 1.

At present, Xuchang Coal Mine has entered the middle and later stage of the mine life cycle. The mining in the mining areas with simple occurrence conditions is basically completed. Most of the remaining mining areas are mining areas with strong influence of geological structure, with complex occurrence conditions of coal seams and developed geological structures such as faults [31]. Working face 3318 is located between Huangqiao East fault and Huangqiao fault. The length of working face changes with the distance between the two faults, that is, the length of working face gradually decreases from about 128 m at the initial mining to about 40 m at the end of mining. For the belt transport roadway of 3318 working face, the Huangqiao fault structure with an inclination of 70° and a drop of more than 22 m has the strongest influence on it; in addition, DF44 and DF48 faults will be crossed during the excavation of belt transport roadway. The north side of the belt transport roadway of 3318 working face is the goaf of 3302 upper working face, the horizontal distance is about 60 m, and the Huangqiao East fault is between the two working faces. The spatial position relationship between 3318 working face and adjacent working face and fault is shown in Figure 2.

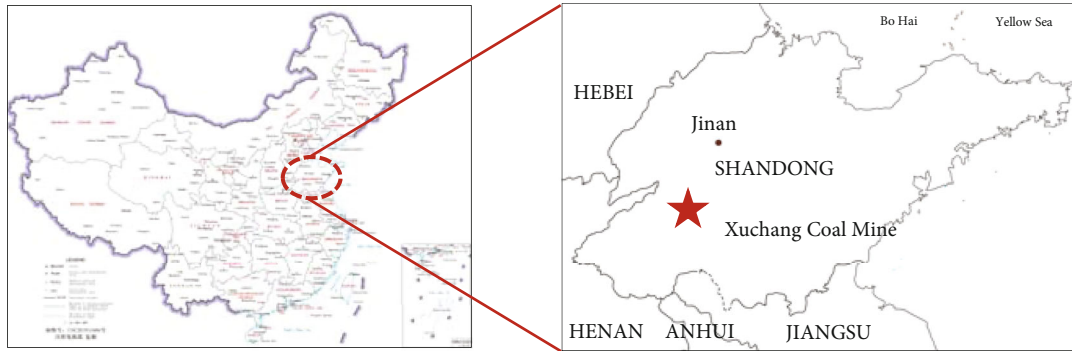


FIGURE 1: Project background.

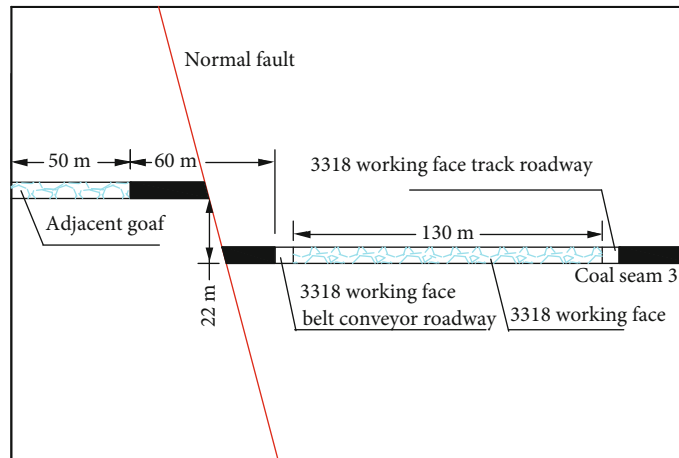


FIGURE 2: Section of spatial position relationship of 3318 working face.

3. Analysis on Deformation Characteristics of Original Supporting Roadway

In order to analyze the surrounding rock deformation law of the secondary high-stress roadway with multiple disturbances in the haulage roadway of working face 3318 of Xuchang Coal Mine, three measuring stations No. 1, No. 2, and No. 3 are arranged in the 3318 belt transport roadway on site, about 200 m, 600 m, and 1000 m away from the setup room, respectively. 16 surrounding rock deformation measuring points are uniformly arranged clockwise from the bottom corner of the left wall of each measuring station section; 1#, 5#, 9#, and 13# measuring points are located at the lower left, upper left, upper right, and lower right corners of the roadway section, respectively; 2#, 3#, and 4# measuring points are located in the left wall of the roadway; 6#, 7#, and 8# measuring points are located in the roadway roof; 8#, 9#, and 10# measuring points are located in the right wall of the roadway; and 14#, 15#, and 16# measuring points are located in the roadway floor. The surrounding rock deformation of the haulage roadway before and after mining is observed through the section measuring points of each measuring station. The roadway surface deformation and non-uniform deformation of each measuring point of the 1# measuring station section of the haulage roadway before and after mining of 3318 working face are shown in

Figures 3 and 4. The nonuniform deformation degree of different parts in a certain section of the roadway is defined as the ratio of the deformation amount of other parts to the deformation amount of this part based on the minimum deformation amount of a certain part of a certain section of the roadway [42, 43]. This value can directly indicate the relative deformation state of roof, slope, and floor surrounding rock.

As shown in Figure 3, when 3318 working face has not been mined, the haulage roadway is affected by the superposition of the lateral bearing pressure and fault structure of the adjacent goaf, and the surrounding rock of the left wall and roof of the roadway is subjected to strong concentrated stress, resulting in a large surface deformation of each measuring point of the left wall and roof relative to the right wall and floor. The deformation of left wall 2#, 3#, and 4# measuring points and side foot 1# measuring points of the roadway is more than 290 mm, and the nonuniform deformation degree is about 14.5; the deformation of the roof 5#, 6#, and 7# three measuring points is more than 355 mm, and the nonuniform deformation reaches 17.75. Compared with the roof and the left wall, the deformation of the right wall 11#, 12#, and 13# measuring points is obviously smaller, and the deformation is between 95 mm and 140 mm; the deformation of the surrounding rock of the roadway floor is small, especially in the middle of the floor. The

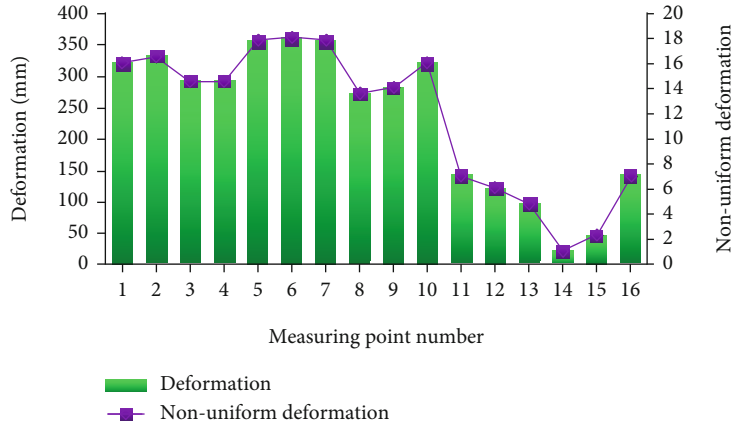


FIGURE 3: Deformation and nonuniform deformation of each measuring point on the section of haulage roadway 1# measuring station when 3318 working face is not mined.

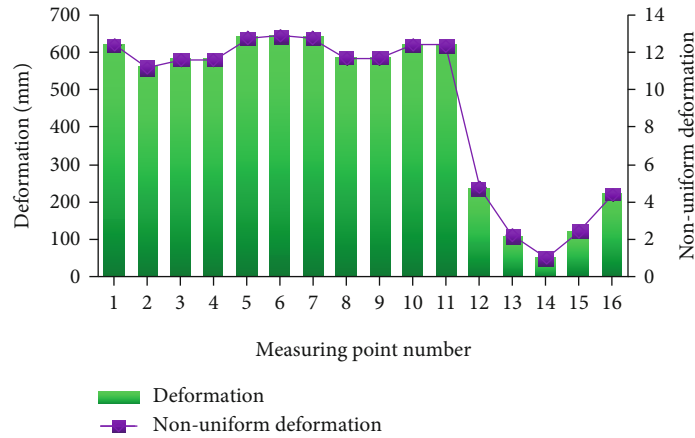


FIGURE 4: Deformation and nonuniform deformation of each measuring point on the section of the haulage roadway 1# measuring station after mining in 3318 working face.

deformation is the minimum value of 20 mm at all monitoring points of the section of the station. Therefore, the deformation at this point is taken as the reference value of the nonuniform deformation of the surrounding rock. It can be seen that when the haulage roadway is not affected by the advance bearing pressure of 3318 working face, the action positions of asymmetric support are top middle, left wall middle, left wall foot, and right wall top in turn.

As shown in Figure 4, when the 3318 working face starts mining, after the haulage roadway is affected by the lateral bearing pressure of the adjacent goaf, the influence of fault structure, and the multiple overlapping influence of the advance bearing pressure of the working face, the deformation increase of surrounding rock in different parts of the roadway reaches more than 50%, especially the surrounding rock of the roadway roof, the left wall, and the right wall, including the middle 6#. The deformation of surrounding rock at 7# and 8# measuring points increases to more than 585 mm, and the deformation of left 1#, 2#, 3#, and 4# measuring points, right middle 10#, 11# measuring points, and roof 9# measuring points are all more than 560 mm. Compared with the top side, the deformation of the floor is small.

The middle position of the floor is the minimum value of the section deformation of the station, and this value is the benchmark value of the nonuniform deformation of surrounding rock. It can be seen that when the haulage roadway is subjected to the advance bearing pressure of 3318 working face, the action positions of asymmetric support are top middle, left wall middle, left wall foot, and right wall top in turn.

4. Simulation of Stress Distribution Law of Surrounding Rock of Multidisturbed Secondary High-Stress Roadway

4.1. Construction of Numerical Simulation Model. In order to analyze the stress distribution and evolution law of surrounding rock of haulage roadway under the superposition effect of lateral bearing pressure in adjacent goaf, fault structure, and advance bearing pressure in 3318 working face, the three-dimensional numerical analysis model established by using FLAC3D numerical analysis software is shown in Figure 5, which comprehensively reflects the superposition

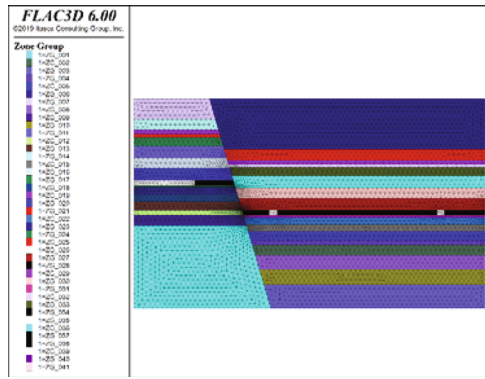


FIGURE 5: Numerical simulation model.

effect of fault structure and lateral bearing pressure of adjacent goaf [44–46]. The physical and mechanical parameters of coal and rock strata referenced by the model are shown in Table 1. The length \times width \times height of the numerical model is 300 m \times 200 m \times 200 m, respectively. 3318 working face and its mining roadway are located in the middle of the model, in which the horizontal distance between the haulage roadway and the fault is 20 m, and the horizontal distance between the haulage roadway and the edge of the adjacent goaf is 60 m; at the same time, the adjacent working face is modeled by the semi-infinite mining method, that is, the adjacent goaf is located at the left boundary of the model. In the model, the mesh stress and deformation iteration adopt the Mohr-Coulomb strength criterion, that is, the failure surface shear stress criterion. In addition, the front, rear, left, and right boundaries of the model are support boundary conditions, the bottom boundary is fixed boundary conditions, and the upper boundary is stress boundary conditions. A uniformly distributed load of 6.5 MPa is applied on the upper part to simulate the self-weight of the 360 m thick rock layer on the model. Due to the development of joints and fissures in the rock mass near the coal seam and serious water deliquescence and weathering, the physical and mechanical parameters of the direct top and bottom strata of the coal seam are slightly weakened. The interface command is used to simulate the fault in the model. The mechanical parameters of the fault contact surface are shear stiffness 200 GPa, normal stiffness 200 GPa, internal friction angle 15°, and cohesion 0.4 MPa, and the sliding mode is opened at the same time. In order to analyze the influence of fault structure and lateral bearing pressure of adjacent goaf on the original rock stress at the roadway position, monitoring points are set at the section center of the haulage roadway of 3318 working face to monitor the evolution law of disturbed secondary stress field formed by the superposition effect of fault structure, lateral bearing pressure of goaf, and advance mining stress of this working face in real time.

4.2. Analysis of Numerical Simulation Results. Through numerical simulation, the vertical stress distribution law of roadway surrounding rock under the superposition effect of multiple factors such as fault structure, goaf lateral bearing pressure, and advance mining stress of the working face

is analyzed, as shown in Figure 6, the peak value of superimposed bearing pressure appears at 10 m of the advance working face. Therefore, this paper mainly analyzes the stress distribution law of roadway surrounding rock around the peak value of superimposed bearing pressure. In the mining process of 3318 working face, the roof strata gradually bend and sink, the load of the overlying strata is transferred to the surrounding rock of the mining roadway, and a semicircular concentrated stress area is formed in the surrounding rock of the two sides of the roadway, which presents asymmetric characteristics.

The peak value of concentrated stress in the surrounding rock of the right wall of the roadway reaches 22.3 MPa, the stress concentration factor reaches about 2.5, and the peak position is 5.5 m away from the surface of the surrounding rock of the right wall; in contrast, the stress concentration degree of the surrounding rock of the left wall is slightly small, but the peak value of the concentrated stress still reaches about 21 MPa and appears 4.5 m away from the surface of the surrounding rock of the left wall. In addition, the stress reduction areas of surrounding rock in the roof and floor of the roadway are large, which are 4 m and 3.8 m, respectively, and the stress drops significantly in the range of 0–3 m of the roof and floor, and their values are below 2 MPa. Compared with the stress distribution law of roadway surrounding rock under the condition of no mining in working face 3318, the concentrated stress range of the two sides of the roadway is significantly developed, especially the surrounding rock of the right wall. The peak value of concentrated stress increases sharply from 14.6 MPa to more than 22 MPa. Moreover, the strongly affected area of concentrated stress develops from a circular area with a radius of about 3 m to a semicircular area with a radius of about 20 m (approximately circular arc distribution in the section shown in the figure), resulting in the strong superposition of lateral bearing pressure and advance bearing pressure on the surrounding rock of the right wall, accelerating the failure and instability of rock mass after the peak; at the same time, the peak value of concentrated stress in the surrounding rock of the left wall also increased significantly, from 14.9 MPa to about 21 MPa, and the distribution range of concentrated stress and the action area of stress peak expanded from a circular area with a diameter of about 4 m to a semicircular area with a diameter of about 18 m, and the action range of high concentrated stress expanded rapidly. In order to further analyze the asymmetric characteristics of the surrounding rock stability of the haulage roadway in working face 3318, the distribution law of the maximum principal stress in the surrounding rock of the roadway is analyzed in detail, and its distribution law is shown in Figures 7 and 8.

As shown in Figure 7, when working face 3318 has not been mined, the maximum principal stress of roadway surrounding rock is mainly affected by the superposition of lateral bearing pressure and fault structure in the goaf adjacent to working face 3302, and its maximum principal stress presents a weak symmetrical distribution. The reduction range of the maximum principal stress on the left wall of the roadway is the smallest, about 0.5 m, but the maximum principal

TABLE 1: Physical and mechanical parameters of coal and rock stratum.

Number	Rock lithology	Thickness (m)	Density (kg · m ³)	Bulk modulus (GPa)	Shear modulus (GPa)	Friction angle (°)	Cohesion (MPa)	Tensile strength (MPa)
1	Loess	34	1960	0.25	0.09	25	8.5	0.35
2	Fine-grained sandstone	7	2610	2.23	1.67	38	3	3.15
3	Mudstone	3	2604	5.88	3.19	41	5.4	3.18
4	Siltstone	2	2603	7	4	43	6.3	4.99
5	Medium-grained sandstone	6	2987	4.34	2.3	40	4.3	2.7
6	Fine-grained sandstone	8	2690	2.23	1.67	32	3.8	3.17
7	Siltstone	7	2558	6.32	3.61	33	8.7	3.07
8	Medium-grained sandstone	8	2987	4.34	2.3	40	4.3	2.07
9	Coal	4	1445	0.71	0.49	22	2.44	0.24
10	Mudstone	1.5	2604	5.88	3.19	41	5.4	3.18
11	Siltstone	5	2603	7	4	43	6.3	4.99
12	Medium-grained sandstone	5	2987	4.34	2.3	40	4.3	2.7
13	Fine-grained sandstone	6	2690	2.23	1.67	32	3.8	3.17
14	Mudstone	3	2604	5.88	3.19	41	5.4	3.18
15	Siltstone	7	2558	6.32	3.61	33	8.7	3.07
16	Fine-grained sandstone	10	2610	2.23	1.67	38	3	3.15
17	Medium-grained sandstone	10	2987	4.34	2.3	40	4.3	2.7
18	Siltstone	16	2603	7	4	43	6.3	4.99

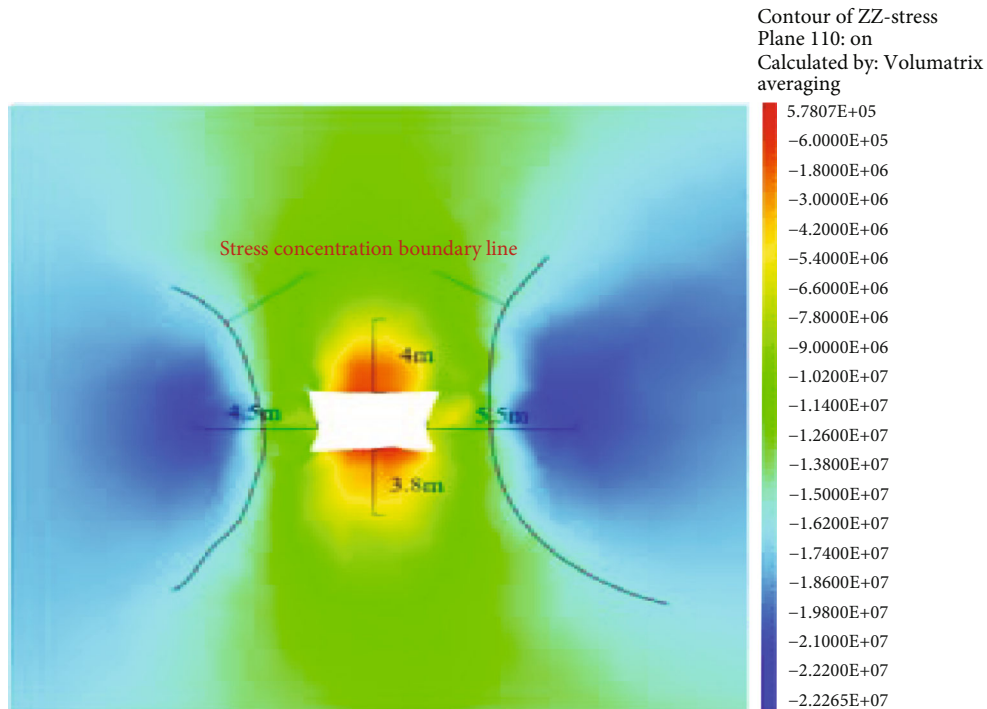


FIGURE 6: Vertical stress distribution law of surrounding rock of multidisturbance secondary high-stress roadway.

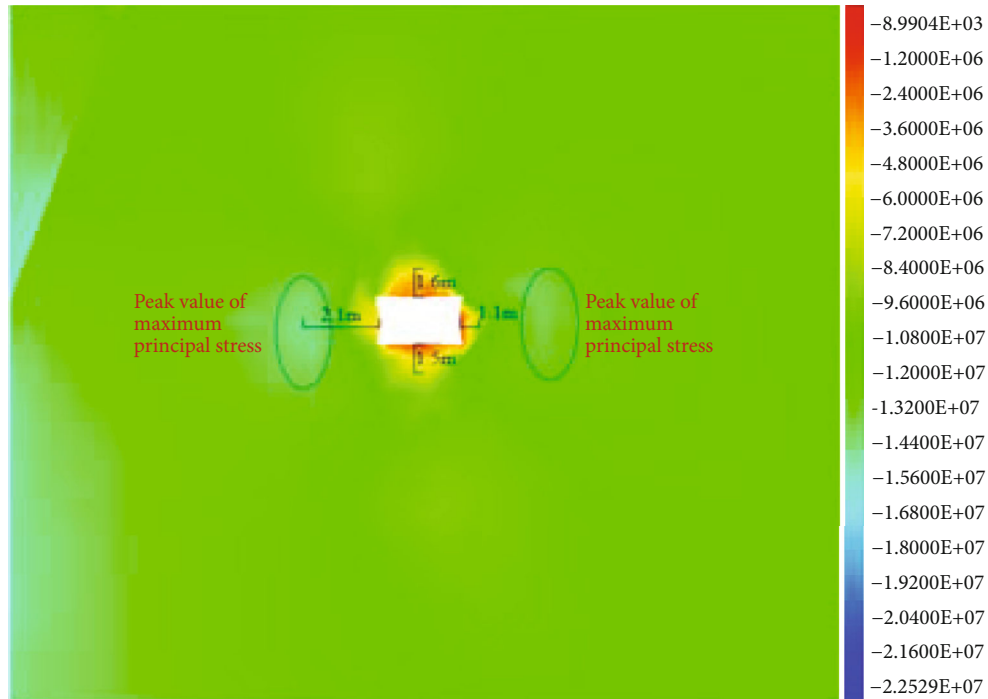


FIGURE 7: Distribution law of maximum principal stress of roadway surrounding rock under the condition of no mining in 3318 working face.

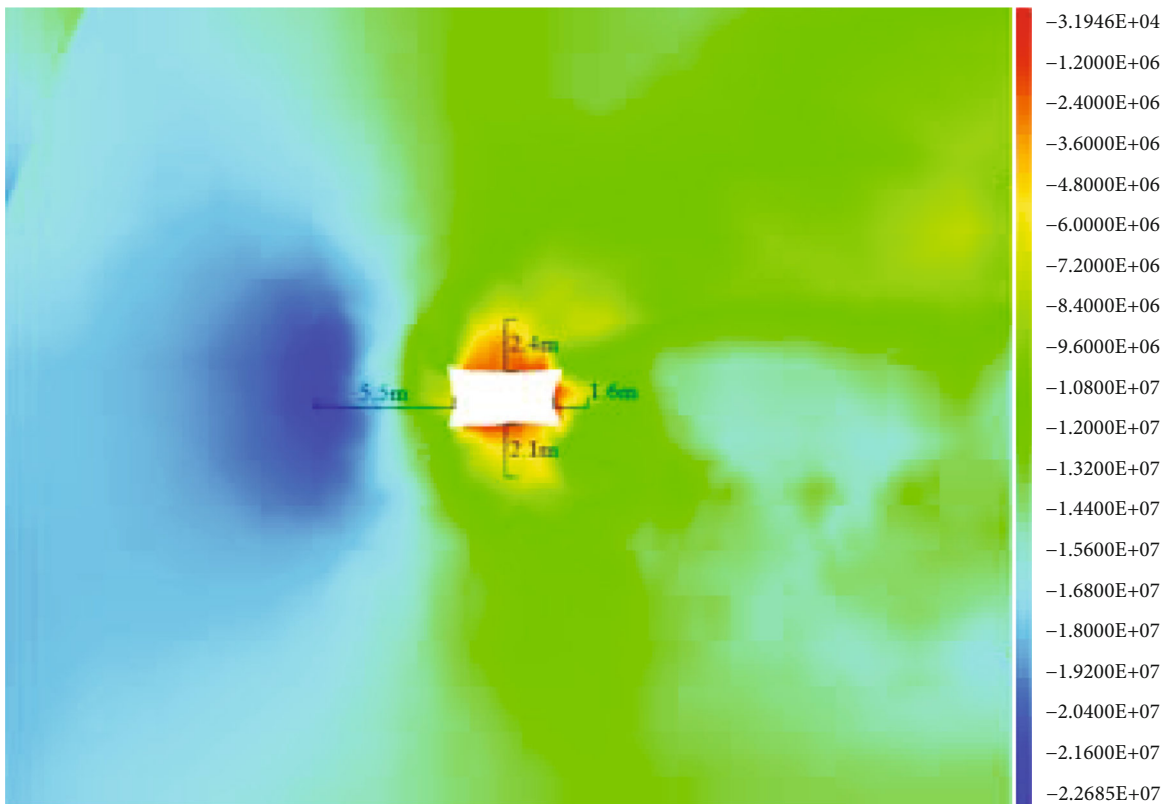


FIGURE 8: Distribution characteristics of maximum principal stress of surrounding rock of multidisturbance secondary high-stress haulage roadway.

stress peak appears at 2.1 m from the surrounding rock surface; secondly, the reduction range of surrounding rock stress on the surface of roadway roof and floor is relatively

consistent, which is about 1.5 m; the stress reduction range of surrounding rock on the surface of the right wall is relatively large compared with that of the left wall, reaching

more than 1.1 m, but the maximum principal stress peak appears at 2 m away from the surrounding rock surface, which is similar to the maximum principal stress peak of the left wall. As shown in Figure 8, in the mining process of working face 3318, the maximum principal stress in the surrounding rock of the haulage roadway shows a significant asymmetric distribution law, and the direction of the maximum principal stress is distributed along the tangential direction of the roadway section. The maximum principal stress at the position 5.5 m away from the left wall rock surface has a significant concentration effect, and the peak value of the maximum principal stress is 22.1 MPa; on the contrary, there is no significant concentration in the surrounding rock of the right wall, roof, and floor of the roadway, but mainly the drop of the maximum principal stress of the surrounding rock on the roadway surface. The stress reduction area of the roof rock mass reaches 2.4 m, which is relatively large compared with other locations, followed by the floor stress reduction area, but it still reaches about 2.1 m, and the stress reduction range of the right wall is relatively small, reaching 1.6 m.

By comparing and analyzing Figures 7 and 8, it can be seen that after the mining of working face 3318 begins, the distribution law of the maximum principal stress of the surrounding rock of the roadway changes from weak symmetry to strong asymmetry, especially the maximum principal stress in the surrounding rock of the two sides. The results show that the superposition effect of advance bearing pressure, lateral bearing pressure, and fault structure has a strong impact on the distribution law of the maximum principal stress of roadway surrounding rock, which is as follows: (1) the concentration of the maximum principal stress of the surrounding rock of the left wall is significant, and the action area of the stress peak and the strong influence range of the maximum principal stress increase sharply; (2) the variation of the maximum principal stress concentration on the right wall is slightly small, but the stress reduction range increases significantly; (3) there is no maximum principal stress concentration in the surrounding rock of roof and floor, but the stress reduction area of surface surrounding rock develops rapidly. The above characteristics show that the superposition effect of the advance bearing pressure produced by the mining of 3318 working face, the lateral bearing pressure of goaf, and fault structure is significant, which makes the rock mass on the roadway surface in a typical unidirectional stress state, especially the concentrated stress on the left wall, accelerates the shear deformation and fracture surface development in the surrounding rock, and leads to the asymmetric instability of the surrounding rock.

5. Optimization Design of Roadway Support Parameters

In the mining process of 3318 working face, the belt transport roadway is in the secondary high-stress field after multiple disturbances, which belongs to a typical complex high-stress roadway. Therefore, according to the surrounding rock stress environment and surrounding rock conditions of belt transport roadway, combined with field measurement

and numerical simulation analysis, and based on the advanced optimization idea and optimal guiding parameters of bolt mesh support parameters of complex high-stress roadway in Xuchang Coal Mine, a new bolt mesh support technical scheme with high strength, high stiffness, and asymmetric characteristics suitable for belt transport roadway in 3318 working face of Xuchang Coal Mine is proposed. In the technical scheme, two support sections A and B of 3318 working face are arranged alternately, with a row spacing of 800 mm, as shown in Figure 9.

- (1) Support parameters of section A: adopted for roadway side $\Phi 18 \times 2400$ mm 20MnSi high-strength full thread steel anchor bolts with spacing of 850 mm are lengthened and anchored with one CK2350 (end) and one K2350 resin anchoring agent, respectively; at the same time, the specification is a 2800×80 mm special-shaped steel belt that connects adjacent anchor bolts in section A. Roof anchor cable $\Phi 21.6 \times 7000$ mm 1860 steel strand is supported with a spacing of 1000 mm. One CK2350 (end) and two K2350 resin anchoring agents are used for lengthening and anchoring, respectively. Meanwhile, the specification is a $4600 \times 280 \times 3$ mm W-shaped steel belt that connects adjacent anchor cables in section A
- (2) Support parameters of section B: roof anchor cable $\Phi 17.8 \times 4000$ mm 1860 steel strand is supported with a spacing of 1000 mm. One CK2350 (end) and two K2350 resin anchoring agents are used for lengthening and anchoring, respectively; the adopted specification is a $4600 \times 280 \times 3$ mm W-shaped steel belt that connects adjacent anchor cables in section A. The upper part of one side of the working face adopts the joint arrangement of the anchor bolt and anchor cable, with a spacing of 850 mm. External binding arrangement of top and bottom $\Phi 18 \times 2400$ mm 20MnSi high-strength full thread steel bolt support, used in the upper $\Phi 17.8 \times 4000$ mm 1860 steel strand support. One CK2350 (end) and one K2350 resin anchoring agent are used for lengthening and anchoring of anchor bolts; one CK2350 (end) and two K2350 resin anchoring agents are used for lengthening and anchoring of anchor cables; the adopted specification is a 2800×80 mm special-shaped steel belt that connects adjacent anchor bolts and anchor cables in section A. The slope on one side of the fault adopts $\Phi 18 \times 2400$ mm 20MnSi high-strength full-thread steel anchor bolt with a spacing of 850 mm. One CK2350 (end) and one K2350 resin anchoring agent are used for lengthening anchoring, respectively. The adopted specification is a 2800×80 mm special-shaped steel belt that connects adjacent anchor bolts in section A
- (3) Parameters of reinforced support at the side of the fault: "Wuhua" 1860 steel strands with $\Phi 17.8 \times 4000$ mm are arranged, the spacing is 1700 mm, and the row spacing is 1600 mm. A CK2350 (end) and two K2350 resin anchoring agents are used for

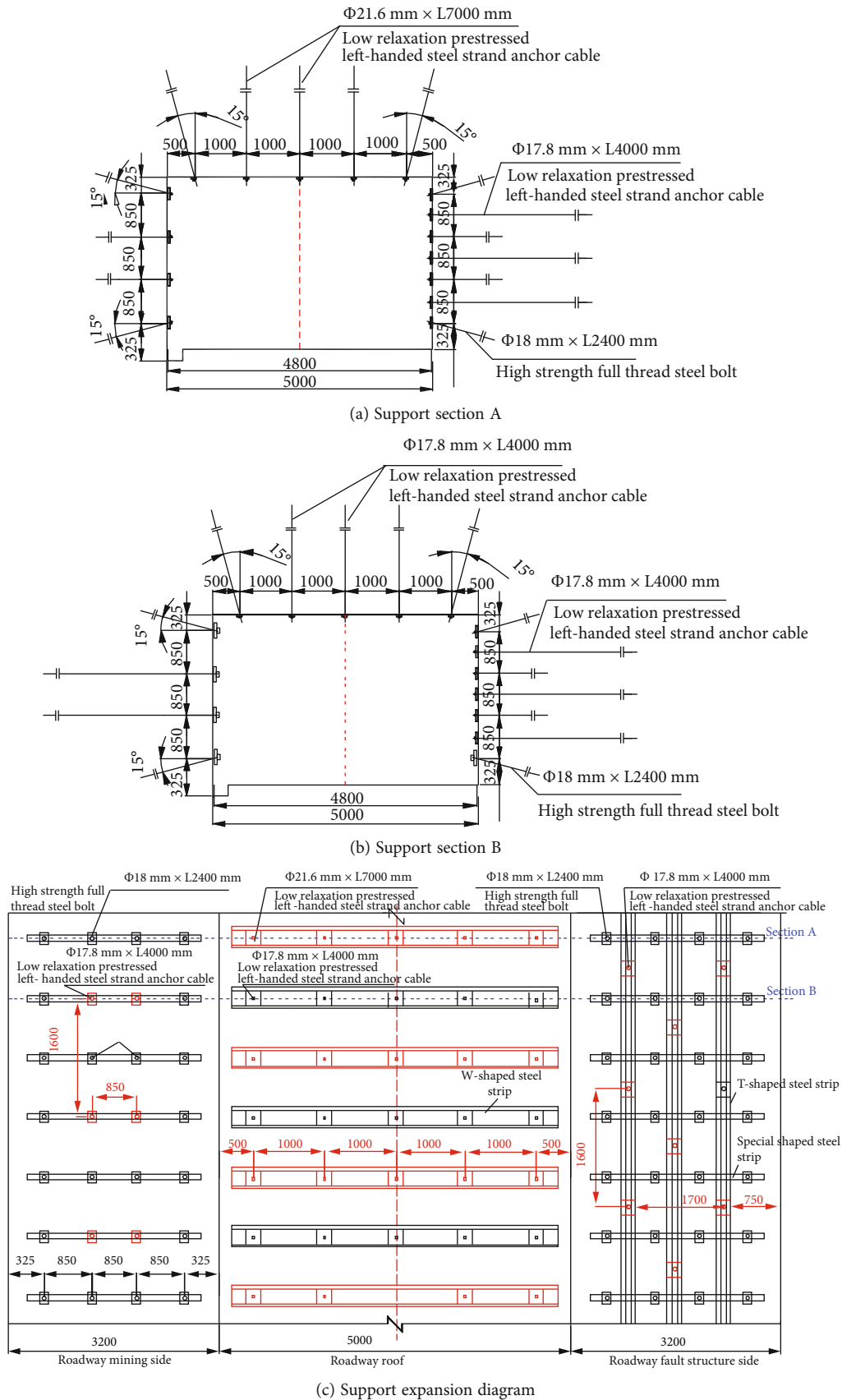


FIGURE 9: Schematic diagram of optimized support of 3318 belt transport roadway (unit: mm).

extension anchoring. A 1800 mm long T-shaped steel belt is arranged along the axial direction of the roadway to connect the adjacent reinforcing anchor cable. There is an overlapping relationship between the adjacent steel belts along the axial direction of the roadway, and the overlapping length is 100 mm. The anchor cable is used to compress the overlapping part

The supporting cast steel nuts shall be used to apply pretightening force to the anchor bolts, and the pretightening torque shall not be less than 300 N·m; the specification of the anchor pallet is an arc-shaped steel pallet of 120 × 120 × 10 mm; the anchor cables shall be pretensioned with supporting two core locks, and the pretightening force shall not be less than 100 kN or the pressure indication of tensioning jack shall not be less than 25 MPa. The mesh made of 10# iron wire is 50 × 50 mm diamond metal mesh that supports the roadway side, and the specification of roof metal mesh is 5200 × 1100 mm. The specification of two sides is 2600 × 2000 mm diamond metal mesh that shall be used for longitudinal overlapping. Single strand 10# iron wire shall be used for connection between top nets, side nets, and top and side nets at a spacing of 200 mm, and the overlapping shall not be less than 100 mm.

6. Field Application Effect Analysis

In order to reasonably evaluate the surrounding rock control effect of high-strength and high-stiffness asymmetric bolt mesh support technology scheme for multidisturbance secondary high-stress roadway, after the new support scheme is adopted, No. 3 observation station is arranged in the belt transport roadway of 3318 working face to measure the surrounding rock deformation of each measurement point in the section of the observation station during the mining process of the working face. By means of field observation, we can see the deformation characteristics of surrounding rock of double-height asymmetric bolt mesh support roadway.

After the implementation of double-height asymmetric anchor mesh support in the roadway, the deformation of surrounding rock in different parts of the roadway is significantly reduced in the mining process of working face 3318, the deformation of surrounding rock in different parts of the roadway is significantly reduced, the deformation of roof is reduced from more than 630 mm to about 185 mm, the deformation of surrounding rock in the left wall is reduced from 550~620 mm to 150~170 mm, and the deformation of surrounding rock in the right wall is reduced from 600 mm to less than 180 mm. If the central deformation of the floor is taken as the benchmark of the nonuniform deformation of the surrounding rock, when the double-height asymmetric anchor mesh support is not adopted, the nonuniform deformation of the middle of the roof, the left wall foot, the right wall foot, and the right wall foot is the largest, reaching between 11 and 12, belonging to the area of strong nonuniform deformation; after the new anchor mesh support is adopted, the nonuniform deformation of the top side is significantly reduced by more than 50%, which is basically

stable within 6~6.5. For the composite structure formed by the anchor mesh support and surrounding rock at the top, the deformation of the surrounding rock at the top of the left side is taken as the benchmark of the nonuniform deformation of the bearing structure. After adopting the double-height asymmetric anchor mesh support scheme, the nonuniform deformation of the top side is within 1~1.13. This phenomenon shows that the anchor net composite bearing structure has uniform deformation and realizes the overall bearing of the structure.

7. Conclusion

- (1) Due to the superposition of advance bearing pressure, lateral bearing pressure, and fault tectonic stress, the stress of roadway surrounding rock shows high asymmetry
- (2) A new bolt mesh support technology scheme with high strength, high stiffness, and asymmetric characteristics suitable for the belt transportation roadway of 3318 working face in Xuchang Coal Mine is put forward
- (3) The field industrial test shows that after the implementation of double-height asymmetric anchor mesh support, the deformation of surrounding rock in different parts of the roadway is significantly reduced. The roof deformation is reduced from more than 630 mm to about 185 mm, the surrounding rock deformation of the left wall is reduced from 550~620 mm to 150~170 mm, the surrounding rock deformation of the right wall is reduced from 600 mm to less than 180 mm, and the nonuniform deformation of the top side is within 1~1.13. It shows that the anchor net composite bearing structure has uniform deformation and realizes the overall bearing of the structure

Data Availability

The Microsoft Excel Worksheet data used to support the findings of this study are available from the corresponding author upon request.

Conflicts of Interest

The authors declare that they have no competing interests.

Acknowledgments

This research was funded by the projects of “the Fundamental Research Funds for the Central Universities (2020ZDPY0221 and 2021QN1003)”, the “National Natural Science Foundation of China (52104106 and 52174089)”, and the “Basic Research Program of Xuzhou (KC21017).”

References

- [1] H. Lin and B. Zhang, "Study of soft rock roadway support technique," in *1st International Symposium on Mine Safety Science and Engineering (ISMSE)*, vol. 26, pp. 321–326, Beijing, PEOPLES R CHINA, 2011.
- [2] Q. Liu, J. Li, and B. Liu, "The stability control theory of deep coal mine roadway," *Energy Education Science and Technology Part a-Energy Science and Research*, vol. 30, no. 1, pp. 521–528, 2012.
- [3] S. G. Liu, J. B. A. Bai, X. Y. Wang, S. Yan, and J. X. Zhao, "Field and numerical study on deformation and failure characteristics of deep high-stress main roadway in Dongpang coal mine," *Sustainability*, vol. 13, no. 15, p. 8507, 2021.
- [4] B. T. Shen, "Coal mine roadway stability in soft rock: a case study," *Rock Mechanics and Rock Engineering*, vol. 47, no. 6, pp. 2225–2238, 2014.
- [5] X. J. Yang, E. Y. Wang, Y. J. Wang, Y. B. Gao, and P. Wang, "A study of the large deformation mechanism and control techniques for deep soft rock roadways," *Sustainability*, vol. 10, no. 4, p. 1100, 2018.
- [6] Y. H. Cheng, F. X. Jiang, and L. H. Kong, "Self-bearing capacity for surrounding rock of composite roof of coal roadways and deformation control in deep high stress mine," in *Proceedings of the ICMHPC-2010 International Conference on Mine Hazards Prevention and Control*, Atlantis Press, p. 415–+, Qingdao, PEOPLES R CHINA, 2010.
- [7] J. C. Feng, S. F. Yin, Z. H. Cheng et al., "Deformation and failure mechanism of surrounding rock in mining-influenced roadway and the control technology," *Shock and Vibration*, vol. 2021, Article ID 5588314, 14 pages, 2021.
- [8] S. T. Gu, B. Y. Jiang, G. S. Wang, H. B. Dai, and M. P. Zhang, "Occurrence mechanism of roof-fall accidents in large-section coal seam roadways and related support design for Bayangaole coal mine, China," *Advances in Civil Engineering*, vol. 2018, Article ID 6831731, 17 pages, 2018.
- [9] Q. S. Wu, P. Kong, Q. L. Wu, X. G. Xu, X. Y. Wu, and T. Guo, "Study on overburden rock movement and stress distribution characteristics under the influence of a normal fault," *Advances in Civil Engineering*, vol. 2020, Article ID 7859148, 16 pages, 2020.
- [10] Y. T. Sun, G. C. Li, N. Zhang, Q. L. Chang, J. H. Xu, and J. F. Zhang, "Development of ensemble learning models to evaluate the strength of coal-grout materials," *International Journal of Mining Science and Technology*, vol. 31, no. 2, pp. 153–162, 2021.
- [11] C. Li, Z. Wu, W. L. Zhang, Y. H. Sun, C. Zhu, and X. H. Zhang, "A case study on asymmetric deformation mechanism of the reserved roadway under mining influences and its control techniques," *Geomechanics and Engineering*, vol. 22, no. 5, pp. 449–460, 2020.
- [12] S. C. Li, Q. Wang, H. T. Wang et al., "Model test study on surrounding rock deformation and failure mechanisms of deep roadways with thick top coal," *Tunnelling and Underground Space Technology*, vol. 47, pp. 52–63, 2015.
- [13] Y. W. Gao, C. Wang, Y. Liu, Y. Y. Wang, and L. C. Han, "Deformation mechanism and surrounding rock control in high-stress soft rock roadway: a case study," *Advances in Civil Engineering*, vol. 2021, Article ID 9950391, 15 pages, 2021.
- [14] Y. T. Sun, R. Y. Bi, Q. L. Chang et al., "Stability analysis of roadway groups under multi-mining disturbances," *Applied Sciences*, vol. 11, no. 17, p. 7953, 2021.
- [15] C. X. Zhao, Y. M. Li, G. Liu, and X. R. Meng, "Mechanism analysis and control technology of surrounding rock failure in deep soft rock roadway," *Engineering Failure Analysis*, vol. 115, p. 104611, 2020.
- [16] W. Zhang, Z. M. He, D. S. Zhang, D. H. Qi, and W. S. Zhang, "Surrounding rock deformation control of asymmetrical roadway in deep three-soft coal seam: a case study," *Journal of Geophysics and Engineering*, vol. 15, no. 5, pp. 1917–1928, 2018.
- [17] J. C. Chang, K. He, Z. Q. Yin, W. F. Li, S. H. Li, and D. D. Pang, "Study on the instability characteristics and bolt support in deep mining roadways based on the surrounding rock stability index: example of Pansan coal mine," *Advances in Civil Engineering*, vol. 2020, Article ID 8855335, 16 pages, 2020.
- [18] Q. Wang, R. Pan, B. Jiang et al., "Study on failure mechanism of roadway with soft rock in deep coal mine and confined concrete support system," *Engineering Failure Analysis*, vol. 81, pp. 155–177, 2017.
- [19] H. L. Zhang, J. B. Jiao, and L. G. Wang, "Yield evolution mechanism and control technology of roadway surrounding rock in deep mine," in *2nd international conference on electronic and mechanical engineering and information technology (EMEIT)*, vol. 23, Shenyang, PEOPLES R CHINA, 2012Atlantis Press.
- [20] Y. T. Sun, G. C. Li, J. F. Zhang, J. B. Sun, J. D. Huang, and R. Taherdangkoo, "New insights of grouting in coal mass: from small-scale experiments to microstructures," *Sustainability*, vol. 13, no. 16, p. 9315, 2021.
- [21] J. C. Chang, D. Li, T. F. Xie, W. B. Shi, and K. He, "Deformation and failure characteristics and control technology of roadway surrounding rock in deep coal mines," *Geofluids*, vol. 2020, Article ID 8834347, 15 pages, 2020.
- [22] S. Q. Yang, M. Chen, H. W. Jing, K. F. Chen, and B. Meng, "A case study on large deformation failure mechanism of deep soft rock roadway in Xin'An coal mine, China," *Engineering Geology*, vol. 217, pp. 89–101, 2017.
- [23] H. Li, W.-J. Liu, and W.-G. Qiao, "Study on high prestressed anchor beam supporting optimization technology in deep roadway," in *3rd International Conference on Civil Engineering, Architecture and Building Materials (CEABM 2013)*, pp. 353–356, Jinan, PEOPLES R CHINA, 2013.
- [24] Y. D. Jiang, L. Xiong, W. X. Zhou, X. J. Han, S. X. Mei, and J. Hu, "Research on high ground stress and soft rock roadway supporting technology of Bide coal mine," in *2nd International Conference on Structures and Building Materials (ICSBM)*, pp. 446–449, Trans Tech Publications Ltd, Hangzhou, PEOPLES R CHINA, 2012.
- [25] W. S. Xu, W. T. Xu, and Y. H. Cheng, "Research on the reasonable strengthening time and stability of excavation unloading surrounding rock of high-stress rock mass," *Geofluids*, vol. 2021, Article ID 3508661, 13 pages, 2021.
- [26] Y. T. Sun, R. Y. Bi, J. B. Sun et al., "Stability of roadway along hard roof goaf by stress relief technique in deep mines: a theoretical, numerical and field study," *Geomechanics and Geophysics for Geo-Energy and Geo-Resources*, vol. 8, no. 2, p. 16, 2022.
- [27] C. W. Zang, M. Chen, G. C. Zhang, K. Wang, and D. D. Gu, "Research on the failure process and stability control technology in a deep roadway: numerical simulation and field test," *Energy Science & Engineering*, vol. 8, no. 7, pp. 2297–2310, 2020.
- [28] R. Peng, X. R. Meng, G. M. Zhao, Z. H. Ouyang, and Y. M. Li, "Multi-echelon support method to limit asymmetry instability in different lithology roadways under high ground stress,"

- Tunnelling and Underground Space Technology*, vol. 108, article 103681, 2021.
- [29] L. J. Zheng, Y. J. Zuo, Y. F. Hu, and W. Wu, "Deformation mechanism and support technology of deep and high-stress soft rock roadway," *Advances in Civil Engineering*, vol. 2021, article 6634299, pp. 1–14, 2021.
- [30] H. W. Jing, J. Y. Wu, Q. Yin, and K. Wang, "Deformation and failure characteristics of anchorage structure of surrounding rock in deep roadway," *International Journal of Mining Science and Technology*, vol. 30, no. 5, pp. 593–604, 2020.
- [31] B. Zhang, H. Q. Zhou, Q. L. Chang, X. Zhao, and Y. T. Sun, "The stability analysis of roadway near faults under complex high stress," *Advances in Civil Engineering*, vol. 2020, article 8893842, pp. 1–10, 2020.
- [32] J. T. Hu, D. G. Lin, and R. M. Zhao, "Stabilization control techniques for a roadway in deep high-stress soft surrounding rock," in *8th Russian-Chinese Symposium on Coal in the 21st Century-Mining, Processing, Safety*, vol. 92, pp. 213–219, Atlantis Press, Kemerovo, RUSSIA, 2016.
- [33] C. K. Liu, J. X. Ren, K. Zhang, and S. J. Chen, "Numerical studies on surrounding rock deformation controlled by pressure relief groove in deep roadway," in *International Symposium on Resource Exploration and Environmental Science (REES)*, vol. 64, Ordos, PEOPLES R CHINA, 2017Iop Publishing Ltd.
- [34] Z. T. Mao and Y. P. Zhu, "Study of stability assessment method for deep surrounding rock," in *3rd International Conference on Civil, Architectural and Hydraulic Engineering (ICCAHE)*, pp. 565–569, Trans Tech Publications Ltd, Hangzhou, PEOPLES R CHINA, 2014.
- [35] G. C. Li, Y. T. Sun, J. F. Zhang et al., "Experiment and application of coalcrete on roadway stability: a comparative analysis," *Advances in Materials Science and Engineering*, vol. 2020, Article ID 6813095, 14 pages, 2020.
- [36] Y. Yuan, W. J. Wang, S. Q. Li, and Y. J. Zhu, "Failure mechanism for surrounding rock of deep circular roadway in coal mine based on mining-induced plastic zone," *Advances in Materials Science and Engineering*, vol. 2018, Article ID 1835381, 14 pages, 2018.
- [37] Z. C. Qin, B. Cao, Y. L. Liu, and T. Li, "Study on in situ stress measurement and surrounding rock control technology in deep mine," *Geofluids*, vol. 2020, Article ID 8839333, 12 pages, 2020.
- [38] M. Su and X. H. Gao, "Research of the surrounding rock deformation control technology in roadway under multiple excavations and mining," *Shock and Vibration*, vol. 2021, Article ID 6681184, 14 pages, 2021.
- [39] Y. L. Xu, K. R. Pan, and H. Zhang, "Investigation of key techniques on floor roadway support under the impacts of superimposed mining: theoretical analysis and field study," *Environment and Earth Science*, vol. 78, no. 15, p. 14, 2019.
- [40] Z. Z. Xie, N. Zhang, X. W. Feng, D. X. Liang, Q. Wei, and M. Y. Weng, "Investigation on the evolution and control of surrounding rock fracture under different supporting conditions in deep roadway during excavation period," *International Journal of Rock Mechanics and Mining Sciences*, vol. 123, article 104122, 2019.
- [41] H. Liu, J. Dai, J. Q. Jiang, P. Wang, and J. Q. Yang, "Analysis of overburden structure and pressure-relief effect of hard roof blasting and cutting," *Advances in Civil Engineering*, vol. 2019, Article ID 1354652, 14 pages, 2019.
- [42] H. Q. Yang, N. Zhang, C. L. Han et al., "Stability control of deep coal roadway under the pressure relief effect of adjacent roadway with large deformation: a case study," *Sustainability*, vol. 13, no. 8, p. 4412, 2021.
- [43] W. H. Zha and D. F. Wu, "Study on coupling relationship between surrounding rock deformation and support parameters in deep roadway," in *International Conference on Civil, Architecture and Disaster Prevention*, vol. 218, Anhui Jianzhu Univ, Sch Civil Engn, Hefei, PEOPLES R CHINA, 2018Iop Publishing Ltd.
- [44] Y. T. Sun, G. C. Li, J. F. Zhang, B. C. Yao, D. Y. Qian, and J. D. Huang, "Numerical investigation on time-dependent deformation in roadway," *Advances in Civil Engineering*, vol. 2021, Article ID 4280139, 7 pages, 2021.
- [45] S. Yang, G. C. Li, R. Y. Bi, B. C. Yao, R. G. Feng, and Y. T. Sun, "The stability of roadway groups under rheology coupling mining disturbance," *Sustainability*, vol. 13, no. 21, p. 12300, 2021.
- [46] S. Zhang, D. S. Zhang, H. Z. Wang, and S. S. Liang, "Discrete element simulation of the control technology of large section roadway along a fault to drivage under strong mining," *Journal of Geophysics and Engineering*, vol. 15, no. 6, pp. 2642–2657, 2018.

Research Article

Numerical and Experimental Study on End Effect of Waste-Soil Samples under Uniaxial Compression

Yukai Wang ¹, Xiaoli Liu ¹, and Bo Pang ²

¹State Key Laboratory of Hydrosience and Engineering, Tsinghua University, Beijing 100084, China

²Information Institute, Ministry of Emergency Management of the People's Republic of China, Beijing 100029, China

Correspondence should be addressed to Yukai Wang; wangyukai@mail.tsinghua.edu.cn

Received 12 January 2022; Revised 16 February 2022; Accepted 28 February 2022; Published 17 March 2022

Academic Editor: Yang Yu

Copyright © 2022 Yukai Wang et al. This is an open access article distributed under the Creative Commons Attribution License, which permits unrestricted use, distribution, and reproduction in any medium, provided the original work is properly cited.

In order to investigate the influence of end effect on the waste-soil sample strength under uniaxial compression, the influence law of end effect on the uniaxial compression strength is numerically simulated by the FLAC^{3D} software, and the reliability of the numerical model is verified by comparing it with the test results. Based on the above model, the influence of end effect on the lateral displacement and stress state of waste-soil samples is simulated, and the formation mechanism of end effect under uniaxial compression is revealed. The results show that, when the friction coefficient increases from 0 to 0.4, the uniaxial compression strength and percentage of triaxial compression units first increase rapidly and then slowly and then finally remain invariant. With the increase of the friction coefficient, the lateral displacement of the sample is significantly reduced. On the end surface, the nearer to the edge one is, the greater the decrease is. The triaxial compression region on the axis section is triangular in distribution; with the increase of the friction coefficient, this region increases first rapidly and then slowly and then finally remains invariant. The end effect produces lateral compression stress by reducing the lateral displacement of the end surface of samples, and lateral compression stress causes the sample to enter the triaxial compression state. With the increase of the friction coefficient, the triaxial compression region increases gradually, and thus, the uniaxial compression strength of the entire sample increases.

1. Introduction

A waste dump is an important part of the open-pit mining, whose component materials are the topsoil and rock removed during open-pit mining, and it sometimes includes recoverable surface ores and lean ores [1, 2]. In recent years, disasters of different scales have occurred in many open-pit mine waste dumps, such as Dagushan iron ore [3], Basundhara coal mine [4], and “South Field” lignite mine [5], which has caused different economic losses and even casualties. The uniaxial compression strength of waste-soil is the most important factor in determining the dump stability, so an accurate measurement of uniaxial compressive strength of waste-soil sample is essential [6, 7]. However, because of the friction between the bearing plate and waste-soil sample in the uniaxial compression experiment, the uneven stress distribution, triaxial compression region, and tensile region will arise locally [8, 9]. The above phenomena will have a

bad effect on the accurate measurement of waste-soil sample parameters and the study of the failure mechanism [10]. Therefore, it is of great significance to study the end effect of waste-soil samples under uniaxial compression.

Many scholars have conducted theoretical and experimental studies on the process of the end effect under uniaxial compression. Liang et al. [11] studied the end effect and failure mode and found that K_p had similar effects as K_s while K_n had relatively less influence on the failure strength. Yu et al. [12] found that the effect of end friction on strength is weakened to a certain extent by reducing the friction coefficient between the indenter and the end face of the specimen. Xu et al. [13] studied the influence of the end effect on rock strength in true triaxial compression and conducted that any enhancement to the rock strength with the increase of σ_2 can be attributed to the end effect. Pan et al. [14] simulated the failure process under uniaxial compression with EPCA2D and found that the attempt to improve the

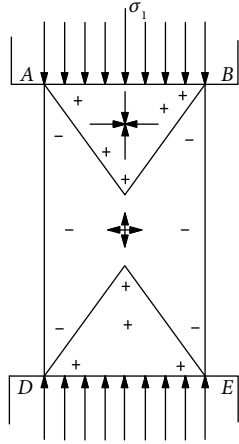


FIGURE 1: Stress distribution of waste-soil sample in uniaxial compression.

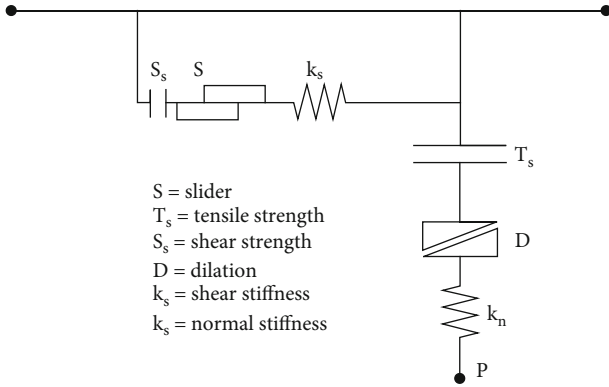


FIGURE 2: Components of the interface constitutive model. (Note: this figure is reproduced from Shuwei Sun et al. 2016.)

experimental quality by reducing the frictions was unreliable. Feng et al. [15] revealed the influence mechanism of end effect in a true triaxial compression test. Hou et al. [16] used FLAC^{3D} to simulate the failure process under uniaxial compression and found that the end effect made the axial stress at the end surface of the sample present a parabolic distribution. Jin et al. [17] simulated the dynamic compression behavior of the concrete under low strain rate conditions and found that the end effect changed the uniaxial stress state and damage distribution of the concrete, which improved the uniaxial compression strength obviously. Shi and Li [18] conducted true triaxial simulation experiments and came to the conclusion that the end effect could produce false intermediate principal stress to increase the maximum failure stress. Liu et al. [19] discussed the evolutionary rule of flaws in rock and its effect on the macromechanical uniaxial compression strength (UCS).

In general, the existence of the end effect in uniaxial compression experiments has been confirmed by many scholars and experts. However, research on the formation mechanism and influence process of the end effect is limited. To further study the formation mechanism of the end effect, a uniaxial compression model under different friction coeffi-

cients is established firstly. Then, through uniaxial compression experiments, the variation law of uniaxial compression strength with friction coefficient is obtained, and the reliability of the model is verified. On this basis, the present paper uses a numerical simulation method to study the stress-strain state of waste-soil samples, and the formation mechanism and influence process of the end effect are summarized. The objectives of this paper are the following: (1) to obtain the variation law of uniaxial compression strength with friction coefficient; (2) to discover the stress-strain state of waste-soil samples under different friction coefficients; and (3) to reveal the formation mechanism of the end effect in uniaxial compression. The main contribution of this study is revealing the formation mechanism, evolutionary process, critical friction coefficient, and failure pattern of the end effect under uniaxial compression, which provides a reference for reducing and eliminating the end effect.

2. Problem Description and Methodology

2.1. Problem Description. The problem description is given in Figure 1. During the uniaxial compression of the waste-soil sample, the uncoordinated deformation between the waste-soil sample and bearing plate is caused by the friction between them, which results in the formation of a stress hoop on the end surface and the rise of a “funnel-shaped” stress area (see Figure 1) [20]. Due to the horizontal constraint on the end surface of waste-soil samples, the compression stress (+) is formed in two triangular areas that contact the bearing plates AB and DE. Due to the decrease of the end constraint, the tensile stress (-) is formed in the middle part of the waste-soil sample [21]. The above uneven stress distribution will lead to the increase of the uniaxial compression strength of waste-soil samples, which will bring adverse effects on the accurate measurement of waste-soil sample parameters and the study of the rock failure mechanism.

2.2. Simulation of Sample-Plate Interface. Compared with other mechanical models, a linear Coulomb shear strength model can better simulate the transfer of stress and deformation between different material interfaces, so the interfaces between samples and plates are characterized by a linear Coulomb shear strength model in this study [22–24]. Interfaces have the properties of friction, cohesion, dilation, normal and shear stiffness, and tensile and shear bond strength. Figure 2 illustrates the components of the constitutive model acting at an interface node (P).

The normal and shear forces that describe the elastic interface response are determined by the following equations:

$$\begin{aligned} F_n^{(t+\Delta t)} &= k_n \mu_n A + \sigma_n A, \\ F_{si}^{(t+\Delta t)} &= F_{si}^{(t)} + k_n \Delta \mu_{si}^{(t+(1/2)\Delta t)} A + \sigma_{si} A, \end{aligned} \quad (1)$$

where $F_n^{(t+\Delta t)}$ and $F_{si}^{(t+\Delta t)}$ are the normal and shear force at time $(t + \Delta t)$, respectively, μ_n is the absolute normal penetration of the interface node into target face, $\Delta \mu_{si}$ is the

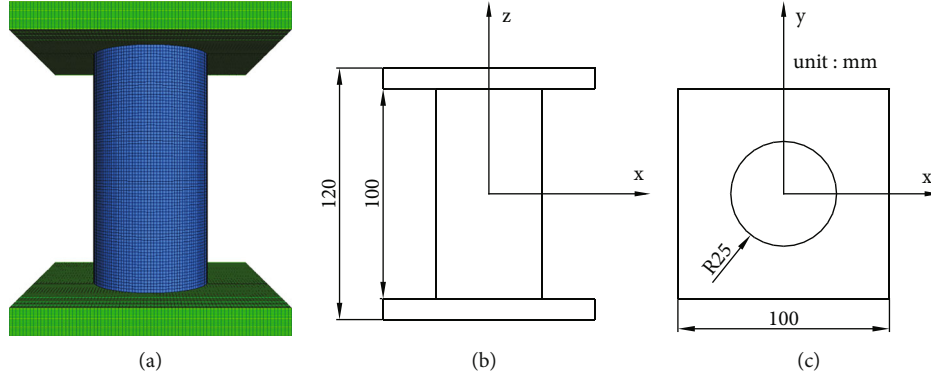


FIGURE 3: Numerical model. (a) Three-dimension view. (b) Elevation view. (c) Top view.

TABLE 1: Table of mechanical parameters of the model.

Material	Bulk modulus (Pa)	Shear modulus (Pa)	Cohesion (MPa)	Friction angle ($^{\circ}$)	Dilation angle ($^{\circ}$)
Waste-soil sample	2×10^2	1×10^2	2.558	36	10
Bearing plate	2×10^5	1×10^5			

TABLE 2: Table of mechanical parameters of the contact surface.

Material	Cohesion (MPa)	Friction angle ($^{\circ}$)	Normal stiffness (GPa m^{-1})	Tangential stiffness (GPa m^{-1})
Contact surface	0	0-27	0.2	0.2

incremental relative shear displacement vector, k_n and k_s are the normal and shear stiffness, respectively, σ_n is the additional normal stress added due to interface stress initialization, σ_{si} is the additional shear stress vector due to interface stress initialization, and A is the representative area associated with an interface node.

In this study, the use of an interface element covers the sample-plate separation, and nonlinear analysis is carried out; the value for the interface stiffness should be high enough to minimize the contribution of those elements to the accumulated displacements. A good rule-of-thumb is that k_n and k_s should be set to at least ten times the equivalent stiffness of the stiffest neighboring zone [25]. To satisfy this requirement, k_n and k_s for the interface elements are both set equal to 0.2 GPa m^{-1} in the current analyses. These values were also adopted by Comodromos and Papadopoulos [26] in their benchmark test on interface elements.

2.3. Modeling of Uniaxial Compression. The numerical model uses cylindrical waste-soil samples with dimensions of $50 \text{ mm} \times 100 \text{ mm}$; the bearing plate's size is $100 \text{ mm} \times 100 \text{ mm} \times 10 \text{ mm}$ [27]. As shown in Figure 3, the blue part represents the waste-soil sample, whereas the green part indicates the bearing plate; the coordinate origin is located at the geometric center of the specimen. These two media, with 483003 grid-points and 460800 zones, compose the calculation model [28, 29]. The interface between the bearing plate and the waste-soil sample is used to simulate the

roughness between the bearing plate and the waste-soil sample [30]. The tangent of the internal friction angle of contact surfaces changes within 0~0.5, and the variation gradient is 0.1. In the numerical simulations, the sample loading mode is uniform distribution displacement loading on the bottom surface with a loading speed of $1.2 \times 10^{-6} \text{ m/step}$. The Mohr-Coulomb failure criterion is adopted as the calculation principle. Tables 1 and 2 list the model calculation parameters [31, 32]. The cohesive forces of the waste-soil sample and contact surface are expressed by C_s and C_c , respectively, and the internal friction angle of the waste-soil sample and contact surface are expressed by φ_s and φ_c , respectively.

In numerical calculations, the axial force is determined using the integral approach at the location with the same z -coordinate. The axial force is divided by the cross-sectional area to determine the axial stress [33–35]. Peak points of stress-strain curves are selected as failure points to study the relationship between the end effect and the uniaxial compression strength.

3. Validation of the Calculation Model

First, uniaxial compression strengths of waste-soil samples under the different friction coefficients are measured by uniaxial compression tests in this paper. Then, the reliability of the numerical analysis model and analysis method is verified by comparing the consistency between the test results and the simulation results [36, 37]. On this basis, the formation mechanism of the end effect is studied by numerical simulation.

3.1. Materials. The chemical composition of test soil samples has a great influence on the friction coefficient between the end surface and the waste-soil sample. The friction coefficient needs to be measured accurately to verify the reliability of the numerical model; it is necessary to give the chemical composition in detail. Three kinds of materials including



FIGURE 4: The (a) waste-soil and (b) binder used in this test.

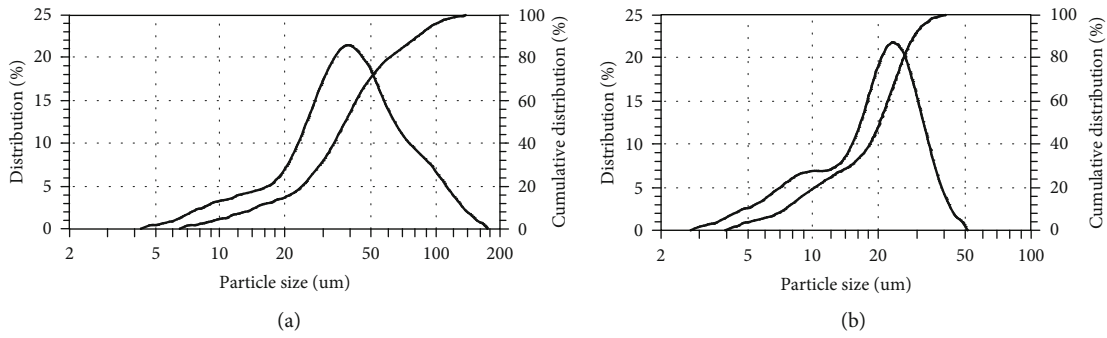


FIGURE 5: Particle size distribution of (a) waste-soil and (b) binder.

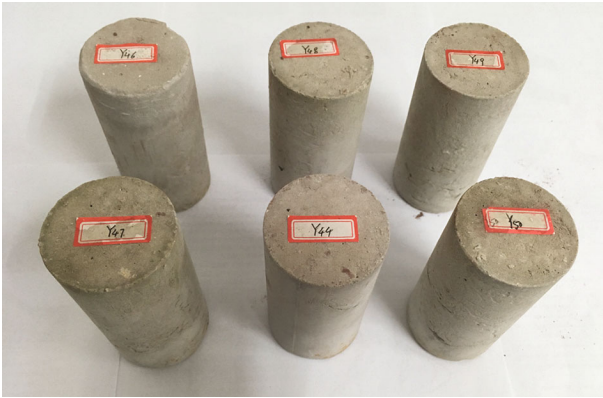


FIGURE 6: Samples.

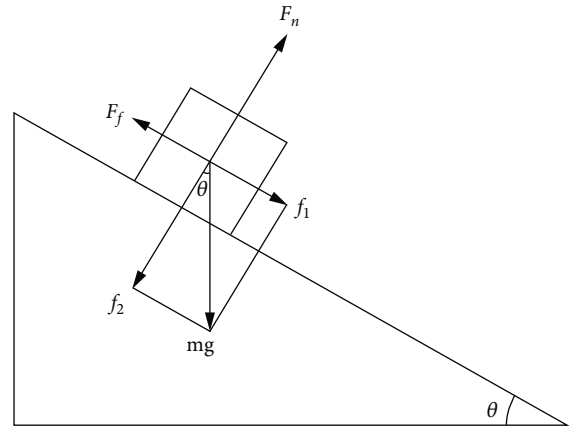


FIGURE 7: Sketch map of slope balance method.

the waste-soil, binder, and water were used in this research. The waste-soil utilized in this study is from a gold ore process plant of Guizhou Jinfeng Mining Limited (see Figure 4(a)), its absolute density is 2.59 t/m^3 , its packing density is 1.6 t/m^3 , its stopping angle is 35° , and its water content is less than 0.25% , so it can be identified as dry sand. The mineral composition of the waste-soil mainly includes quartz, chlorite, calcite, diopside, and a small amount of gypsum, pyrite, and sericite. The chemical composition of the waste-soil mainly includes SiO_2 , Al_2O_3 , CaO , FeO , and MgO . The particle size distribution of the waste-soil measured by the LS-C(IIA)-type laser particle sizer at China

University of Mining and Technology (Beijing) is shown in Figure 5(a). The effective particle sizes of the waste-soil are $D_{10} = 14.55 \mu\text{m}$, $D_{30} = 26.6 \mu\text{m}$, $D_{90} = 82.3 \mu\text{m}$, and $D_{97} = 106.71 \mu\text{m}$; the constrained particle size is $D_{60} = 54.27 \mu\text{m}$; the medium size $D_{50} = 38.30 \mu\text{m}$; the nonuniformity factor is $\varphi = 3.73$; and the curvature coefficient is $C_u = 0.896$, so the waste-soil belongs to the fine-grained soil.

The binder used in this study is the Portland cement of 32.5 MPa (P.O. 32.5, see Figure 4(b)). The chemical composition of the binder mainly includes CaO , SiO_2 , Al_2O_3 , Fe_2O_3 , and MgO . The particle size distribution of the binder



FIGURE 8: TYE-300D type test machine.

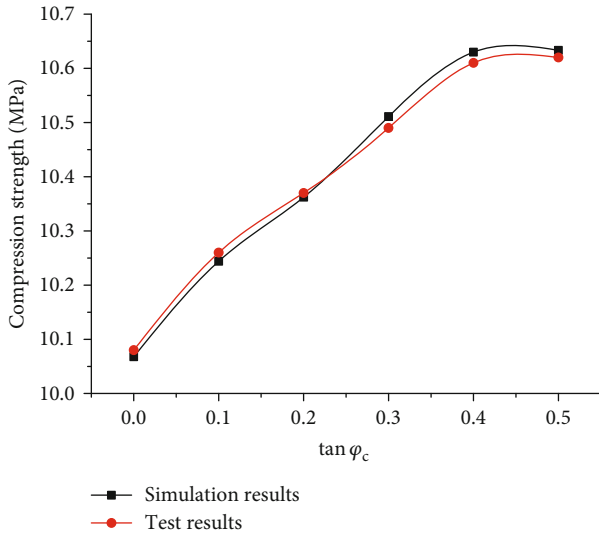


FIGURE 9: Uniaxial compression strength curve.

is shown in Figure 5(b). The effective particle sizes of the binder are $D_{10} = 7.48 \mu\text{m}$, $D_{30} = 12.26 \mu\text{m}$, $D_{90} = 29.60 \mu\text{m}$, and $D_{97} = 34.54 \mu\text{m}$; the constrained particle size is $D_{60} = 25.30 \mu\text{m}$; the medium size is $D_{50} = 20.39 \mu\text{m}$; the non-uniformity factor is $\varphi = 3.38$, and the curvature coefficient is $C_u = 0.794$. The water used in this study is common tap water.

3.2. Sample Preparation. The process of waste-soil sample preparation can be divided into three main parts: mortar mixing, molding, and sample maintenance [38–42]. (1) Pour the waste-soil and cementing agent into the mixing pot and stir evenly, and then add tap water into the mixing pot and stir evenly again. The mass ratio of water, cementing agent, and waste-soil is 7.6:1:10. Stir the slurry with a 5K5SS-type lifting multifunction mixer at low speed for 2 minutes, and then pause for 1 minute. Scrape the slurry on the mixing blades and on the wall of the mixing pot into the mixing pot, and then upturn the bottom slurry. Stir the slurry at high speed for 4 minutes. Complete the mixing and close the machine. (2) Pour the uniform-mixed slurry into the cylindrical test mold. The diameter of the cylindrical test mold is 5 cm, and the height is 10 cm. Then, tamp the slurry with

a tamping bar along the periphery of the test mold. Each waste-soil sample is tamped 30 times, and 20 instances of manual vibration are needed to drive out the bubbles in the slurry. Then, take a small amount of slurry to fill up the test mold, use a small scraper to smooth the surface, seal the test mold with a plastic cover, and seal the plastic cover with waterproof tape to prevent evaporation of the water in the mold. The test mold is finished and placed in a horizontal position. (3) Place the test mold in the thermostat box with a temperature of $20 \pm 1^\circ\text{C}$ and a relative humidity $\geq 90\%$. One day later, disassemble the test mold and remove the waste-soil sample, and then leave the waste-soil sample in the thermostat box for 28 days.

The waste-soil sample taken from the thermostat box may have an irregular shape because of the settlement phenomenon and small breakage during the process of taking out the block. Therefore, certain processing is needed, especially the upper section of the waste-soil sample, which needs to be smoothed with the metal scraper, to ensure that the load applied to the waste-soil sample is uniform when the mechanical properties are tested. Put the rapidly processed waste-soil sample into a sealed bag to limit the humidity change. Test waste-soil samples are shown in Figure 6.

3.3. Experiment Scheme. In the uniaxial compression test, the friction coefficient between the end surface and the waste-soil sample is adjusted by changing the surface roughness of the bearing plate and applying different types of lubricating oil; the friction coefficient is measured by the slope balance method (see Figure 7) [43, 44]. The gravity, slope support force, and friction force of the waste-soil sample are expressed by mg , F_n , and F_f , respectively; f_1 and f_2 are the components of the gravity along and perpendicular to the slope, respectively. For testing convenience, a cube waste-soil sample with a size of 4 cm is adopted to measure the friction coefficient. Adjust the slope (bearing plate) angle (θ) to ensure that the waste-soil sample is in the critical sliding state, at which point there are

$$\begin{aligned} F_f &= f_1 = mg \sin \theta, \\ F_n &= f_2 = mg \cos \theta, \\ F_f &= \mu F_n, \end{aligned} \quad (2)$$

So the conclusion of $\mu = \tan \theta$ is drawn. Due to the limitations of the experimental conditions, the case of $\mu = \tan \theta = 0.02$ is considered a complete smooth contact.

The uniaxial compression experiment was carried out using a TYE-300D-type cement mortar compression bending test machine (see Figure 8) at China University of Mining and Technology (Beijing), and the loading rate is 0.1 kN/s. In the process of testing, the test machine can record the load applied to the waste-soil sample at any time. When the waste-soil sample suddenly breaks down, the maximum load of the waste-soil sample is recorded, the test machine shuts down automatically, and the corresponding strength is the uniaxial compression strength of the waste-soil sample [45].

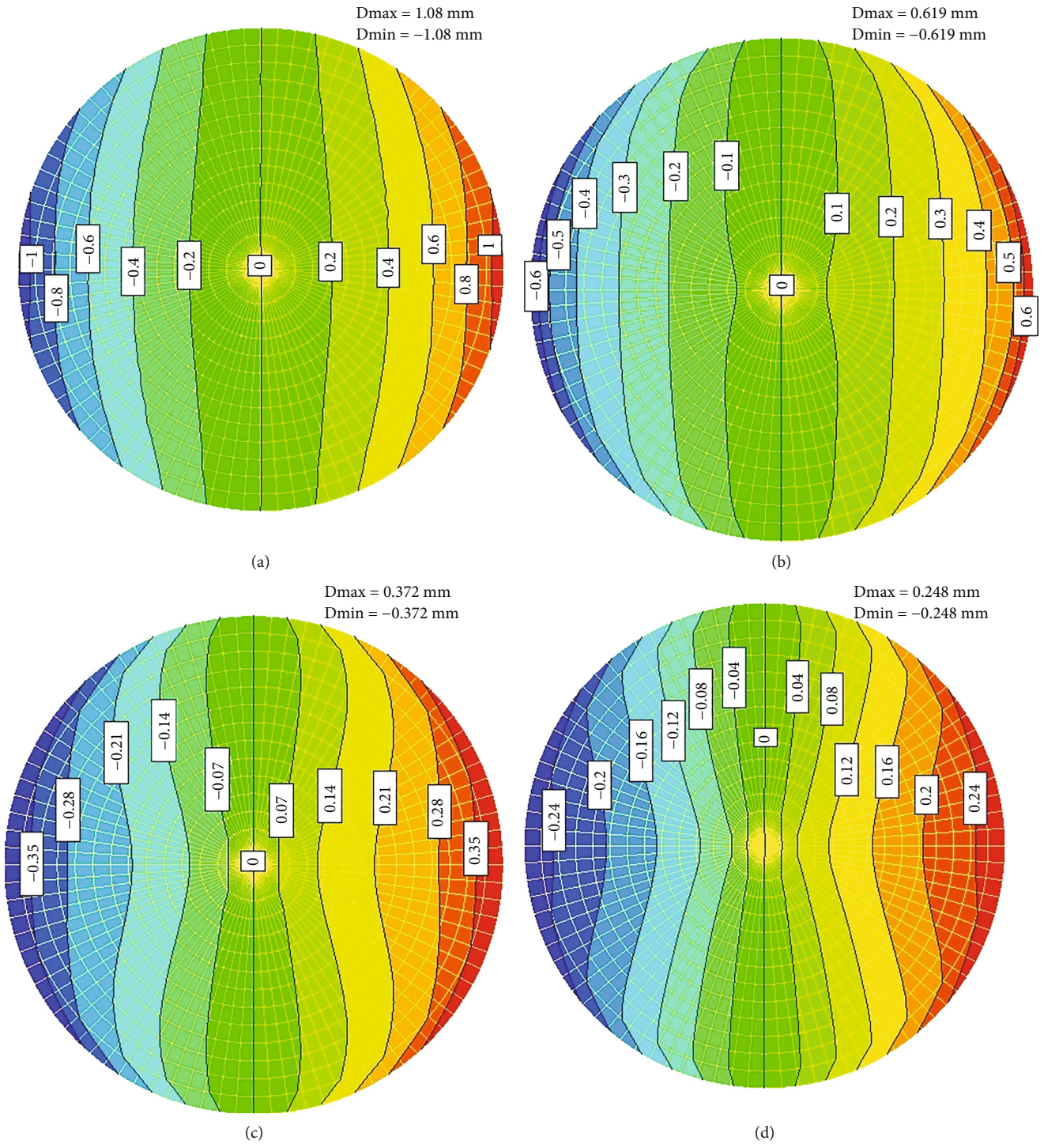


FIGURE 10: Continued.

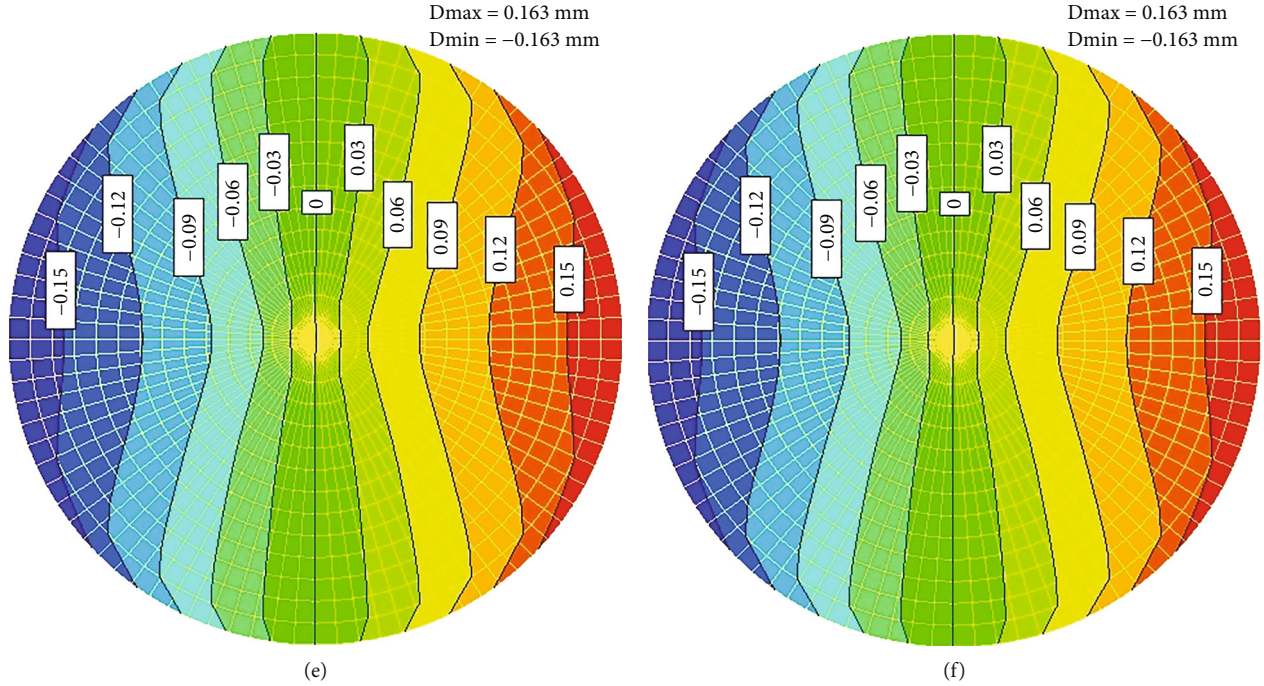


FIGURE 10: Isoline of lateral displacement. (a) $\tan \varphi_c = 0$. (b) $\tan \varphi_c = 0.1$. (c) $\tan \varphi_c = 0.2$. (d) $\tan \varphi_c = 0.3$. (e) $\tan \varphi_c = 0.4$. (f) $\tan \varphi_c = 0.5$.

3.4. Test Results. Figure 9 shows the uniaxial compression strength of waste-soil samples with the friction coefficient varying from 0 to 0.5. When the end surface of the waste-soil sample is smooth ($\tan \varphi_c = 0$), the uniaxial compression strength is 10.06 MPa. When the friction coefficient is within the range 0-0.4, the uniaxial compression strength sharply increases from 10.06 MPa to 10.6 MPa with the increase of the friction coefficient. After the friction coefficient reaches 0.4, the uniaxial compression strength remains 10.6 MPa invariantly, and the end friction has no further influence on the uniaxial compression strength. The curve slope initially remains invariant and then gradually decreases to 0. The maximum slope of the curve is 1.39 MPa, which indicates that, when the friction coefficient increases by 1%, the compression strength increases by 13.9 kPa. The result of the uniaxial compression test is almost the same as that of the numerical analysis, which verifies the reliability of the numerical analysis model and analysis method. The uniaxial compression strength curve also indicates that the end effect enhances the axial load capacity of the waste-soil samples significantly.

4. Calculation Results

4.1. Influence of End Effect on Lateral Displacement. The end effect directly affects the lateral displacement at the end of the waste-soil sample. Figure 10 shows the lateral displacement of the waste-soil sample with the coordinate of $z = -50$ mm. When the end surface is smooth ($\tan \varphi_c = 0$), the lateral displacement of each node on the end surface is outward along the radius; the displacement isoline is a set of vertical parallel lines with uniform distribution. The closer to the center of the end surface one is, the smaller the lateral dis-

placement is; the lateral displacement increases with the increase of distance from the center point, with the maximum displacement of 1.08×10^{-3} m. With the increase of the friction coefficient, isolines near the center first concave inward, forming a W shape; then, marginal isolines concave inward, forming a set of contour lines with a W shape. As the friction coefficient increases from 0 to 0.4, the displacement of each node of the end surface decreases; the maximum lateral displacement decreases from 1.08×10^{-3} m to 1.63×10^{-4} m. After the friction coefficient reaches 0.4, the end friction has no further influence on the lateral displacement. This phenomenon indicates that the end friction significantly prevents lateral deformation of the waste-soil sample; the closer to the edge one is, the greater the influence of the end friction is.

4.2. Influence of End Effect on Principal Stress State. In this paper, the region where the maximum principal stress, the minimum principal stress, and the intermediate principal stress are compression stress is defined as the triaxial compression zone. The distribution of triaxial compression zones along the axis section is shown in Figure 11, and the green part represents the triaxial compression zone. When the end surface is smooth, all of the regions are almost tensile stress zones, and this is the reason why the failure mode of the waste-soil sample is columnar cleavage. When the friction coefficient varies from 0 to 0.4, the triaxial compression regions on the axial section are approximately two isosceles triangles whose apex angle is approximately 74° . Triaxial compression regions in a three-dimensional space are two cones whose bottoms are end surfaces of the waste-soil sample. With the increase of the friction coefficient, the base and height of the isosceles triangle increase,

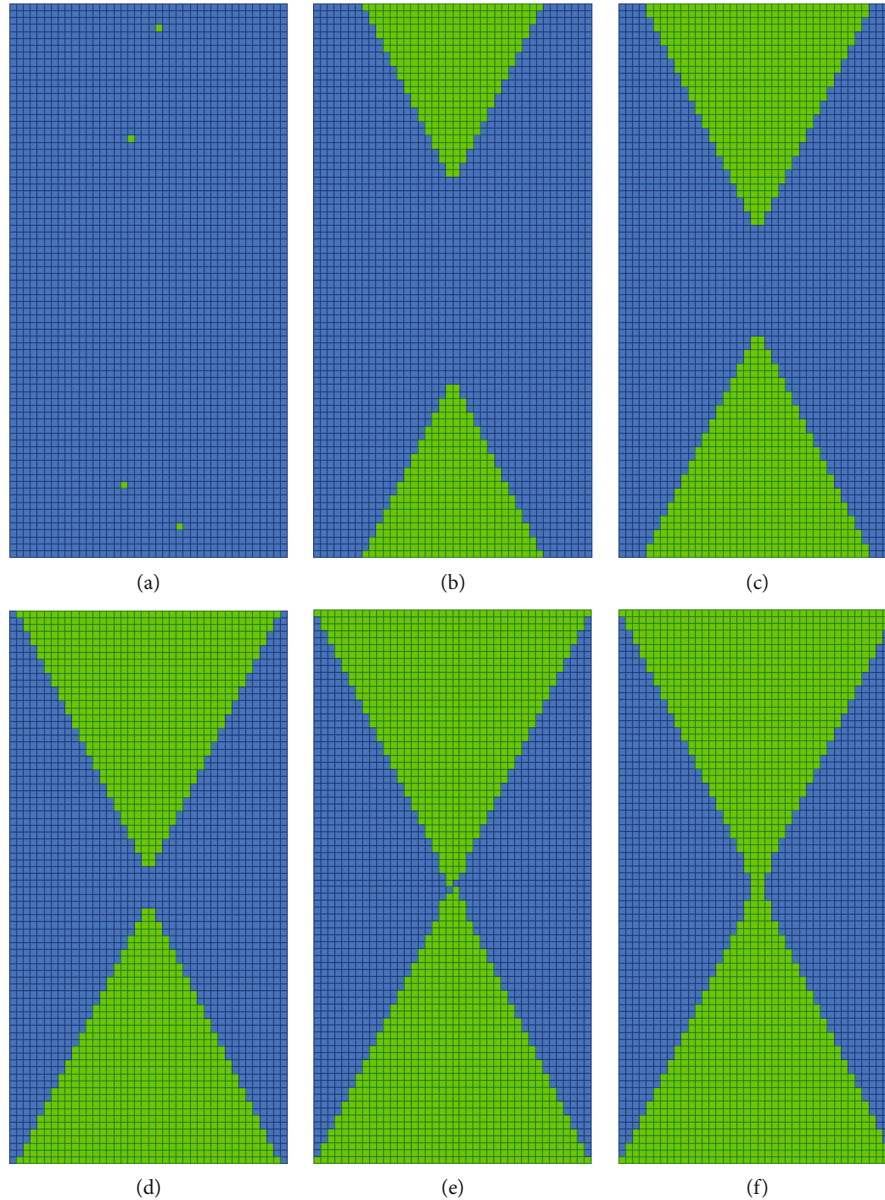


FIGURE 11: Distribution of triaxial compression area. (a) $\tan \varphi_c = 0$. (b) $\tan \varphi_c = 0.1$. (c) $\tan \varphi_c = 0.2$. (d) $\tan \varphi_c = 0.3$. (e) $\tan \varphi_c = 0.4$. (f) $\tan \varphi_c = 0.5$.

while the ratio of the height to the base remains constant. The increase rate of the height and base of the isosceles triangle gradually decreases to 0. When the friction coefficient reaches 0.4, the top and bottom triangles are joined together, and the triaxial compression zone remains unchanged. This is the reason why the failure mode of the waste-soil sample is transformed from columnar cleavage to conical shear fracture with the contact surface varying from smooth to rough.

In addition, the change of triaxial compression regions directly affects the number of triaxial compression units. In this paper, the change of triaxial compression units is described by the percentage of triaxial compression units to total units, and the number of triaxial compression units is counted by the homemade FISH function. The percentage of triaxial compression units is presented in Figure 12. When the end surface is smooth, there are almost no triaxial com-

pression units, and the percentage of triaxial compression units is essentially equal to 0. When the friction coefficient increases from 0 to 0.3, the percentage of triaxial compression units increases linearly, and the percentage value increases from 0 to 28.42%. When the friction coefficient increases from 0.3 to 0.4, the percentage of triaxial compression units shows an upward trend from 28.42% to 32.91%, but the increase rate gradually decreases to 0. After the friction coefficient reaches the threshold of 0.4, the percentage of triaxial compression units does not increase with the increase of the friction coefficient.

5. Analysis and Discussion

From the calculation results shown in Figures 9 and 12, uniaxial compression strength has a similar change tendency

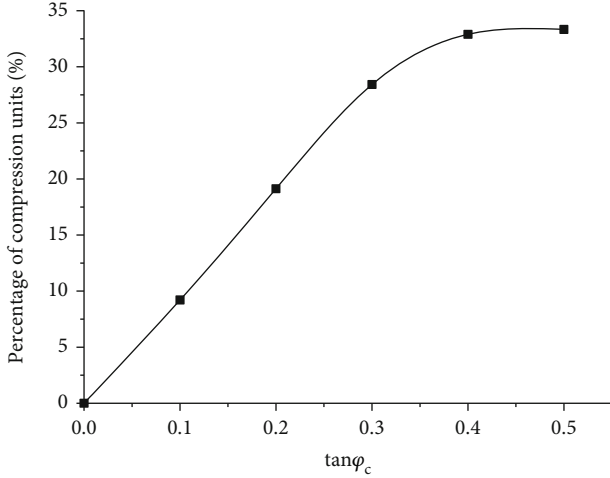


FIGURE 12: Percentage of triaxial compression units.

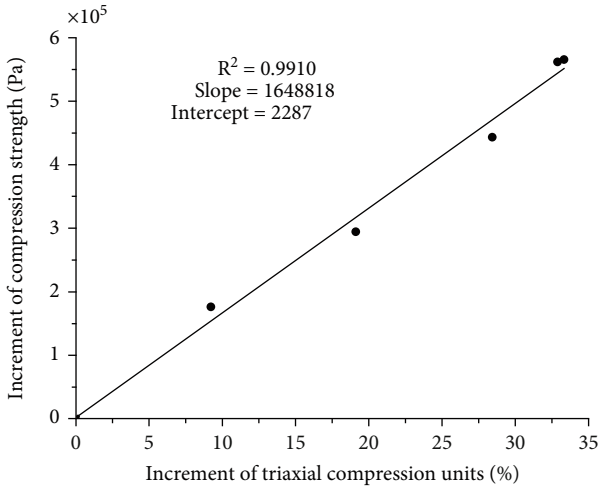


FIGURE 13: Increment between triaxial compression unit and compression strength.

with the percentage of triaxial compression units. The percentage increment of triaxial compression units and the uniaxial compression strength increment show an obvious linear relationship (see Figure 13). As shown in Figure 13, the vertical axis represents the increment of uniaxial compression strength between the rough and smooth end surface; the horizontal axis represents the increment of triaxial compression units between the rough and smooth end surface. Via linear fitting, the correlation coefficients of the simple fitting are determined to be equal to 0.991, which proves the reliability of the fitting. Figure 13 also shows that the corresponding slope is 1.6488 MPa, which indicates that, when the triaxial compression units increase by 1%, the uniaxial compression strength increases by 16.4882 kPa. This finding indicates that the end effect enhances the axial load capacity of the waste-soil samples by increasing the triaxial compression units.

The end effect directly reduces the lateral displacement near the end surface. The lateral compression stress (σ_3) is caused by restricting the lateral expansion of waste-soil samples, so the smaller the lateral displacement is, the greater the

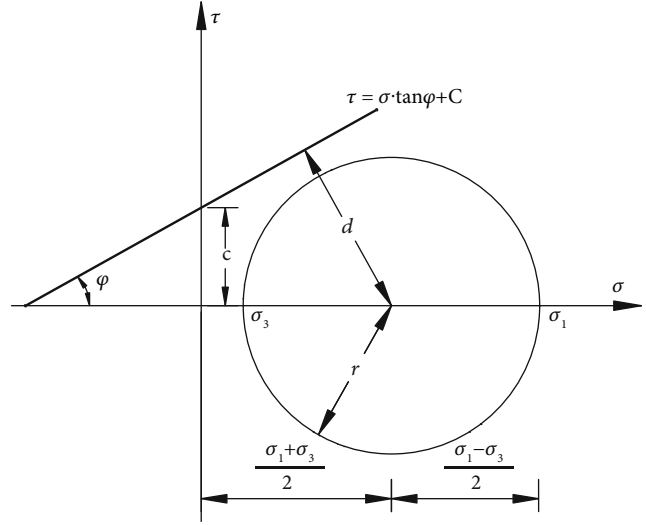


FIGURE 14: The Mohr strength curve and the Mohr circle.

lateral compression stress is. It is known from the lateral displacement distribution of waste-soil samples (see Figure 10) that, the closer to the end surface one is, the greater the lateral compression stress is; the greater the roughness of the contact surface is, the greater the lateral compression stress is. Accordingly, the principal stress state of samples under different contact surface parameters is shown in Figure 11. Compression stress is positive while tensile stress is negative in geotechnical mechanics, so the Mohr strength curve and Mohr circle can be described in Figure 14. The formulas for the Mohr circle and Mohr strength curve are $(\sigma - ((\sigma_1 + \sigma_3)/2))^2 + \tau^2 = (\sigma_1 - \sigma_3)^2/4$ and $\tau = \sigma \tan \phi + C$, respectively. When the distance from the Mohr circle's center to the strength curve is greater than the Mohr circle's radius, that is, $\Delta = d - r$, the waste-soil sample is in the elastic stage; otherwise, shear failure occurs in the waste-soil sample. By substituting rock mechanics parameters ($\phi_s = 36^\circ$ and $C_s = 2.558$ MPa) into the above equations, we can get $\Delta = 0.7939\sigma_3 - 0.2601\sigma_1 + 2.0694$. When the lateral stress (σ_3) is greater than 0, greater axial stress (σ_1) is required to make the Δ less than 0, so the lateral compression stress can improve the axial compression strength of the waste-soil sample. This is why the uniaxial compression strength and triaxial compression units have the same variation tendency and linear increments.

Through the above analysis, the formation mechanism of the end effect is described as follows. The end effect produces lateral compression stress by reducing the lateral displacement of the end surface of waste-soil samples, and the lateral compression stress makes the waste-soil sample locally enter the triaxial compression state. With the increase of the friction coefficient of the end surface, the triaxial compression region increases gradually, and thus, the uniaxial compression strength of the entire waste-soil sample is increased.

6. Conclusions

In this paper, the formation mechanism of the end effect in uniaxial compression was revealed through uniaxial

compression tests and by simulating the uniaxial compression process of cylindrical waste-soil samples under different contact surface parameters using a finite difference technique (FLAC^{3D}). The following findings are obtained:

- (1) When the friction coefficient increases from 0 to 0.3, the uniaxial compression strength linearly increases from 10.06 MPa to 10.52 MPa. When the friction coefficient increases from 0.3 to 0.4, the uniaxial compression strength gradually increases from 10.52 MPa to 10.6 MPa. After the friction coefficient reaches 0.4, the uniaxial compression strength remains invariant at 10.6 MPa
- (2) With the increase of the friction coefficient, the lateral displacement of the waste-soil sample decreases significantly. On the end surface of the waste-soil sample, the nearer to the edge one is, the greater the decrease is, and the isoline of the lateral displacement is transformed from a parallel line to a W-shaped curve
- (3) The triaxial compression region on the axis section is a triangle whose base is the end surface of the waste-soil sample. When the friction coefficient increases from 0 to 0.4, the triangle area increases first rapidly and then slowly. After the friction coefficient reaches the threshold of 0.4, the triaxial compression region remains constant. With the increase of the friction coefficient, the uniaxial compression strength and triaxial compression units have the same variation tendency and linear increments
- (4) The end effect produces the lateral compression stress by reducing the lateral displacement of the end surface of the waste-soil samples, and the lateral compression stress makes the waste-soil sample locally enter the triaxial compression state. With the increase of the friction coefficient of the end surface, the triaxial compression region increases gradually, and thus, the uniaxial compression strength of the entire waste-soil sample increases

Data Availability

All data used to support the findings of this study are included within the article.

Conflicts of Interest

The authors declare that they have no conflicts of interest.

Acknowledgments

This work was supported by the National Key Research and Development Plan (No. 2018YFC1504902), the National Natural Science Foundation of China (No. 52079068), and the State Key Laboratory of Hydrosience and Hydraulic Engineering (No. 2021-KY-04).


References

- [1] Y. Wang, S. Sun, B. Pang, and L. Liu, "Base friction test on unloading deformation mechanism of soft foundation waste dump under gravity," *Measurement*, vol. 163, no. 8, article 108054, 2020.
- [2] J. Wang and C. Chen, "Stability analysis of slope at a disused waste dump by two-wedge model," *International Journal of Mining, Reclamation and Environment*, vol. 31, no. 8, pp. 575–588, 2017.
- [3] Y. Wang, S. Sun, and L. Liu, "Mechanism, stability and remediation of a large scale external waste dump in China," *Geotechnical and Geological Engineering*, vol. 37, no. 6, pp. 5147–5166, 2019.
- [4] B. Poulsen, M. Khanal, A. Rao, D. Adhikary, and R. Balusu, "Mine overburden dump failure: a case study," *Geotechnical & Geological Engineering*, vol. 32, no. 2, pp. 297–309, 2014.
- [5] E. Steiakakis, K. Kavouridis, and D. Monopolis, "Large scale failure of the external waste dump at the "south field" lignite mine, northern Greece," *Engineering Geology*, vol. 104, no. 3–4, pp. 269–279, 2009.
- [6] Y. Bao, X. Han, J. Chen et al., "Numerical assessment of failure potential of a large mine waste dump in Panzhihua City, China," *Engineering Geology*, vol. 253, no. 4, pp. 171–183, 2019.
- [7] Y. Wang, S. Sun, B. Pang, and L. Liu, "Experimental study on unloading deformation mechanisms of soft base dumps of open-pit mines," *Chinese Journal of Rock Mechanics and Engineering*, vol. 39, no. 2, pp. 359–373, 2020.
- [8] Z. Li, J. Song, X. Du, and X. Yang, "Size effect of confined concrete subjected to axial compression," *Journal of Central South University*, vol. 21, no. 3, pp. 1217–1226, 2014.
- [9] J. Rimen and D. Arghya, "Size effect in FRP-confined concrete under axial compression," *Journal of Composites for Construction*, vol. 21, no. 6, 2017.
- [10] J. Dong and L. Shao, "Study of unsaturated compacted soil considering influence of end effect by triaxial test," *Chinese Journal of Rock Mechanics and Engineering*, vol. 29, no. 9, pp. 1937–1944, 2010.
- [11] Z. Liang, X. Wu, S. Tang, and W. Wang, "Numerical simulation on end effect of rock specimens based on the anisotropic interface element model," *Journal of Basic Science and Engineering*, vol. 26, no. 3, pp. 526–537, 2018.
- [12] J. Yu, Y. Wang, Q. Wang, Q. Zhu, and S. Fu, "Study of triaxial mechanical test based on MSV method for reducing end friction effect," *Journal of China Three Gorges University*, vol. 41, no. 5, pp. 59–64, 2019.
- [13] Y. Xu, M. Cai, X. Zhang, and X. Feng, "Influence of end effect on rock strength in true triaxial compression test," *Canadian Geotechnical Journal*, vol. 54, no. 6, pp. 862–880, 2017.
- [14] P. Pan, H. Zhou, and X. Feng, "Research on effect of loading conditions on failure processes of rocks with different sizes under uniaxial compression," *Chinese Journal of Rock Mechanics & Engineering*, vol. 27, no. 2, pp. 3636–3642, 2008.
- [15] X. Feng, X. Zhang, C. Yang, R. Kong, X. Liu, and S. Peng, "Evaluation and reduction of the end friction effect in true triaxial tests on hard rocks," *International Journal of Rock Mechanics & Mining Sciences*, vol. 4, no. 2, pp. 699–704, 2017.
- [16] H. Hou, S. Zhang, and G. Wu, "Influence of stress distribution regulation of sample ends on uniaxial compression with pad,"

- Journal of Anhui University of Science and Technology(Natural Science)*, vol. 35, no. 3, pp. 59–62, 2015.
- [17] L. Jin, Y. Han, Z. Ding, and X. Du, “Effect of end friction on the dynamic compressive mechanical behavior of concrete under medium and low strain rates,” *Journal of Vibration and Shock*, vol. 2016, no. 11, pp. 1–20, 2016.
- [18] L. Shi and X. Li, “Analysis of end friction effect in true triaxial test,” *Rock and Soil Mechanics*, vol. 30, no. 4, pp. 1159–1164, 2009.
- [19] X. Liu, S. Wang, E. Wang, J. Wang, and B. Hu, “Evolutionary rules of flaws in rock subjected to uniaxial compression and rock strength,” *Chinese Journal of Rock Mechanics and Engineering*, vol. 27, no. 6, pp. 1195–1201, 2008.
- [20] M. Shen and J. Chen, *Rock Mass Mechanics*, Tongji University Press, Shanghai, China, 2006.
- [21] J. Wang and S. Sun, *Open-pit mine slope engineering*, Science Press, Beijing, China, 2016.
- [22] S. Sun, W. Wang, and F. Zhao, “Three-dimensional stability analysis of a homogeneous slope reinforced with micropiles,” *Mathematical Problems in Engineering*, vol. 2014, Article ID 864017, 11 pages, 2014.
- [23] Q. Du, X. Liu, and E. Wang, “Strength reduction of coal pillar after CO₂ sequestration in abandoned coal mines,” *Minerals*, vol. 7, no. 2, p. 26, 2017.
- [24] S. Dai, X. Liu, and K. Nawnit, “Experimental study on the fracture process zone characteristics in concrete utilizing DIC and AE methods,” *Applied Sciences*, vol. 9, no. 7, p. 1346, 2019.
- [25] E. M. Comodromos and K. D. Pitilakis, “Response evaluation for horizontally loaded fixed-head pile groups using 3-D non-linear analysis,” *International Journal for Numerical and Analytical Methods in Geomechanics*, vol. 29, no. 6, pp. 597–625, 2005.
- [26] E. M. Comodromos and M. C. Papadopoulou, “Response evaluation of horizontally loaded pile groups in clayey soils,” *Geotechnique*, vol. 62, no. 4, pp. 329–339, 2012.
- [27] S. Sun, H. Lin, and L. Ren, *Application of FLAC3D in Geotechnical Engineering*, China Water and Power Press, Beijing, China, 2011.
- [28] H. Lin, P. Cao, and Y. Wang, “Numerical simulation of a layered rock under triaxial compression,” *International Journal of Rock Mechanics and Mining Sciences*, vol. 60, no. 6, pp. 12–18, 2013.
- [29] X. Fan, R. Chen, H. Lin, H. Lai, C. Zhang, and Q. Zhao, “Cracking and failure in rock specimen containing combined flaw and hole under uniaxial compression,” *Advances in Civil Engineering*, vol. 2018, Article ID 9818250, 15 pages, 2018.
- [30] S. Sun, F. Zhao, and K. Zhang, “Stability of slopes reinforced with truncated piles,” *Advances in Materials Science and Engineering*, vol. 2016, Article ID 1570983, 16 pages, 2016.
- [31] X. Sun, X. Fang, and L. Guan, *Mechanics of Materials*, High Education Press, Beijing, China, 2009.
- [32] J. Liu, “Simulation to the effects on strain localization due to end friction,” *Soil Engineering and Foundation*, vol. 20, no. 5, pp. 47–50, 2006.
- [33] H. Lin, Z. Xiong, T. Liu, R. Cao, and P. Cao, “Numerical simulations of the effect of bolt inclination on the shear strength of rock joints,” *International Journal of Rock Mechanics & Mining Sciences*, vol. 66, no. 1, pp. 49–56, 2014.
- [34] H. Sun, X. Liu, and J. Zhu, “Correlational fractal characterisation of stress and acoustic emission during coal and rock failure under multilevel dynamic loading,” *International Journal of Rock Mechanics and Mining Sciences*, vol. 117, no. 2, pp. 1–10, 2019.
- [35] X. Liu, G. Han, E. Wang, S. Wang, and K. Nawnit, “Multiscale hierarchical analysis of rock mass and prediction of its mechanical and hydraulic properties,” *Journal of Rock Mechanics and Geotechnical Engineering*, vol. 10, no. 4, pp. 694–702, 2018.
- [36] D. Yin, S. Chen, X. Liu, and H. Ma, “Simulation study on strength and failure characteristics for granite with a set of cross-joints of different lengths,” *Advances in Civil Engineering*, vol. 2018, Article ID 2384579, 10 pages, 2018.
- [37] C. Wang, Y. Zhao, Y. Zhao, and W. Wan, “Study on the interaction of collinear cracks and wing cracks and cracking behavior of rock under uniaxial compression,” *Advances in Civil Engineering*, vol. 2018, Article ID 5459307, 10 pages, 2018.
- [38] Y. Wang, M. Fall, and A. Wu, “Initial temperature-dependence of strength development and self-desiccation in cemented paste backfill that contains sodium silicate,” *Cement and Concrete Composites*, vol. 67, no. 8, pp. 101–110, 2016.
- [39] F. Moghbel and M. Fall, “Response of compost biocover to freeze-thaw cycles: column experiments,” *Cold Regions Science and Technology*, vol. 131, no. 5, pp. 39–45, 2016.
- [40] W. Li, *Characteristics and Mechanism of Sulphate Effect on the Early Age Properties of Cemented Paste Backfill*, China University of Mining & Technology-Beijing, Beijing, China, 2016.
- [41] W. Li and M. Fall, “Sulphate effect on the early age strength and self-desiccation of cemented paste backfill,” *Construction and Building Materials*, vol. 106, no. 3, pp. 296–304, 2016.
- [42] J. C. H. Célestin and M. Fall, “Thermal conductivity of cemented paste backfill material and factors affecting it,” *International Journal of Surface Mining Reclamation & Environment*, vol. 23, no. 4, pp. 274–290, 2009.
- [43] H. Zhen and H. Liu, “Accurate measurement of static friction coefficient by inclined plane method,” *Modern Manufacturing Technology and Equipment*, vol. 28, no. 3, pp. 73–74, 2009.
- [44] L. Zhang, “Error handling for proving Newton’s second law with an inclined car,” *Education Teaching Forum*, vol. 21, no. 1, pp. 72–73, 2012.
- [45] C. Sun, F. Liu, M. Jiang, and H. Chen, “Size effect of compression strength and end constraint of rocks by distinct element simulation,” *Chinese Journal of Rock Mechanics & Engineering*, vol. 33, no. S2, pp. 3421–3428, 2014.

Research Article

Influence of Arch Foot Defect of Primary Support on Mechanical Behaviors of an Arch Frame in Underground Tunnels

Yakun Wang,¹ Junwei Guo ,¹ Jizeng Zhao,² Xuxu Yang,¹ Weiteng Li,¹ and Junfeng Liu¹

¹Shandong Key Laboratory of Civil Engineering Disaster Prevention and Mitigation, Shandong University of Science and Technology, Qingdao 266590, China

²Qingdao Metro Group Co. LTD, Qingdao 266000, China

Correspondence should be addressed to Junwei Guo; 1802895825@qq.com

Received 30 December 2021; Revised 10 February 2022; Accepted 17 February 2022; Published 8 March 2022

Academic Editor: Yang Yu

Copyright © 2022 Yakun Wang et al. This is an open access article distributed under the Creative Commons Attribution License, which permits unrestricted use, distribution, and reproduction in any medium, provided the original work is properly cited.

During the blasting excavation of the large-span tunnels, the instability of the blasting caused the overexcavation phenomenon, making the grille arch difficult to land completely in the primary support of the tunnel, thus forming an arch foot defect. In order to reduce the security issues of tunnel engineering construction and scientifically evaluate the influence of arch foot defects on the force performance of the overall structure of the arch frame, combining the Qingdao Metro long-span hard rock tunnel project, this paper designs two grille arch test sections with arch foot defects and one conventional section to carry out field tests. Combining with FLAC^{3D} numerical simulation, the results of the study were used for analyzing the stress characteristics of arch foot defect grille arch in the primary support of the tunnel. The results indicated that (1) the arch foot of conventional section arch frame is subjected to the force transferred from the upper part and the deformation pressure of surrounding rock within the arch foot range, and the upper transfer force borne by the arch foot mainly comes from the deformation of arch waist. (2) When the arch frame has arch foot defects, the deformation of surrounding rock at the arch foot and the deformation transferred from the upper part mainly depend on the shotcrete, thus resulting in the increase of shotcrete strain. (3) Anchoring bolt and shotcrete can integrate the grid arch with the surrounding rock, thus bearing local loads in the arch crown, arch waist, and shotcrete. (4) The numerical calculation of arch frame with arch crown, arch waist, and arch foot defects claims that the force reduction of the arch frame caused by the arch foot defect was the most obvious, and the calculation results were consistent with the actual project.

1. Introduction

It is the rapid development of transportation that has accelerated the construction of many tunnel projects all over China, such as Chengdu Longquanshan Tunnel, Ji³nan Yellow River Tunnel, and Qingdao Metro Tunnel. The successful constructions of these tunnel projects have a great correlation with the good primary support efficiency. The primary support has significant capability of adjusting the stress state of surrounding rocks, improving the mechanical parameters of surrounding rock, and reducing the deformation of tunnel rock mass.

Combined with Sanshilipu Tunnel, Han et al. [1] comprehensively studied the stress characteristics of various lining structures of shallow buried tunnel in loess area; Luo

et al. [2], based on the large-span three-arch tunnel, analyzed the mechanical characteristics of the tunnel lining by using the field monitoring method. The results show that after the installment of tunnel lining, the lining pressure and steel rib stress increase rapidly and then tend to be stable until the surrounding rock is disturbed by the subsequent excavation; Li et al. [3] obtained the surrounding rock pressure and the mechanical characteristics of each subcomponent of the primary support system through on-site monitoring and pointed out that the surrounding rock pressure, steel frame stress, and shotcrete stress changed sharply with the excavation process, and the sensitivity decreased in turn; and Luo et al. [4] took Loess Tunnel as an example and combined the primary support monitoring results with FLAC^{3D} numerical simulation, and the primary support stress

showed the law of “the stress at the arch was greater than the stress at the bottom, and the stress was symmetrical”, and the main support structures were in compression state.

Relying on the on-site tunnel engineering, many scholars have carried out a large number of model tests and numerical calculations to study the stress of the model in the cracking process under the indoor test. Based on the shallow buried tunnel in layered rock mass, Fan et al. [5] explore the cracking mechanism of lining structure in the model with different joint angle combination; Chen et al. [6] mainly studied the stress distribution and cracking process at different positions of the tunnel opening model; Fan et al. [7] studied the stress distribution and evolution of fractured block and porous block under uniaxial compression by combining test and numerical simulation; and Gong et al. [8] conducted true triaxial tests on red sandstone samples with prefabricated holes, revealing the mechanism of rock burst induced by spalling damage and the characteristics of rock burst failure caused by spalling damage.

Based on the research on the stress characteristics of tunnel primary support, many scholars have optimized the primary support combined with actual engineering. Based on the Xinzhuangling Tunnel, Qiu et al. [9] found that the load borne by the primary support structure was not large; on this basis, the corresponding optimization countermeasures were put forward, and their rationality was verified by numerical calculation; Langford et al. [10] proposed a quantitative risk method based on reliability, which can be combined with the monitoring results during construction to design safer primary support structures. Xue et al. [11] carried out an on-site monitoring and numerical simulation on the support effectiveness of three super large-span multiarch tunnels and improved the tunnel support according to the research results.

The primary support of tunnel is mainly composed of steel arch frame (section steel, grid), shotcrete, and anchor bolt. As the main bearing structure of rock mass pressure, many scholars have studied the structure and stress of steel arch frame. Yang et al. [12] in order to explore the support performance of high-strength reinforced grid arch in the surrounding rock of soft tunnel, combined with the circular tube elastic strain theory, the support characteristic curve of high-strength reinforced grid arch was obtained, and its mechanical properties and deformation characteristics were further analyzed by finite element numerical calculation method; Li et al. [13] established “grid arch frame + shotcrete” by using the elastic thin shell theory, and the influence of shotcrete thickness and arch spacing on the support effect was studied. Taking the full-section hard rock tunnel as an example, Wang et al. [14] monitored the stress of reinforcement on the inner and outer sides of steel arch and analyzed its distribution characteristics and variation law. The results show that the stress on the inner side is generally greater than that on the outer side at the same measuring point; Song et al. [15] designed a kind of spatial steel tubular grid (SSTG) with high strength and large stiffness, the bending test of the arch frame was carried out through the combination of test and numerical calculation, and the mechan-

ical performance of the arch frame in the whole loading process was studied; Hou et al. [16] tested the mechanical properties of thin-walled concrete-filled steel tube arch and compared it with traditional grid steel frame, and it is concluded that the deformation resistance of thin-walled concrete-filled steel tube arch frame is stronger; Wen et al. and Li et al. [17, 18] established the foundation curved beam mechanical model of tunnel primary support and deduced the internal force of tunnel steel arch through tunnel monitoring data; and Li et al. [19] embedded the yield criterion of beam element into FLAC^{3D} main program by using Fish language and realized the correction of beam model and the yield failure simulation of supporting arch.

The above scholars mainly study the stress characteristics of the complete steel arch frame in the initial support and conduct numerical calculation and optimization of the complete arch frame. They do not study the stress characteristics of the defective arch frame, which actually exists in tunnel engineering. This paper mainly explores the stress characteristics of the defective arch frame. In the process of on-site construction, due to blasting overexcavation, imperfect construction methods, and other reasons, the steel arches often have some defects due to blasting overexcavation, imperfect construction methods, and other reasons. These factors may have some impacts on the support function of the steel arch, which in turn makes the construction of tunnel project a safety hazard. Therefore, combined with the field conditions, two grid arches with arch foot defects were designed and monitored for a long time. The monitoring analysis results were combined with FLAC^{3D} numerical simulation to expand the field arch problem and better study the mechanical characteristics of steel arch in Qingdao Metro Tunnel. The study has guiding significance for the support design and construction of large-span hard rock tunnel.

2. Experiment Program

2.1. Support Scheme. The test section was selected in underground excavation station of Qingdao Metro Line 6. The tunnel was mainly constructed by arch cover method, half package waterproof design, and divisional excavation. The primary support of arch lining adopted the combined support structure of “grid steel frame + shotcrete + anchor bolt” and internal support. The support parameters were as follows: grid steel frame at 0.75 m and spacing at 1.2 m, and the steel grid was laid inside and outside $\Phi 8$ at 200 mm \times 200 mm double-layer reinforcement mesh, and an additional grid with a length of 2.5 m was added at the arch foot; C30 net shotcrete, 300 mm thick; arch anchor bolt $\Phi 25$ hollow grouting anchor bolt, $L = 3.5$ m, at 1.5 \times 0.75 m (ring \times longitudinal), and plum blossom layout.

2.2. Test Design. Three monitoring sections were set in the field test, including two test sections (section A and section B) and one conventional section. For comparative analysis, the location of the conventional section was set between the two test sections A and B. The design scheme of the grid

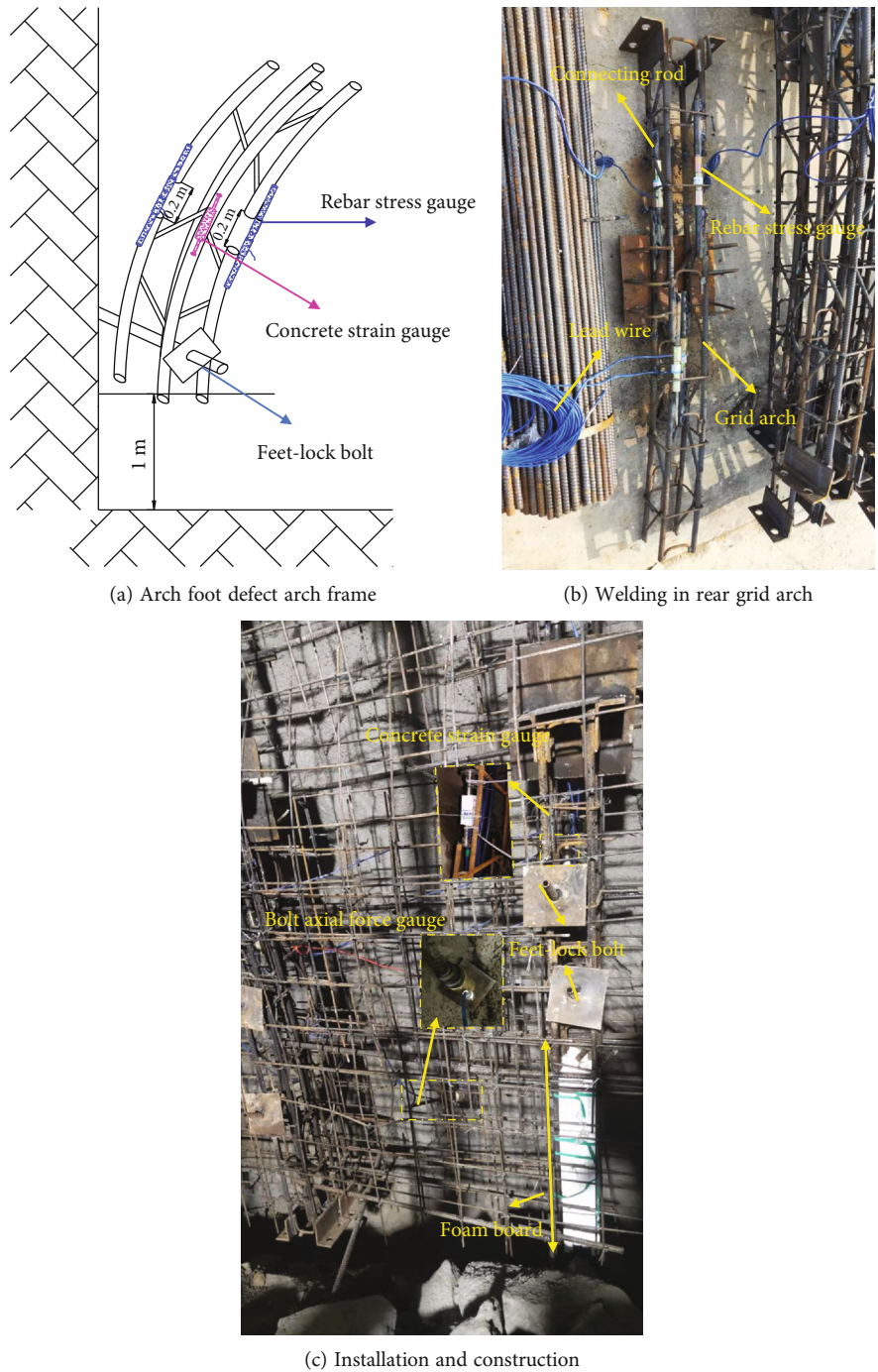


FIGURE 1: Test design scheme and monitoring.

arch of the test section was shown in Figure 1(a), in which the steel rib with a length of 20 cm was cut at the oblique opposite side of the grid arch, the connecting rods on both sides of the rebar stress gauge were welded at the cut position, and the arch length at the arch foot was shortened by one meter compared with the conventional section. The test arch after welding was shown in Figure 1(b). During construction, the welding will raise the temperature of the rebar stress gauge, which will inevitably lead to the inaccurate data measured by the rebar stress gauge. Therefore, after the

rebar stress gauge is welded, cool the temperature with cold water and take the frequency value of the welded rebar stress gauge as the initial value of the test. And to ensure that the bottom of the arch support was not supported by the ground and shotcrete, the foam board was used to fill and the feet-lock bolts were struck at the bottom of the shortened arch. Foam board has the characteristics of small density and stress isolation. It can effectively isolate the force transmitted from the upper part, thus simulating the defect of arch foot perfectly. The installation and construction process of the

TABLE 1: Monitoring parameters and instrument installation.

Monitoring items	Physical quantity	Instrument name	Specification	Quantity
Bolt axial force	F/KN	Bolt axial force gauge	MSJ	5 measuring points
Concrete strain	ε_c	Concrete strain gauge	EM-30	7 measuring points
Steel rib stress	σ/MPa	Rebar stress gauge	STG-25	5 measuring points

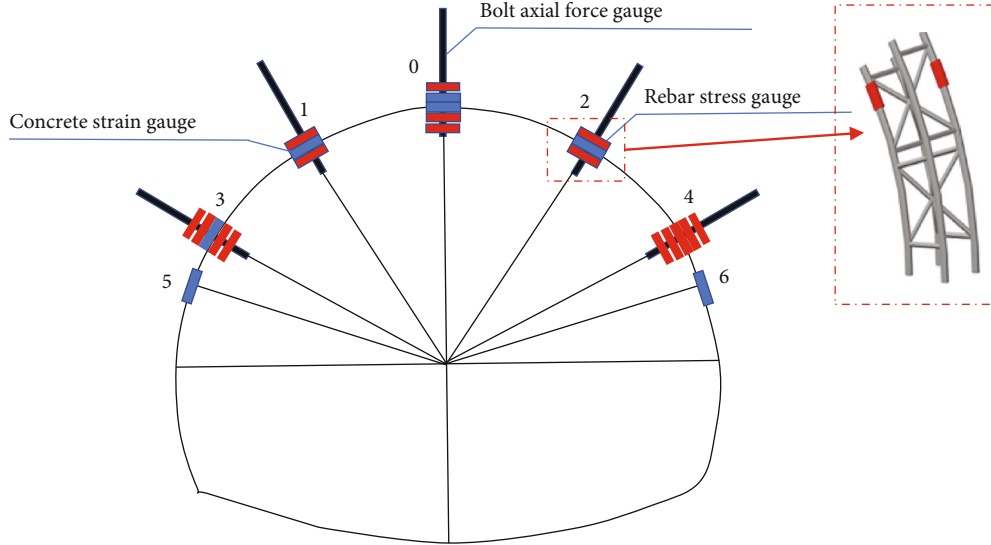


FIGURE 2: Layout of monitoring points and number of instruments at the test section.

monitoring instrument of the test section was shown in Figure 1(c).

2.3. Test Content. In order to study the size and distribution characteristics of steel rib stress, bolt axial force and shotcrete strain of primary support arch frame of long-span hard rock metro tunnel under the condition of arch foot defects, the steel rib stress monitoring, shotcrete strain monitoring, and bolt axial force monitoring were carried out (both steel rib stress and shotcrete strain are specified as the positive compression and negative tension, and the axial force of bolt as the positive tension). The on-site monitoring parameters and instrument installation are detailed in Table 1, and the instrument installation was shown in Figure 2.

3. Test Results and Analysis

3.1. Stress of Steel Rib. Grid arch mainly bores the vertical load of surrounding rock to enhance the stability of the surrounding rock. The bearing capacity of grid arch is greatly different due to the influence of section shape, connecting nodes, and other factors [20]. In this paper, based on the arch with arch foot defects, the arch reinforcement of the above three monitoring sections is monitored for long-term stress, and the stress-time curve of the reinforcement is shown in Figure 3. It can be seen from the figure that before the excavation of the arch foot, both sides of the arch steel rib of the arch crown and arch waist of the monitoring section were compressed, and the change law can be basi-

cally divided into three stages: rapid growth stage, stress decline stage, and stable stage. The main reasons of these changes were that the tunnel section span was large, the flattening rate was small, the grid arch steel rib bores the main load, and the self-stability of the tunnel surrounding rock was good, so the steel rib stress decreased in a short time and was in a stable state.

After the excavation of the arch foot, the arch foot support and monitoring instruments were installed according to the design scheme, and the stress curves of the arch foot steel rib of the two kinds of grid arch frames were obtained, as shown in Figure 4. According to Figures 3–4, it can be found that the surrounding rock of most measuring points of arch crown and arch waist was disturbed due to the excavation of arch foot, resulting in the increase of steel rib stress; the steel rib stress at the arch foot also conformed to the above basic law of stress change. Due to the small excavation area at the arch foot, the stress distribution of the arch frame was characterized by “large at the top and small at the bottom” [21]. On the whole, the stress growth range of the arch foot of the arch frame was 38.8% lower than that of the upper arch frame, and the stabilization time was shorter, which tended to be stable in about 7 days.

After the monitoring data were all stable, the data comparison of the two monitoring sections was obtained, as shown in Figures 5–6:

- (1) As can be seen from Figure 5(a), the steel rib stress at the inside of the conventional section is 87.6 MPa,

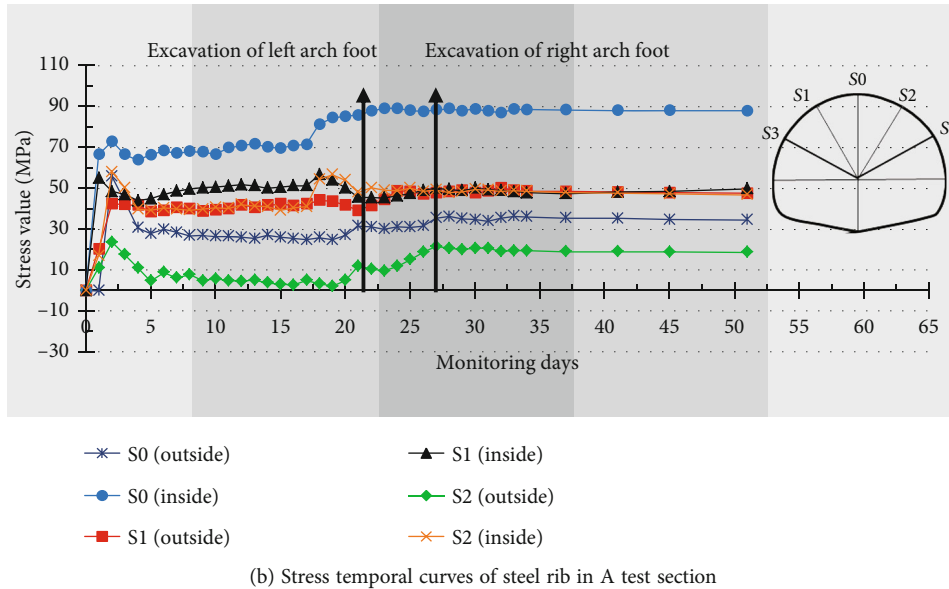
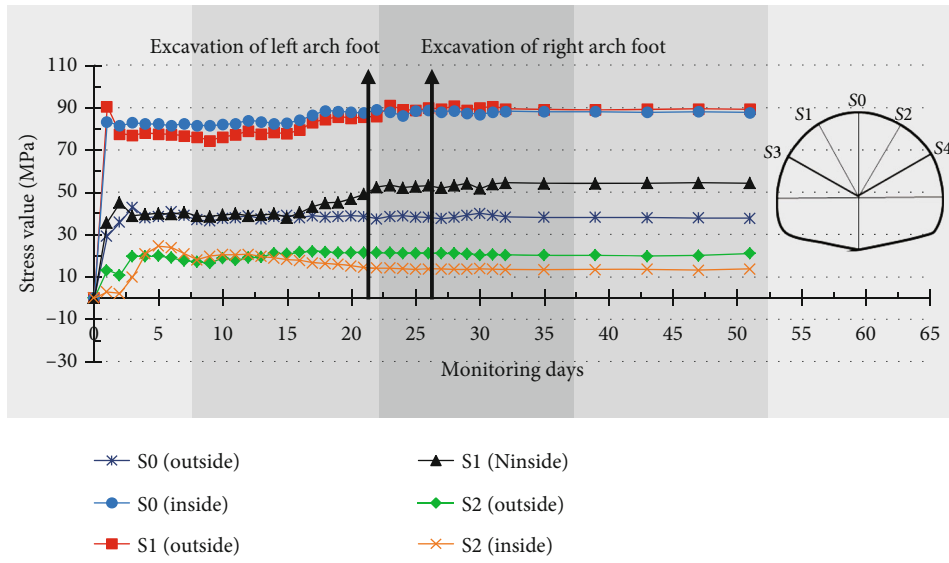
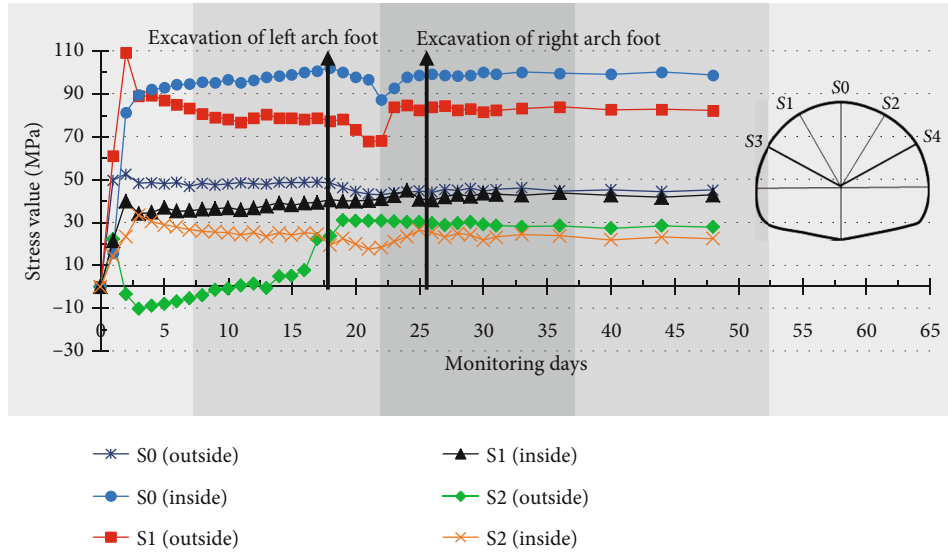


FIGURE 3: Continued.



(c) Stress temporal curves of steel rib in B test section

FIGURE 3: Stress temporal curves of steel rib.

and the steel rib stress at the outside is 37.2 MPa; the average stress of steel rib at the inside of the two groups of test sections is 93.4 MPa and 40.2 MPa at the outside. It can be clearly seen from the average values of all points of each section that the steel rib stress at the crown of the test section was 7% higher than that of the conventional section

- (2) As can be seen from Figure 5(b), the steel rib stress at the inside of the conventional section is 35.8 MPa, and the steel rib stress at the outside is 59.7 MPa; the average stress of steel rib at the inside of the two groups of test sections is 30.3 MPa and 54.5 MPa at the outside. The steel rib stress at the waist of the test section was 12% lower than that of the conventional section
- (3) According to the monitoring data in Figure 6, it can be found that the average steel rib stress at the arch foot of the conventional section is mainly concentrated at the inside, and the steel rib stress at the inside is 52.5 MPa and 67.8 MPa, respectively. After stabilization, the average steel rib stress at each measuring point is 35.3 MPa; the stress distribution of steel rib in the test section is relatively uniform, the stress of steel rib at the inside is 23.6 MPa and 13.8 MPa, respectively, and the stress of steel rib at the outside is 10.4 MPa and 34.3 MPa, respectively. The steel rib stress at the arch foot defect of the test section was 41.8% lower than that of the conventional section

The data analysis results showed that the steel rib stress at the defect position of the arch foot of the test section decreased and the test section isolated the force transmitted

from the upper part. Therefore, the arch steel rib stress measured by the arch foot defect arch is only the surrounding rock deformation pressure within the arch foot, and there is no force transmitted from the upper part. Indicating that the arch foot of the conventional section bores the force transferred from the upper part and the surrounding rock deformation pressure within the arch foot range at the same time. The steel rib stress at the arch crown basically did not change, and the steel rib stress at the arch waist decreased a little. Therefore, the upper transfer force borne by the arch foot of conventional section arch frame mainly comes from the deformation of arch waist.

3.2. Strain of Shotcrete. The shotcrete strain of three monitoring sections was monitored for a long time. The monitoring results showed that some shotcrete strains were very large, but there were no abnormal phenomena such as cracking on the shotcrete surface. After preliminary analysis, it was considered that no cracking phenomenon was the impact of the large spraying force in the process of concrete spraying. The field test showed that when spraying directly at the concrete strain gauge, the concrete strain gauge will produce large strain. Therefore, the monitoring value after spraying concrete was regarded as the initial value for data analysis.

The adjusted shotcrete strain curves were shown in Figure 7. From the figure, it can be seen that the shotcrete strain basically presented the change law of “rise-stabilization”. After the excavation of arch foot, the shotcrete strain curves of arch crown and arch waist will have a sudden change, which was caused by the large disturbance of surrounding rock caused by arch foot excavation.

After the excavation of arch foot of conventional section, due to the good integrity of upper support and surrounding rock, the shotcrete strain at the arch foot was very small, and the overall strain is $30 \mu\epsilon$ within.

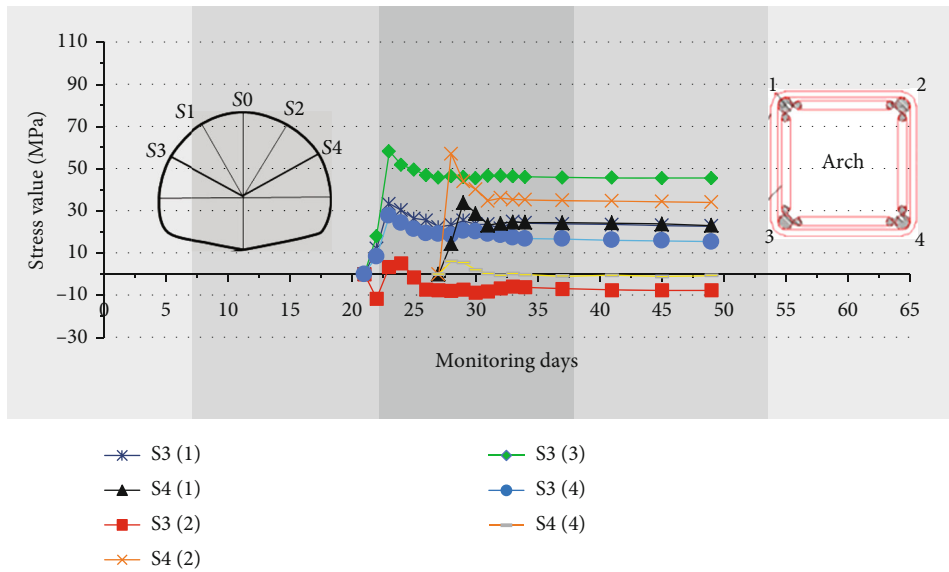
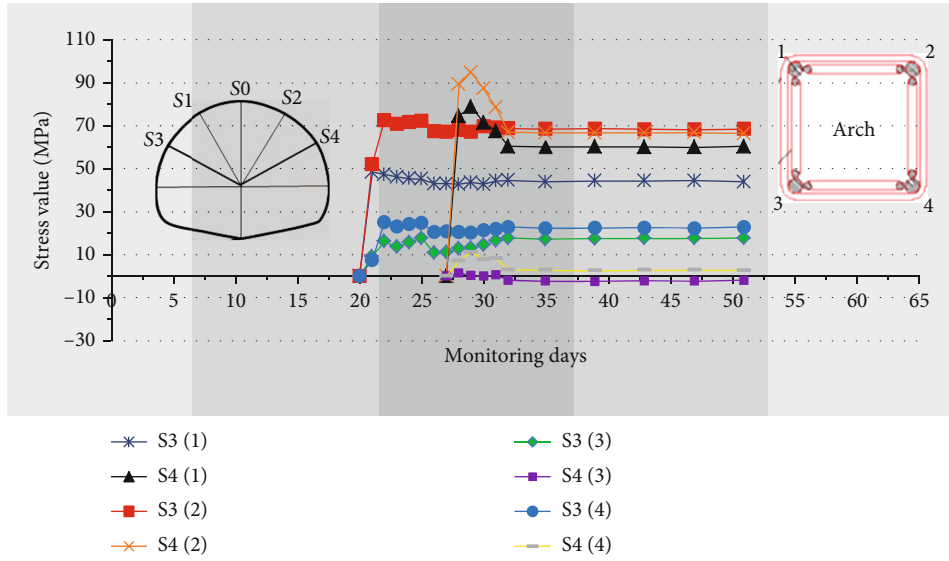
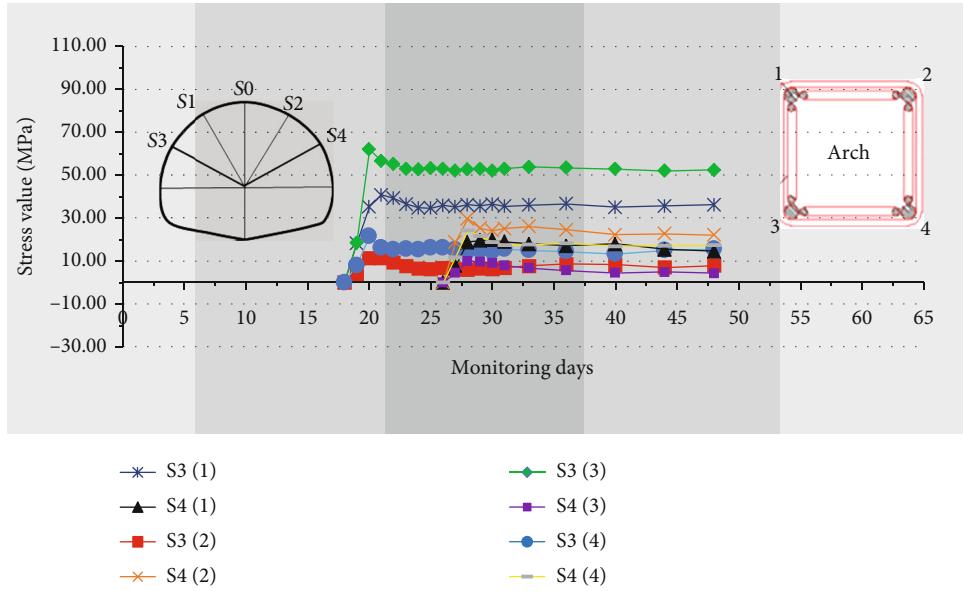
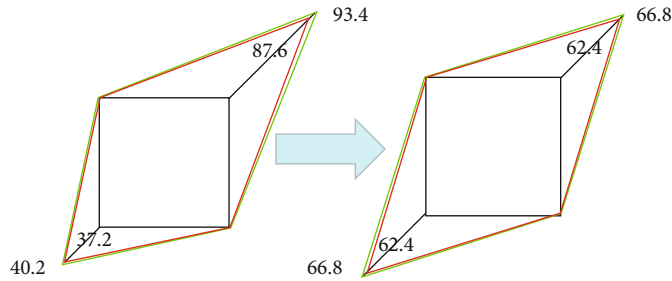


FIGURE 4: Continued.

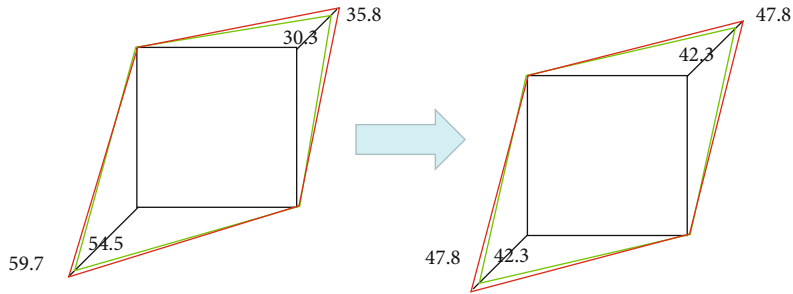


(c) Stress temporal curves of arch foot steel rib in B test section

FIGURE 4: Stress temporal curves of arch foot steel rib.



(a) Comparison of data of two monitoring sections at the arch crown



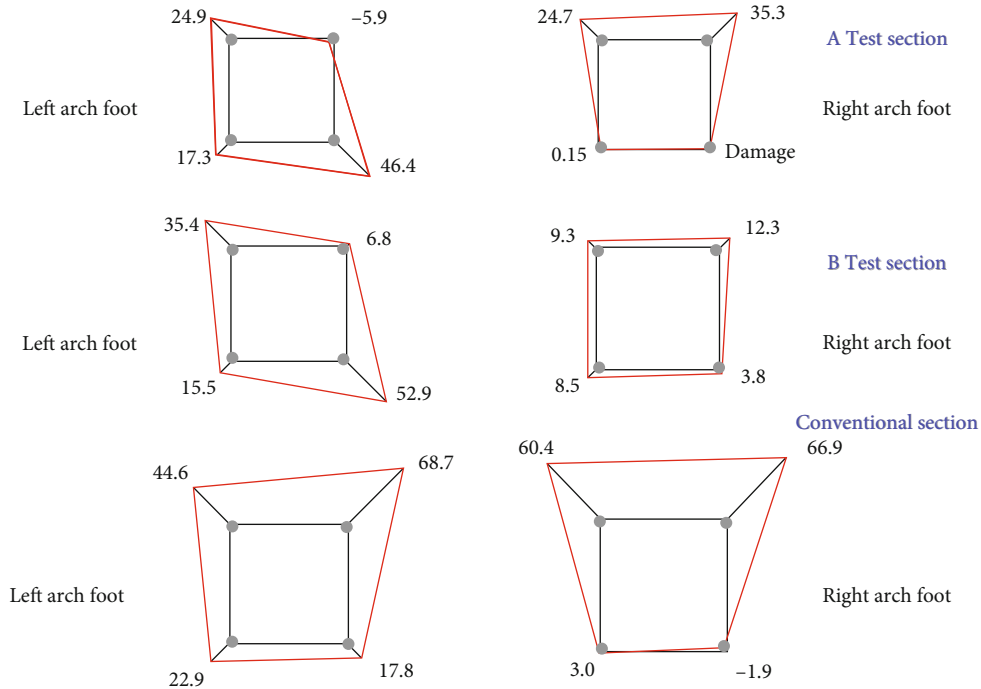
(b) Comparison of data of two monitoring sections at the arch waist

FIGURE 5: Comparison of data of two monitoring sections (Unit: MPa).

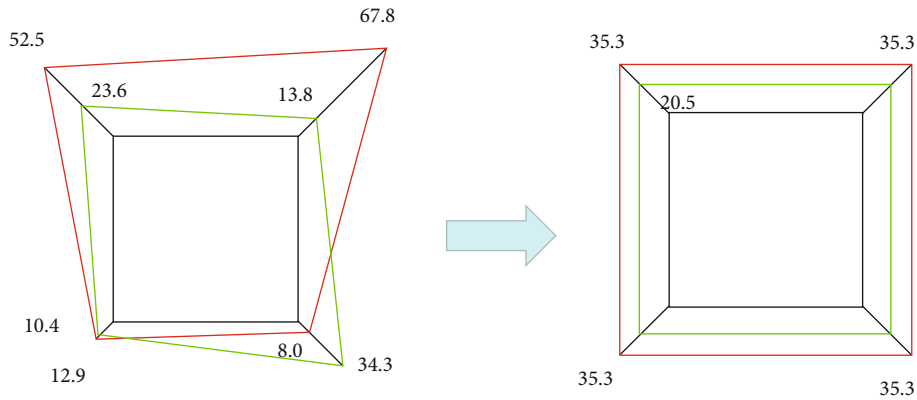
Compared with the conventional section, some shotcrete strains of the test section were larger, for example, the C5 strain value of group A test section is $125 \mu\epsilon$ and the C6 strain value of group B test section is $122 \mu\epsilon$. Due to the weak tensile capacity of shotcrete, it was necessary to carefully observe whether there was cracking on the shotcrete surface of the monitoring section after spraying. During the monitoring period of nearly 50 days, there was no cracking on the shotcrete surface, and the maxi-

imum tensile value of arch foot shotcrete is $-61 \mu\epsilon$; after the shotcrete strain was stable, the strain was generally $-50 \sim 100 \mu\epsilon$, and the deformation rate was stable, so it was considered that the strain of the test section was large, but it was still in a safe state.

After the monitoring data was stable, the shotcrete strain and average strain of arch crown, arch waist, and arch foot were compared, and the comparison results were shown in Figure 8.



(a) Comparison of arch foot steel rib stress data



(b) Comparison of average stress of arch foot steel rib

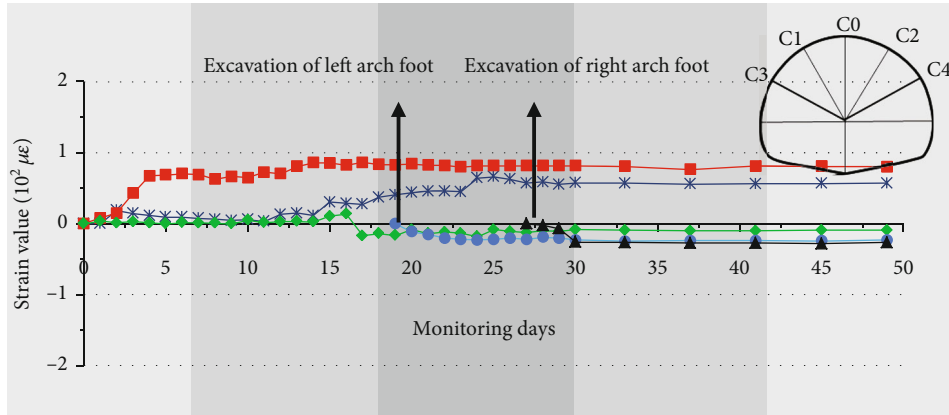
FIGURE 6: Comparison of data after stress stability of arch foot reinforcement in two monitoring sections (Unit: MPa).

The shotcrete strain at the crown of the test section was only 13% higher than that of the conventional section; only from the perspective of shotcrete deformation value, the shotcrete strain at the arch waist of the test section was 30% higher than that of the conventional section, and the shotcrete strain at the arch foot defect of the test section changes greatly, which was 64% higher than that of the conventional section. Grid arch and shotcrete were widely used as the primary support structure, and they affected the support effect of the tunnel through interaction.

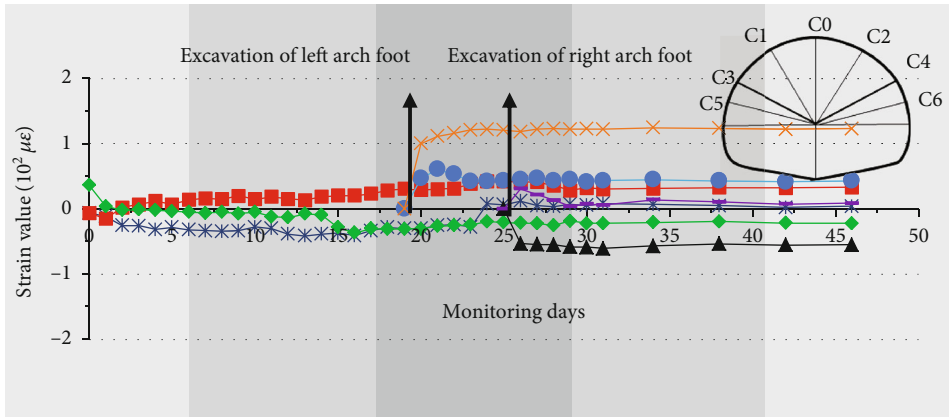
The test results showed that compared with the conventional section, the shotcrete strain at the crown of the test section basically did not change, and the change of the arch waist position was small. The increase of shotcrete strain was mainly reflected in the defect position of the arch foot, indicating that the grid arch and shotcrete

jointly controlled the deformation of the surrounding rock. When the grid arch has arch foot defects, the bearing capacity of the arch foot position decreased and the deformation of surrounding rock at the arch foot and the deformation transferred from the upper part mainly depend on the shotcrete, resulting in the increase of shotcrete strain at the defect position of the arch foot.

3.3. Axial Force Test Results of Bolt. The active support construction method was adopted in the underground excavation station of Qingdao Metro. Its basic principle is to actively improve the mechanical parameters of the surrounding rock, reduce the deformation of the surrounding rock, and actively and timely provide support force for the surrounding rock, so as to give full play to the self-stability ability of the surrounding rock [22, 23].

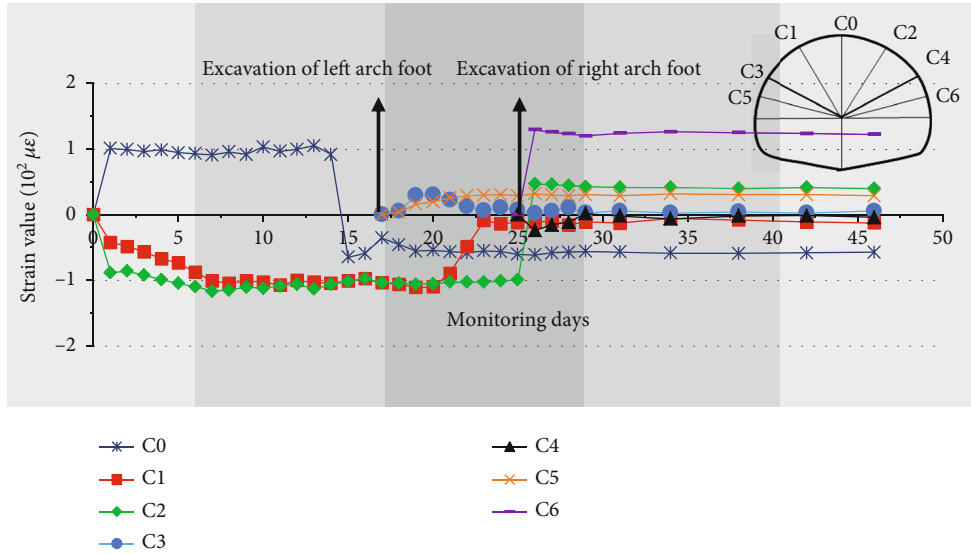


(a) Strain temporal curves of shotcrete in conventional section



(b) Strain temporal curves of shotcrete in A test section

FIGURE 7: Continued.



(c) Strain temporal curves of shotcrete in B test section

FIGURE 7: Strain temporal curves of shotcrete.

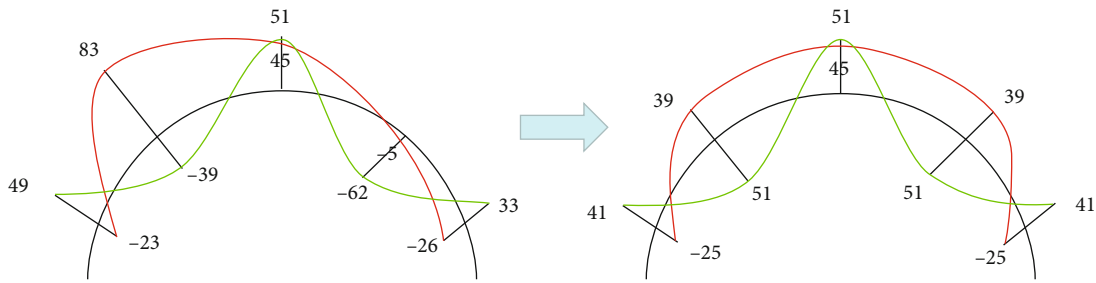


FIGURE 8: Comparison of shotcrete strain data (Unit: $\mu\epsilon$).

The bolt-shotcrete support composed of bolt and shotcrete can significantly improve the strength and bearing capacity of the surrounding rock and effectively control the deformation of the tunnel-surrounding rock [24]. During the active support construction, the prestressed anchor bolt was used to actively provide the axial force of the anchor bolt above 100 kN, which can directly interact with the tunnel-surrounding rock and change the properties of the tunnel-surrounding rock.

The axial force of the prestressed anchor bolt of the primary support was monitored at the monitoring section. The variation curves of the axial force of the anchor bolt with time were shown in Figure 9. Through the comparison between the conventional section and the test section of each part, it can be found that

(i) The change of anchor shaft axial force was mainly concentrated in the early stage of installation, and when the anchor shaft axial force rapidly increased to more than 100 kN, the anchor shaft axial force will be partially lost. After more than 50 days of monitoring, the axial force curve of the anchor rod generally showed a slight decrease and stabilization. And it tended to be stable after 20 days. The stress after stabilization is concentrated at about 100 kN; the aver-

age is greater than 100 kN, and the rate of change is less than 1 kN/d.

The test results showed that the surrounding rock stress was released within 20 days of active support. After the excavation of the left and right arch feet, the change of the axial force of the bolt was not obvious, and there was little difference between the axial force of the bolt in each part of the test section and the conventional section, indicating that the arch foot defect arch frame has little effect on the anchoring effect of the bolt. Combined with the stress and deformation of the arch frame and shotcrete, it can be concluded that the anchoring bolt effect and shotcrete can integrate the grid arch with the surrounding rock and can bear local loads in the arch crown, arch waist, and shotcrete.

4. Analysis of Mechanical Characteristics of Primary Support Structure

4.1. Model and Parameters. According to the technical code for civil engineering construction of Qingdao Metro and basic mechanical parameters of joints obtained from the on-site rock laboratory test and on-site geological survey report, aiming at the engineering geological conditions, surrounding

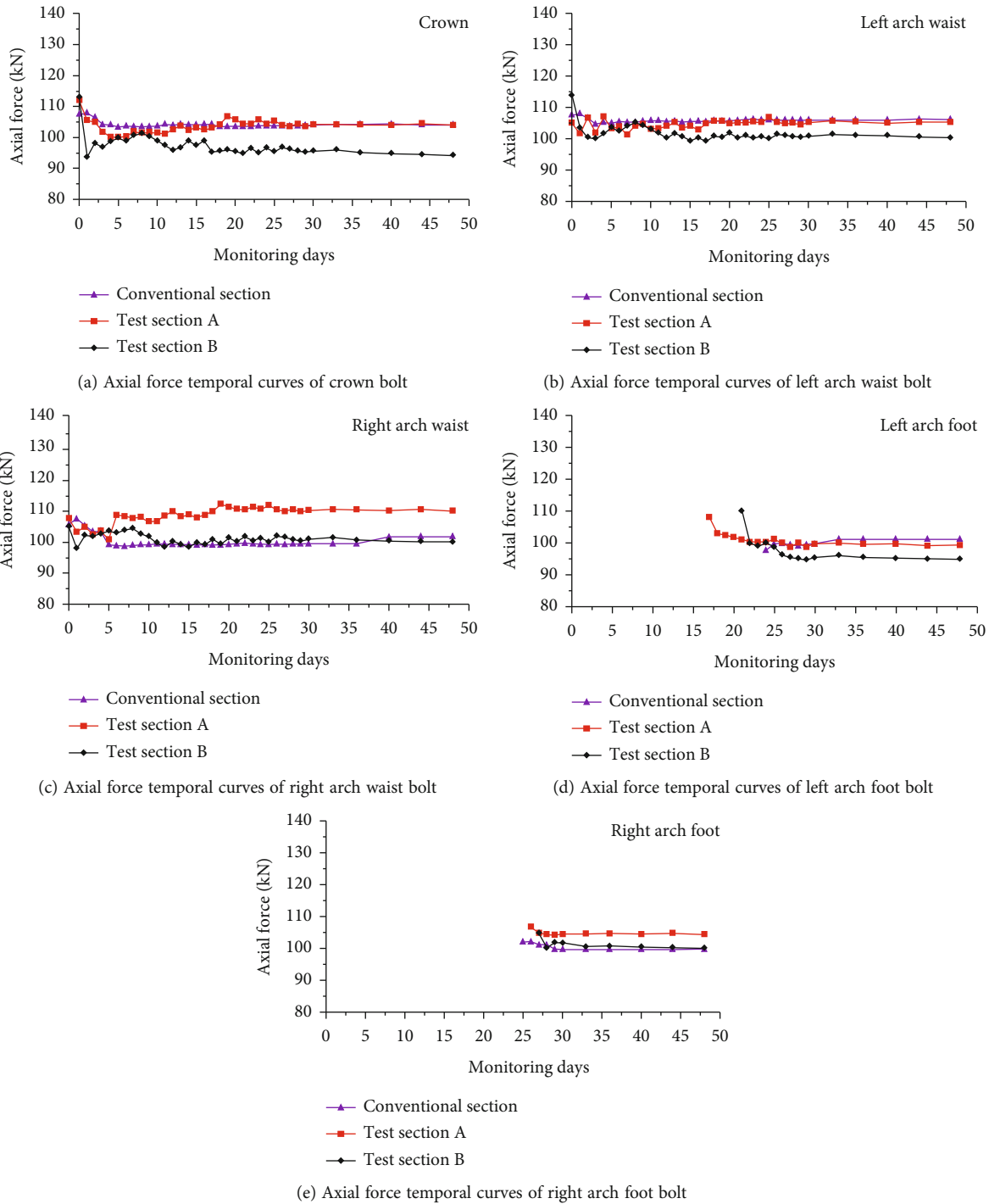
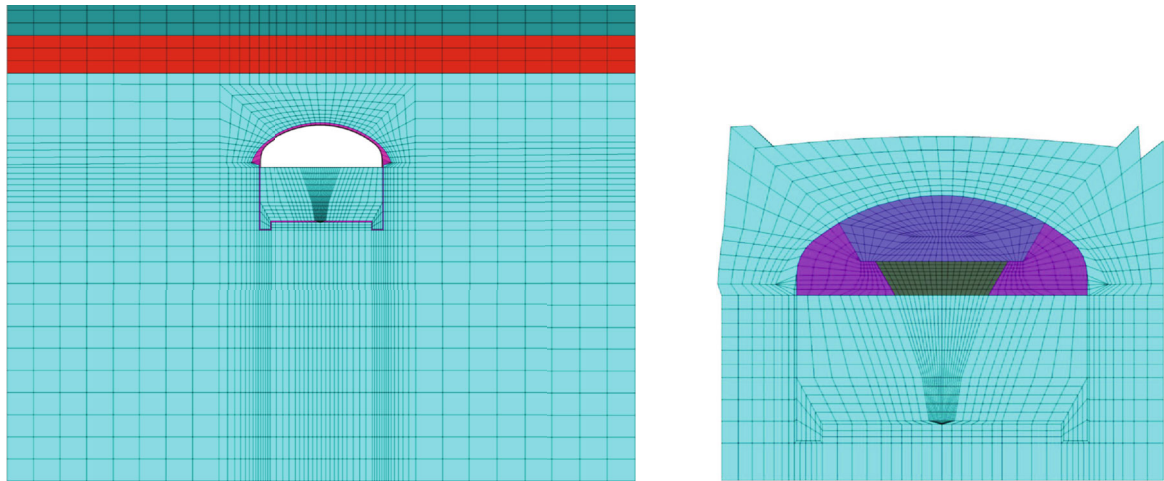


FIGURE 9: Axial force temporal curves of bolt.

rock mechanics parameters, and tunnel excavation construction process design of the tunnel, the $FLAC^{3D}$ numerical simulation software was adopted to simulate the force changes of the grille arch under the influence of factors such as blasting and overexcavation during the excavation of the tunnel division.

As shown in Figure 10(a), the width, height, and thickness of the numerical calculation model were 80 m, 100 m, and 0.8 m, respectively. The tunnel arch was semicircular

in shape and modeled with brick grid. The surrounding rock of the model was divided into three types from top to bottom: strongly weathered, moderately weathered, and slightly weathered. The surrounding rock of the tunnel arch was excavated in four parts according to the on-site construction sequence, as shown in Figure 10(b). Except the top of the model, where the node normal velocity of all faces was fixed. Mohr-Coulomb model was selected for surrounding rock, and the material parameters are shown in Table 2.



(a) Numerical model of excavation of surrounding rock on the upper bench of tunnel (b) Divisional excavation model diagram

FIGURE 10: Tunnel bench excavation model.

TABLE 2: Mechanical parameters of granite.

Surrounding rock	Young's modulus, E (MPa)	Poisson's ratio, μ	Cohesion, C (MPa)	Internal friction angle, ψ ($^{\circ}$)	Density, D (kg/m^3)
Strongly weathered	1300	0.35	0.1	27	2250
Moderately weathered	1600	0.35	0.2	27	2300
Slightly weathered	2000	0.34	0.2	30	2400

TABLE 3: Primary support parameters of tunnel surrounding rock.

(a) Shotcrete parameters

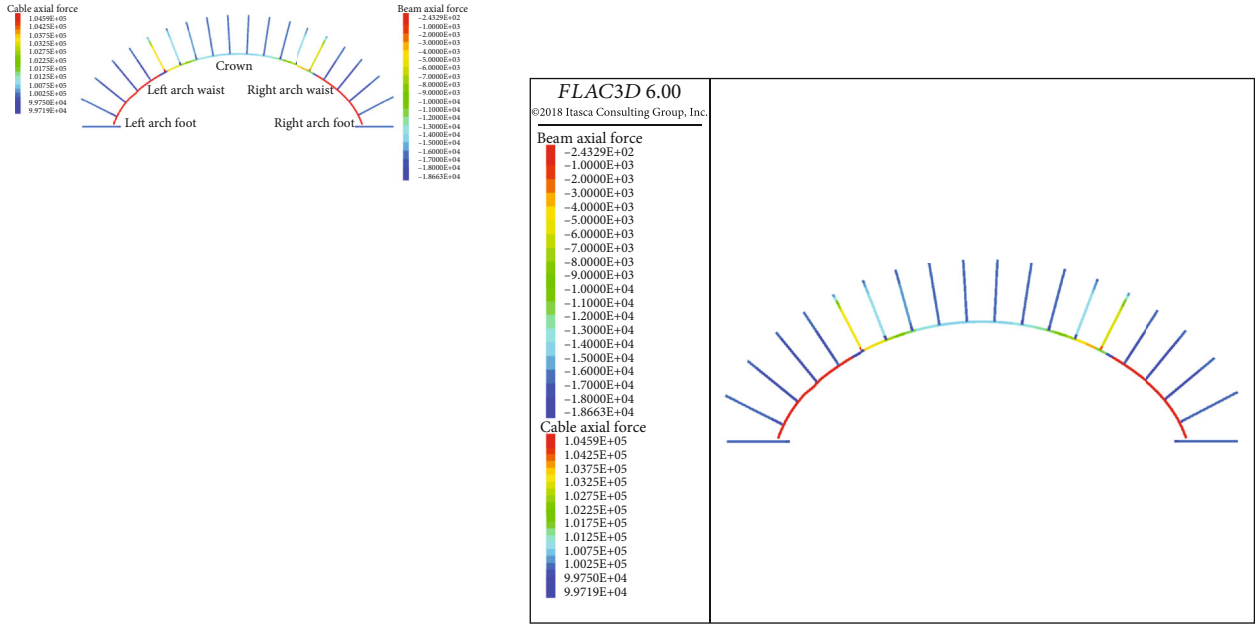
Young's modulus, E (MPa)	Poisson's ratio, μ	Bulk modulus, K (GPa)	Shear modulus, G (GPa)	Cohesion, C (MPa)	Internal friction angle, ψ ($^{\circ}$)	Density, D (kg/m^3)
2000	0.34	16	9.6	2	60	2500

(b) Parameters of bolt and grouting body

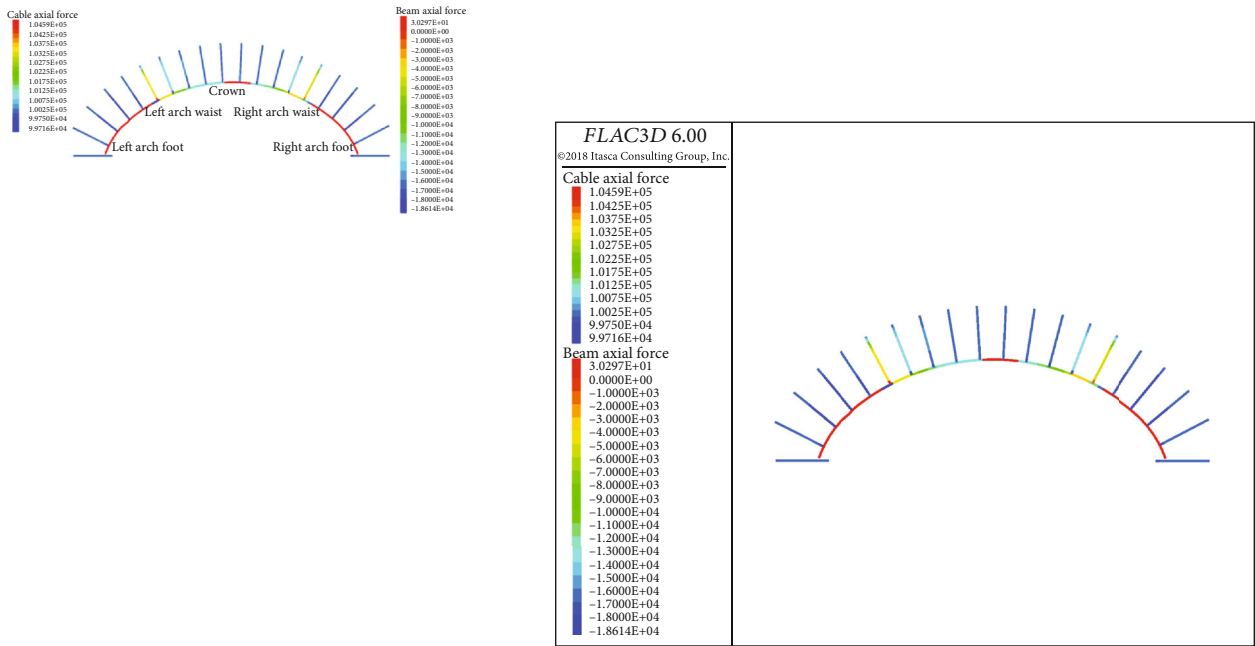
Simulated object	Young's modulus, E (MPa)	Cross sectional area, A (cm^2)	Density, D (kg/m^3)	Tensile strength, σ_t (MPa)
Bolt	200	2.54	7850	0.24
Simulated object	Cohesion, C_g (MPa)	Internal friction angle, ψ_g ($^{\circ}$)	Shear stiffness k_g (MPa/mm)	Outer ring perimeter p_g (m)
Grout	2	30	20	0.0942

(c) Grid arch parameters

Simulated object	Young's modulus, E (MPa)	Cross sectional area, A (cm^2)	Density, D (kg/m^3)	Poisson's ratio, μ
Grid arch	200	19.63	7850	0.25
Defective arch	2.2	19.63	20	0.39

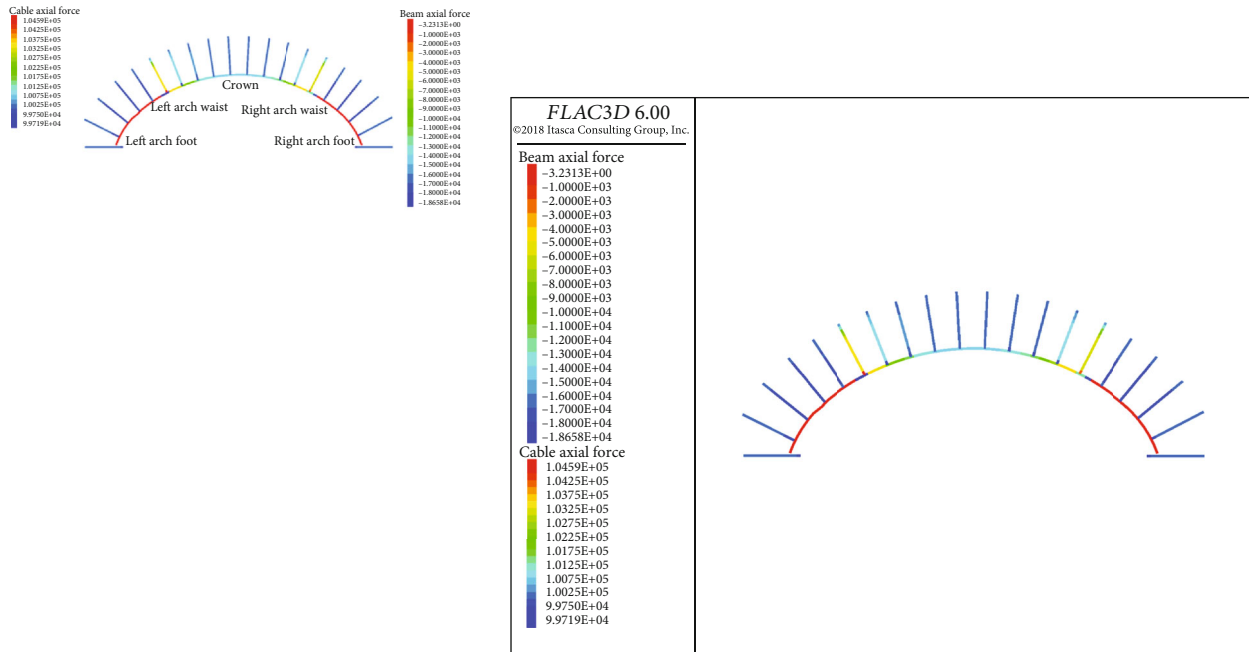


(a) Stress nephogram of conventional arch

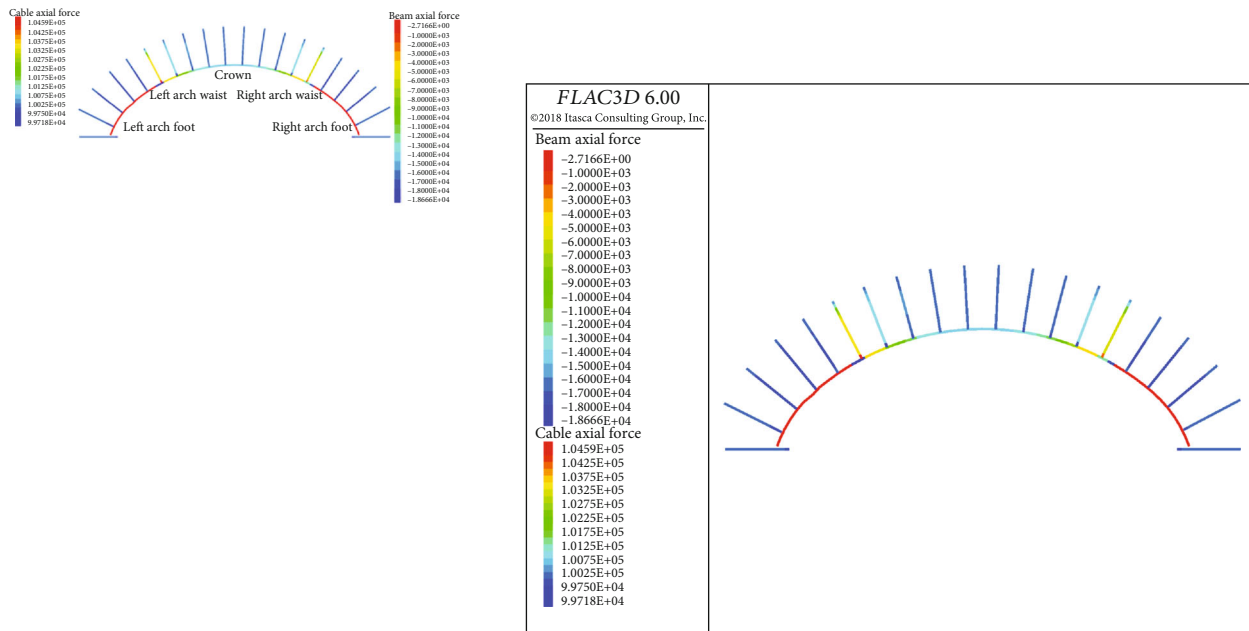


(b) Stress nephogram of crown defect

FIGURE 11: Continued.



(c) Stress nephogram of arch waist defect



(d) Stress nephogram of arch foot defect

FIGURE 11: Stress nephogram of grid arch.

After the tunnel was excavated, anchor bolt, grid arch, and shotcrete were installed immediately. The concrete lining was modeled by solid elements. The anchor structure elements were used to simulate the bolt and grouting body, and the preload of 100 kN was applied; the grid arch was simulated by the beam element. According to the field test design, the low strength material such as foam was used to replace the defect position of the arch. So as to simulate the influence of defective arch on the overall stress of arch. See Table 3 for various parameters of primary support.

4.2. Analysis of Stress Characteristics of Grid Arch. According to the numerical simulation results, the force nephograms of the grid arch in the primary support of the tunnel were shown in Figure 11. The force at the low-strength material position of the arch was basically 0, which was consistent with the force at the defect position of the arch. From the calculation results, it can be found that the axial force of the four kinds of grid arch bolts basically does not change and has been maintained at about 100kN; the force of the steel rib at the arch foot of the grid arch was the smallest,

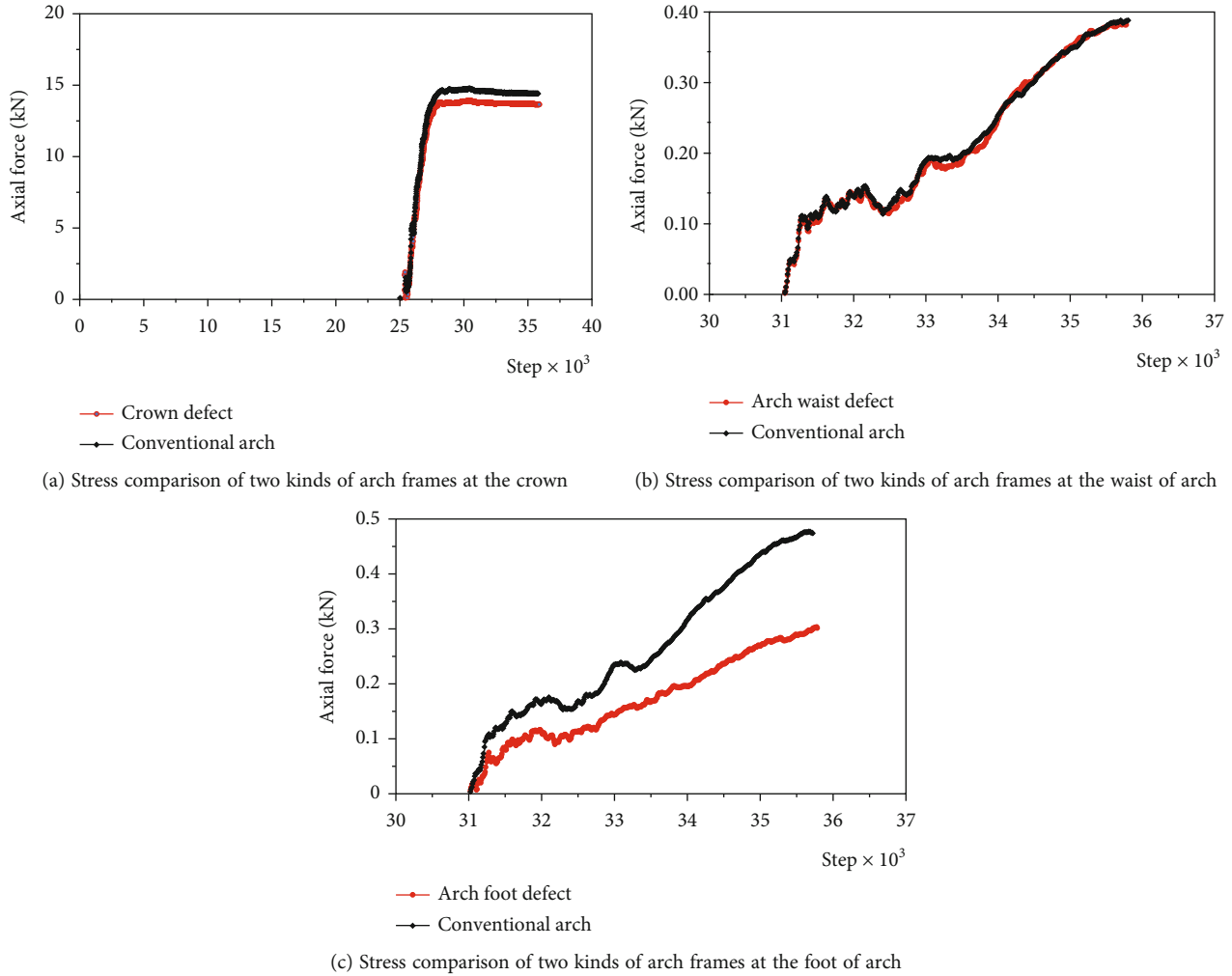


FIGURE 12: Stress comparison of two arch frames at the same position.

and the force of the steel rib at the arch crown was larger, which was consistent with the results of the field monitoring. Compared with the conventional grid arch, the force reduction of the defective grid arch was small, which was mainly concentrated near the defect position of the arch.

The selected different arches at the same position for data monitoring and the monitoring results were shown in Figure 12. From the curves change in the figure, it can be seen that the force of arch steel rib with defects was smaller than that of conventional section. From Figures 12(a)–12(c), it can be seen that the force of arch foot defects was reduced by 28% compared with that of conventional arch, while the force of arch with arch crown and waist defects was reduced by 7% and 2%, respectively, compared with conventional arch; this was because the upper transfer force borne by the arch crown and arch waist was small, and the upper transfer force of the whole arch frame mainly depends on the arch foot. When the arch foot has defects, the arch foot position only bores the deformation pressure of surrounding rock within the arch foot, resulting in a large reduction in the force of the arch frame at the defect position of the arch foot. The calculation results were basically the same as the test results. The above results showed that the unfavorable

situation in the primary support of the arch such as defects will lead to a decrease in the support of the arch, so the occurrence of the above situation should be avoided as much as possible in the tunnel engineering. However, when the above situation is inevitable, it can be improved by adding bolts and sand to fill the over excavated part, so as to ensure the safety of primary support and reduce accidents.

5. Conclusions

Based on the on-site monitoring test of the nonfloor grid arch and the FLAC^{3D} numerical simulation, the force characteristics of the grid arch of the subway tunnel are studied in this paper. The main conclusions are as follows:

(i) Compared with the normal section, the average reduction of reinforcement stress is 41.8% in the test section (arch foot defect location). It indicated that the foot of the arch of the conventional section is subjected to both the force transmitted from above and the deformation pressure of the surrounding rock within the foot of the arch. Basically, there is no change in the reinforcement stress at the top of the arch, and the reinforcement stress at the arch waist is reduced by 12%. Therefore, the upper transfer force of the

arch foot of the conventional section arch mainly comes from the deformation of the arch waist.

(ii) The concrete strain at the location of the arch footing defect increase by 64% compared to the conventional section. The increase in concrete strain is caused by the presence of arch footing defects in the grating arch leading to the reduction of the bearing capacity at the arch footing position. Furthermore, the deformation of the surrounding rock at the arch footing location and the deformation transmit from above mainly rely on concrete to bear.

(iii) Anchoring bolt and shotcrete can integrate the grid arch with the surrounding rock and can bear local loads in the arch crown, arch waist, and shotcrete; however, the grid arch still exerted the overall bearing arch effect, and the arch foot bores the load transferred from the upper part.

(iv) Through FLAC^{3D} numerical calculation, the results show that the stress of the deficient arch frame was less than that of the complete arch frame, while the stress of the arch with arch foot defects was the most obvious, and the stress of the arch with arch crown and arch waist defects was only slightly reduced, which was consistent with the fact that the upper transfer force in the actual project was mainly borne by the arch foot.

Data Availability

The data used to support the findings of this study were supplied by [Junwei Guo] under license and so cannot be made freely available. Requests for access to these data should be made to [Junwei Guo, 1802895825@qq.com].

Conflicts of Interest

The authors declared that they have no conflicts of interest to this work.

Acknowledgments

The research reported in this manuscript was financially supported by the National Natural Science Foundation of China (Grant No. 51704183) and the Postdoctoral Science Foundation of China (Grant No. 2018M640646).

References

- [1] G. W. Han, B. Liu, and H. Fan, "Mechanical characteristics of tunnel lining structure in shallow-buried loess area," *Chinese Journal of Rock Mechanics and Engineering*, vol. 26, no. Supp.1, pp. 3250–3256, 2007.
- [2] J. Luo, D. Zhang, Q. Fang, D. Liu, and T. Xu, "Mechanical responses of surrounding rock mass and tunnel linings in large-span triple-arch tunnel," *Tunnelling and Underground Space Technology incorporating Trenchless Technology Research*, vol. 113, article 103971, 2021.
- [3] P. F. Li, S. M. Tian, Y. Zhao, Y. Q. Zhu, and S. D. Wang, "In-situ monitoring study of mechanical characteristics of primary lining in weak rock tunnel with high grostress," *Chinese Journal of Rock Mechanics and Engineering*, vol. 32, no. Supp.2, pp. 3509–3519, 2013.
- [4] Y. Luo, J. Chen, Z. Shi, J. Li, and W. Liu, "Mechanical characteristics of primary support of large span loess highway tunnel: a case study in Shaanxi Province, loess plateau, NW China primary," *Tunnelling and Underground Space Technology incorporating Trenchless Technology Research*, vol. 104, article 103532, 2020.
- [5] X. Fan, Z. J. Yang, and K. H. Li, "Effects of the lining structure on mechanical and fracturing behaviors of four-arc shaped tunnels in a jointed rock mass under uniaxial compression," *Theoretical and Applied Fracture Mechanics*, vol. 112, article 102887, 2021.
- [6] H. Chen, X. Fan, H. Lai, Y. Xie, and Z. He, "Experimental and numerical study of granite blocks containing two side flaws and a tunnel-shaped opening," *Theoretical and Applied Fracture Mechanics*, vol. 104, article 102394, 2019.
- [7] X. Fan, X. Jiang, Y. Liu, H. Lin, K. Li, and Z. He, "Local stress distribution and evolution surrounding flaw and opening within rock block under uniaxial compression," *Theoretical and Applied Fracture Mechanics*, vol. 112, article 102914, 2021.
- [8] F. Q. Gong, Y. Luo, X. B. Li, X. F. Si, and M. Tao, "Experimental simulation investigation on rockburst induced by spalling failure in deep circular tunnels," *Tunnelling and Underground Space Technology*, vol. 81, pp. 413–427, 2018.
- [9] W. G. Qiu, K. G. Sun, L. C. Wang et al., "Primary support optimization of large section tunnel based on surrounding rock stability," *China Civil Engineering Journal*, vol. 50, Suppl.2, pp. 8–13, 2017.
- [10] J. C. Langford, N. Vlachopoulos, and M. S. Diederichs, "Revisiting support optimization at the Driskos tunnel using a quantitative risk approach," *Journal of Rock Mechanics and Geotechnical Engineering*, vol. 8, no. 2, pp. 147–163, 2016.
- [11] Y. G. Xue, H. Gong, F. Kong, W. Yang, D. Qiu, and B. Zhou, "Stability analysis and optimization of excavation method of double-arch tunnel with an extra-large span based on numerical investigation," *Frontiers of Structural and Civil Engineering*, vol. 15, no. 1, pp. 136–146, 2021.
- [12] Y. A. N. G. Yang, T. A. N. Zhong-sheng, X. U. E. Jun, and L. I. Song-tao, "High-strength lattice girders supporting performance of highway tunnel with soft broken surrounding rock," *China Journal of Highway and Transport*, vol. 33, no. 2, pp. 125–134, 2020.
- [13] S. C. Li, B. Y. Feng, T. F. Ma, S. C. Li, and X. Ping, "Researches on mechanics behavior of lattice girder reinforced shotcrete support for tunnels," *Journal of China Coal Society*, vol. 39, no. S1, pp. 57–63, 2014.
- [14] L. M. Wang, F. Y. Li, B. Zhang, B. Wen, and G. Yang, "Mechanical property and stability of tunnel boring machine tunnel steel arch support field test," *Science Technology and Engineering*, vol. 20, no. 34, pp. 14223–14228, 2020.
- [15] Y. Song, M. Huang, X. Zhang, Z. Li, and X. Peng, "Experimental and numerical investigation on bearing capacity of circumferential joint of new spatial steel tubular grid arch in mined tunnel," *Symmetry*, vol. 12, no. 12, pp. 2065–2065, 2020.
- [16] H. Hou, S. Ma, Q. Wang, Y. Jin, W. C. Zhu, and L. Chen, "Experimental study on mechanical behavior of concrete-filled thin-walled steel tube supported in tunnel," *Journal of Central South University (Science and Technology)*, vol. 48, no. 5, pp. 1316–1325, 2017.
- [17] J. Z. Wen, Y. X. Zhang, C. Wang, and Z. H. Jiang, "Back analysis for the mechanical properties of initial tunnel support based on steel arch stresses," *China Civil Engineering Journal*, vol. 45, no. 2, pp. 170–175, 2012.

- [18] J. J. Li, Q. N. Chen, X. G. Wang, X. D. Zhang, and G. Zou, "Internal force analysis on tunnel supporting structure considering axial strain," *Chinese Journal of Underground Space and Engineering*, vol. 17, no. 2, pp. 430–438, 2021.
- [19] W. T. Li, N. Yang, T. C. Li, Y. H. Zhang, and G. Wang, "A new approach to simulate the supporting arch in a tunnel based on improvement of the beam element in FLAC^{3D}," *Journal of Zhejiang University-SCIENCE A*, vol. 18, no. 3, pp. 179–193, 2017.
- [20] J. H. Chen, B. J. Chen, Y. Zhuang, L. X. Wang, and M. J. Liu, "Comparison of vertical bearing capacity of tunnel grille arch frame with different cross-section shapes," *Tunnel Construction*, vol. 40, no. s3, pp. 364–370, 2020.
- [21] J. Guo, J. S. Yang, W. Chen, D. Shen, T. Liu, and W. Chai, "Research on large deformation of surrounding rock and mechanical characteristics of lining of carbonaceous slate tunnel based on field measurement," *Chinese Journal of Rock Mechanics and Engineering*, vol. 38, no. 4, pp. 832–841, 2019.
- [22] S. M. Tian, K. F. Wu, D. G. Liu, M. N. Wang, and Z. L. Wang, "Study on active support technology for deformation control of tunnels in soft surrounding rock," *Journal of the China Railway Society*, vol. 43, no. 6, article 158, 2021.
- [23] W. A. N. G. Bo, Y. U. Wei, L. I. U. Jin-chao, W. A. N. G. Zhen-yu, X. U. Jian-qiang, and W. U. De-xing, "Timely-active support theory and its application in transportation/hydraulic tunnels based on pre-stressed anchorage system," *China Journal of Highway and Transport*, vol. 33, no. 12, pp. 118–129, 2020.
- [24] H. Wei, M. Qinyong, Y. Wenhua, and Y. Pu, "Study on mechanism of bolt-shotcrete support and analysis of its mechanical properties in deep rock roadway," *Chinese Journal of Underground Space and Engineering*, vol. 7, no. 1, pp. 28–32, 2011.